Melting and Solidification Phenomena in a Molten Salt Fast Reactor

A Combined Experimental and Numerical Investigation

Kaaks, B.J.

DOI
10.4233/uuid:c566870e-e503-4b37-a7d8-93fbca9488c1

Publication date
2024

Document Version
Final published version

Citation (APA)
Kaaks, B. J. (2024). *Melting and Solidification Phenomena in a Molten Salt Fast Reactor: A Combined Experimental and Numerical Investigation*. [Dissertation (TU Delft), Delft University of Technology]. https://doi.org/10.4233/uuid:c566870e-e503-4b37-a7d8-93fbca9488c1

Melting and Solidification Phenomena in a Molten Salt Fast Reactor

A Combined Experimental and Numerical Investigation

MELTING AND SOLIDIFICATION PHENOMENA IN A MOLTEN SALT FAST REACTOR

A COMBINED EXPERIMENTAL AND NUMERICAL INVESTIGATION

Proefschrift

ter verkrijging van de graad van doctor
aan de Technische Universiteit Delft,
op gezag van de Rector Magnificus prof. dr. ir. T.H.J.J. van der Hagen,
voorzitter van het College voor Promoties,
in het openbaar te verdedigen op maandag 13 mei 2024 om 15:00 uur

door

Bouke Johannes KAAKS

Master of Science in Chemical Engineering,
Technische Universiteit Delft, Delft, Netherlands,
geboren te Rotterdam, Nederland.

Dit proefschrift is goedgekeurd door de

promotor: Dr. ir. M. Rohde
promotor: Dr. ir. D. Lathouwers
copromotor: Prof. Dr. ir. J.L. Kloosterman

Samenstelling promotiecommissie:

Rector Magnificus,	voorzitter
Dr. ir. M. Rohde,	Technische Universiteit Delft, promotor
Dr. ir. D. Lathouwers,	Technische Universiteit Delft, promotor
Prof. Dr. ir. J.L. Kloosterman,	Technische Universiteit Delft, copromotor
Onafhankelijke leden:	
Prof. dr. S. Kenjereš	Technische Universiteit Delft
Prof. dr. ir. D. Brüggemann	Universiteit van Bayreuth
Prof. dr. R. Pecnik	Technische Universiteit Delft
Prof. dr. C. Markides	Imperial College London

Keywords: Molten salt reactor, Solid-liquid phase change, Benchmark experiments, ESPRESSO, Particle Image Velocimetry, Laser Induced Fluorescence, Numerical phase change modelling, Linearized Enthalpy approach, Energy-conservative discontinuous Galerkin method, Finite volume method, Adaptive mesh refinement, Residual error estimate, Freeze-valve, Numerical benchmark exercise

ISBN 978-94-6496-115-7

Printed by: Gildeprint - Enschede

This research was performed in the Reactor Physics and Nuclear Materials (RPNM) group of the Department of Radiation Science and Technology (RST) of Delft University of Technology (Delft, Netherlands). This project has received funding from the Euratom research and training programme 2014–2018 under grant agreement no. 847527.

An electronic version of this dissertation is available at
http://repository.tudelft.nl/.

CONTENTS

SUMMARY

Over the next couple of decades, the world will face the challenge of drastically reducing carbon emissions. Innovative Generation-IV nuclear reactor designs can play an important role in driving this energy transition. One of these designs is the Molten Salt Fast Reactor (MSFR), characterized by a fast neutron spectrum and the use of a liquid fuel. Because of the liquid fuel, melting and solidification phenomena need to be considered. To this end, this thesis presents a combined experimental and numerical investigation of melting and solidification phenomena in the MSFR. The experimental part was primarily motivated by the lack of suitable experimental data for the transient development of an ice-layer in internal flow, which is a relevant case for the analysis of accident scenarios in a MSFR where solidification may pose a risk. The main focus of the numerical part was to improve the computational efficiency of current state-of-the-art melting and solidification models.

As part of the experimental investigation, a new experimental facility (ESPRESSO) was designed and built (described in chapter 2). The ESPRESSO facility consists of a water tunnel capable of reaching both laminar and turbulent flow rates, in which ice is grown from a cold plate at the bottom of a square channel. The ESPRESSO facility was designed to have well-described experimental boundary conditions, through careful consideration of the inflow and cold-plate specifications. Subsequently, experimental data was generated for the transient development of an ice layer in laminar internal flow using particle image velocimetry (PIV), which may be used for numerical validation purposes (see chapter 3 for more information on the experimental investigation and chapter 5 for the numerical validation). The onset of ice formation was found to coincide with a sudden increase of the cold-plate temperature, which was therefore used to identify the zero time instant in our experiments. This was attributed to subcooling effects prior to nucleation, of which evidence was obtained using laser induced fluorescence (LIF) temperature measurements, detailed in chapter 4.

In addition, non-intrusive temperature measurements have been performed for the transient development of an ice layer in laminar channel flow using LIF, which is so far only the second application of LIF as a non-intrusive temperature measurement technique in solid-liquid phase change experiments. The LIF method presented in this thesis is a novel approach for solid-liquid phase change experiments because of the use of a two color (instead of a one color) technique, the use of a post-processing algorithm to remove top to bottom striations and reduce other measurement noise, and a detailed analysis of the uncertainty in the temperature fields. Good results were obtained for sufficiently large temperature differences of approximately 15 °C with an uncertainty of $\sigma = 0.3 - 0.5$°C, however further improvements are needed to remove artefacts as a result of laser light scattering from the solid-liquid interface, and to obtain a sufficiently high accuracy for numerical validation purposes, especially for smaller temperature differences.

The numerical work performed as part of this thesis aims to address the need for more efficient melting and solidification models, which can accurately capture the solid-liquid interface and resolve the recirculation zones in the fluid region at a lower computational cost. To this end, an energy-conservative DG-FEM approach based on the 'linearized enthalpy melting/solidification model' was developed and validated in chapter 5. Although certain solid-liquid phase change problems with strong gradients in the flowfield can benefit from the use of the higher order DG-FEM method, overall a suboptimal O(h) mesh convergence rate was obtained due to an inaccurate numerical solution of the discontinuities at the solid-liquid interface. Therefore, further development of the DG-FEM solid-liquid phase change solver is needed to fully benefit from the arbitrarily high order of accuracy of the hierarchical polynomial basis function set.

Very promising results were obtained with a parallel finite volume adaptive mesh refinement method for solid-liquid phase change (see chapter 6). Cells were refined based on the maximum difference in the liquid fraction over the cell faces and the estimated numerical discretization error in the flow and temperature fields, using the cell residual method. With this approach, a very good agreement was obtained between the adaptive mesh results and the reference solutions on a uniformly refined grid with significantly less degrees of freedom. This demonstrates the potential of the proposed finite volume adaptive mesh refinement approach as a more computationally efficient numerical method for solid-liquid phase change problems.

The final part of this thesis details a five-stage benchmark for modelling phase change in molten salt reactors, modelled after the MS(F)R freeze-valve design (chapter 7). With each stage, an additional layer of complexity is added, which enabled the identification of potential sources of discrepancy between different numerical modelling approaches. Results were obtained with three different codes: STAR-CCM+, OpenFOAM and DGFlows (inhouse DG-FEM based code for computational fluid dynamics). The results from the benchmark showed an overall good agreement between the three codes, although some discrepancies were observed when adding conjugate heat transfer effects. Therefore, we recommend some caution when coupling different solid-liquid phase change and conjugate heat transfer modelling approaches.

To summarize, this thesis presents new experimental data for the transient ice-growth in laminar internal flow, driven by a general lack hereof. In addition, this thesis illustrates the potential of LIF as a non-intrusive temperature measurement technique for solid-liquid phase change experiments. Two new numerical methods were developed and validated for solid-liquid phase change problems, and especially the finite volume adaptive mesh refinement approach showed promising results in terms of enhanced computational efficiency. On a final note: solid-liquid phase change is a vast and ongoing field of research. We believe this thesis is a substantial addition to the field, yet there are still a lot of opportunities for future work. Some suggestions are given in the concluding chapter (chapter 8).

SAMENVATTING

De komende decennia staat de wereld voor de uitdaging om de koolstofuitstoot drastisch te verminderen. Innovatieve Generatie-IV nucleaire reactorontwerpen kunnen een belangrijke rol spelen in deze energietransitie. Een van deze ontwerpen is de Molten Salt Fast Reactor (MSFR), gekenmerkt door een snel neutronenspectrum en het gebruik van vloeibare brandstof. Vanwege de vloeibare brandstof moet er rekening worden gehouden met smelt- en vriesverschijnselen. Daarom presenteert dit proefschrift een gecombineerd experimenteel en numeriek onderzoek naar smelt- en vriesverschijnselen in de MSFR. Het experimentele deel werd voornamelijk gemotiveerd door het gebrek aan geschikte experimentele gegevens voor de tijdsafhankelijke ontwikkeling van een ijslaag in interne stroming, wat een relevant geval is voor de analyse van ongevalsscenario's in een MSFR waarbij bevriezing een risico kan vormen. Het voornaamste doel van het numerieke deel was het verbeteren van de rekenefficiëntie van de huidige state-of-the-art smelt- en vriesmodellen.

Als onderdeel van het experimentele onderzoek werd een nieuwe experimentele opstelling (ESPRESSO) ontworpen en gebouwd (beschreven in hoofdstuk 2). De ESPRESSO opstelling bestaat uit een watertunnel die zowel laminaire als turbulente stroomsnelheden, waarin ijsgroei plaatsvindt vanaf een koelplaat aan de onderkant van een vierkant kanaal. De ESPRESSO opstelling werd ontworpen om goed beschreven experimentele randvoorwaarden te hebben, door zorgvuldige overweging van de specificaties van de instroom en de koelplaat. Vervolgens werden experimentele gegevens gegenereerd voor de tijdsafhankelijke ontwikkeling van een ijslaag in laminaire kanaal stroming met behulp van deeltjesbeeldsnelheidsmeting (PIV), die die gebruikt kunnen worden voor numerieke validatiedoeleinden (zie hoofdstuk 3 voor meer informatie over het experimentele onderzoek en hoofdstuk 5 voor de numerieke validatie). Het begin van ijsvorming bleek samen te vallen met een plotselinge stijging van de temperatuur van de koelplaat, die daarom werd gebruikt om het nultijdstip in onze experimenten te identificeren. Dit werd toegeschreven aan overkoelingseffecten voorafgaand aan de nucleatie, waarvoor bewijs werd verkregen met behulp van laser geïnduceerde fluorescentie (LIF) temperatuurmetingen, gedetailleerd beschreven in hoofdstuk 4.

Daarnaast zijn er niet-intrusieve temperatuurmetingen uitgevoerd voor de tijdsafhankelijke ontwikkeling van een ijslaag in laminaire kanaalstroming met behulp van LIF, wat pas de tweede toepassing van LIF is als niet-intrusieve temperatuur meettechniek in smelt-vries experimenten tot nu toe. De in dit proefschrift gepresenteerde LIF-methode is een nieuwe benadering voor smelt- en vriesexperimenten vanwege het gebruik van een tweekleurentechniek (in plaats van één kleur), het gebruik van een nabewerkingsalgoritme om strepen van boven naar beneden te verwijderen en andere meetruis te verminderen, en een gedetailleerde analyse van de onzekerheid in de temperatuurvelden. Er werden goede resultaten verkregen voor voldoende grote temperatuurverschillen van ongeveer 15 °C met een onzekerheid van $\sigma = 0,3-0,5$°C. Verdere verbeteringen zijn ech-

ter nodig om artefacten als gevolg van verstrooiing van laserlicht aan het vast-vloeibaar grensvlak te verwijderen en om een voldoende hoge nauwkeurigheid te verkrijgen voor numerieke validatiedoeleinden, vooral voor kleinere temperatuurverschillen.

Het numerieke werk dat is uitgevoerd als onderdeel van dit proefschrift is gericht op de behoefte aan efficiëntere smelt- en vriesmodellen, die het vast-vloeibaar grensvlak nauwkeurig kunnen weergeven en de recirculatiezones in het vloeistofgebied kunnen oplossen tegen lagere rekenkosten. Hiertoe werd een energiebehoudende DG-FEM aanpak gebaseerd op het 'gelineariseerde enthalpie smelt/vries model' ontwikkeld en gevalideerd in hoofdstuk 5. Hoewel bepaalde vast-vloeibaar faseovergangsproblemen met sterke gradiënten in het stromingsveld voordeel kunnen halen uit het gebruik van de hogere orde DG-FEM methode, werd over het algemeen een suboptimale O(h) mesh convergentiesnelheid verkregen door een onnauwkeurige numerieke oplossing van de discontinuïteiten op het vast-vloeistof grensvlak. Daarom is verdere ontwikkeling van de DG-FEM vast-vloeibaar faseovergang solver nodig om volledig te profiteren van de willekeurig hoge nauwkeurigheidsorde van de hiërarchische polynomiale basisfunctieset.

Veelbelovende resultaten werden verkregen met een parallelle eindige-volume adaptieve mesh verfijningsmethode voor vast-vloeibaar faseovergang (zie hoofdstuk 6). Cellen werden verfijnd op basis van het maximale verschil in de vloeistoffractie over de celvlakken en de geschatte numerieke discretisatiefout in de stromings- en temperatuurvelden, met behulp van de cel residu methode. Met deze aanpak werd een zeer goede overeenkomst verkregen tussen de resultaten van de adaptieve meshes en de referentieoplossingen op een uniform verfijnd rooster met aanzienlijk minder vrijheidsgraden. Dit toont het potentieel aan van de voorgestelde eindige volume adaptieve mesh verfijningsmethode als een rekenkundig efficiëntere numerieke methode voor problemen met vast-vloeibaar faseovergang.

Het laatste deel van deze scriptie beschrijft een vijf-traps benchmark voor het modelleren van faseovergang in gesmolten zoutreactoren, gemodelleerd naar het MS(F)R vriesklep ontwerp (hoofdstuk 7). Met elke trap wordt een extra laag complexiteit toegevoegd, waardoor potentiële bronnen van discrepantie tussen verschillende benaderingen van numerieke modellering konden worden geïdentificeerd. Er werden resultaten verkregen met drie verschillende codes: STAR-CCM+, OpenFOAM en DGFlows (eigen DG-FEM gebaseerde code voor computationele vloeistofdynamica). De resultaten van de benchmark toonden over het algemeen een goede overeenkomst tussen de drie codes, hoewel er enkele discrepanties werden waargenomen bij het toevoegen van geconjugeerde warmteoverdrachtseffecten. Daarom raden we enige voorzichtigheid aan bij het koppelen van verschillende benaderingen voor het modelleren van vast-vloeibaar faseovergang en geconjugeerde warmteoverdracht.

Samengevat presenteert dit proefschrift nieuwe experimentele gegevens voor de tijdsafhankelijke ijsgroei in laminaire interne stroming. Daarnaast illustreert dit proefschrift het potentieel van LIF als een niet-intrusieve temperatuurmeettechniek voor experimenten met een vast-vloeibaar faseovergang. Twee nieuwe numerieke methoden werden ontwikkeld en gevalideerd voor vast-vloeistof faseovergangsproblemen, en vooral de eindige-volume adaptieve mesh verfijning aanpak toonde veelbelovende resultaten in termen van verbeterde rekenefficiëntie. Tot slot: vast-vloeibaar faseovergangen zijn een omvangrijk en voortdurend onderzoeksgebied. Wij geloven dat dit proefschrift een substantiële toevoeging is aan het vakgebied, maar toch zijn er nog veel mogelijkheden voor toekomstig werk. Enkele suggesties worden gegeven in het afsluitende hoofdstuk (hoofdstuk 8).

1

INTRODUCTION

1.1. The need for innovative nuclear reactor designs

In 2015, 197 countries adopted the Paris Agreement, a legally binding international treaty to "limit the increase in the global average temperature to well below 2 °C above pre-industrial levels" [1]. In recent years, world leaders have adopted the more stringent target of limiting global warming to a maximum of 1.5 °C, based on an IPCC report stressing the dangers of exceeding this threshold [2]. Consequently, the European Union has made a commitment to reduce the net greenhouse gas emissions by 55% in 2030 (compared to 1990 levels), and to achieve net carbon neutrality by 2050 [3]. However, to reach the 1.5 °C threshold target, a rapid and drastic transformation of the world energy supply is needed within the next decades. In 2022, human-induced global warming had already reached an estimated 1.26 °C [4], and will exceed 1.5 °C in 2032 with a 50% likelihood based on the current global emissions [5].

At the same time, energy demands are increasing. In particular, the generation of electricity, already accounting for one third of the global energy-related CO_2 emissions in 2021, is projected to rise by 25-30% in 2030 [6]. In addition, Europe has recently adopted a policy of pursuing energy independency aiming to reduce the reliance on imported fossil fuels [7]. Decarbonizing the electricity grid can accommodate both the need for cutting down on the global CO_2 emissions whilst at the same time ensuring energy security in the face of mounting geopolitical tensions. At the moment, nuclear energy is the second largest source of low-carbon electricity (after hydro-power), responsible for 10% of the global electricity supply in 2018 [8]. Compared to (other) renewables such as wind or solar power, nuclear power has the advantage of having a high energy density and being non-intermittent. As such, nuclear power can provide a reliable and stable electricity supply without depending on fossil-fired backup power or large scale energy storage [9]. On average, the IPCC foresees a tripling of the nuclear energy output by 2050 in the future energy pathways consistent with the 1.5 °C scenario [2]. However, public opinion on nuclear power is mixed with opponents raising concerns regarding the safety, the production and long-term storage of radioactive waste, and the possible use for military purposes.

In 2001, the Generation IV International Forum (GIF) was formed, resulting in the selection of six innovative nuclear reactor designs that are inherently safer, more sustainable, economically viable and more proliferation resistant [10]. These are the Very High Temperature Reactor (VHTR), the Molten Salt (Fast) Reactor (MS(F)R), the Supercritical Water Cooled Reactor (SWCR), the Gas-cooled Fast Reactor (GFR), the Sodium-cooled Fast Reactor (SFR) and the Lead-cooled Fast Reactor (LFR). Research is currently ongoing to bring these innovative nuclear reactor designs to a higher technology readiness level. This thesis focuses on the MS(F)R, characterized by the use of liquid fuel (i.e. molten salt). As a consequence, solid-liquid phase change can play a role during both the steady-state and the transient operation of the reactor. In this context, we present a combined experimental and numerical investigation of melting and solidification phenomena. Our aim is that the knowledge generated by this thesis will be applied to the analysis of the MS(F)R, and to other applications where solid-liquid phase change plays a role such as latent heat storage or metallurgy.

1.2. A brief history of the Molten Salt Reactor

Molten Salt Reactors were originally developed at Oak Ridge National Laboratory (ORNL), in first instance to create a nuclear powered military aircraft. In 1954, the Aircraft Reactor Experiment (ARE) was performed [11], [12]. After the interest for military purposes had faded, the potential of the technology for civilian applications was investigated. Between 1964 and 1969, the Molten Salt Reactor Experiment (MSRE) was operated, consisting of a 8 MW_{th} reactor in which molten fluoride salt was recirculated at around 650 °C through an assembly of vertical graphite bars acting as the moderator [13], [14]. The MSRE operations were considered a success, and as a result the Molten Salt Breeder Reactor (MSBR) was proposed, a 1000 MW_{th} single fluid thermal reactor operating on the Th_{232}-U_{233} fuel cycle [15]. The proposed fuel consisted of a molten salt mixture of the fluorides of lithium, beryllium, thorium and uranium, i.e. $LiF-BeF_2-ThF_4-UF_4$ (71.7-16.0-12.0-0.3 mole %). Despite the good results obtained from the MSRE operation, the program was terminated in favor of the competing liquid-metal breeder reactor technology and little progress was made until 2002, when the decision by the Generation IV International Forum (GIF) to select the MS(F)R as one of the six Generation IV reactor concepts led to a renewed interest in the MS(F)R technology.

Nowadays, a variety of MSR concepts are being investigated worldwide [16], such as the TMSR (Thorium Molten Salt Reactor) in China [17], the MSR-FUJI in Japan [18], MOSART (MOlten Salt Actinide Recycler and Transmuting system) in Russia [19] and the Molten Salt Fast Reactor (MSFR) in Europe. In addition, several startups have been founded in recent years aiming to commercialize molten salt reactor technology, amongst which Seaborg and Copenhagen Atomics in Denmark, Moltex Energy and Terrestrial Energy in Canada, FliBe Energy and TerraPower in the USA and Thorizon in the Netherlands.

This thesis was performed in the context of the Euratom Horizon 2020 project Severe Accident MOdelling and Safety Assessment for Fluid-fuel Energy Reactors (SAMOSAFER, https://samosafer.eu/). SAMOSAFER builds on the results of the SAMOFAR project and aims to develop and demonstrate new safety barriers for a more controlled behaviour of the MSFR in severe accident scenarios, such that the MSFR may comply with all safety

regulations in 30 years time. For this reason, we focus on the MSFR in the remainder of this introductory chapter (although many of the points covered also apply to other MSR designs).

1.3. The Molten Salt Fast Reactor

The MSFR concept is based on a re-evaluation of the MSBR design, which found that the fuel reprocessing required to achieve the desired high breeding ratio was very complex [20], [21]. In addition, modern numerical simulations showed that the global feedback coefficient of the MSBR system was positive, which could produce unstable (and therefore unsafe) reactor behaviour in some situations [21]. A fast spectrum reactor was found to solve both problems, leading to the MSFR concept which has large negative feedback coefficients and lower fuel reprocessing requirements compared to the MSBR [22]. The MSFR and the MOSART concept represent the two fast-spectrum MSRs currently researched within the GIF framework [23].

Figure 1.1 shows a schematic overview of the MSFR power plant. The current design under study consists of a 3000 MW_{th} reactor with a total fuel salt volume of 18 m^3, operated at an average temperature of 725 °C [24]. Two fuel compositions are being investigated at the moment [25]. These are the U^{233} based $LiF-ThF_4-U^{233}F_4$ (77.5-20-2.5 mole %) and the $TRU-U^{235}$ based $LiF-ThF_4-U^{enr}F_4-(TRU)F_3$ (77.5-6.6-12.3-3.6 mole %), where the transuranium elements (TRU) consist mainly of plutonium and the uranium is enriched at 13%. The liquid salt enters the reactor core from the bottom and flows to the top while heating up by approximately 100°C, before exiting the core to one of the sixteen groups of pumps and heat exchangers equally divided around the core [26]. The core is surrounded by radial neutron reflectors which include a $LiF-ThF_4$ (77.5-22.5 mole %) breeding blanket, and thick top and bottom reflectors made from nickel-based alloys [26]. The energy released by the nuclear fission is transferred to the energy conversion system through an intermediate energy system.

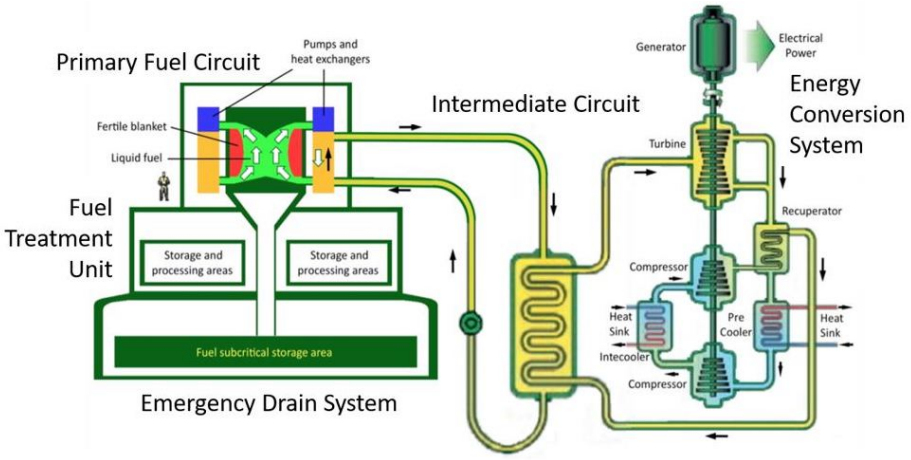

Figure 1.1: Schematic representation of the MS(F)R power plant.

The use of a liquid fuel, together with the fast neutron spectrum, give the MSFR several advantages compared to conventional generation II and generation III nuclear reactor types (such as the pressurized water reactor, the boiling water reactor, and the European pressurized water reactor) in terms of safety, fuel consumption and radioactive waste production and economic viability which are summarized below [16], [27]–[30]:

- (Inherent) safety. Due to the use of a liquid fuel, continuous online refueling becomes possible, meaning a lower excess reactivity can be maintained. No fuel cladding is needed, so leakage of fission products from the cladding is not an issue. In addition, the strong negative temperature and Doppler feedback coefficients of the fuel effectively makes the reactor self-regulating. Because the fuel has a very high boiling point (around 2000 K) and a low vapor pressure, the reactor can be operated at a comparatively low pressure, reducing the risk of pipe breaks. In addition, since the reactor is not cooled by water, no steam or hydrogen explosion can occur during accident scenarios. Finally, a key passive safety component of the MSFR is the freeze valve. The freeze valve is located below the reactor core and is designed to melt in case of a reactor anomaly (such as a loss of coolant accident, a loss of flow accident or a temperature excursion), draining the salt into an emergency drainage system (EDS). The EDS is designed to ensure subcriticality by geometrical design and a passive removal of the decay heat. Because of these safety features, an uncontrolled/inadvertent release of radioactive substances to the environment is much less likely, compared to current reactor designs.

- Fuel consumption and radioactive waste production. Thorium is approximately four times as abundant as natural uranium in the earth's crust, therefore the use of a thorium fuel cycle would expand the global nuclear fuel supply. In addition, the continuous salt re-circulation combined with the onsite removal of fission products in the chemical processing plant (see figure 1.1) through a combination of chemical and physical (i.e. helium bubbling) processing results in a better fuel utilization (as well as being required for achieving a sufficiently high breeding ratio). The thorium fuel cycle produces less actinides compared to the uranium fuel cycle, and the burning of actinides in the reactor is enhances through the fast spectrum. This leads to an overall much lower long-term radio-toxicity of the produced radioactive waste, which reaches the level of natural uranium ore within 'only' a few hundred years as opposed to ten thousand years as is the case for traditional nuclear reactor designs.

- Economic viability. The ambient operating pressure and the high heat capacity of the salt facilitate the production of compact, less expensive nuclear reactor designs which can be mass produced and shipped to reactor sites, reducing construction costs. Because of the liquid fuel, the manufacture of the fuel elements is no longer required and there is no need to shut down the reactor for refueling. Finally, the high operating temperature of approximately 700 °C improves the efficiency of electricity generation to over 44 % compared to 33 % for the current light water reactors.

Evidently, there are many benefits associated with the MS(F)R. However, several (technological) challenges need to be addressed to bring the current reactor designs to a sufficiently high technology readiness level. Some of these challenges are summarized below:

- Current structural alloys, such as Hastelloy N and 316 stainless steel are not resistant to corrosion in the molten salt high temperature environment [31], [32]. Research to find more suitable materials is still ongoing.
- Our knowledge of the thermodynamics and chemistry of the salt and its fission products is still incomplete. Research is ongoing in order to construct a sufficiently complete database with the thermal-physical and the thermodynamic properties of the various salt systems [33]–[39].
- Due to the significant differences between the MS(F)R and conventional nuclear reactor designs, a new framework with suitable safety requirements for licensing is required [40]–[42].
- The chemical and physical processes to clean the salt online (for instance through helium bubbling) and properly process the (radioactive) waste for storage are still under development [43], [44].
- Proliferation concerns. U^{233} is bred from Th^{232} through the following reaction:

$$Th_{90}^{232} + n \xrightarrow{\beta^-} Th_{90}^{233} \xrightarrow{\beta^-} Pa_{91}^{233} \xrightarrow{\beta^-} U_{92}^{233}. \tag{1.1}$$

  By separating protactinium from thorium, the fissile material U^{233} (slightly contaminated with up to 400 ppm U^{232}) can be obtained [45]. Whilst it would be impossible to divert nuclear materials directly from the salt recirculating in the reactor, appropriate safeguards need to be designed to avoid misuse of the salt reprocessing plant [46].
- The use of a liquid, recirculating fuel presents additional challenges in terms of modelling and simulation of the MSFR (a key aspect during the design and licensing stage), as opposed to conventional nuclear reactors where the fuel is solid and static. Amongst these challenges are a stronger coupling between the neutronics and the thermohydraulics [47] and an accurate modelling of solid-liquid phase change [29], [48].

1.4. Melting and solidification in the MS(F)R

One of the consequences of the use of a liquid fuel is that melting and solidification phenomena play a role both during the normal operation of the MSF(R) and during accident transients. During normal operation, a thin layer of frozen salt may form at the core vessel wall of the MS(F)R, protecting the wall against corrosion by the molten fuel salt [49]. The two accident scenarios in the MS(F)R where melting or solidification plays a role are a sudden solidification in the heat exchangers and the melting of the freeze valve. Since the goal of the SAMOSAFER project is to demonstrate the safety barriers of the MSFR, we mainly focus on the latter.

1.4.1. Freezing inside the heat exchanger

One of the challenges when working with molten salt is its high melting point. Therefore, protective measures are needed to prevent the salt from cooling down too much [30]. Freezing in a MSR is mainly a risk in the heat exchangers and can lead to equipment damage through volumetric expansion of the salt due to phase change and to clogging of the pipes, preventing the circulation of fluid for heat removal [50]. These issues were already recognized during the Molten Salt Reactor Experiment, which featured a series of auxiliary electric heaters to prevent the salt from solidifying [13]. However, these safety features relied on an external power supply and are therefore not in line with the generation IV reactor design philosophy regarding passive safety requirements.

So far, the risk of salt freezing has been mainly analyzed with respect to the direct auxiliary cooling system (DRACS) of the Fluoride-salt-cooled High-temperature Reactor (FHR) which combines features of the high-temperature gas-cooled reactors and molten salt reactors [50]–[53]. In the FHR, the molten salt only serves as the coolant and not the fuel. Therefore, no internal heat generation takes place, making the FHR particularly sensitive to undesirable freezing. The DRACS has been designed to ensure the passive heat removal during abnormal reactor conditions. Solidification inside the DRACS loop and subsequent blockage could therefore lead to loss of function and trigger a severe reactor accident such as the degradation of the reactor core as a result of the loss of heat sink [53]. Whilst these studies are not directly applicable to the MSFR, it is expected that freezing in the MSFR can lead to similar harmful consequences. For instance, it has been shown that the inlet temperature of the fuel salt can be reduced to below the melting point during an unprotected loss of flow (ULOF) accident or during fuel salt overcooling (for instance caused by a depressurization of the steam generator), possibly leading to freezing within the heat exchangers [54], [55].

1.4.2. The freeze valve

The freeze-valve is a key safety component of the MS(F)R, consisting of a valve made of frozen fuel salt located below the reactor core (see figure 1.1). The freeze-valve is designed to melt in case of an accident scenario, draining the reactor core into the emergency drainage system. According to a preliminary safety assessment, the draining should commence within approximately 480 s to avoid reaching a temperature of 1200 °C, at which structural damage may occur [56]. Therefore, the freeze-valve needs to have a short enough opening time.

Freeze-valves were first used in the Molten Salt Reactor Experiment due to the difficulty in finding a mechanical valve which was suitable for the aggressive environment of the molten salt system [57]. The horizontally-oriented MSRE freeze valves were frozen within approximately 5-10 min using high pressure compressed cooling air and thawed within approximately 10-15 min using radiant heater elements. However, due to the reliance on auxiliary heating, the MSRE freeze valve was not a passive safety system. A similar design to the MSRE is now being investigated in the context of the Thorium Molten Salt Reactor (TMSR) pilot project in China [58], [59]. Recently, an enhanced concept was investigated where fins were added to the pipe containing the freeze plug, allowing the salt to freeze without active cooling (but still requiring auxiliary heaters in order to melt the plug) [60].

The reference configuration of the MSFR includes a vertically-oriented freeze valve at the base of each of the sixteen fuel loops of the primary circuit (see figure 1.1). The design of the freeze valve is similar to those of the MSRE, however the freeze-valve must melt passively, relying on the transfer of the decay heat to the plug through the draining pipe walls. However, a preliminary numerical investigation showed that a freeze valve relying exclusively on the decay heat most likely does not melt fast enough, unless the freeze valve is located within 0.01 m of the reactor core [29]. However, such a small distance is undesirable, due to a risk of the freeze valve melting during normal operation as a result of temperature oscillations in the liquid fuel. Both a single- and a multi-plug configuration were investigated. As a result of the inefficient melting of the thin layer of frozen salt above the metal plate containing the multiple plugs, the single-plug configuration was shown to have the better performance [29].

In order to reduce the melting time of the freeze-valve, the SWATH (Salt at Wall: Thermal excHanges) freeze valve design proposes the addition of steel masses to the freeze valve pipe, as shown in figure 1.2 [61]. During normal operation, the steel masses are actively heated. During an accident scenario requiring the draining of the plug, both the cooling and heating are stopped and the thermal energy stored in the steel mass is transferred to the solid plug by means of conduction, causing it to melt passively. A combined experimental and numerical study predicted an opening time of around 380 s, well within the target time of 480 s [61]. In addition, it was shown that a shorter melting time could be obtained by increasing the thickness of the freeze valve tube wall [62] or by adjusting the inclination angle of the plug in order to enhance natural convection [63], [64]. Alternatively, a c-shaped freeze-valve was investigated, based on better pressure resistance compared to the conventional cylindrical valves and an easier manufacture process [65]. For a recent and comprehensive overview of the freeze valve design and development, see *Chisholm et al.* [66].

1.5. Current state of the art of melting and solidification research

Melting and solidification phase change has been studied extensively in literature due to its complex physical and mathematical behavior and its importance in applications such as metallurgy [67]–[69], latent heat storage [70], [71] and the MS(F)R. Modelling and simulation are key aspects while designing and licensing nuclear power plants, and MS(F)R's are amongst the most challenging reactors to model and simulate [72]. Part of the reason is the role of melting and solidification, which despite extensive research is still difficult to solve numerically due to the mathematical complexity of solving the moving boundary problem, with a discontinuity in both the enthalpy and the temperature gradient at the solid-liquid interface. Therefore, it is crucial to validate the developed numerical solvers with high fidelity experimental data.

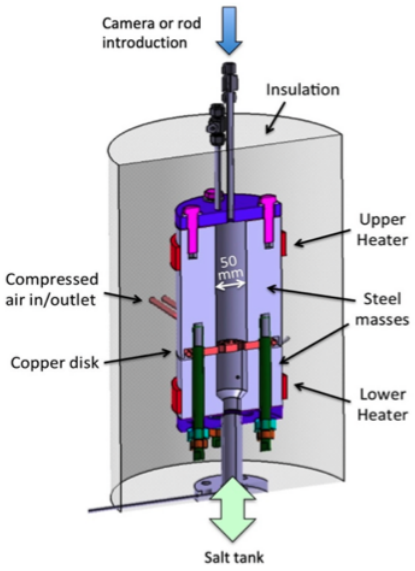

Figure 1.2: Schematic representation of the SWATH freeze valve design [61].

1.5.1. Experimental investigations

Boger et al. [73] was the first to obtain experimental evidence of the role of natural convection during the melting and freezing of water in a rectangular cavity, observing that natural convection enhanced the melting and retarded the freezing. Further prove of the role of natural circulation during the melting process was provided by *Sparrow et al.* [74] and *Hale et al.* [75]. Subsequently, many experimental studies have been performed on melting or freezing in an enclosure, characterized by a natural convection heat transfer regime. Examples are the melting of gallium in a rectangular enclosure with a heated side wall [67], [69], the melting of octadecane in a rectangular enclosure with a heated side-wall [70], [71] and the freezing of water in a cubical enclosure [76].

However, few of these studies are suitable for numerical benchmarking purposes. The majority of the numerical articles still compare their results to the classical gallium melting experiment of *Gau et al.* [67], who used the intrusive pour-out method for evaluating the solid-liquid interface and thermocouples for measuring the temperatures. However, thermocouples distort the flow field within the liquid phase and potentially affect the melting and freezing process, as demonstrated by *Tan et al.* [77]. In addition, the use of insufficient insulation may have led to considerable heat losses to the environment. For this reason, recent efforts have been dedicated towards using non-intrusive techniques for measuring the solid-liquid interface, the flow-field and the temperatures during the melting and freezing process using optical imaging techniques, and to impose well-described experimental boundary conditions through careful temperature control [78] or thermal insulation [71].

On the other hand, relatively few experiments have been performed for melting or freezing in a forced or mixed convection heat transfer regime, as opposed to melting or freezing in a natural convection heat transfer regime. The earliest experimental investigations of freezing in forced convection flow provided data on the heat-transfer at the cooled wall as well as evidence of sub-cooling of the liquid phase [79]–[81]. Subsequent investigations focused on steady state freezing under a laminar flow regime [82], [83] [84], the effect of a transition from laminar to turbulent flow on the morphology of the ice layer [85]–[90] and the conditions under which a so-called freeze-off may occur [91].

Whereas the previous studies focused on the study of the steady state ice layer (or the question of whether a steady state ice layer may be formed under a given condition), the transient development of an ice-layer in internal flow has mainly been studied theoretically using an analytical or numerical treatment (see for instance *Ozisik et al.* [92] or *Weigand et al.* [93]). This is believed to be due to the difficulty in accurately measuring the increase in the ice-layer thickness [52]. Only four relevant studies detailing the transient development of the ice layer were found in literature. These are the freezing of water flowing over a chilled flat plate experiment by *Savino et al.* [94] performed in the 1960s and three recent studies including a study of the transient melting of an ice layer formed in a cylinder with a rotating lid after the onset of turbulent mixing [95], the study of the transient development of ice-scallops in a turbulent channel flow [96], and the study of the transient development of an ice layer in a laminar flow between two parallel plates under a constant heat flux condition [52]. As such, experimental data suitable for the numerical validation of the transient growth of an ice layer in internal flow is currently not sufficiently available. It should be noted that the transient growth of an ice layer in internal flow is a case particularly relevant to the analysis of accident scenarios in a MS(F)R where solidification of the salt is a risk.

1.5.2. Numerical modelling

Many different approaches exist to modelling melting and solidification problems (such as the transformed grid approach [97], [98], the level-set method [99]–[102] and the phase field method [103]–[107]). In this thesis, we chose to restrict ourselves to implicit fixed grid approaches. Here, 'implicit fixed grid' refers to the solution of the melting/solidification problem on a single fixed domain where the solid-liquid interface is tracked implicitly, i.e. the interface position is inferred from the enthalpy or temperature field at the current time-step, instead of being obtained by solving a separate equation. This approach has the advantage of being applicable to a wide range of melting and solidification problems, not requiring mesh deformation, co-ordinate transformation or grid-generation and not having to calculate interface curvatures, impose boundary conditions at the interface or having to deal with complex thermodynamic derivations. For this reason, the implicit fixed grid approach has been the most popular choice for modelling macroscale phase change phenomena in industrial applications.

The most widely used implicit fixed grid methods are the apparent heat capacity method, which accounts for the latent heat release through a modified form of the heat capacity around the melting point [108]–[110], and the source-based enthalpy approach [111]–[113] where the latent heat release is captured through a source term. The trade-off between these two methods is speed versus robustness. Whilst the apparent heat capacity method is fast, a naive implementation of the method (such as using too large time-steps, a too small mushy zone or a too fine mesh without the proper precautions) can lead to an incorrect amount of the latent heat being released and therefore a deteriorated solution quality [114]. On the other hand, the source-based enthalpy approach requires an iterative procedure and can be slow to converge. To overcome these deficiencies, the 'linearized enthalpy approach' (also referred to as 'a generalized enthalpy approach' or 'an optimum approach') has been developed [115]–[119]. With this approach, the volumetric enthalpy is linearized around the latest temperature values and the energy equation is iterated until convergence has been reached. Compared to the source-based approach, the 'linearized enthalpy approach' requires significantly less non-linear iterations to converge the energy equation [118]. In addition, the 'linearized enthalpy approach' does not necessarily depend on the use of a so-called 'mushy zone', eliminating the energy error arising from the smearing of the latent heat peak in the model equations. In order to impose the no-slip condition at the solid-liquid interface, typically the *Darcy* source term approach is used [120], which mimicks the Carman-Kozeny pressure drop equation for a porous material and drives the velocity to zero in the solid [113].

An important drawback of implicit fixed grid methods is their relatively low accuracy in capturing the melting or solidification front. This is mainly due to the difficulty of resolving the discontinuity in the enthalpy and temperature solutions within the cell leading to a maximum mesh convergence rate of O(h) [121]–[123]. In addition, a high mesh resolution may be required for properly resolving the recirculation zones in the fluid region [124]. Therefore, often a very fine mesh is needed locally in order to obtain grid-independent results [97], [98], [124]. This will result in a considerable increase of computational time when using a uniform mesh, even for 2D cases. In order to improve the computational efficiency of the implicit fixed grid approach for modelling melting and solidification problems, recent studies have investigated the use of finite elements with adaptive mesh refinement algorithms [125], [126], using extended finite element methods [101], [127], [128] or using discontinuous Galerkin finite element methods (DG-FEM) [129]–[132] for solving solid-liquid phase change problems. The present work presents both a discontinuous Galerkin discretization of the linearized enthalpy solid-liquid phase change model, and a finite volume adaptive mesh refinement implementation.

1.6. Content of this thesis

This thesis consists of both an experimental and a numerical part. The experimental campaign performed as part of this thesis was mainly driven by the current lack of suitable experimental data for the transient development of an ice layer in forced internal flow. The numerical methods developed in this thesis address the need for more accurate and computationally efficient solid-liquid phase change models.

Chapter 2 covers the design of the ESPRESSO (ExPeriment for RE-melting and Salt SOlidification) facility, in which transient freezing experiments were performed. The ESPRESSO facility features a flow loop containing a square channel test section with a cold plate at the bottom from which an ice layer is grown. Special attention was paid to the selection of an appropriate phase change material and to the design of both the upstream conditions and the cold plate in order to impose well-described experimental boundary conditions.

Chapter 3 presents the experimental data generated for the transient growth of an ice-layer in a laminar square channel flow, measured using planar particle image velocimetry (PIV). Results were presented for both the thermal entrance region and the (almost) fully developed flow region, and a parametric study was performed on the effect of the cold plate temperature and the flow rate on the ice growth rate. In addition, suitable approximations to the experimental boundary conditions were obtained from thermocouple recordings of the cold plate temperature response. As such, a comprehensive and well described experimental data set for the transient growth of an ice layer in laminar internal flow was generated.

In chapter 4, non-intrusive temperature measurements were performed using laser induced fluorescence (LIF). Non-intrusive temperature measurements for solid-liquid phase change experiments are rare, and LIF has only been used once before for solid-liquid phase change experiments by *Gong et al.* [133], for measuring the temperature distribution of melting n-octadecane in a rectangular cavity. Compared to the work by *Gong et al.*, important novelties of the present work are the use of a two color LIF technique (instead of the one color technique employed by *Gong et al.*), the use of a post-processing algorithm to remove striations and other artefacts, and a detailed analysis of the uncertainty in the measured temperature fields.

Chapter 5 presents an energy-conservative DG-FEM approach for solid-liquid phase change. The combination of an arbitrarily high numerical order of accuracy with local conservation and the possibility for upwinding makes the discontinuous Galerkin method a potentially vary attractive numerical technique for solid-liquid phase change simulations. So far, several promising results have been obtained [129]–[132], possibly demonstrating a higher computational efficiency as compared to the commonly used finite volume method. The most important novelties of the present work are the coupling of the DG-FEM method to the 'linearized enthalpy approach' (as opposed to the source-based enthalpy approach and the apparent heat capacity method used in the previous work), the guarantee of thermal energy conservation through the convergence criterion and a quantitive analysis of the mesh convergence rates to demonstrate the performance of the method.

Chapter 6 features the development of a finite volume parallel adaptive mesh refinement method for solid-liquid phase change. The most important novelties in this work are the use of the residual error method by *Jasak et al.* [134], [135] to estimate the numerical discretization errors in the flow and the temperature fields as a basis for the refinement criteria, the use of a dynamic load balancing procedure to maintain a high parallelization efficiency and the application of the adaptive mesh refinement method to a simulation of one of the MSFR freeze-valve designs.

Chapter 7 proposes a numerical benchmark for modelling phase change in molten salt reactors, modelled after the MSFR freeze-valve design. The benchmark was motivated by the need for determining the margin of error in CFD simulations when predicting the melting time of the freeze-valve. The benchmark consists of five stages, with a step-wise addition of complexity allowing to pinpoint potential sources of discrepancy between various numerical codes. The work for this final chapter was carried out together with Mateusz Pater from the DTU in Denmark as part of a research collaboration. Finally, in chapter 8 the overall conclusions of this thesis are drawn and some recommendations are given for future work.

2

DESIGN OF THE ESPRESSO EXPERIMENTAL FACILITY

2.1. Introduction and motivation

In particular for the MSFR, accurate numerical models for predicting transient freezing in forced or mixed convection flow regimes are of paramount importance for analysing accident scenarios where solidification plays a role, such as the sudden solidification inside the exchanger following an ULOF or fuel salt overcooling accident (see chapter 1). At the moment, high fidelity experimental benchmark data for transient melting and freezing in a forced or mixed convection heat transfer regime is not sufficiently available. For this reason, the ESPRESSO (ExPeriment for RE-melting and Salt SOlidification) facility was designed and built. The ESPRESSO facility consists of a water tunnel with a square channel test section, where ice growth is initiated from a cold plate at the bottom.

The objectives of the ESPRESSO facility are twofold:

1. Contribute to our understanding of the physics surrounding the interaction between the solid-liquid interface, the surrounding flow, the heat fluxes from the flow into the ice-layer, and the role of turbulence.

2. Generate detailed experimental data suitable for numerical benchmarking.

To achieve these objectives, the ESPRESSO facility must satisfy two constraints:

1. The ESPRESSO facility must be capable of generating an ice-layer in forced internal flow, for both laminar and turbulent flow conditions.

2. Experiments in ESPRESSO must generate data which can be compared to numerical methods. Therefore the boundary conditions of the ESPRESSO facility must be as simple as possible such that they can be captured by a numerical model. In addition, the thermophysical properties of the phase-change material must be well described and the experimental methods used to record the solid-liquid interface

position, and the velocity and temperature fields must be non-intrusive, accurate and have a high spatial and temporal resolution.

The remainder of this chapter is organized as follows. In section 2.2, we explain the choices made with respect to the selection of the phase change material. In section 2.3, we present an early-stage investigation of the different concepts that were considered before proceeding to the final design. In sections 2.4 and 2.5, a detailed design study of respectively the cold plate and the upstream section (diffuser, settling chamber and converging nozzle) is presented. Section 2.6 described the final design, including the design schematics and images of the built setup.

2.2. Selection of phase change material

The phase change material was selected based on the following criteria:

1. The thermophysical properties should be well-known, since they are needed as input for the numerical simulations and to properly analyse the experimental results.

2. The Prandtl (Pr) number should be close to the actual fuel salt foreseen in the MSFR, to have similar behavior within the thermal boundary layer.

3. The phase change material (PCM) should be liquid at room-temperature. A PCM which is solid at room temperature would require the setup to be continuously heated to prevent a freeze off in the coolant loop and the pump, which could lead to the break-down of the equipment.

4. The melting point should be as close as possible to room temperature, to reduce the heat exchange with the environment.

5. Other desired properties are a transparent liquid phase, a low viscosity (which follows the Newton viscosity law), sufficient contrast between the liquid and the solid phase (e.g. opaqueness, density), cheap and non-toxic.

The thermophysical properties of the blanket salt (LiF-THF_4 (0.78-0.22)) and two different fuel compositions (respectively LiF-ThF_4-UF_4-PuF_3 (78.6-12.9-3.5-5) and LiF-ThF-UF_4-$(TRU)F_3$ (77.5-6.6-12.3-3.6)) [25] are given in table 2.1. It should noted that the thermophysical properties of both the blanket salt and the fuel salt were evaluated at values significantly above their melting point, in order to respect the boundaries of the given relationships for the viscosity, which is expected to increase as the melting point is approached. In addition, both the viscosity and especially the thermal conductivity data have a large degree of uncertainty [33], [34]. The thermal conductivity was not estimated directly, instead its value was estimated based on the thermal conductivities of other molten salts. Whilst data (from 1947) is available for the viscosity of the blanket salt [33], only single point measurements are available for the viscosity of the fuel salt and instead the viscosity-temperature relationship was obtained from a molecular dynamics simulation [34]. Finally, no data on the latent heat of fusion could be found. Using the given values for the thermophysical properties, the Pr of the blanket salt and the two fuel

salt compositions is determined as: $Pr = \frac{\mu c_p}{k} = 4.7$, 7.8, and 15 respectively. Here, μ is the dynamic viscosity, c_p the specific heat and k the thermal conductivity. However, the Prandtl number may be significantly higher for lower temperatures (around the melting point). Also note that the viscosity, and therefore the Prandtl number, is quite different for the two fuel compositions.

Table 2.1: Thermophysical properties of the blanket salt, evaluated at 923 K [33] and two different fuel compositions, evaluated at 973 K [34].

	Blanket Salt	Fuel Composition 1	Fuel Composition 2
Melting temperature [K]	841	872	854.15
Density [$\mathrm{kg\,m^{-3}}$]	4389	4344	4306
Specific heat capacity [$\mathrm{J\,K^{-1}\,kg^{-1}}$]	1000	1020	1010
Dynamic viscosity [Pa s]	$7.07 \cdot 10^{-3}$	$13.0 \cdot 10^{-3}$	$25.3 \cdot 10^{-3}$
Thermal conductivity [$\mathrm{W\,m^{-1}\,K^{-1}}$]	1.5	1.7	1.7
Prandtl number	4.7	7.8	15

Considering the aforementioned criteria for the selection of the PCM, and the current knowledge of the thermophysical properties of the blanket and the fuel salts in the MSFR, water was selected as the PCM. Water is liquid at room temperature, its thermophysical properties are well-known, it is a Newtonian fluid with low viscosity, it is cheap, non-toxic and easy to use and at a temperature around the freezing point (i.e. $T = 273$K) its Pr is around 13.4, which is of similar order as that of the fuel salt (see see table 2.2). In addition, experimental data on the freezing of water in internal flow has already been used for validating a thermal hydraulic code for simulating the freezing of molten salts in pipe flows in the MSFR [50]. However, water exhibits an anomalous expansion behaviour during the freezing process, with a density inversion around 4 °C. This could lead to phenomena such as penetrative Rayleigh-Bénard convection [136] or flow reversal during solidification [137]. Therefore, we recommend some caution when extrapolating the results for the transient freezing of water to the MSFR.

Table 2.2: Thermophysical properties of water, evaluated at 273 K [138].

	Solid	Liquid
Melting temperature [K]	273	
Latent heat [$\mathrm{kJ\,kg^{-1}}$]	333	
Density [$\mathrm{kg\,m^{-3}}$]	916.7	999.8
Specific heat capacity [$\mathrm{J\,K^{-1}\,kg^{-1}}$]	2100	4217
Dynamic viscosity [Pa s]	n/a	$1.79 \cdot 10^{-3}$
Thermal conductivity [$\mathrm{W\,m^{-1}\,K^{-1}}$]	2.16	0.565
Thermal expansion coefficient [$\mathrm{K^{-1}}$]	160	$-6.88 \cdot 10^{-5}$
Prandtl number	n/a	13.4

Other phase-change materials were considered as well. EAN (ethyl-ammonium nitrate) was considered as an ionic liquid with a melting point close to room temperature[1], and therefore possibly exhibiting a similar melting or freezing behaviour as the MSFR salt. However, in addition to a high cost per unit volume, EAN has a very high viscosity and no data on the thermal conductivity could be found. Paraffin waxes have the advantage of a sharp contrast between liquid and solid phase, a melting point close to room temperature and a high Pr (around 50 depending on which wax is used, which might be closer to the value of the fuel salt around the melting point). However, the melting point of most common paraffin waxes are above room-temperature, which is highly unpractical for a forced convection setup.

2.3. Preliminary study of various conceptual designs

During the initial design phase, multiple concepts were considered for the ESPRESSO facility. The first concept was a cylinder, where the flow was initiated through the rotation of the upper lid, and an ice-layer was grown from a cold plate at the bottom[2]. A preliminary investigation of the suitability of this design was performed using OpenFOAM 4.0 as a computer aided design tool. Figure 2.1a shows that the velocity decreases rapidly from the upper lid to the cold plate at the bottom, where the ice layer is located. As such, the velocities above the ice layer are very small, resulting in little interaction between the flow field and the solid-liquid interface. Therefore, this concept was no longer considered. For the second concept, the flow was generated through a rotating inner cylinder (shown in figure 2.1b). To initiate the ice growth, the rotating cylinder is simultaneously cooled[3].

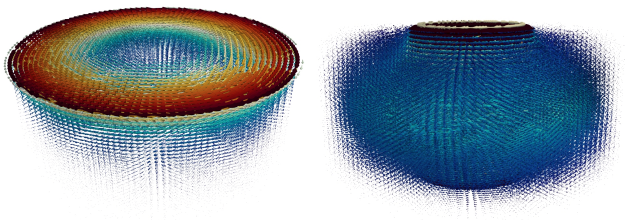

(a) (b)

Figure 2.1: Flow field for concept 1 (a) and concept 2 (b). Simulations were performed with OpenFOAM 4.0, for Re = 100.

[1] The use of an ionic liquid as the phase change material was suggested in the original proposal.

[2] The first concept was suggested in the original project proposal and was similar to the experimental campaign performed by *Ramadu et al.* [95].

[3] This configuration is similar to the experimental campaign performed by *Retamales et al.* [139].

The second concept presented two difficulties. First of all, it is challenging to design a cylinder which is simultaneously rotated and cooled and meets the requirement of having a well-described experimental boundary condition. This is due to the difficulty of maintaining a water tight connection between the stationary coolant tubing and the rotating cylinder, ensuring a high enough coolant flow rate such that the experimental boundary condition may be approximated by either a constant heat flux or uniform temperature condition and the fact that all sensors within the cylinder (such as thermocouples) either need to be wireless or the sensor wires need to be prevented from rotating along with the cylinder. In addition, at higher *Re* the flow between two rotating cylinders is prone to the onset of the Taylor-Coutte instability [140], leading to large scale unsteadiness. For $Re = 3000$, vortex structures could indeed be observed in the time-averaged flow field (as shown in figure 2.2). Whilst the Taylor-Couette instability is an interesting object of study in and of itself, it would complicate the analysis of the formation of the ice-layer and the comparison with numerical models.

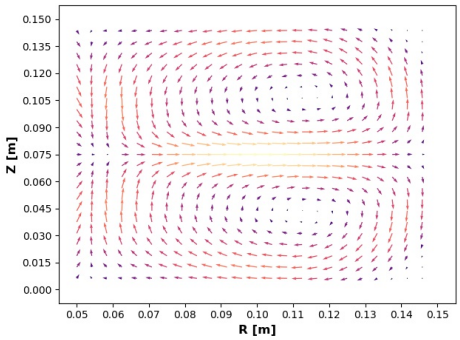

Figure 2.2: Time averaged flow-field for the ESPRESSO concept 2, showing the formation of vortex structures. Results shown for long-time average behaviour. Simulations were performed with OpenFOAM 4.0, for Re = 3000.

The third and final concept featured a water tunnel with a square channel test section, where ice grows from a cold plate at the bottom.The third concepts meets all the design constraints (see section 2.1). In addition, freezing in internal flows where the wall temperature drops to below the melting point is a relevant case for the MSFR from a safety perspective. This concept builds on previous investigations of freezing in forced convection flows inside channels [93]. The novelty of the present experimental campaign is that it will generate detailed quantitative data of the transient growth of the ice layer, include non-intrusive measurements of both the flow field and the temperature field, and pay specific attention to the design of the boundary conditions in order to generate experimental data which is both meaningful and suitable for numerical benchmarking purposes.

2.4. Design of the aluminium cold plate

One of the objectives of the ESPRESSO facility was to perform benchmark experiments suitable for numerical validation purposes. Therefore, the experimental boundary conditions of the ESPRESSO facility should be properly imposed and well described. The goal was to impose a uniform velocity profile at the inlet and a spatially uniform temperature boundary condition at the cold plate, under both laminar and turbulent flow conditions. For this reason, special attention was devoted to the design of the cold-plate and the upstream section (diffuser, settling chamber and converging nozzle). In this section we describe the design of the cold-plate. The design of the upstream section will be covered in the subsequent section. As a starting point, the following criteria were formulated for the cold plate design:

1. The temperature of the cold plate should match that of the heat transfer fluid (HTF).
2. The distribution of the cold plate temperature should be uniform. The thermocouples have an uncertainty of $\pm 0.2^{\circ}$C. Therefore, the cold-plate should be designed such that the temperatures along the length of the cold-plate (excluding entry and exit effects) are within 0.4°C of each other.
3. The cold plate should be able to utilize the maximum cooling capacity ($23\,\mathrm{L\,min^{-1}}$) of the *Julabo FL1701* recirculating cooler.
4. The pressure drop inside the cold plate cannot exceed 1 bar, which is the maximum pumping pressure of the *Julabo FL1701* recirculating cooler.

Therefore, a high performance heat sink with an optimized off-trade between the heat transfer coefficient and the pressure drop is needed. The heat sinks with the highest performance are the so-called extended surface (or brazed / folded fin) heat sinks. Two configurations were investigated: an array of rectangular fins and an array of offset fins[4]. The offset fin heat sink was expected to lead to the highest overall performance, due to the continuous destruction and regrowth of the temperature boundary layer as a result of the acceleration and deceleration of the heat transfer fluid [141]. A schematic of the two designs is shown in figure 2.3.

Both designs were investigated through conjugate heat transfer simulations in Comsol multi-physics. Based on a preliminary analysis using empirical correlations from literature [141], [142], the heat sink height in the Comsol simulations was set at 25 mm and the height of the bottom and top plates (i.e. cold plate) were set at 2.5 mm[5]. The simulated rectangular fin cold plate featured 21 fins of 1.0 mm thick, and the offset fin cold plate featured 13 fins of 1.0 mm thick. The length of an individual fin structure was set at 3.75 cm for the offset fin configuration. Both simulated heat sinks were made out of copper[6].

[4] A preliminary investigation was also performed of a heat sink with pressed tubes, however the pressure drop of this configuration was found to scale very badly with the flowrate of the heat transfer fluid.

[5] Please note that these heights are the heights in the simulation, not the height of the actual heat sink. The actual cold plate is significantly thicker to provide enough structural support and leave enough room for the thermo-couples, see figure 2.5.

[6] To stay within budget, the actual heat sink was constructed from aluminium 7075-T6.

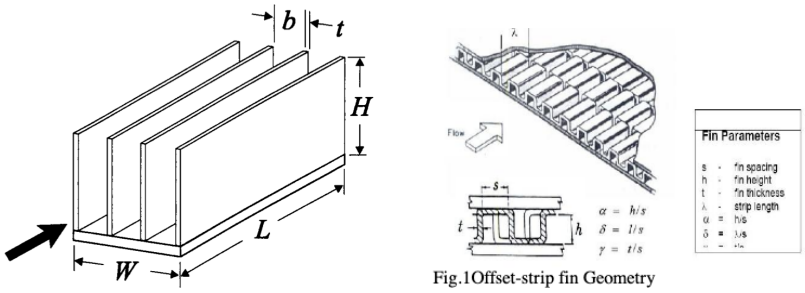

(a) (b)

Figure 2.3: Schematic of plate fin heat sink [142] (a) and offset fin heat sink [141] (b).

The performance of the two cold plates was investigated for fully turbulent channel flow with $Re = 10000$, $T_{in} = 276\,\mathrm{K}$, $T_{HTF,in} = 258\,\mathrm{K}$. The heat transfer fluid (*Thermal* G from *Julabo*)) flows in the reverse direction, in order to increase the heat transfer rate. The exact composition of *Thermal G* is unknown, however it consists of 40-60 % ethylene glycol. Assuming the rest is water, its thermophysical properties are estimated assuming a 50 % water 50% ethylene glycol mixture (see table 2.3).

Table 2.3: Thermophysical properties of Thermal G, estimated assuming 50 % ethylene glycol and 50 % water.

Property	Value
Density [$\mathrm{kg\,m^{-3}}$]	1080
Specific heat capacity [$\mathrm{kJ\,kg^{-1}\,K^{-1}}$]	3350
Dynamic viscosity [Pa s]	$19.0 \cdot 10^{-3}$
Thermal conductivity [$\mathrm{W\,m^{-1}\,K}$]	0.153

The simulation was run in steady state and ice growth was not considered. The Jones-Launder low-Reynolds $k-\epsilon$ turbulence model [143] was used to simulate the channel flow and the Kays-Crawford model was used for the turbulent heat transfer. Approximately 1.5 million linear elements were used for the rectangular fin configuration and 7 million elements were used for the offset fin configuration. Figure 2.4a shows a front view of the finite element mesh used for the offset fin simulation and figure 2.4b shows the obtained temperature profile along the length of the cold plate, for both the offset fin and the rectangular fin configurations. Compared to the rectangular fin configuration, the offset fin configuration had a better performance. The overall temperature in the cold plate was lower and the entry and exit effects were smaller. The oscillations in the temperature for the offset fin configuration were attributed to the acceleration and deceleration of the flow after each fin segment. In addition, the simulations predicted a lower pressure drop (35000 Pa) in the offset fin configuration as opposed to the rectangular fin configuration (80000 Pa). Therefore, the offset fin heat sink configuration was selected for the ESPRESSO facility. Please note that the present simulation was performed for turbulent flow conditions. For laminar flow, an even more uniform temperature distribution in the cold plate is expected.

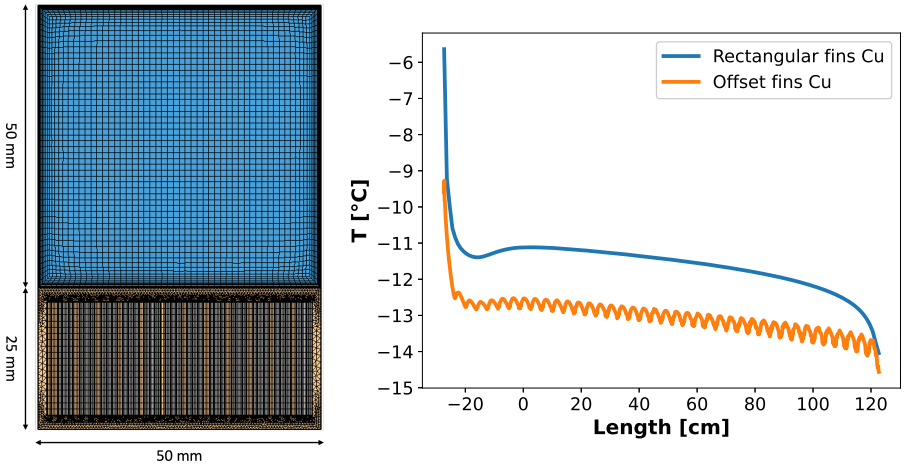

(a) (b)

Figure 2.4: Front view of the mesh for the offset fin configuration (a) and temperature profile along the length of the cold plate, for both the offset fin and the rectangular fin configurations (b).

2.5. Design of the settling chamber and the converging nozzle

The upstream section consists of the following parts: a diffuser (to bridge the change in cross section between the recirculating loop and the settling chamber), a settling chamber (to remove disturbances in the flow as much as possible) and a converging nozzle. Based on Mehta's design chart [144], a straight-walled diffuser with an angle of 20 ° and 3 gauze screens installed was used. The screens were equally spaced, with one placed at the diffuser entry to account for the sudden change in angle. The settling chamber has a square cross section of 15 cm × 15 cm and a length of 30 cm. The goal of the settling chamber is to remove swirl, turbulence and other flow irregularities before entering the contraction nozzle. To this end, a combination of a honey comb grid with an opening of 1.5 ± 0.1 mm to remove swirl and lateral turbulence and 3 screens (one coarse screen with an opening of 4.0 mm and two fine screens with an opening of 1.0 mm, geometrical tolerances unknown) for the reduction of axial turbulence [145] were used.

The objective of the converging nozzle is to yield a uniform velocity profile at the exit. Although a shorter contraction length is desirable both in terms of space and cost and for minimizing the boundary layer thickness at the contraction exit, the risk of flow separation also increases. As such, a good contraction shape achieves a high degree of uniformity for the velocity profile, whilst avoiding flow separation and limiting the contraction length [146], [147]. This is done by minimizing the second derivative of the velocity with respect to the contraction length, hereby achieving a (almost) linear acceleration of the flow. Two popular choices for the contraction shape are the matched cubics by *Morel et al.* [147] and the 5^{th} order polynomial by *Bell et al.* [146], of which the latter was selected for the ESPRESSO facility. Therefore, the shape of the converging nozzle is defined as:

$$y(x) = 0.5H_{ex} + 0.5\,(H_{in} - H_{ex})\left[6\left(\frac{x}{L}\right)^5 - 15\left(\frac{x}{L}\right)^4 + 10\left(\frac{x}{L}\right)^3\right] \tag{2.1}$$

Here, $H_{in,ex}$ are the inlet and exit diameters of the nozzle respectively, and L is the length of the nozzle. This contraction shape yields good flow uniformity, is free of separation, and has a low minimum $\frac{L}{H_{in}}$ of 0.89.

2.6. Overview of the ESPRESSO facility design

Figure 2.5 depicts a graphical representation of the ESPRESSO facility. Please see appendix A for additional illustrations, including the design drawings and fotographs of the completed setup. The ESPRESSO facility consists of a water tunnel with a square channel test section ($H \times W \times L = 5.00 \pm 0.03\,\text{cm} \times 5.00 \pm 0.03\,\text{cm} \times 145.0 \pm 0.1\,\text{cm}$), made of poly(methyl methacrylate) (PMMA) in order to guarantee optical access (which is needed for the non-intrusive flow field, temperature and ice growth measurements). The side walls of the test section have a thickness of $d = 5.0 \pm 0.1\,\text{mm}$ and the removable top lid has a thickness of $d = 2.00 \pm 0.02\,\text{cm}$. The ice layer is grown from an aluminium (7075-T6) cold plate at the bottom of the test section ($H = 2.10 \pm 0.02\,\text{cm}, L = 148.5 \pm 0.1\,\text{cm}, W = 9.50 \pm 0.03\,\text{cm}$), capable of reaching a minimum temperature of $T_c = -20.0\,^\circ\text{C}$.

The cold plate (see section 2.4) is connected to an offset fin heat sink ($H = 4.60 \pm 0.03\,\text{cm}$), containing 14 offset fins (1/8 lanced offset from Robinson Fin Machines, USA) with a flow length of $L = 15.00 \pm 0.03\,\text{cm}$, a height of $H = 2.35 \pm 0.01\,\text{cm}$ and a thickness of $d = 0.025\,\text{cm}$ (geometrical tolerance unknown). The rest of the heat sink is made of PMMA, to provide thermal insulation. The heat sink is coupled to a *Julabo FL1701* recirculating cooler, with a maximum power of $P = 1.7\,\text{kW}$ and a maximum flow rate of $\phi_v = 23.0\,\text{L}\,\text{min}^{-1}$. The coolant used is *Julabo's Thermal G* (i.e. an ethylene-glycol water mixture). A series of 8 thermocouples with an accuracy of $\pm 0.2\,^\circ\text{C}$ are equally distributed along the length of the cold plate at a spacing of 20.5 cm. The thermocouple tips are inserted at a height of $H = 1.05 \pm 0.02\,\text{cm}$ and a depth of $W = 5.00 \pm 0.03\,\text{cm}$, in the centre of the cold plate.

To impose a uniform inlet velocity profile at the entrance of the test section, the upstream section features a combination of a diffuser, settling chamber and a converging nozzle (see section 2.5). The settling chamber has a cross-section of $H \times W = 15.00 \pm 0.05\,\text{cm} \times 15.00 \pm 0.05\,\text{cm}$ and a length of $L = 30.00 \pm 0.05\,\text{cm}$. Due to geometric constraints, a development length of $L = 13.50\,\text{cm}$ long (more than 2 times the hydraulic diameter of the test section) was included between the outlet of the converging nozzle and the entrance of the test section.

The water is stored in a buffer vessel of approximately 100 L in volume and recirculated through the test section by a pump with an electronic frequency drive, capable of reaching a maximum flow rate of $\phi_v = 1.4\,\text{L}\,\text{s}^{-1}$. To remove the (large) air bubbles introduced by the pump, the flow is passed through a bubble column. A brazed plate liquid heat exchanger (SWEP, Sweden), located after the pump and coupled to a second *Julabo FL1701* recirculating cooler[7], is used for controlling the inlet temperature between

[7] Instead of ethylene glycol, the second recirculating cooler uses water as the coolant.

a range of approximately 20 and 5 °C. In addition to the temperatures of the cold plate, the temperatures of the buffel vessel as well as the bulk inlet and outlet temperatures are recorded using K-type thermocouples. The flowrate is recorded using a Proline Promag 10W magnetic flow metre (Endress Hausser, Germany) with an accuracy of $\sigma_{\phi_v} = \pm 0.5\%$ or $\sigma_u = \pm 2\,\mathrm{mm\,s^{-1}}$ for flow-rates outside the official measurement range. Finally, to limit the heat flux through the side walls and the top lid, the test section is thermally insulated using styrofoam, except in those regions where optical access is needed.

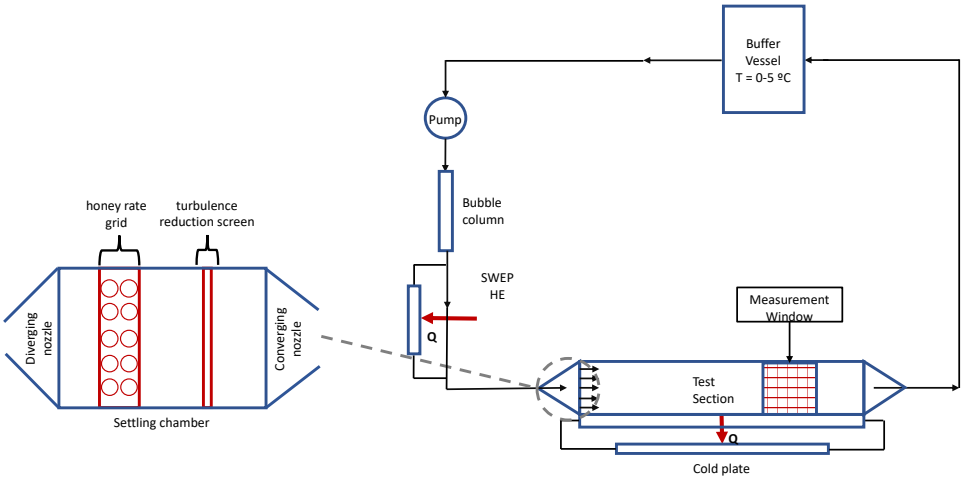

(a) Sketch of ESPRESSO Experimental Facility.

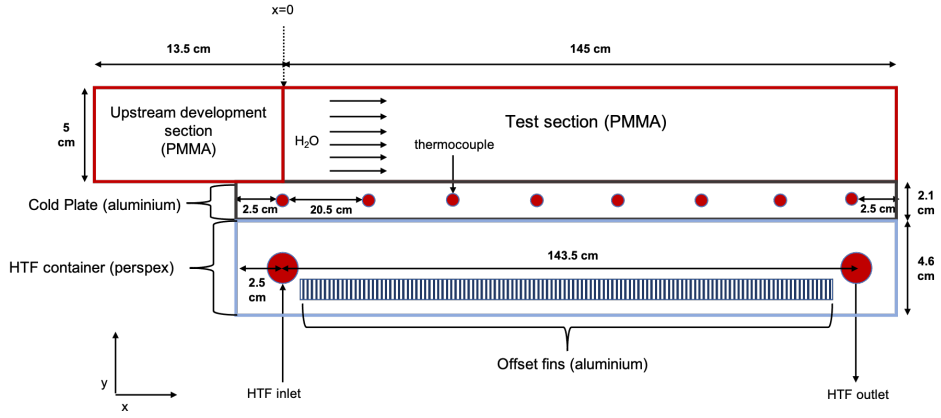

(b) Zoom in of test section (side view).

Figure 2.5: Graphical representation of ESPRESSO experimental facility. Here, PMMA stands for poly(methyl methacrylate), HE stands for heat exchanger and HTF stands for heat transfer fluid.

2.7. Summary

This chapter describes the design of the ESPRESSO facility, designed to generate high fidelity experimental data for transient ice growth in internal forced convection flow. The ESPRESSO facility consists of a water tunnel with a rectangular channel test section, in which ice growth is initiated from a cold plate at the bottom. The ESPRESSO facility is capable of reaching both laminar and turbulent flow, and can reach an inlet temperature of between 20 and 5 °C and a minimum cold plate temperature of -20 °C. To allow for non-intrusive optical measurements of the ice layer, the flow field and the temperature field, the top lid is made of transparent PMMA. Special attention was paid to the design of the cold-plate and the upstream section, in order to impose well-described experimental boundary conditions. This is an important novelty in the design of the present setup, with respect to previous investigations.

3

FLOW FIELD AND ICE LAYER MEASUREMENTS FOR THE TRANSIENT FREEZING OF WATER IN A SQUARE CHANNEL

We present an experimental study for the transient growth of an ice layer in a square channel under laminar flow conditions and a mixed convection heat transfer regime. The ice layer was grown from a cold plate located at the bottom of the channel, capable of reaching temperatures between 0 and -20 °C. The onset of ice formation was marked by a sudden sharp increase of the cold plate temperature followed by a rapid spreading of the ice over the cold plate surface. This was attributed to subcooling effects within the thermal boundary layer of the flow. The flow field was measured using particle image velocimetry (PIV) and the ice profiles were measured at several instances of time after the onset of freezing by a visual tracing of the solid-liquid interface. In addition, a parametric study was performed regarding the effect of the cold plate temperature and the flow rate on the ice growth rate. Suitable approximations to the experimental boundary conditions were found after a detailed analysis of the cold plate's transient temperature response, which could be readily implemented in numerical software. An important novelty of the present work is the measurement of the transient ice development of the ice-layer near the inlet of the channel, in addition to the center of the channel where the flow is more developed. As such, a comprehensive and well-described experimental data set was generated for transient freezing in laminar internal flow to be used for numerical validation purposes.

This chapter is based on B.J. Kaaks, D.Lathouwers, J.L. Kloosterman, M. Rohde. Transient Freezing of Water in a Square Channel: An Experimental Benchmark. Submitted for publication.

3.1. Introduction and motivation

In this chapter, we present experimental results of the transient freezing of water in a square channel with a cold-temperature plate at the bottom, obtained using the ESPRESSO facility (please see chapter 2 for a detailed description). The primary aim of this experimental campaign is to generate the most comprehensive experimental data set of freezing in laminar internal flow up to date, to be used for numerical benchmarking purposes. To this end, particle image velocimetry (PIV) measurements and ice profile measurements (using a manual extraction from photographic observations) were performed at different time-instances and for a variety of flow rates and cold plate temperatures.

PIV has been used in recent solid-liquid phase change experiments to measure the flow field and the solid liquid interface [52], [70], [71]. For transparent PCM's, the solid-liquid interface is clearly visible on the PIV images, and the solid-liquid interface can be traced manually [71]. For opaque PCM's on the other hand, ultrasound Doppler velocimetry can be used to measure the flow field [69], employing X-ray [68] or thermal neutron radiography [148] to measure the solid-liquid interface position. As such, the experimental techniques used in the current experimental campaign are according to the latest standards in solid-liquid phase change experiments.

In addition, special attention was paid to the selection of simple experimental boundary conditions, which can readily be implemented in numerical methods. Compared to the experiments of *Savino et al.* and *Voulgorapoulos et al.* [52], [94] who only conducted transient ice growth measurements in the center of the channel where the heat transfer is close to one-dimensional, and *Hirata et al.* and *Kikuchi et al.* [82], [83] who conducted steady-state measurements of the ice-profiles near the inlet of the channel, the measurements of the transient ice growth near the inlet of the channel is an important novelty of the present experimental campaign.

The remainder of this chapter is organized as follows. Section 3.2 covers the experimental procedure and the applied PIV and interface tracking methods. The results of the experimental campaign including an analysis of the experimental boundary conditions is presented in section 3.3. Finally, the conclusions are presented in section 3.4.

3.2. Experimental methodology

The full experimental setup consists of the ESPRESSO facility (please see chapter 2) and a planar PIV system consisting of a laser source, a laser guiding arm and a high speed camera. The laser sheet enters the test section through the top lid and illuminates a flow region of approximately $L \times H = 8\,\text{cm} \times 5\text{cm}$. The PIV images are recorded from the front side of the PMMA test section wall.

3.2.1. Particle image velocimetry

The velocity was measured in a two-dimensional xy-plane using a planar PIV measurement technique. The flow was seeded with hollow borosilicate glass spheres (LaVision, Germany), with an average density of $\rho = 1.1\,\text{g}\,\text{cm}^{-3}$ and a mean diameter of $d_p = 10\,\mu\text{m}$. For a bulk velocity of $U_\infty \approx 1.5\,\text{cm}\,\text{s}^{-1}$, the particle *Stokes* number is defined as

$$Stk = \frac{\rho_p d_p^2}{18\mu} \frac{u_\infty}{D_h} \approx 1.5 \cdot 10^{-6}. \tag{3.1}$$

Therefore, the velocity lag of the particles was considered to be negligible [149]. A class-IV, 5W shuttered continuous wave laser (diode pumped, solid-state) with a wave length of $\lambda = 532nm$ (LaVision, Germany) was used as the light source of the PIV images. The laser sheet was generated through a combination of a spherical and a cylindrical lens, with a beam waist thickness of approximately 1 mm. A laser guiding arm (LaVision, Germany) was used to introduce the laser sheet from the top of the test section. The motion of the particles and the growth of the ice layer was imaged from the side using a Complementary Metal-Oxide Semiconductor (CMOS) Imager MX-4M (LaVision, Germany) camera with 4 MP of resolution (pixel size of 5.5 µm × 5.5 µm) and mounting an AF-S 50 mm F/1.4 (Nikon) lens. To ensure maximum overlap between the field of view (FOV) and the area of interest (AOI), the camera was located at approximately 40 cm from the centre of the channel and in-focus images were obtained using a focus close to the maximal focal length of 50 mm. Subsequently, the magnification factor is defined as

$$M_0 = \frac{Z_0}{z_0}, \tag{3.2}$$

where Z_0 is the image distance from the center of the lens to the image plane and z_0 is the object distance to the effective center of the lens (i.e. 40 cm). Z_0 is estimated applying the *Gauss* lens law

$$\frac{1}{Z_0} + \frac{1}{z_0} = \frac{1}{f}, \tag{3.3}$$

where f is the focal length of the camera, resulting in a magnification factor of approximately $M_0 = 0.14$. To obtain sufficient exposure, we selected a laser pulse duration of $t = 1000\,\mu s$ and an aperture of $f^{\#} = 4.0 - 5.6$. This yields the following depth of field [149]:

$$\delta_z = 4\left(1 + \frac{1}{M_0}\right)^2 f^{\#2}\lambda = 2.0 - 4.4\,\text{mm}, \tag{3.4}$$

where δ_z is the depth of view and λ is the wavelength of the laser. Since the depth of view is larger than the beam waist thickness of the laser, all PIV particles within the laser sheet are considered to be in focus. A single-pulsed, double-frame recording mode was used, with a pulse separation of $dt = 10$ ms and $dt = 5$ ms for $Re = 474$ and $Re = 1118$ respectively based on a desired mean particle displacement shift of approximately 5 pixels. At each measurement, 25 pairs of images were recorded with a frequency of 10 Hz. The camera and laser were synchronized using a programmable timing unit (PTU, LaViSion, Germany), operated by the Davis v8 software.

3.2.2. Image analysis and estimation of errors

Ice layer thickness measurements

The camera images were visually and manually translated from the image plane to the physical space using the height of the channel as a reference distance, followed by a rotation correction to correct for a slight tilting of the camera lens of approximately 0.5 – 0.6° using the edge of the cold plate as a reference line. Because light diffraction was very small thanks to the planar surface of the test section, and image distortion effects due to

the curvature of the lens were considered to be negligible [149], this image calibration was sufficient in our case. Sufficient contrast between the ice and the water allowed for a manual evaluation of the ice-water interface position using the *WebPlotDigitizer* software (similar to the approach used by *Faden et al.* [71]).

The following sources of uncertainty were identified in the measurements of the ice layer profiles:

1. An estimated uncertainty of approximately 0.5 % in the x and approximately 0.25 % y scale calibration. The estimated uncertainty in the x scale calibration is larger due to a higher difficulty in identifying $x = 0$ as compared to $y = 0$.

2. An uncertainty in identifying the zero time instant (time at which the onset of ice-formation first occurred), estimated at ± 3 s which was very small compared to the timescale at which ice-formation occurs.

3. An uncertainty in timing the subsequent image samples. This uncertainty was estimated at ± 5 s for the 5 min intervals and ± 15 s for the 15 min and 30 min intervals.

4. An uncertainty in the exact manual tracing of the solid-liquid interface. The exact size of this uncertainty was difficult to determine, however based on our personal experience it was estimated to be around ± 0.05 mm. This uncertainty was larger close to the inlet of the channel, where low laser light intensity combined with the formation of condense could lead to poor image quality.

It is difficult to gauge the combined effect of the individual uncertainties. For this reason, a series of 5 independent measurements was performed for the same experimental conditions, i.e. $Re = 474$ and $T_{c,set} = -10\,^{\circ}$C. From the post-processed ice layers, an uncertainty of approximately $0.1 - 0.2$ mm was obtained, which is between 0.2-0.4 % of the channel height. As such, these experiments were considered to be sufficiently reproducible and reliable.

Velocity measurements

The images were pre-processed to enhance the signal to noise ratio of the particles. The pre-processing step consisted of the application of a non-linear sliding average filter, applied over 5 pixels and substracted from the images, followed by a min-max filter and an intensity normalization filter. Due to the transient nature of the experiments (i.e. the growth of the ice layer) and its effect on the laser scattering signal, no background substraction was performed. The velocity vectors were calculated using a multi-pass option where the initial size of the correlation window was 64×64 pixels and after three passes the window size was decreased towards 32×32 for the final pass. The postprocessing consisted of a median filter to remove outliers as well as the removal of out of bounds velocity values, followed by a statistical averaging and a 3×3 Gaussian smoothing filter.

The following sources of uncertainty were considered:

1. A statistical uncertainty σ_{stat} given by:

$$\sigma_{stat} = \frac{\sigma}{\sqrt{N}} = \sqrt{\frac{1}{N_t N_x N_y (N_t - 1)} \sum_{i=1}^{N} (u_i - \bar{u})^2}, \tag{3.5}$$

where σ is the standard deviation, $N = N_t N_x N_y$ is the total number of samples, N_t is the number of time samples (25 in our case), N_x and N_y are the number of pixels in the x- and y-direction over which smoothing is applied (3,3 respectively) and $\bar{u}$ is the mean value of the velocity.

2. A systematic uncertainty (σ_{sym}), resulting from the uncertainties in the x and y scale calibration (see section 3.2.2). The systematic uncertainty is evaluated by:

$$\sigma_{sys} = \sqrt{\left(\frac{\partial u_x}{\partial x}\Delta x\right)^2 + \left(\frac{\partial u_x}{\partial y}\Delta y\right)^2 + \left(\frac{\partial u_y}{\partial x}\Delta x\right)^2 + \left(\frac{\partial u_y}{\partial y}\Delta y\right)^2}, \tag{3.6}$$

where Δx and Δy are the tolerances in the calibration of the x and y scales respectively. Possible other systematic uncertainties were considered 'unknown unknowns', and were therefore not included.

Assuming independence of the statistical and systematic uncertainties, the total uncertainty in the velocity measurements was estimated as:

$$\sigma_{tot} = \sqrt{\sigma_{stat}^2 + \sigma_{sys}^2} \tag{3.7}$$

The statistical variation of the velocity (σ_{stat}) was used to confirm laminarity of the flow. The standard deviation was approximately 2 % of the bulk velocity value (which gives an uncertainty of approximately 0.04 % due to the number of time samples and the applied smoothing), and spatial coherence was absent apart from the regions where a larger uncertainty could be expected due to poor optical access or reflections (such as close to the ice layer). These results for the statistical uncertainty were consistent with our expectations for laminar flow.

3.2.3. Experimental procedure

The velocity fields and ice layer profiles were measured for two different flow rates (corresponding to $Re = 474$ and $Re = 1118$) and four different set point temperatures of the cold plate (i.e. $T_{c,set} = -5\,^\circ$C, $T_{c,set} = -7.5\,^\circ$C, $T_{c,set} = -10\,^\circ$C and $T_{c,set} = -15\,^\circ$C). Measurements were performed at both the inlet (thermal entrance region) and at the centre of the test section where the heat transfer is close to one-dimensional. The experiment was initialized as follows. First the water was recirculated at the maximum available flow rate whilst the cold plate and the inlet were cooled to the desired temperatures. After the cold plate reached a temperature of around $T_c = -1.5\,^\circ$C, the flow rate was reduced to the desired value. Sometimes, the sudden lowering of the flow-rate resulted in the release of air bubbles, obstructing the laser sheet[1]. To remove these air bubbles from the test section, the flow rate was increased again to 100% capacity and multiple iterations of increasing and decreasing the maximum flow-rate could be needed until the lowering of the flow-rate no longer resulted in the release of air bubbles. Subsequently, the flow rate remained fixed at the desired set point value.

[1] Especially smaller air bubbles may pass through the bubble column.

Because the cold plate was in direct contact with the water flow above, reducing the flow rate of the water (and therefore the heat exchange between the water and the surface of the cold plate) resulted in a further decrease of the cold plate temperature. As soon as the cold plate reached a temperature below $T_c = -2.0\,°C$, freezing would occur, consistent with the findings of *Voulgaropoulos et al.* [52]. The onset of freezing was marked by a sudden sharp increase of the measured cold plate temperature, which was therefore used to determine $t = 0$ in our experiments (see section 3.3.3).

Whilst this approach to initialize the experiment resulted in a significant transient in the cold plate, it was highly reproducible. Alternatively, an initialization approach was considered where the cold plate was cooled until the set point temperature was reached, upon which the test section was filled with water. However, this approach was more difficult to reproduce whilst resulting in a similarly large temperature transient in the cold plate after filling the test section. During the first hour after the onset of ice-formation at $t = 0$, an image recording was made every 5 min. During the second hour, this frequency was reduced to each 15 min and after the third hour to 30 min. Preliminary tests showed this temporal resolution was sufficient to capture the transient growth of the ice layer. During the experiments, the temperatures measured by the thermocouples as well as the flow rate were recorded in real time and stored using the LabView software.

3.2.4. Flow and heat transfer regime

The thermophysical properties of the water, ice and aluminium are given in table 3.1. Constant thermophysical properties were considered for each phase, except for the thermal expansion coefficient which was calculated by the following temperature-dependent function to account for the anomalous expansion of water [138]:

$$\beta(T) = -6.88 \cdot 10^{-5} + 2.17 \cdot 10^{-5}\,T - 2.12 \cdot 10^{-6}\,T^{1.5} + 7.72 \cdot 10^{-8}\,T^2, \tag{3.8}$$

where T is the temperature in °C. Based on the thermophysical properties, and the inflow conditions, the flow and heat transfer regime was characterized as follows (depending on the imposed flow rate): $Re = \frac{\rho u_\infty H}{\mu} \approx 474 \quad \text{or} \quad 1118$, $Pr = \frac{\nu}{\alpha} \approx 11$, $Pe = RePr \approx 5263 \quad \text{or} \quad 12414$, $Ra = \frac{g\beta\Delta T H^3}{\nu\alpha} \approx -2.0 \cdot 10^6$, $Gr = {}^{Ra}/_{Pr} \approx 1.8 \cdot 10^5$ and $Ri = {}^{Gr}/_{Re^2} \approx -0.8 \quad \text{or} \quad -0.15$. Here, we considered a temperature difference of $\Delta T = 5\,K$ and a thermal expansion coefficient of $\beta(T) = -6.88 \cdot 10^{-5}\,K^{-1}$ (evaluated at the melting point). As such, the flow is laminar with a mixed convection heat transfer regime. Therefore, we recommend to include the role of natural convection when using these experiments for numerical validation, especially for $Re = 474$.

The effect of natural convection is expected to decrease as the ice layer thickens, since the hydraulic diameter is reduced whilst the temperature difference between the ice and the bulk fluid remains constant. The Rayleigh number is above the critical value for which penetrative Rayleigh-Bénard phenomena have been observed [136]. However, *Large et al.* conducted their experiments for a fluid at rest, whilst in our case the fluid was in constant motion, which could prevent the onset of instabilities within the thermal boundary layer.

Table 3.1: Thermophysical properties of water and aluminium 7075-T6.

Property	Water	Ice	Aluminium
Density [kg m^{-3}]	1000	1000	2810
Specific heat capacity [J kg^{-1}]	4200	2100	714.8
Thermal conductivity [W m^{-1} K^{-1}]	0.575	2.16	140.0
Latent heat [k J kg^{-1}]	333		
Melting Temperature [K]	273	N/A	
Thermal expansion coefficient [1/K]	$f(T)$		
Dynamic viscosity [Pa s]	$1.52 \cdot 10^{-3}$		

3.3. Results and discussion

3.3.1. Transient ice growth and velocity measurements

Figure 3.1 depicts the camera images taken with the LaVision Imager MX4M of the first 8 cm of the ESPRESSO facility after respectively 10, 30 and 90 min of ice growth. The flow conditions were $Re = 474$, $T_{in} \approx 4.7\,^{\circ}\text{C}$ and $T_{c,set} = -10\,^{\circ}\text{C}$. Sufficient contrast between the ice layer and the water above allowed for a manual tracing of the solid-liquid interface position. The solid-liquid interface position was found to coincide with the scattering signal of the laser, also shown by *Voulgorapoulos et al.* [52]). The bottom and top wall boundaries, as well as the solid-liquid interface, can be clearly distinguished due to their higher intensity value. The ice grows fastest near the inlet of the channel, with the ice layer profile becoming more and more flat as the downstream distance increases, consistent with the findings of *Zerkle et al.* and *Hirata et al.* [79], [82].

The corresponding contour plots of the velocity in the xy-plane are given in figure 3.2, where the ice layer is characterized by very low velocities. The velocity vectors are included to indicate the direction of the flow. With the growth of the ice layer, the effective cross section decreases and consequently the flow accelerates (since a fixed flowrate is imposed by the pump). We expect the pressure drop to increase correspondingly, based on the results provided by *Zerkle et al.* and *Mulligan et al.* [79], [81]. Whilst the freezing of water from the bottom could potentially lead to penetrative Rayleigh-Bénard convection [136], no convection cells were present in the PIV results. Possibly, the constant motion of fluid prevents the development of Rayleigh-Bénard type instabilities. Finally, the expansion of the ice, as well as the onset of natural convection, could lead to the generation of secondary flow in the z-direction [150]. Therefore, we recommend the measurement of the spanwise (z) velocity components (for instance using stereoscopic PIV) as a subject for further investigation.

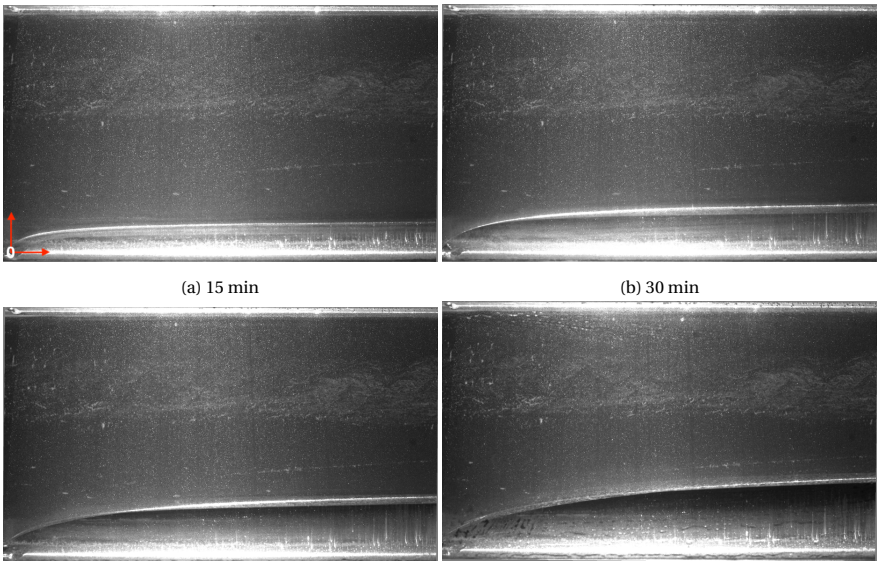

(a) 15 min (b) 30 min

(c) 45 min (d) 90 min

Figure 3.1: Camera images of transient ice growth taken with the LaVision Imager MX4M close to the inlet of the test section, after respectively 15, 30, 45 and 90 min starting from the onset of ice formation. The experimental conditions were: $Re = 474$, $T_{in} \approx 4.7\,^{\circ}\text{C}$, $T_{c,set} = -10\,^{\circ}\text{C}$. The origin of the xy Cartesian coordinate system is indicated in the top left image.

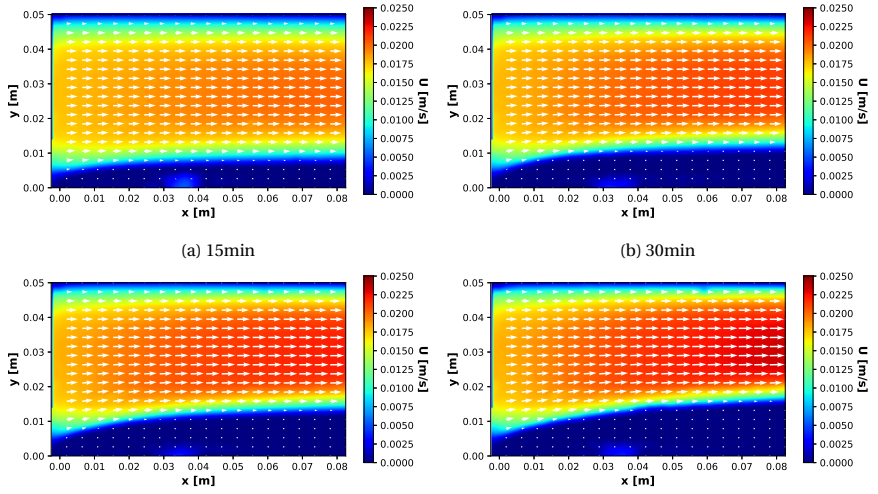

(a) 15min (b) 30min

(c) 45min (d) 90min

Figure 3.2: Measured velocity fields after respectively 15, 30, 45 and 90 min starting from the onset of ice formation. The experimental conditions were: $Re = 474$, $T_{in} \approx 4.7\,^{\circ}\text{C}$, $T_{c,set} = -10\,^{\circ}\text{C}$.

Figure 3.3 shows the ice profiles after respectively 15, 30, 45 and 90 minutes of ice growth, obtained by carefully tracing the solid-liquid interface in the camera images (see figure 3.1) using the *WebPlotDigitizer* software. For the same set of experimental conditions (i.e. $Re = 474$, $T_{in} \approx 4.7°C$, $T_{c,set} = -10°C$), 5 independent measurements were performed[2]. The results from the five measurements are highly consistent with each other, and a low uncertainty in the thickness of the ice layer was calculated of approximately $\sigma = 0.1 - 0.2$ mm based on the standard deviation from the mean. This uncertainty is assumed to be representative for the other experimental conditions as well, although it should be noted that in some measurements the true uncertainty might be larger due to uncertainties unaccounted for by the statistical analysis (such as a systematic uncertainty in determining $t = 0$ in the experiment). The obtained ice layer profiles agree well with the flow measurements and the raw camera images shown above (see figures 3.1 and 3.2). The maximum ice-thickness reached after 90 min is approximately 1.5 cm.

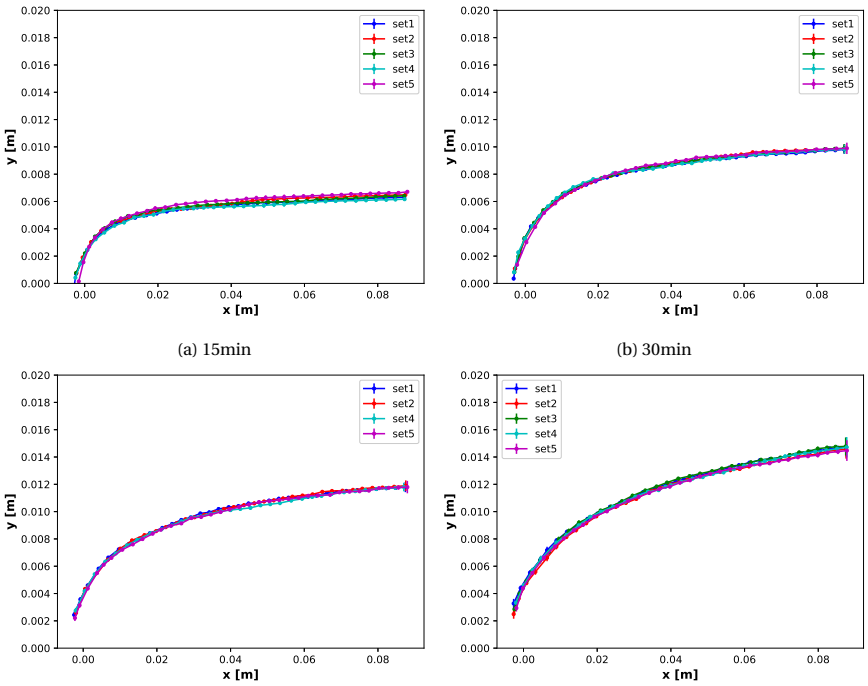

(a) 15min

(b) 30min

(c) 45min

(d) 90min

Figure 3.3: Measured ice layer profiles after respectively 15, 30, 45 and 90 min starting from the onset of ice formation. 5 sets of independent measurements are given. The experimental conditions were: $Re = 474$, $T_{in} \approx 4.7°C$, $T_{c,set} = -10°C$. From these 5 measurements, an uncertainty of approximately $\sigma = 0.1 - 0.2$ mm was calculated, as shown by the error bars.

[2] For $t = 45$ min, no data is available for the third measurement.

3.3.2. Ice growth for different cooling parameters and flow rates

Figure 3.4 shows the growth of the ice layer at two different locations downstream in the channel, i.e. at $x = 5\,\text{cm}$ and $x = 75\,\text{cm}$. The rate of ice growth decreases as the ice layer thickens, due to the combined effect of an increased thermal resistance of the ice and an enhanced heat transfer from the 'warm' fluid to the ice-water interface as the flow accelerates. This decrease in the ice growth rate is most pronounced near the inlet of the channel where the flow experiences significant development. A clear relationship is observed between the rate of ice growth and the temperature of the cold plate: for a cold plate temperature of $-10\,^\circ\text{C}$ (corresponding to a cooling parameter of $\theta_c = \frac{T_m - T_C}{T_H - T_m} \approx 2$ for an inlet temperature of $T_{in} \approx 5\,^\circ\text{C}$) the ice after $t = 120\,\text{min}$ is almost twice as thick as for a cold plate temperature of $-5\,^\circ\text{C}$. Likewise, a higher flow rate results in a decreased rate of ice growth, especially near the inlet of the channel where the heat transfer from the fluid to the ice layer has a stronger dependence on the velocity. Near the inlet, for the smaller cooling parameters, a steady state ice layer thickness is reached. No steady state is reached within the center of the channel for the given time-frame.

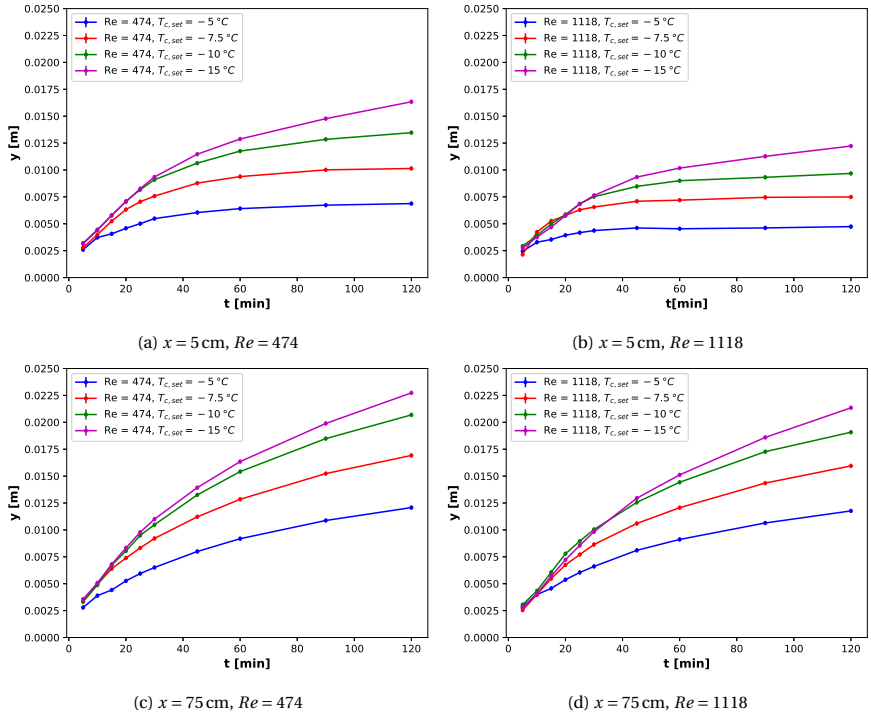

(a) $x = 5\,\text{cm}$, $Re = 474$

(b) $x = 5\,\text{cm}$, $Re = 1118$

(c) $x = 75\,\text{cm}$, $Re = 474$

(d) $x = 75\,\text{cm}$, $Re = 1118$

Figure 3.4: Transient ice layer thicknesses for four different cold plate temperature set points and two different flow rates, evaluated close to the inlet of the channel at $x = 5\,\text{cm}$ and at the center of the channel at $x = 75\,\text{cm}$. From the set of five repeated measurements, the uncertainty in the ice layer is estimated at $\sigma = 0.1 - 0.2\,\text{mm}$. Error bars are plotted for the conservative value of $\sigma = 0.2\,\text{mm}$.

3.3.3. Evaluation of experimental boundary conditions

As mentioned in chapter 2, one of the objectives of the design of the ESPRESSO facility was to have well-described experimental boundary conditions which can readily be implemented in numerical codes. Figure 3.5 shows the temperature response of the cold plate for one of the freezing experiments where $Re = 474$, $T_{in} \approx 4.7\,^{\circ}\text{C}$, $T_{c,set} = -10\,^{\circ}\text{C}$. From these measurements, the boundary condition was derived which was imposed at the bottom of the cold plate in our numerical simulations.

The first three and a half hours correspond to the initial cooling of the water flow prior to the start of the experiment (as described in section 3.2.3), indicated by the letter 'A'. After approximately 30 minutes, when the temperature in the cold plate reaches 4 °C, a sudden change in the temperature response is observed, indicated by the number '2'. Possibly, this is due to the onset of natural convection as a consequence of the anomalous expansion of water. After approximately 3 hours and 45 minutes have passed, the flow-rate is lowered to the desired setpoint value. As described in section 3.2.3, the test section is cleared of air bubbles by briefly increasing the flow rate to full capacity before the final reduction of the flow-rate to the setpoint value. The first temperature transient in the cold plate, indicated by the number '3', corresponds to the rapid adjustment of the flow rate.

A second sudden change in the cold plate temperature (indicated by the number '4'), where the temperature increases from approximately $T_c = -2\,^{\circ}\text{C}$ to $T_c = -0.5\,^{\circ}\text{C}$ marks the onset of freezing, at which ice rapidly spreads over the entire plate. Such a sharp increase was also observed by *Savino et al.* [94] and is possibly related to subcooling of the water prior to freezing, of which evidence had previously been provided by *Savino et al.* through a thermocouple measurement taken within the thermal boundary layer of the water during a short time span from before the ice was formed till after the probe became embedded within the ice-layer [94]. Based on the sequence of the thermo-couple response (with T0 being the first to respond and T7 the last), the nucleation of the ice is believed to commence at the inlet of the channel. The ice crystals rapidly propagate through the subcooled water from the inlet to the outlet of the channel and the release of latent heat increases the temperature of the water. Since the water and the cold plate form a coupled system, a corresponding increase of the cold plate will follow as the cold plate adjusts to the new conditions, explaining the sudden sharp increase of the cold plate temperature.

During the first 30 min following the onset of ice-formation, the temperatures in the cold plate continue to decrease until the setpoint value of the coolant is reached (indicated by the letter 'B'). Subsequently, a thermal equilibrium is established between the coolant recirculated underneath the test section and the water flowing through the test section. As a consequence, the temperature in the cold plate reaches a quasi steady state, at approximately 1 °C above the setpoint value of the coolant (indicated by the letter 'C'). The small decrease in the cold plate temperature still observed after the establishment of thermal equilibrium is probably a consequence of the growth of the ice layer, which acts as a thermal insulator.

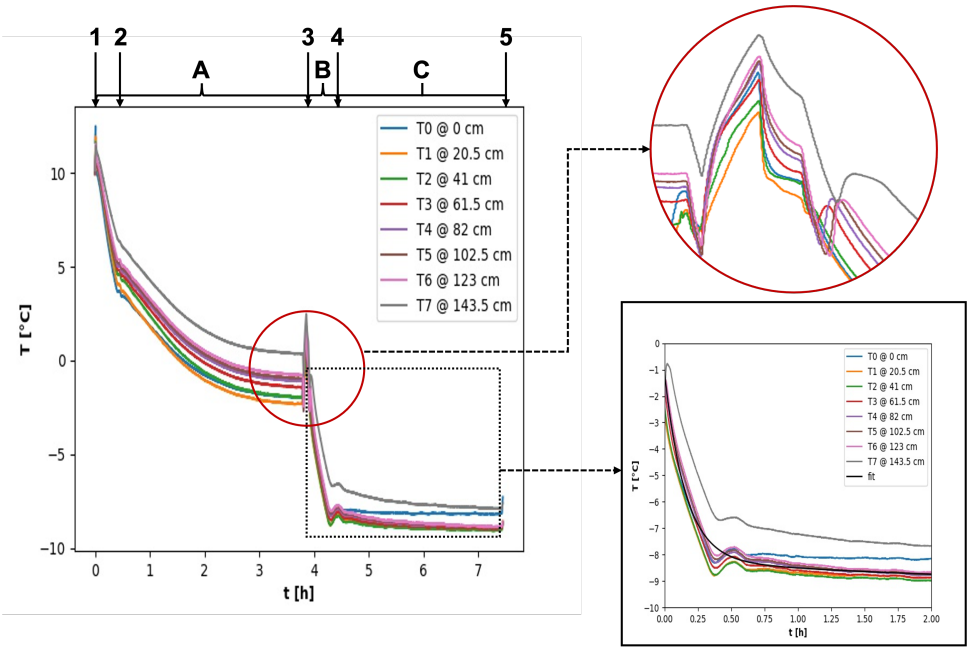

Figure 3.5: Temperature response of the cold plate for all 8 thermo-couples, where the zoom-ins refer to the temperature response of the cold plate at the onset of ice-formation (where $t = 0$ is determined) and the transient temperature development after $t = 0$, including the empirical fit which can be used as a boundary condition in numerical simulations. The 3 different stages of the experiment are indicated by the letters A, B and C, where A refers to the initialization of the experiment prior to $t = 0$, B refers to roughly the first 30 min after $t = 0$ where the temperature in the cold plate experiences a significant transient and C refers to the remainder of the experiment at which a thermal equilibrium appears to exist between the coolant recirculating underneath the cold plate and the fluid flow in the square channel above. The numbers 1-5 refers to specific instances in the temperature evolution of the cold plate, 1 being the start of the experiment, 2 being a reduction in the rate at which the temperature declines, 3 being the onset of freezing, 4 being the establishment of thermal equilibrium within the cool-plate and 5 being the end of the experiments (where the pumps and the recirculating coolers are switched off). The experimental conditions were: $Re = 474$, $T_{in} \approx 4.7\,^{\circ}\mathrm{C}$, $T_{c,set} = -10\,^{\circ}\mathrm{C}$.

Apart from entrance and exit effects (recognized by deviating temperature values for thermocouples $T0$ at the inlet and $T7$ at the exit of the cold plate), the differences between the temperatures of the other thermocouples (T1-T6) at a given time instance fall within the temperature uncertainty of the K-Type thermocouples (i.e. $\pm 0.2\,^{\circ}\mathrm{C}$). For this reason, we suggest modelling the effect of the cold plate in the numerical simulations through a time-dependent, yet spatially uniform temperature boundary condition. In the present work, the following function is used as a reasonable approximation for the transient temperature behaviour of the cold plate:

$$A \exp(-Bt) + C \tanh(Dt) + E \tag{3.9}$$

The resulting fit parameters as well as the flow rate and inlet and outlet temperatures of the 8 different experimental conditions are shown in table 3.2 and the fits are plotted in figure 3.6. A large degree of consistency was observed for both the flow rate and the bulk inlet temperature (which varied between approximately $T_{in} = 4.5-4.8°C$). The bulk outlet temperature is slightly lower than the inlet temperature, as a consequence of the heat extracted by the cold plate. For practical purposes, the heat flux through the side and top walls of the test section was assumed to be negligible compared to the heat content of the recirculated water and the 1.7 kW capacity of the *Julabo FL1701* cooler connected to the cold plate. For $T_{c,set} = -5\,°C$ and $T_{c,set} = -10\,°C$, the first 30 minutes of the experiment were characterized by a significant transient as the cold plate approaches the set point value, after which a thermal equilibrium was established. However, for $T_{c,set} = -15\,°C$ the time required to achieve a thermal equilibrium exceeded the duration of the experiment. Some difference in the dynamics of the cold plate were observed between the two different flow rates, especially for the lowest set point temperature. However, it is unclear whether these differences were related to the flow rate or were caused by other factors (e.g. initialization procedure, ambient temperature, etc).

Table 3.2: Model fit parameters of the transient cold plate response, as well as the averaged flow rates and inlet and outlet temperatures, for all 8 different experimental conditions.

	$T_{c,set}$	A	B	C	D	E	$\phi_v(Ls^{-1})$	$T_{in}(°C)$	$T_{out}(°C)$
Re = 474	−5 °C	10.071	3.373	7.429	2.251	-11.647	0.035 ± 0.004	4.46 ± 0.05	4.3 ± 0.1
	−7.5 °C	22.465	3.609	16.812	2.284	-23.369	0.035 ± 0.004	4.61 ± 0.09	4.3 ± 0.2
	−10 °C	7.040	6.363	0.791	-0.401	-8.215	0.034 ± 0.004	4.68 ± 0.05	4.1 ± 0.3
	−15 °C	6.410	6.303	6.631	-0.251	-8.205	0.035 ± 0.004	4.61 ± 0.08	4.2 ± 0.2
Re = 1118	−5 °C	9.220	3.509	6.602	2.292	-10.764	0.085 ± 0.004	4.56 ± 0.06	4.4 ± 0.1
	−7.5 °C	4.079	16.142	-1.000	0.781	-5.566	0.085 ± 0.004	4.45 ± 0.07	4.1 ± 0.3
	−10 °C	1.006	0.452	-6.329	4.139	-2.763	0.085 ± 0.004	4.8 ± 0.1	4.4 ± 0.4
	−15 °C	7.019	5.293	-6.282	0.328	-7.985	0.085 ± 0.004	4.59 ± 0.07	4.3 ± 0.2

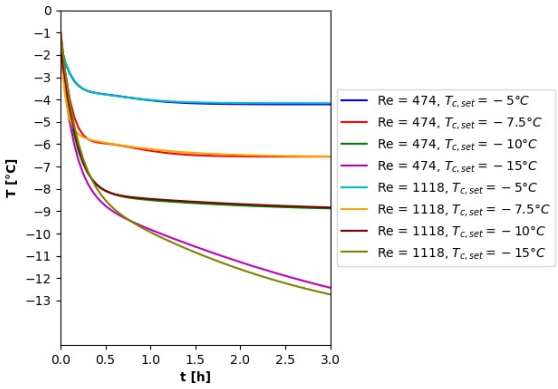

Figure 3.6: Modelled transient behaviour of the cold plate for the 8 different experimental conditions, according to equation 3.9 and table 3.2.

3.4. Conclusions and recommendations

This chapter presents an experimental benchmark study on the transient freezing of water in a square channel under laminar flow conditions, where ice is grown from a cold plate at the bottom. This is one of the few studies reporting the transient development of an ice layer in internal flow. In this work, both planar PIV velocity measurements and ice profiles sampled at multiple times during the experiment were presented, for both the inlet and the center of the test-section. The measurement of the transient development of the ice-layer near the inlet of the channel is an important novelty of the present experimental campaign. Furthermore, a study was performed regarding the effect of the cooling parameter and the bulk velocity on the rate of the ice-growth. As such, a comprehensive and well-described experimental data set was generated for transient freezing in laminar internal flow to be used for numerical validation purposes.

The onset of ice-formation was found to coincide with a sudden increase of the cold-plate temperature. This behaviour of the cold plate was attributed to subcooling occurring in the thermal boundary layer prior to nucleation, based on the findings of *Savino et al.* [94]. The sequence of the thermocouples' response showed that ice nucleation first occurs at the inlet of the channel, from which the ice subsequently spreads over the entire cold plate surface. From the data provided by the thermocouples in the cold plate, we were able to define a set of boundary conditions which provided a simple yet accurate description of the conditions during the experimental campaign.

Water is characterized by an anomalous expansion behaviour during the freezing process, with a density inversion around 4 °C. Based on the Richardson number, natural convection possibly played a role in our experiments. However, no evidence of (significant) natural convection was present in our PIV flow measurements. Possibly, the constant motion of the fluid prevented the development of convection cells.

For future work, we recommend to perform stereoscopic PIV measurements to obtain the spanwise (z) velocity components, and to perform non-intrusive temperature measurements within the channel, for instancing using laser induced fluorescence. Such measurements would be a further addition to the experimental benchmark data available for numerical model validation, in addition to providing insight into the possible generation of secondary flow during the transient development of the ice layer.

Data Availability

The experimental data from the PIV measurements is made available at `https://doi.org/10.5281/zenodo.7573327`.

4

NON-INTRUSIVE TEMPERATURE MEASUREMENTS FOR TRANSIENT FREEZING IN LAMINAR INTERNAL FLOW USING LASER INDUCED FLUORESENCE

This work presents two color LIF temperature measurements for the transient freezing in a square channel under laminar flow conditions. This is the first time non-intrusive temperature measurements were performed within the thermal boundary layer during the transient growth of an ice layer in internal flow. A combination of a local outlier factor algorithm and a smoothing operation was used to remove the top to bottom striations and reduce the other measurement noise. The temperature uncertainty in our measurements was between $\sigma = 0.3\,^{\circ}\mathrm{C}$ *and* $\sigma = 0.5\,^{\circ}\mathrm{C}$*. For the largest temperature difference between the bulk and the melting point of* $14.6\,^{\circ}\mathrm{C}$*, good results were obtained. As such, the current campaign demonstrates the potential of LIF as a non-intrusive temperature measurement technique for solid-liquid phase change experiments. However, some artefacts were present within the vicinity of the ice-layer due to the scattering of the laser light, especially near the inlet of the channel where the ice-layer is curved instead of flat. LIF measurements taken within a short time span prior to the onset of ice freezing showed approximately* $2\,^{\circ}\mathrm{C}$ *of subcooling, consistent with previous findings. In addition, an anomalous behaviour within the thermal boundary layer was observed, with a much smaller temperature gradient within the first few mm above the cold plate and a point of inflection in*

This chapter is based on B.J. Kaaks, D.Lathouwers, J.L. Kloosterman, M. Rohde. Non-intrusive temperature measurements for transient freezing in laminar internal flow using laser induced fluorescence. Submitted for publication.

the temperature profile. The anomalous temperature behaviour is possibly attributed to enhanced natural convection as a result of the subcooling at the cold plate surface.

4.1. Introduction

In the past, solid-liquid phase change experiments relied on intrusive techniques such as the pour-out method for identifying the solid-liquid interface and thermocouples for measuring the temperature [67]. However, these methods are invasive and may disturb the melting process [69]. It is therefore recommended to use non-intrusive techniques when conducting solid-liquid phase change experiments, especially when the purpose is to generate experimental data suitable for numerical model validation. Indeed, more recent experimental campaigns used photographic observations [78], [151], [152], X-ray diffraction [68], or the shadowgraph technique [70] for tracing the solid-liquid interface position. In addition, recent efforts were made to measure the velocity field using particle image velocimetry (PIV) [52], [70], [71], [76], [153] or ultra-sound doppler velocimetry [69].

On the other hand, very few non-intrusive temperature measurements have been performed for solid-liquid phase change experiments. Even in recent experimental campaigns (for instance those of *Ben David et al.* [69] and *Vogel et al.* [70]), thermocouples were used for measuring the temperature distributions in the solid and the liquid fields. However, it has been shown that the use of thermocouples leads to a distorted flow-field within the liquid phase and can considerably alter the melting and freezing-process[71], [77]. A few examples in literature report the use of an alternative, non-intrusive approach for measuring the temperature distributions. *Kowalewski et al.* [76] measured the temperature during the freezing of water using thermochromic liquid crystal (TLC) particles [76]. *Chen et al.* measured the temperature distribution in a melting paraffin wax (with embedded aluminium foam) using an infrared camera [154]. *Kumar et al.* measured the temperature fields during the freezing of water based on the temperature dependency of the refractive index, using Mach-Zender interferometry [137]. *Gong et al.* [133] measured the temperature distribution of melting n-octadecane using laser induced fluorescence (LIF).

LIF uses temperature sensitive dyes excited by laser light to measure the temperature field [155]. So far, LIF temperature measurements have been performed for a variety of cases, such as a heated jet [156], [157], a buoyant plume [158], [159], natural convection flow in a cavity [160], temperature measurements of evaporating and combusting droplets [161], an impinging jet [162]–[164], Rayleigh-Bènard convection [165] and the temperature distribution in the wake of a heated cylinder [166]. Furthermore, LIF has been used to identify the gas-liquid interfaces in multiphase flow [167] and to measure the ice fraction in supercooled water droplets [168]. Compared to TLC, LIF has a better range. However, the accuracy of LIF is largely dependent on the intensity resolution [159]. For instance, *Coolen et al.* achieved an accuracy of ±1.7°C over a temperature range of 19.8-55.2 °C and using an 8 bit camera whilst *Funatani et al.* reported an uncertainty of ±0.3°C using a colour CCD camera with 10 bits for each RGB, and a temperature range of 30.0-60.0 °C.

The main purpose of this chapter is to demonstrate the potential and limitations of LIF as a non-intrusive technique for measuring the temperature distribution in the liq-

uid phase during solid-liquid phase change experiments. To this end, we present two-color LIF temperature measurements of the water above the ice-water interface during the transient freezing of ice in a square channel under laminar flow conditions. Compared to the work by *Gong et al.*, several improvements were incorporated. These are the use of a two color (instead of a one color) LIF technique, the use of a post-processing algorithm to remove striations and other artefacts, and a detailed analysis of the uncertainty in the measured temperature fields. So far, the experimental data available for the transient growth of an ice-layer in internal flow is limited to three investigations only [52], [94], [153]. This is the first time non-intrusive temperature measurements were performed above an evolving solid-liquid interface in internal flow.

Additional temperature measurements were performed in the minutes prior to the onset of freezing. In our previous PIV campaign (see chapter 3), the onset of freezing was marked by a sudden increase of the cold plate temperature, accompanied by a rapid spreading of the ice over the cold plate. A similar behaviour of the cold-plate was observed by *Savino et al.* [94], who collected evidence of sub-cooling by performing thermocouple measurements within the thermal boundary layer in the time span from before the ice formed until after the thermocouple became embedded in the ice layer. The present work is the first to confirm the presence of subcooling within the thermal boundary layer of a flowing liquid through non-intrusive temperature measurements.

The structure of this chapter is as follows: in section 4.2 we describe the experimental method, including the design of the experimental measurements, the basic principle behind the LIF measurements, the optical setup, the experimental procedure, the image postprocessing, the temperature calibration and the uncertainty quantification. In section 4.3 we show our results and discussion, including temperature measurements taken both near the inlet and at the center of the channel for four different inlet temperatures, and temperature measurements taken during the 'lag time' prior to the onset of freezing. Finally, we present our conclusion and recommendations for future work in section 4.4.

4.2. Experimental Methodology

The full experimental setup consists of the ESPRESSO facility (please see chapter 2) and a LIF system consisting of a laser source, a laser guiding arm, two high speed cameras, a beam splitter and two high band pass filters (to separate the optical spectra of the dyes used). The laser sheet enters the test section through the top lid and illuminates a flow region of approximately $L \times H = 8\,\text{cm} \times 5\text{cm}$. The LIF images are recorded from the front side of the PMMA test section wall.

4.2.1. Laser induced fluorescence: principle

Laser induced fluorescence uses temperature-sensitive fluorescent dyes as a whole-field temperature diagnotistic. Upon excitation through exposure to laser light, the dyes emit light at a certain wave-length, of which the intensity can be used to determine the temperature. Neglecting Beer's attenuation of the incident laser light, the fluorescent energy I ($\mathrm{W\,m^{-3}}$) emitted per unit volume is defined as:

$$I = I_0 C \phi \epsilon \tag{4.1}$$

where I_0 is the incident light flux ($\mathrm{W\,m^{-2}}$), ϕ is the quantum efficiency of the dye (i.e. ratio of the total energy emitted per quantum of energy absorbed), C is the concentration of the dye solution ($\mathrm{kg\,m^{-3}}$) and ϵ ($\mathrm{m^2\,kg^{-1}}$) is a coefficient to correct for the fluorescence re-adsorption [155]. When recording camera images, the image intensity G is proportional to the fluorescence intensity [164]:

$$G = \alpha I + G_{noise} \tag{4.2}$$

where α is an optical transfer function and G_{noise} is the camera offset noise.

For some organic dyes, the quantum efficiency is dependent on the temperature, resulting in a temperature sensitive fluorescent intensity. Thus, if one can keep the incident light flux I_0 and the concentration constant, one can measure the temperature (on the other hand, when keeping the incident light flux and the temperature constant, one can measure the concentration, see for instant *Hjertager et al.* [169]).

In practice, I_0 is affected by a variety of factors, such as convergence and divergence of the light sheet, refraction of the light sheet (for instance due to gradients in the refractive index as a result of the temperature differences), variation in incident laser intensity (in particular for setups using a pulsed laser), and scattering of the laser light due to air bubbles or other particles blocking the laser transmission and the transient growth of the ice-layer.

For (quasi) steady-state experiments, a careful normalization is performed using a series of reference images taken at a known uniform temperature field to correct for the spatial distribution of the laser sheet intensity. In addition, by recording the energy of the laser, the pulse-to-pulse energy of the laser can be taken into account [159], [166]. However, it is difficult to eliminate the effect of the laser light reflection due to the transient growth of the ice layer using these techniques. In addition, the transient freezing process possibly affects the dye concentration.

Instead, a temperature-insensitive reference dye can be used as a means of measuring the local, instantaneous intensity of the laser sheet [155]. This leads to the use of a mixture of two different dyes, one temperature sensitive and one temperature insensitive, with different emission spectra. Assuming the emission spectra can be perfectly separated using a combination of beam-splitting optics and band-pass filters, and neglecting the offset noise, the ratio between the two dyes is written as:

$$\frac{G_\alpha}{G_\beta} = \frac{I_\alpha}{I_\beta} = \frac{C_\alpha \phi_\alpha \epsilon_\alpha}{C_\beta \phi_\beta \epsilon_\beta} \tag{4.3}$$

where the subscript α and β refer to the temperature-sensitive dye and the reference dye respectively. In theory, the intensity ratio is now independent of the incident

light flux I_0, whilst still dependent on the temperature [155], [163]. In practice, there is some overlap between the emission spectrum of the two fluorescent dyes, resulting in an imperfect separation of the spectra. Consequently, some fraction of I_α is detected by camera β and vice versa. This can be accounted for by a proper calibration procedure [155], [163].

4.2.2. Selection of the fluorescent dyes

Rhodamine B (RhB) was selected as the temperature-sensitive dye, due to its high temperature sensitivity (2.3 % K^{-1}) and because its absorption spectrum covers the range of 470-600 nm, making excitation easy by conventional lasers [155]. Rhodamine 110 has a similarly suitable adsorption spectrum, but has a very low temperature sensitivity and was thus selected as the reference dye. The dye concentrations were optimised in order to achieve a good signal output in both camera feeds. The procedure involved adding droplets of a concentrated solution of each dye to the buffer vessel, until the maximum intensity of camera α (i.e. for RhB) reached half the dynamic range at 20 °C (leaving room for intensity changes due to a change in temperature) and the maximum intensity of camera β (i.e. for Rh110) was close to the maximum dynamic range. Due to the procedure and the large volume of fluid involved, it was difficult to quantify the exact concentration of the dyes, but the range falls within 10 to 100 $\mu g L^{-1}$. The basic properties of the fluorescent dyes used are given in table 4.1.

Table 4.1: Basic characteristics of RhB and Rh110 dissolved in deionized water (T = 20 °C) [155].

Dye	Molecular weight	λ_{abs} [nm]	λ_{em} [nm]	ϕ	Temperature sensitivity [K^{-1}]
Rhb	479.02	554	575	0.31	2.3 %
Rh110	366.8	496	520	0.8	0.13 %

4.2.3. Optical setup

The dissolved dyes were excited using a class-IV, 5W shuttered continuous wave laser (diode pumped, solid-state) with a wave length of $\lambda = 532nm$ (LaVision, Germany). A laser guiding arm (LaVision, Germany) was used to introduce the laser sheet from the top of the test section and a combination of a spherical and a cylindrical lens was used to generate the laser sheet. The sheet has a beam waist thickness of approximately 1 mm. The region of interest is observed simultaneously by two CMOS cameras (Imager MX-4M, LaVision, Germany) with 12 bit of dynamic range and 4 MP of resolution (pixel size of 5.5µm × 5.5µm). Both cameras mount an AF-S 50mm F/1.4 (Nikon) lens. A first separation of the two spectral bands is achieved using a dichroic beamsplitter (ZT561rdc-UF3 of Chroma, USA) and a second separation is achieved using interference filters at 600 nm and 550 nm respectively, both with a full width half maximum (FWHM) of 20 nm. To limit the reflection of the laser, black aluminium tape was applied to the surface of the cold wall and the back wall of the test section. A schematic of the optical setup is shown in figure 4.1.

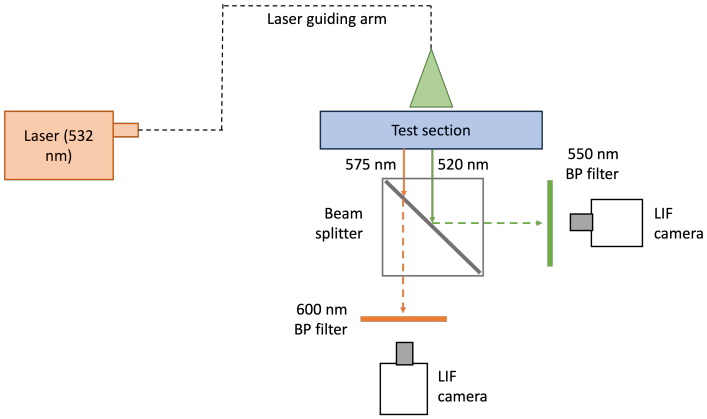

Figure 4.1: Optical setup of LIF experiments.

Prior to the start of the experimental campaign, an image calibration procedure is performed using a calibration plate. A 3rd order polynomial function was fitted by the least-squares method in order to transform the image coordinate to the physical coordinate. An additional self calibration step is performed to correct for possible errors due to light sheet or calibration plate misalignment. The root mean square errors of the image calibration are 1.1 pixel and 1.6 pixel for camera α and β respectively.

4.2.4. Experimental procedure

The temperature fields were measured for four different set point temperatures of the inlet temperature (i.e. $T_{in,set} = 15\,^{\circ}\text{C}$, $T_{in,set} = 10\,^{\circ}\text{C}$, $T_{in,set} = 5\,^{\circ}\text{C}$ and $T_{in,set} = 0.5\,^{\circ}\text{C}$). The flow-rate corresponds to $Re = 474$ and the set point of the cold plate is set to $T_{c,set} = -10\,^{\circ}\text{C}$. Measurements were performed at both the inlet and at the centre of the test section. The experiment was initialized as follows. First the water was recirculated at the maximum available flow rate whilst the cold plate and the inlet were being cooled according to the desired set-point temperatures. After the cold plate and the inlet temperatures stabilized, the flow rate was reduced to the desired value. Because the cold plate was in direct contact with the water flow above, reducing the flow rate of the water (and therefore the heat exchange between the water and the surface of the cold-plate) resulted in a further decrease of the cold plate temperature. The onset of freezing was marked by a sudden sharp increase of the cold plate temperature, and was therefore used to determine $t = 0$ in our experiments (see chapter 3).

During the first hour after the onset of ice-formation at $t = 0$, an image recording was made every 5 min. At each measurement, 25 pairs of images were recorded with a frequency of 10 Hz. The camera and laser were synchronized using a programmable timing unit (PTU, LaViSion, Germany) operated using Davis v8 software. During the second hour of the experiment, this frequency was reduced to each 15 min and after the third hour to 30 min. During the experiment, the temperatures measured by the thermocouples as well as the flow rate were recorded in real time and stored using the LabView software.

4.2.5. Post-processing of images

The images are pre-processed using the LaVision 8 software. First, an average of 100 camera dark images (taken with the lens cap on) is substracted from the LIF images of camera α and camera β in order to remove the dark current noise from the images. Next, a white image correction is performed. Here, the white image is the average of 25 images of the area of interest taken at an uniform reference temperature of $T_{ref} = 17.8 \pm 0.2°C$. The whole preprocessing operation is described as:

$$\tilde{I}_{\alpha,\beta}(x,y) = \frac{\left(I_{\alpha,\beta}(x,y) - I_{dark_{\alpha,\beta}}(x,y)\right)}{I_{WI_{\alpha,\beta}}(x,y)} \overline{I}_{WI_{\alpha,\beta}} \tag{4.4}$$

Here, $\overline{I}_{WI_{\alpha,\beta}}$ is the spatial average of the white image in the area of interest.

The corrected image intensities from camera α and camera β are subsequently divided by one another to obtain the ratio used as a basis for the temperature calculations:

$$I_R = \frac{\tilde{I}_\alpha}{\tilde{I}_\beta}, \tag{4.5}$$

where I_R is used as the symbol for the ratio between the image intensities.

Finally, the average intensity ratio of each sample set (containing 25 images from both camera's α and β) is calculated. An example of the intensity ratio map is shown in figure 4.2a. Here, $y = 0$ denotes the bottom of the test section where the cold-plate is located and $x = 0$ denotes the center of the area of interest.

The intensity ratio map is contaminated by the presence of multiple top-bottom striations running through the area of interest. These striations are caused by the refraction of the laser light due to factors such as the fluid's irregular density, air bubbles[1], or inhomogeneities in the top lid of the test section where the laser enters (caused by dirt particles, fat stains or surface damage). Due to the use of the two-color LIF technique, these striations were expected to be canceled out. However, as shown by *Sakibara et al.* [165], a mismatch in the intensity profiles between the images of cameras α and β can prevent the elimination of the striations, leading to a significant error in the intensity ratio (and thus the temperature). This mismatch can be caused by small errors in the image calibration (as shown in the previous section), a different focusing and aberrations of the object lenses, or from astigmatic abberation caused by the inclined beam splitter. In previous work, striations were corrected using a correction map based on a reference region with a uniform temperature (and therefore uniform intensity) [166] [159] [164], or using a transfer function in the Fourier domain in order to achieve perfect overlap between the intensity profiles of the α and β camera images [165]. In the present work, a different approach was adopted and the top to bottom striations were consider to be outliers. The outliers were removed by scanning the intensity ratio map from top to bottom and using a local outlier factor (LOF) algorithm [170]. The LOF algorithm assigns a degree of being an outlier to each data point, depending on how isolated the data point is with respect to its neighbours. As such, the LOF algorithm differs from other outlier removal algorithms which consider being an outlier as a binary property. The LOF of each

[1] Especially small air bubbles may pass through the bubble trap.

sample point is calculated according to a density-based clustering algorithm, where the density is calculated according to the assigned number of neighbours (500 for the center of the channel based on a very small temperature gradient in the x-direction and 100 for the inlet of the channel, where the temperature gradient in the x-direction is more significant) and the distance from the data point to each neighbour. The thresholds for the LOF are determined based on a user-defined degree of contamination (here, 0.5 was used for the center of the channel and 0.33 for the inlet of the channel). Data points for which the LOF exceeds the threshold are replaced by a linear interpolation.

Finally, the remaining image noise was reduced by smoothing the image using a moving average window. For the center of the channel (between x = 70cm and x = 80cm), a smoothing window of $N_x \times N_y = 200 \times 25$ pixels was used. The large degree of smoothing in the x-direction for the center of the channel was justified, because the temperature variation in this direction is very small as a result of the flow being (almost) fully developed. For the inlet of the channel, a smoothing window of $N_x \times N_y = 50 \times 25$ pixels was used. Here, there is a more significant temperature gradient in the x-direction due to the development of the thermal boundary layer. The chosen window sizes were believed to be a good compromise between achieving sufficient spatial resolution and reducing the image noise. The different steps in the post-processing procedure (after pre-processing, after the LOF outlier removal and after the smoothing operation) are shown in figure 4.2 for the center of the channel and figure 4.3 for the inlet of the channel.

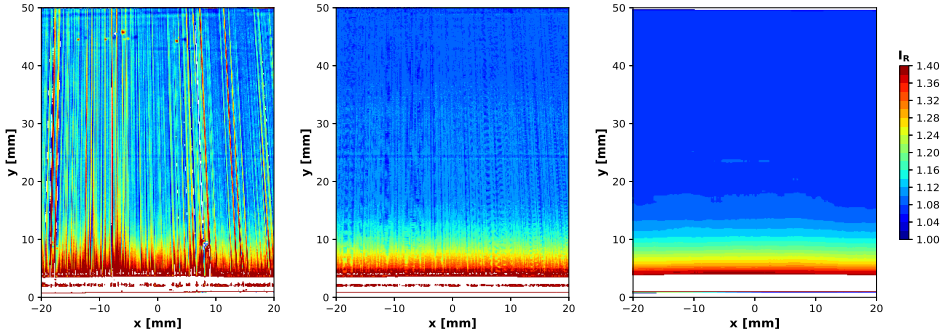

(a) Intensity ratio map after pre-processing.

(b) Intensity ratio map after striation removal through LOF algorithm.

(c) Intensity ratio map after smoothing.

Figure 4.2: Intensity ratio map after the different postprocessing steps (pre-processing (a), striation removal (b), smoothing (c)), taken at the center of the test-section for $t = 5$ min after the onset of ice-formation. The experimental settings were: $Re \approx 474$, $T_{in,set} = 15°C$ and $T_{c,set} = -10°C$.

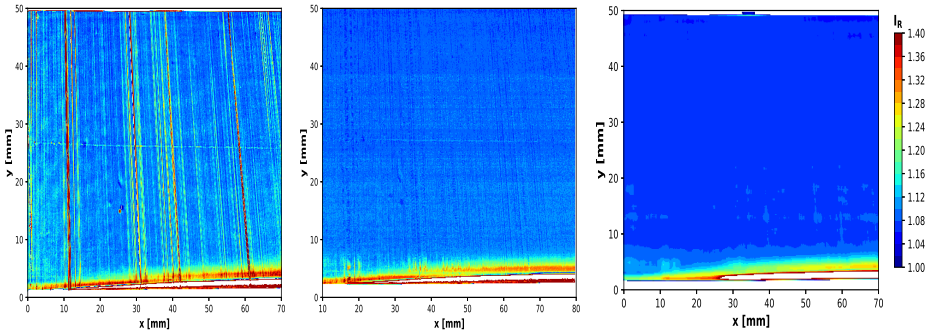

(a) Intensity ratio map after pre-processing.

(b) Intensity ratio map after striation removal through LOF algorithm.

(c) Intensity ratio map after smoothing.

Figure 4.3: Intensity ratio map after the different postprocessing steps (pre-processing (a), striation removal (b), smoothing (c)), taken at the inlet of the test-section for $t = 5$ min after the onset of ice-formation. The experimental settings were: $Re \approx 474$, $T_{in,set} = 15°C$ and $T_{c,set} = -10°C$.

4.2.6. Temperature calibration procedure

The temperature calibration procedure was performed by using the same set-point temperature for the pre-cooling of the inlet and the cold plate. Hereby, 13 images were recorded at uniform temperatures ranging from 17 to 5 °C. The images were pre-processed using the procedure outlined in section 4.2.5, and the average intensity in the area of interest was calculated. The temperature calibration data points are given in table 4.2 and plotted in figure 4.4. The temperature intensity-ratio relationship is described by the following linear relationship:

$$T[°C] = a(I_R - 1.0) + b \tag{4.6}$$

The coefficients of the fit were found using the orthogonal distance regression algorithm [171], which is capable of taking into account both the uncertainties in the intensity ratio data and the uncertainties in the temperature (since the thermo-couples have an uncertainty of 0.2 °C): $a = -45.9 \pm 0.8$ K, $b = 18.1 \pm 0.1$ K.

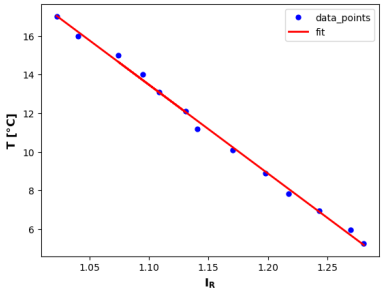

Figure 4.4: Temperature calibration curve.

Table 4.2: Temperature calibration data.

Average intensity ratio	Relative standard deviation	Temperature
1.0222 %	3.29 %	$17.0 \pm 0.2^{\circ}$C
1.0405 %	4.53 %	$16.0 \pm 0.2^{\circ}$C
1.07416 %	10.55 %	$15.0 \pm 0.2^{\circ}$C
1.09484 %	6.08 %	$14.0 \pm 0.2^{\circ}$C
1.10848 %	6.06 %	$13.1 \pm 0.2^{\circ}$C
1.13094 %	6.48 %	$12.1 \pm 0.2^{\circ}$C
1.14077 %	7.22 %	$11.2 \pm 0.2^{\circ}$C
1.17054 %	7.35 %	$10.1 \pm 0.2^{\circ}$C
1.19784 %	7.51 %	$8.9 \pm 0.2^{\circ}$C
1.21764 %	7.69 %	$7.9 \pm 0.2^{\circ}$C
1.124342 %	7.92 %	$7.0 \pm 0.2^{\circ}$C
1.26958 %	7.97 %	$6.0 \pm 0.2^{\circ}$C
1.28080 %	7.87 %	$5.3 \pm 0.2^{\circ}$C

The experimental campaign was performed over the course of roughly two months, during which the same calibration was used. To correct for possible changes to the experimental conditions (such as quenching of the dye, a change in the concentration ratio or the presence of a reflective ice layer), a constant correction factor was used. At the start of the experiment, the temperature above the half-width of the channel should be equal to the bulk temperature (from now on referred to as the region of reference). For the center of the channel (between x = 70cm and x = 80cm), we defined the region of reference (ROR) to be $[x_0 : x_{end}, y_0 : y_{end}] = [-20 : 20, 25 : 45]$ mm^2 . The expected bulk temperature T_0 can be obtained from the inlet and outlet temperatures (as measured by the thermo-couples). Using the calibration, the bulk temperature is converted to an intensity ratio $I_{R,0}$ using equation 4.6:

$$T_0[^{\circ}\text{C}] = a\left(I_{R,0} - 1.0\right) + b \tag{4.7}$$

$$\frac{T_0}{a} + 1.0 - \frac{b}{a} = I_{R,0}. \tag{4.8}$$

The expected intensity ratio is compared with the average intensity ratio in the region of reference from the LIF measurements ($\bar{I}_{R,ROR}$). Subsequently, the correction factor is calculated as

$$C_F = \frac{I_{R,0}}{\bar{I}_{R,ROR}} \tag{4.9}$$

and the intensity ratio is corrected as:

$$\tilde{I}_R = C_F \times I_R. \tag{4.10}$$

The corrected temperatures are thus calculated as:

$$T[^{\circ}\text{C}] = a(\tilde{I}_R - 1.0) + b = a\left(\frac{I_{R,0}}{\bar{I}_{R,ROR}} I_R - 1.0\right) + b. \tag{4.11}$$

4.2.7. Uncertainty quantification

Using the formula for the propagation of uncertainties, the uncertainty in the temperature is derived from equation 4.11:

$$\sigma_T^2[^\circ\mathrm{C}] = \left(\frac{\partial T}{\partial a}\right)^2 \sigma_a^2 + \left(\frac{\partial T}{\partial b}\right)^2 \sigma_b^2 + \left(\frac{\partial T}{\partial \tilde{I}_R}\right)^2 \sigma_{\tilde{I}_R}^2 = \underbrace{\left[(\tilde{I}_R - 1.0)\sigma_a\right]^2 + \sigma_b^2}_{\sigma_{T,cal}} + \underbrace{(a\sigma_{\tilde{I}_R})^2}_{\sigma_{T,\tilde{I}_R}}. \tag{4.12}$$

The total uncertainty can be split into an uncertainty in the temperature calibration and an uncertainty in the measured (corrected) intensity ratio. The uncertainty in the temperature calibration is obtained from the uncertainties in the fit coefficients ($\sigma_a \approx 0.8\,^\circ$C and $\sigma_b \approx 0.1\,^\circ$C) and translates into a temperature uncertainty of approximately $\sigma_{T,cal} = 0.15\,^\circ$C for a temperature of $T = 15\,^\circ$C.

The uncertainty in the corrected intensity ratio $\sigma_{\tilde{I}_R}$, is derived from equation 4.10:

$$\sigma_{\tilde{I}_R}^2 = \left(\frac{\partial \tilde{I}_R}{\partial C_F}\right)^2 \sigma_{C_F}^2 + \left(\frac{\partial \tilde{I}_R}{\partial I_R}\right)^2 \sigma_{I_R}^2 = (I_R\sigma_{C_F})^2 + (C_F\sigma_{I_R})^2. \tag{4.13}$$

As such, the uncertainty in the corrected intensity ratio is determined by both the uncertainty in the correction factor and the uncertainty in the measured (uncorrected) intensity ratio. The uncertainty in the measured (uncorrected) intensity ratio σ_{I_R} consists of a statistical and a systematic uncertainty contribution:

$$\sigma_{I_R}^2 = \sigma_{I_{R,stat}}^2 + \sigma_{I_{R,sys}}^2 \tag{4.14}$$

The statistical uncertainty originates from factors such as the camera noise or fluctuations in the laser intensity. The statistical contribution to σ_{I_R} is calculated as

$$\sigma_{I_{R,stat}}^2 = \frac{1}{N_t N_x N_y (N_t - 1)} \sum_{i=1}^{N_t} \left(I_{R_i} - \bar{I}_R\right)^2, \tag{4.15}$$

where $N_t = 25$ is the number of samples used for the time-averaging, and N_x, N_y are the number of pixels in the x- and y-direction over which the smoothing operation is performed[2].

The systematic uncertainty originates from the presence of artefacts such as the striations and the sensitivity of the camera. The systematic uncertainty is estimated by calculating the standard deviation within the region of reference (ROR) where a uniform intensity ratio is expected, and subtracting the statistical uncertainty:

$$\sigma_{I_{R,sys}}^2 = \left(\frac{1}{N_{ROR}(N_{ROR} - 1)} \sum_{i=1}^{N_{ROR}} \left(I_{R_i} - \bar{I}_{R,ROR}\right)^2\right) - \sigma_{I_{R,stat}}^2, \tag{4.16}$$

[2] Using a larger averaging window in either time or space will reduce the statistical error (and also require either more time samples or result in the loss of spatial resolution), since we consider the statistical uncertainty to be caused by random fluctuations in quantities such as the camera pixel gain or the laser intensity which cancel each other out upon averaging.

where N_{ROR} is the number of data points in the ROR. We consider the estimated systematic uncertainty within the region of reference to be representative of the systematic error within the entire area of interest.

Finally, the uncertainty in the correction factor is derived from equation 4.9:

$$\sigma_{C_F}^2 = \left(\frac{\partial C_F}{\partial I_{R,0}}\right)^2 \sigma_{I_{R,0}}^2 + \left(\frac{\partial C_F}{\partial \bar{I}_{R,ROR}}\right)^2 \sigma_{\bar{I}_{R,ROR}}^2 = \left(\frac{1}{\bar{I}_{R,ROR}} \sigma_{I_{R,0}}\right)^2 + \left[\left(\frac{I_{R,0}}{\bar{I}_{R,ROR}^2}\right) \sigma_{\bar{I}_{R,ROR}}\right]^2. \quad (4.17)$$

The uncertainty in the average intensity in the window of reference $\bar{I}_{R,ROR}$ is calculated as

$$\sigma_{\bar{I}_{R,ROR}}^2 = \frac{\frac{1}{N_{ROR}(N_{ROR}-1)} \sum_{i=1}^{N_{ROR}} \left(I_{R_i} - \bar{I}_{R,ROR}\right)^2}{N_{ROR}}. \quad (4.18)$$

The uncertainty the reference intensity $I_{R,0}$ is calculated as

$$\sigma_{I_{R,0}}^2 = \left(\frac{\partial I_{R,0}}{\partial T_0}\right)^2 \sigma_{T_0}^2 + \left(\frac{\partial I_{R,0}}{\partial a}\right)^2 \sigma_a^2 + \left(\frac{\partial I_{R,0}}{\partial b}\right)^2 \sigma_b^2 = \left(\frac{1}{a} \sigma_{T_0}\right)^2 + \left(\frac{T_0 - b}{a^2} \sigma_a\right)^2 + \left(\frac{1}{a} \sigma_b\right)^2, \quad (4.19)$$

where $\sigma_{T_0} = 0.2°\text{C}$ (the uncertainty in the thermo-couple). The contribution from the uncertainty in the measured (corrected) intensity ratio amounts to approximately $\sigma_{T,\tilde{I}_R} \approx 0.3°\text{C}$, but may vary across the different measurements.

4.3. Results and Discussion

4.3.1. Observing the transient growth of an ice-layer using laser induced fluorescence

Figure 4.5 shows the image intensities for camera α (corresponding to the temperature sensitive dye Rhodamine B), after respectively 15, 30, 45 and 60 min of ice-growth. The experimental settings were: $Re \approx 474$, $T_{in,set} = 0.5°\text{C}$ and $T_{c,set} = -10°\text{C}$. The highest intensities were observed between $x = 20\,\text{mm}$ and $x = 40\,\text{mm}$, where the laser sheet is centered. Several top to bottom striations were present in the raw LIF images from camera α. These striations were not eliminated upon calculating the intensity ratio between the images of camera α and camera β, and therefore need to be removed using the proposed post-processing procedure described in section 4.2.5.

The ice has a significantly lower fluorescence emission intensity compared to the liquid water above. We believe this is both because of the scattering of the laser light by the ice-water interface and due to the fact that the concentration of Rhodamine B (and also Rhodamine 110) is significantly lower in the ice than in the water as a result of the rejection of the dyes during the crystallization process, leaving the dyes behind in the solution. This hypothesis is supported by the transparent color of the ice in our experiments, whilst the liquid water had a red-greenish color from the dissolved dyes. Based on this observation, we therefore recommend using two color LIF for solid-liquid phase change experiments, especially for freezing or melting in an enclosure where the phase change may significantly affect the dye concentrations [3].

For comparison purposes, the ice-layer thickness measurements from our previous PIV campaign (see chapter 3) was plotted on top of the LIF image intensities. A good match was observed between the scattering signal of the laser light from the ice-water interface (characterized by a high intensity line following the curvature of the ice layer) and the PIV ice layer measurements. Therefore, in principle it is possible to use the scattering of the laser by the ice-water interface to determine its position. However, very close to the inlet (within roughly the first 10 to 25 mm depending on the time after the onset of ice-formation) no clear LIF signal from the scattering of the laser could be observed. Alternatively, the location of the ice-layer can be determined based on $T = 0\,^{\circ}\mathrm{C}$. However, the scattering of the laser light may pose a challenge for an accurate measurement of the temperature within in the thermal boundary layer, as shown in section 4.3.2 and by *Gong et al.* and [133] who described similar challenges. Therefore, whenever possible we recommend using an alternative technique for determining the solid-liquid interface (such as PIV), due to the associated difficulties with using LIF for interface tracking . Please also refer to *Voulgorapoulos et al.* [52] who conducted early-stage experimental trials attempting to use LIF for locating the solid-liquid interface and concluded that a more accurate and reliable tracking methodology could be established when using PIV.

[3] We would like to point out that *Gong et al.* used one-color LIF for measuring the temperature fields during the melting of n-octadecane in a cuboid, possibly influencing the results especially towards the end of the experiment.

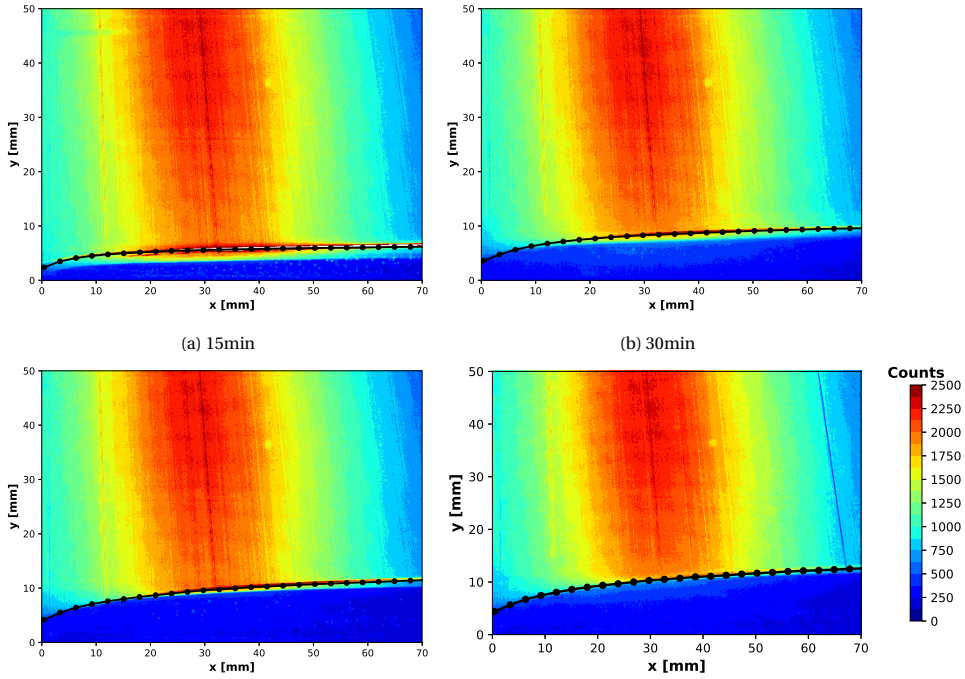

(a) 15min (b) 30min

(c) 45min (d) 60min

Figure 4.5: Intensity counts for camera α (detecting the emission intensity of Rhodamine B) after respectively 15, 30, 45 and 60 min of ice-growth. The experimental settings were: $Re \approx 474$, $T_{in,set} = 0.5°C$ and $T_{c,set} = -10°C$. The ice growth measurements from the previous PIV campaign (see chapter 3) are plotted in white.

4.3.2. LIF Temperature measurements

Figure 4.6 shows the LIF temperature measurements at the center of the channel for four different set points of the inlet temperature, these are $T_{in,set} = 15\,°C$, $T_{in,set} = 10\,°C$, $T_{in,set} = 5\,°C$ and $T_{in,set} = 0.5\,°C$. The in and outlet temperatures measured by the thermo-couples, as well as the used correction factors, are given in table 4.3. Overall, qualitatively promising results were obtained. The thermal boundary layer is clearly visible above the ice, demonstrating the potential of LIF as a non-intrusive temperature measurement techniques. Even for the smallest set point temperature of $T_{in,set} = 0.5\,°C$ (where the actual inlet temperature is approximately equal to 4.7 °C and the outlet temperature is around 4.5 °C resulting in a temperature difference of around 4.5-4.7 °C between the bulk and the melting point), the thermal boundary layer is clearly visible indicating an adequate temperature resolution of the technique. Consistent with expectations, the temperature variation in the x-direction is very small. Despite the promising results, we would like to note that the post-processing involved a significant amount of smoothing (as shown in section 4.2.5). The large amount of smoothing produced the temperature artefact near the top of the channel at $y = 50$ mm and may lead to spatial inaccuracies. For the smallest temperature range, the relative uncertainty was quite

significant at about 10%. In addition, the absolute temperature uncertainty was higher for the smaller temperature ranges (around $\sigma = 0.5\,^{\circ}\mathrm{C}$ for $T_{in,set} = 0.5\,^{\circ}\mathrm{C}$ compared to $\sigma = 0.3\,^{\circ}\mathrm{C}$ for $T_{in,set} = 15\,^{\circ}\mathrm{C}$). This is caused by a smaller signal to noise ratio, resulting in a less efficient removal of the top to bottom striations using the local outlier factor algorithm, as well as a higher uncertainty in the temperature calibration at the lowest temperatures (recall that the uncertainty in the calibration scales with the intensity ratio, which is higher at lower temperatures, as shown in section 4.2.7).

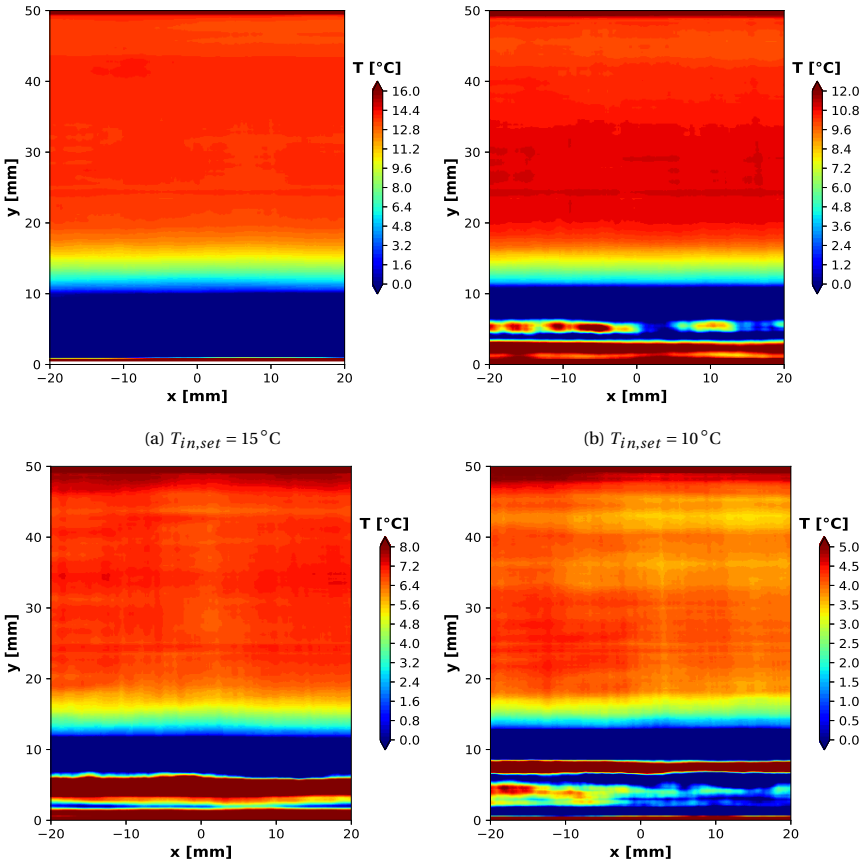

(a) $T_{in,set} = 15\,^{\circ}\mathrm{C}$

(b) $T_{in,set} = 10\,^{\circ}\mathrm{C}$

(c) $T_{in,set} = 5\,^{\circ}\mathrm{C}$

(d) $T_{in,set} = 0.5\,^{\circ}\mathrm{C}$

Figure 4.6: LIF temperature field measurements at the center of the channel after 30 min of ice growth, for different inlet temperature conditions.

Figure 4.7 shows the temperature measurements at the inlet of the channel. Compared to the measurements at the center, the measurements at the inlet were more challenging because the curvature of the ice-layer introduced additional noise due to the scattering of the laser light, and because the variation of the temperature in the x-direction resulted in a more troublesome removal of the striations (and other outliers), with a smaller degree of smoothing being applied (as shown in section 4.2.5). In addition, the thermal boundary layer above the ice-layer is thinner. Although the thermal boundary layer above the ice-layer is visible for all four measurements, the results are relatively noisy.

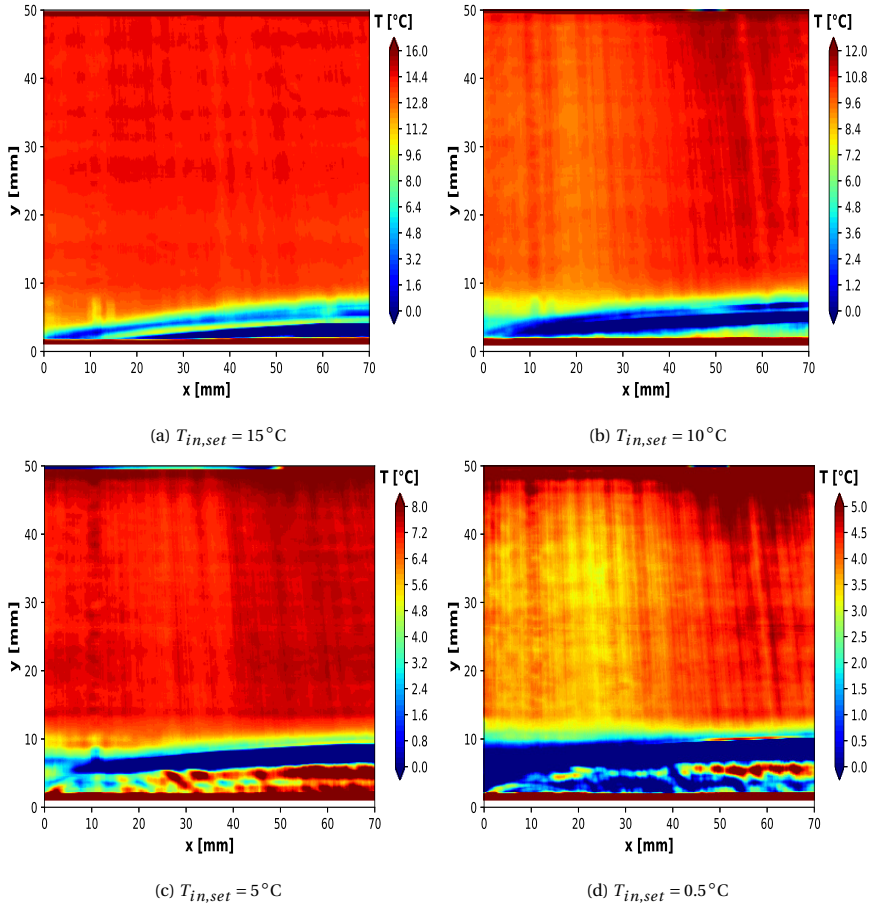

(a) $T_{in,set} = 15\,^{\circ}\mathrm{C}$

(b) $T_{in,set} = 10\,^{\circ}\mathrm{C}$

(c) $T_{in,set} = 5\,^{\circ}\mathrm{C}$

(d) $T_{in,set} = 0.5\,^{\circ}\mathrm{C}$

Figure 4.7: LIF temperature field measurements at the inlet of the channel after 30 min of ice growth, for different inlet temperature conditions.

Table 4.3: Correction factor and representative uncertainty.

Location	$T_{in,set}$	ϕ_v(Ls^{-1})	T_{in}(°C)	T_{out}(°C)	Correction factor	$\overline{\sigma}_T$
center	15 °C	0.038 ± 0.004	14.60 ± 0.04	13.7 ± 0.4	1.009 ± 0.005	0.3 °C
	10 °C	0.038 ± 0.004	10.73 ± 0.04	10.1 ± 0.2	1.023 ± 0.005	0.4 °C
	5 °C	0.037 ± 0.004	6.9 ± 0.2	6.8 ± 0.3	1.030 ± 0.005	0.4 – 0.6 °C
	0.5 °C	0.036 ± 0.007	4.7 ± 0.2	4.6 ± 0.3	1.020 ± 0.006	0.4 – 0.5 °C
inlet	15 °C	0.038 ± 0.004	14.56 ± 0.05	13.6 ± 0.4	1.008 ± 0.005	0.3 °C
	10 °C	0.037 ± 0.004	10.56 ± 0.02	10.26 ± 0.07	0.999 ± 0.005	0.5 °C
	5 °C	0.036 ± 0.004	6.7 ± 0.1	6.4 ± 0.2	0.999 ± 0.005	0.4 °C
	0.5 °C	0.036 ± 0.004	4.71 ± 0.07	4.5 ± 0.3	1.015 ± 0.005	0.5 °C

Figure 4.8 shows the temperature profiles for different times and two different inlet temperatures, i.e. T_{in} = 15 °C and T_{in} = 0.5 °C. For T_{in} = 15 °C, good results were obtained. Especially for the center of the channel at x = 75cm, the relative temperature uncertainty appears to fall within an acceptable range, with smooth temperature profiles obtained and a sufficiently high temperature resolution within the thermal boundary layer. Compared to the center of the channel, a steeper temperature gradient is observed within the temperature boundary layer near the inlet, which is consistent with the expected behaviour. However, for the inlet of the channel at x = 5 cm, the scattering of the laser light from the ice-water interface (also see figure 4.5) introduced some artefacts in the camera images, which led to unphysical temperature oscillations within the thermal boundary layer for some of the measured time instances. This unphysical behavior was not included in our uncertainty analysis. In addition, for the smallest temperature range with T_{in} = 0.5°C, the relative uncertainty is approximately ±10%, resulting in less smooth temperature profiles. For such small temperature ranges, improvements to the present setup are needed in order to perform sufficiently accurate LIF temperature measurement results which can be used for numerical benchmarking purposes. These improvements should consist of less air-bubbles and a lid specially designed to ensure optimal transition of the laser, an improved optical setup (for instance using more sensitive cameras or changing the dyes or filters to achieve a better separation between the spectra in each camera image) or an additional post-processing routine to reduce the noise caused by the scattering of the laser light from the ice-water interface.

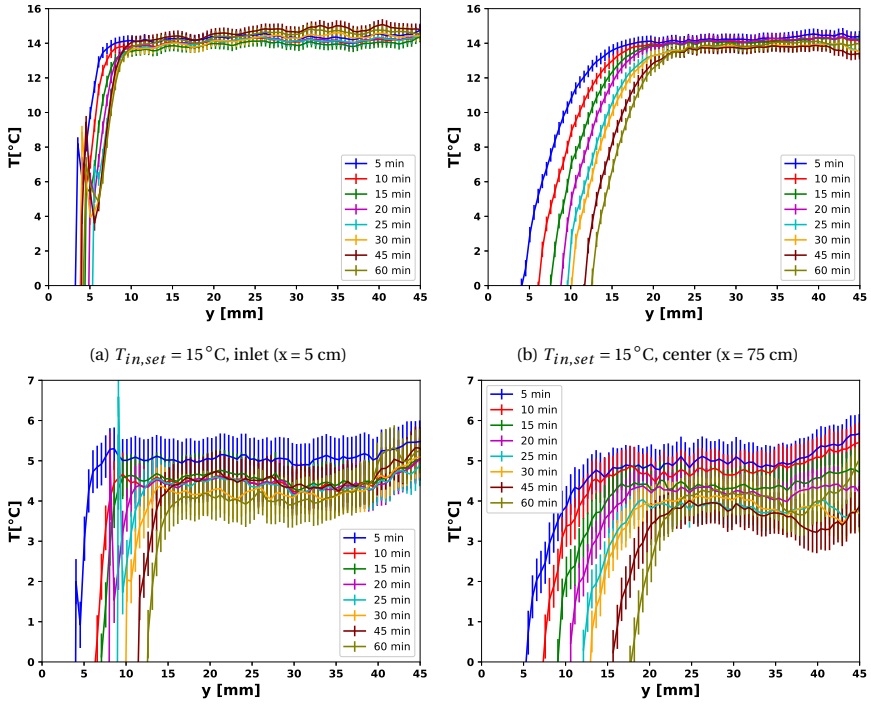

(a) $T_{in,set} = 15\,^{\circ}\mathrm{C}$, inlet (x = 5 cm)

(b) $T_{in,set} = 15\,^{\circ}\mathrm{C}$, center (x = 75 cm)

(c) $T_{in,set} = 0.5\,^{\circ}\mathrm{C}$, inlet (x = 5 cm)

(d) $T_{in,set} = 0.5\,^{\circ}\mathrm{C}$, center (x = 75 cm)

Figure 4.8: LIF temperature profiles at the inlet and the center of the channel for two different inlet temperatures, i.e. $T_{in,set} = 15\,^{\circ}\mathrm{C}$ and $T_{in,set} = 0.5\,^{\circ}\mathrm{C}$ Results are shown for both the inlet and the center of the channel.

4.3.3. Temperature measurement in the lag time prior to freezing

Consistent with our previous PIV campaign [153] and the results obtained by *Savino et al.* [94], the onset of freezing was marked by a rapid spreading of ice over the entire cold plate, accompanied by a sudden increase of the cold plate temperature, as can be seen in figure 4.9. Thermocouple 0 at the inlet of the channel is the first to experience a sudden temperature increase, and the ice nucleus is shown to propagate at a near constant velocity of approximately 5 $\mathrm{cm\,s^{-1}}$ towards the exit of the channel, as shown by the quasi linear relationship between the different time-instances at which the thermocouples notice the effect of phase change. The total delay between the response of thermocouple 7 at the end of the cold plate and thermocouple 0 at the inlet was less than 30 s. Freezing only occurred after the cold plate had reached a subzero temperature of between -4 and -6 °C for an inlet temperature of $T = 15\,^{\circ}\mathrm{C}$. Previously, *Savino et al.* had presented evidence of subcooling within the thermal boundary layer of the liquid [94], collected through a thermocouple probe before the formation of ice occurred.

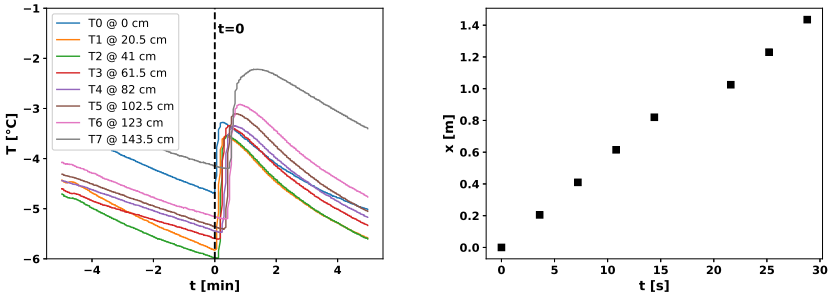

(a) (b)

Figure 4.9: Cold plate temperature response in the 5 min before and after the onset of freezing (a), for $T_{in,set} = 15\,°C$. T0-T7 refer to the different locations of the thermocouples. Propagation of the ice nucleus from the inlet to the exit of the channel (b). The vertical axis denotes the location of the thermocouples and the horizontal axis denotes the time after which the first thermocouple (T0) recorded the onset of freezing.

The present experimental campaign is the first to present non-intrusive temperature measurements within the thermal boundary layer prior to the start of the freezing process. Figure 4.10 shows the temperature profiles at the center of the test section in the moments before the onset of ice-formation, for $T_{in,set} = 15\,°C$. Please note that a smaller degree of smoothing in the y-direction was used of $N_x \times N_y = 200 \times 5$ in order to detect the subcooling which occurred very close to the cold plate surface. Consistent with the experiments of *Savino et al.*, a subcooling of approximately 2 °C was observed. We therefore recommend including the presence of subcooling before the spreading of ice over the cold plate in numerical models of freezing in internal flow.

In addition, a very interesting behaviour was observed within the thermal boundary layer prior to ice formation (for $t \approx -2.5$ min and $t \approx -10$ s). These temperature profiles clearly depart from the expected behaviour for the thermal boundary layer in (almost) fully developed channel flow, with a smaller temperature gradient than expected in the first few mm above the cold plate and a point of inflection at approximately $y = 5$mm. This point of inflection was not present for longer times prior to ice formation (i.e. $t \approx -4.5$ min) and for the measurements taken during the growth of the ice-layer (see figure 4.8). This point of inflection appears to build up in the time-span leading up to the sudden formation of ice, at which ice rapidly spreads over the entire cold plate.

The anomalous temperature behaviour is possibly related to an enhanced natural convection, occurring as a result of the subcooling of the water at the cold plate surface, as was previously suggested by *Mulligan et al.* [81]. *Mulligan et al.* performed an experimental study of the steady-state ice deposition in a laminar pipe flow with a cooled tube wall, and observed a decrease in the heat transfer rate at the wall as its temperature dropped below the freezing point. Similarly, we observed a faster decrease in the cold-plate temperature after the onset of ice formation compared to before (see figure 4.9). PIV measurements taken a short time prior to ice growth could confirm the presence of enhanced natural convection due to subcooling at the cold plate surface.

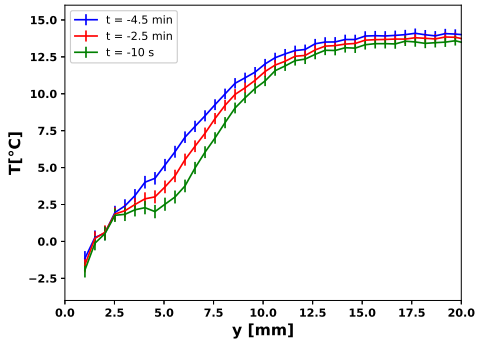

Figure 4.10: LIF temperature profiles for $T_{in,set} = 15\,^{\circ}\text{C}$ at the center of the channel (x = 75 cm), taken for various times prior to the onset of ice formation.

4.4. Conclusions

This work presents two color LIF temperature measurements for the transient freezing in a square channel for laminar flow conditions ($Re \approx 474$), for four different set-points of the inlet temperature ($T_{in,set} = 15\,^{\circ}\text{C}$, $T_{in,set} = 10\,^{\circ}\text{C}$, $T_{in,set} = 5\,^{\circ}\text{C}$ and $T_{in,set} = 0.5\,^{\circ}\text{C}$). LIF has only been used once before for solid-liquid phase change experiments by *Gong et al.* [133], for measuring the temperature distribution of melting n-octadecane in a cuboid cavity. Important novelties of the present LIF campaign were the use of a two color (instead of a one color) LIF technique, the use of a post-processing algorithm to remove striations and other artefacts, and a detailed analysis of the uncertainty in the measured temperature fields. In addition, this work presents the first measurements of the temperature distributions within the thermal boundary layer both during and prior to the transient freezing of a liquid in a laminar channel flow.

Measurements were performed at both the inlet and the center of the test section. The postprocessing involved the use of the local outlier factor algorithm followed by a smoothing operation using a moving average window. In addition, a correction factor was used to reduce the temperature bias as a result of variations in experimental conditions throughout the experimental campaign. Our approach resulted in an absolute temperature uncertainty of between $\sigma = 0.3\,^{\circ}\text{C}$ and $\sigma = 0.5\,^{\circ}\text{C}$ which is comparable to related LIF temperature measurement campaigns.

The primary aim of this work was to demonstrate the potential and limitations of LIF as a non-intrusive temperature measurement technique for solid liquid phase change experiments. We showed that good results could be obtained for a sufficiently large temperature range of approximately 15 °C in our case. For a small temperature ranges of approximately 5 °C however, the large relative uncertainty in the temperature deteriorated the quality of the results. As such, further improvements are needed to use LIF to generate high fidelity experimental data for numerical validation purposes. Some suggested improvements are to ensure a very clean entry surface for the laser sheet (without air bubbles, dirt particles or surface roughness), to use a camera with a large dynamic range and to improve the post-processing such that the noise as a result of the scattering of the laser light by the ice-layer can be removed.

LIF temperature measurements within the thermal boundary layer taken within a short time span prior to the onset of ice formation showed approximately 2 °C of subcooling, consistent with the findings of *Savino et al.* [94]. The onset of ice formation was accompanied by a sudden increase in the cold plate temperature (used to determine $t = 0$ in our experiments). The thermocouple recordings of the cold plate showed that the ice nucleus propagated from the inlet to the exit of the channel at a near constant velocity of approximately 5 $\mathrm{cm\,s^{-1}}$ for the given flow conditions ($Re = 474$, $T_{in,set} = 15\,^{\circ}\mathrm{C}$, $T_{c,set} = -10\,^{\circ}\mathrm{C}$). Based on these findings, we recommend that subcooling effects are taken into account in numerical models of ice growth in internal flow. In addition, an anomalous behaviour within the thermal boundary layer was observed, with a significantly smaller temperature gradient within the first few mm above the cold plate than would be expected for fully developed channel flow, and a point of inflection around $y = 5\,\mathrm{mm}$. Possibly, the anomalous temperature behaviour was caused by an enhanced natural convection as a result of the subcooling within the thermal boundary layer. This hypothesis could be confirmed by PIV measurements taken within a short time span before ice growth starts to occur.

Data Availability

The raw data from the LIF measurements can be found under the associated link: https://doi.org/10.5281/zenodo.10054186.

5

AN ENERGY-CONSERVATIVE DG-FEM APPROACH FOR SOLID-LIQUID PHASE CHANGE

We present a discontinuous Galerkin method for solid-liquid phase change problems based on the 'linearized enthalpy approach', which is derived from the conservative form of the energy transport equation and does not depend on the use of a so-called mushy zone. The Symmetric Interior Penalty method and the Lax-Friedrichs flux are used to discretize diffusive and convective terms respectively. Time is discretized with a second order implicit backward differentiation formula, and two outer iterations with second order extrapolation predictors are used for the coupling of the momentum and energy. The numerical method was validated with four different benchmark cases, i.e. the one-dimensional Stefan problem, octadecane melting in a square cavity, gallium melting in a rectangular cavity and transient freezing in a square duct. The performance of the method was quantified based on the L^2 norm error and the number of iterations needed to convergence the energy equation at each time-step. A mesh convergence rate of approximately O(h) was obtained, which is below the expected accuracy of the numerical method. Only for the gallium melting case, the use of a higher order method proved to be beneficial. The results from the present numerical campaign demonstrate the promise of the discontinuous Galerkin finite element method for modelling certain solid-liquid phase change problems where large gradients in the flow-field are present or the phase change is highly localized, however further enhancement of the method is needed to fully benefit from the use of a higher order numerical method when solving solid-liquid phase change problems.

This chapter is based on B.J. Kaaks, M. Rohde, J.L. Kloosterman, D.Lathouwers. An Energy-Conservative DG-FEM Approach for Solid-Liquid Phase Change. Published in *Numerical Heat Transfer, Fundamentals (B) 84* (2023), (Kaaks et al., 2023).

5.1. Introduction

Discontinuous Galerkin methods have gained interest over the last decade as an attractive numerical method for computational fluid dynamics, due to its combination of desired features of both the finite volume (FVM) and finite element (FEM) methods, such as local conservation, the possibility for upwinding, an arbitrarily high order of discretization and high geometric flexibility [172]–[174]. In addition, the high locality of the numerical scheme makes the discontinuous Galerkin method efficient for parallelization [174]. Recent advances in the applicability of DG-FEM methods to computational fluid dynamics include the simulation of turbulent flow with a high-order discontinuous Galerkin method and RANS or LES turbulence modelling [175]–[179], the development of discontinuous Galerkin methods for low-Mach number flow [180], [181], the simulation of multiphase flows [182], [183] and a DG-FEM multiphysics solver for simulating the Molten Salt Fast Reactor [174]. When coupled to a melting and solidification model, DG-FEM is expected to offer a more reliable capture of non-linear phase change phenomena as compared to the finite-volume method [129]. Indeed, *Schroeder et al.* [130] obtained qualitatively similar results on a mesh that was 14 times coarser as compared to the mesh used in a similar finite volume numerical benchmark study [124]. For these reasons, DG-FEM is an attractive numerical method for modelling solid-liquid phase change problems.

This chapter introduces the Symmetric Interior Penalty - Discontinuous Galerkin (SIP-DG) discretization of the 'linearized enthalpy approach' with the aim of developing an accurate and computationally efficient numerical method for modelling melting and solidification. Previous investigations employing the DG-FEM method to simulate melting and/or solidification problems used the apparent heat capacity method [129], [132] or the source-based enthalpy approach [130] for modelling the phase transition. This is the first time the 'linearized enthalpy' approach has been implemented in a DG-FEM framework. Unlike the apparent heat capacity method or the source-based approach, the 'linearized enthalpy approach' used in this work is based on the conservative form of the energy transport equation. An important novelty here is the imposition of thermal energy conservation through the convergence criterion. Furthermore, the present approach is thoroughly validated through comparison against three different benchmark cases (i.e. the one-dimensional Stefan problem, octadecane melting in a square enclosure and gallium melting in a rectangular enclosure). Finally, the performance of the discontinuous Galerkin with 'linearized enthalpy approach' method is quantified by calculating and comparing mesh convergence rates for two different element orders.

The rest of this chapter is organized as follows. Section 5.2 presents the governing equations and the boundary conditions that close them. Section 5.3 introduces the semi-discrete variational formulation with the discontinuous Galerkin method. Section 5.4 describes the temporal discretization scheme, with special attention devoted to the time-integration of the non-linear energy transport equation and the coupling of the energy and momentum transport equations. Section 5.4.4 details the numerical solution procedure. The results from the three benchmark cases and accompanying numerical performance metrics are presented in section 5.5. Finally, the conclusions and recommendations for future work based on the obtained results are given in section 5.6.

5.2. Governing equations

We consider the energy and the momentum transport equations in conservative form and use the volumetric enthalpy as the main variable. As such, the energy transport equation is written as

$$\frac{\partial H}{\partial t} + \nabla \cdot (\boldsymbol{u} H) = \nabla \cdot (k \nabla T), \tag{5.1}$$

where H is the volumetric enthalpy, $\boldsymbol{u}$ is the velocity, k is the thermal conductivity and T is the temperature.

The energy transport equation contains two unknowns, the volumetric enthalpy in the accumulation and the convection terms and the temperature in the diffusion term, coupled through the enthalpy-temperature relationship. For most heat transfer problems, the enthalpy-temperature relationship is smooth and the temperature gradient in the diffusion term may be expressed in terms of the enthalpy ($\nabla T = \frac{1}{\rho c_p} \nabla H$) with ρ being the density and c_p the specific heat capacity, hereby eliminating the temperature as the unknown and resulting in a linear energy transport equation that may be solved by standard solution methods. However, for solid-liquid phase change problems, the enthalpy-temperature relationship is non-smooth resulting in a non-linear energy transport equation. For this reason, dedicated numerical methods are needed for modelling solid-liquid phase change.

Figure 5.1 depicts the enthalpy-temperature relationship for isothermal solid-liquid phase change. For temperatures below the melting point ($T < T_m$), the enthalpy temperature derivative is equal to $\frac{dH}{dT} = \rho_s c_{p,s}$. For temperatures above the melting point ($T > T_m$), the enthalpy temperature derivative is equal to $\frac{dH}{dT} = \rho_l c_{p,l}$. Here, the subscripts 's' and 'l' refer to the solid and liquid phase respectively. At the melting point, the volumetric enthalpy has a jump discontinuity with a magnitude of $\rho_l L$ where L is the latent heat and $\rho_l L$ is the energy required for a unit volume of solid at the melting temperature to be transformed into liquid.

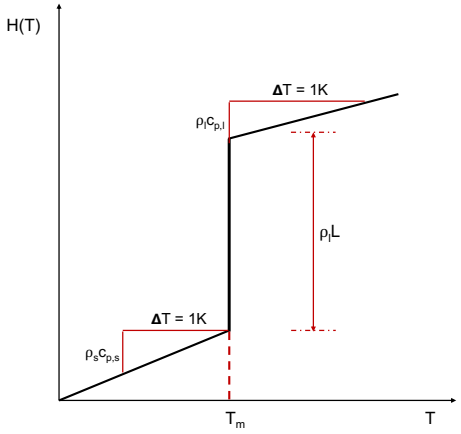

Figure 5.1: Enthalpy temperature relationship, for isothermal solid-liquid phase change. Here, ρ is the density, c_p is the specific heat capacity, L is the latent heat and the subscripts 'l' and 's' refer to the liquid and the solid phases respectively.

Assuming constant thermophysical properties in each phase, and neglecting the volume expansion effect as a consequence of the difference in densities between the solid and the liquid, the enthalpy-temperature relationship is written as a piece-wise continuous function:

$$T(H) = \begin{cases} \dfrac{H}{\rho_s c_{p,s}}, & H \leq \rho_s c_{p,s} T_m \\ T_m, & \rho_s c_{p,s} T_m < H < \rho_s c_{p,s} T_m + \rho_l L \\ T_m + \dfrac{H - (\rho_s c_{p,s} T_m + \rho_l L)}{\rho_l c_{p,l}}, & H \geq \rho_s c_{p,s} T_m + \rho_l L. \end{cases} \tag{5.2}$$

Following the recommendation of *König-Haagen et al.* [184], who experienced numerical instabilities when using the convection of the total enthalpy coupled to their implementation of the 'linearized enthalpy approach', we use a 'sensible enthalpy only' formulation for the convection term. Theory predicts that for isothermal solid-liquid phase change, under the condition that no solid-settling occurs and possible volume expansion effects due to different solid and liquid densities are neglected, the velocity at the solid-liquid interface is equal to zero and therefore the convection of the latent heat is also equal to zero [113]. In practice however, the finite element approximation of the volumetric enthalpy by piece-wise continuous functions will lead to an inevitable smearing of the latent heat peak within an element and the convection of the latent heat will no longer be zero after the finite element discretization. This 'false numerical convection of latent heat' may result in poor convergence and deteriorated quality of results. Following the rational of the source-based approach [113], the convection of the total enthalpy is split into a sensible and a latent heat contribution: $\nabla\cdot(\boldsymbol{u}H_{tot}) = \nabla\cdot(\boldsymbol{u}H_{sens}) + \nabla\cdot\left(\boldsymbol{u}\phi_l L\right)$. Here, ϕ_l is the liquid fraction, defined as

$$\phi_l(T) = \begin{cases} 0, & T \leq T_m \\ 1, & T > T_m. \end{cases} \tag{5.3}$$

Since the latent heat contribution is considered equal to zero, only the sensible contribution remains. The sensible contribution is expressed in terms of the temperature: $\nabla\cdot(\boldsymbol{u}H_{sens}) = \rho_l c_{p,l}\nabla\cdot(\boldsymbol{u}T)$. The 'sensible enthalpy only' formulation of the energy transport equation is thus written as

$$\frac{\partial H}{\partial t} + \rho_l c_{p,l}\nabla\cdot(\boldsymbol{u}T) = \nabla\cdot(k\nabla T)\,. \tag{5.4}$$

For the momentum equation, we consider incompressible flow and a Newtonian fluid with constant viscosity, and use the *Boussinesq* approximation to model the effect of buoyancy. The *Darcy* source term approach is used to enforce the no-slip condition at the solid-liquid interface position. This approach is most commonly used and has demonstrated better performance compared to other approaches such as the switch-off and variable viscosity techniques [112], [120]. The momentum equation thus reads

$$\frac{\partial\left(\rho_l\boldsymbol{u}\right)}{\partial t} + \nabla\cdot\left(\boldsymbol{u}\otimes\left(\rho_l\boldsymbol{u}\right)\right) = \nabla\cdot\left[\mu\left(\nabla\boldsymbol{u} + (\nabla\boldsymbol{u})^T\right)\right] - \nabla p + \rho_l\boldsymbol{g}\beta(T - T_m) - C\frac{\left(1-\phi_l\right)^2}{\phi_l^3 + b}\boldsymbol{u}. \tag{5.5}$$

The large parameter $C > 0$ in the *Darcy* source term is responsible for the attenuation of the velocity in the solid phase. $b > 0$ is a small parameter to prevent division by zero when the liquid fraction α becomes equal to zero.

Finally, the continuity equation for incompressible flow reads

$$\nabla\cdot\boldsymbol{u} = 0. \tag{5.6}$$

In order to close the system of coupled volumetric enthalpy transport and momentum transport equations, a set of boundary conditions and initial conditions are supplied. In the present work, the boundary $\partial\Omega$ is decomposed into two pairwise disjoint sets Γ^D and Γ^N such that $\partial\Omega = \Gamma^D \cup \Gamma^N$. On the Dirichlet boundary Γ^D the temperature is given, i.e. $T = T^D$, whereas on the Neumann boundary Γ^N the heat flux is specified, i.e. $k\nabla T\cdot\boldsymbol{n} = q$. Here, $\boldsymbol{n}$ is the outward unit normal vector of $\partial\Omega$. The no-slip condition $\boldsymbol{u} = 0$ is imposed on the entire boundary $\partial\Omega$. Initially, the temperature in the whole domain Ω is known, and the fluid is at rest, i.e. $\boldsymbol{u} = 0$ and $p = 0$ at $t = 0$.

5.3. Spatial discretization

This section describes the spatial discretization of the volumetric enthalpy and the mass flux transport equations with the discontinuous Galerkin finite element method. First, we introduce the basic definitions required for writing the variational formulation. Let Ω be the computational domain and $\Gamma = \Gamma^D \cup \Gamma^N$ its boundary. The domain is meshed into a set of non-overlapping elements $\mathscr{T}_h$, with $\mathscr{F}^i$, $\mathscr{F}^D$ and $\mathscr{F}^N$ being the set of interior, Dirichlet and Neumann boundary faces respectively. For each element $\mathscr{T} \in \mathscr{T}_h$ we assign a set of faces $\mathscr{F}^T$, and for each face $\mathscr{F}$ we assign a set of neighbouring elements $\mathscr{T}_h^F$. All faces $\mathscr{F} \in \mathscr{F}^i \cup \mathscr{F}^D \cup \mathscr{F}^N$ are assigned a unit normal vector $\boldsymbol{n}^F$, which has an arbitrary but fixed direction for all interior faces and coincides with the unit outward normal vector $\boldsymbol{n}$ for the boundary faces.

We use a hierarchical set of orthogonal modal basis functions (normalized Legendre polynomials to be specific) to approximate the unknown variables on $\mathscr{T}_h$. The solution space within each element is the span of all polynomials up to an order $\mathscr{P}$ and is written as

$$\mathcal{V}_{h,\phi} := \left\{ v \in L^2(\Omega) \quad | \quad v|_T \in \mathbb{P}_{\mathscr{P}_\phi}, \quad \forall \mathscr{T} \in \mathscr{T}_h \right\}, \tag{5.7}$$

where ϕ is a generic unknown variable and ϕ_h represents its FEM approximation. The basis functions are continuous within each element, but discontinuous at the interface between two neighbouring elements. As such, the trace of ϕ_h on the interior faces $\mathscr{F}^i$ is not unique, and we need to define the average and the jump operator, these are $\{\phi_h\} = \frac{1}{2}\left(\phi_h^+ + \phi_h^-\right)$ and $[[\phi_h]] = \phi_h^+ - \phi_h^-$ respectively. Here, for any point $\boldsymbol{r}$ on an interior face $\mathscr{F} \in \mathscr{F}^i$, the function traces ϕ_h^+ and ϕ_h^- are defined as

$$\phi_h^\pm (\boldsymbol{r} \in F) = \lim_{\zeta \downarrow 0} \phi_h \left(\boldsymbol{r} \pm \zeta \boldsymbol{n}^F \right). \tag{5.8}$$

5.3.1. Variational formulation

The semi-discrete variational formulation of the coupled system of transport equations is obtained by replacing the mass flux, pressure, volumetric enthalpy and temperature with their DG-FEM approximations $(\boldsymbol{m}_h, p_h, H_h, T_h)$, by multiplying equations 5.4, 5.5, 5.6 with the test functions $\boldsymbol{v}_h \in \mathcal{V}_{h,m}^d$, $q_h \in \mathcal{V}_{h,p}$ and $w_h \in \mathcal{V}_{h,T,H}$ respectively, and subsequently integrating over the whole domain. Note that the superscript d denotes the dimensionality of the vector space to which the DG-FEM approximation of the mass flux belongs. To close the system of equations, the enthalpy-temperature coupling needs to be included. With these considerations, the semi-discrete variational formulation reads

$$Find \quad m_h \in \mathcal{V}^d_{h,m} \quad and \quad p_h \in \mathcal{V}_{h,p,H,T} \quad and \quad H_h \in \mathcal{V}_{h,p,H,T} \quad and \quad T_h \in \mathcal{V}_{h,p,H,T}$$
$$such \quad that \quad \forall v_h \in \mathcal{V}^d_{h,m} \quad and \quad \forall q_h, \forall w_h \in \mathcal{V}_{h,p,H,T},$$

$$\sum_{\mathcal{T} \in \mathcal{T}_h} \int_{\mathcal{T}} \boldsymbol{v}_h \cdot \frac{\partial \boldsymbol{m}_h}{\partial t} + a^{conv}(\boldsymbol{u}_h, \boldsymbol{m}_h, \boldsymbol{v}_h) + a^{diff}(\boldsymbol{m}_h, \boldsymbol{v}_h) + a^{div}(\boldsymbol{v}_h, p_h) + a^{source}(\boldsymbol{m}_h, \boldsymbol{v}_h) = l^{conv}(\boldsymbol{u}_h, m^D_k \mathbf{v}_h) + l^{diff}(\boldsymbol{v}_h) + l^{source}(\boldsymbol{v}_h, T_h) \tag{5.9a}$$

$$a^{div}(\boldsymbol{m}_h, q_h) = l^{div}(q_h) \tag{5.9b}$$

$$\sum_{\mathcal{T} \in \mathcal{T}_h} \int_{\mathcal{T}} w_h \frac{\partial H_h}{\partial t} + a^{conv}(\boldsymbol{m}_h, T_h, w_h) + a^{diff}(T_h, w_h) = l^{conv}(\boldsymbol{u}_h, w_h) + l^{diff}(w_h) \tag{5.9c}$$

$$T_h = T(H_h). \tag{5.9d}$$

5

By solving the variational formulation of the coupled system of transport equations, the numerical mass-flux m_h, the pressure p_h, the volumetric enthalpy H_h and the temperature T_h are obtained. As opposed to the source-based enthalpy approach employed by *Schroeder et al.* [130], the present variational formulation follows directly from the conservative form of the transport equations. In addition, the present formulation does not depend on the use of an artificial smearing of the latent heat peak through the introduction of a so-called mushy-zone, and directly preserves the enthalpy-temperature coupling through inclusion in the system of equations. The non-linear coupling between the enthalpy and the temperature does not allow for a straightforward solution of the discretized energy transport equation. Therefore, we chose an iterative solution method for the energy equation, based on the work of *Swaminathan et al.* [115], *Nedjar et al.* [116] and *Faden et al.*[118]. The iterative solution of the energy equation is described in more detail in section 5.4.1.

In the present work, a mixed-order discretization for the mass-flux and the enthalpy, temperature and pressure was used (i.e. $\mathscr{P}_{p,H,T} = \mathscr{P}_m - 1$). The mixed-order formulation for the mass-flux and pressure (i.e. $\mathscr{P}_{p,T} = \mathscr{P}_m - 1$) is inf-sup stable and therefore no pressure stabilization terms are needed in the discretized continuity equation [174], [185] as opposed to using an equal-order formulation. In addition, it has been shown that the solution space of a transported scalar quantity (in the present work, the enthalpy and the temperature) must be a subset of the solution space of the pressure [174], [181]. The reason is that the continuity equation is weighted by the pressure basis functions (see equation 5.9) and therefore the convective discretization in the scalar transport equation can only be consistent up to order $\mathscr{P}_p$. For this reason, we selected $\mathscr{P}_{H,T} = \mathscr{P}_p$, resulting in the final mixed-order formulation $\mathscr{P}_{p,H,T} = \mathscr{P}_m - 1$.

We will now specify the convection, diffusion, divergence and source term operators in the discretized momentum and continuity equations. The treatment of the convection and diffusion operators in the energy equation proceeds along the same lines. The treatment of the time-operator will be described in detail in section 5.4.

5.3.2. Convective term

The discretization of the convective term is given by

$$a^{conv}(\boldsymbol{u_h}, \boldsymbol{m}_h, \boldsymbol{v}_h) = -\sum_{\mathscr{T}\in\mathscr{T}_h}\int_{\mathscr{T}} \boldsymbol{m}_h\cdot(\boldsymbol{u}_h\cdot\nabla)\,\boldsymbol{v}_h + \sum_{\mathscr{F}\in\mathscr{F}^i}\int_{\mathscr{F}} [[\boldsymbol{v}_h]]\,\mathscr{H}^F(\boldsymbol{u}_h,\boldsymbol{m}_h) + \sum_{\mathscr{F}\in\mathscr{F}^N}\int_{\mathscr{F}} \left(\boldsymbol{n}^F\cdot\boldsymbol{u}_h\right)\boldsymbol{m}_h\cdot\boldsymbol{v}_h + \sum_{\mathscr{F}\in\mathscr{F}^D}\int_{\mathscr{F}} \max\left(0,\boldsymbol{n}^F\cdot\boldsymbol{u}_h^D\right)\boldsymbol{m}_h\cdot\boldsymbol{v}_h \tag{5.10}$$

$$l^{conv}(\boldsymbol{u}_h,\boldsymbol{v}_h) = -\sum_{\mathscr{F}\in\mathscr{F}^D}\int_{\mathscr{F}} \min\left(0,\boldsymbol{n}^F\cdot\boldsymbol{u}_h^D\right)\boldsymbol{m}_h^D\cdot\boldsymbol{v}_h, \tag{5.11}$$

where $\mathscr{H}^F$ is the numerical flux function defined on an internal face $\mathscr{F}\in\mathscr{F}^i$. In this work, the Lax-Friedrichs flux is used [186]:

$$\mathscr{H}^F(\boldsymbol{u}_h,\boldsymbol{m}_h) = \frac{\alpha^F(\boldsymbol{u}_h)}{2}[[\boldsymbol{m}_h]] + \boldsymbol{n}^F\cdot\{\boldsymbol{u}_h\otimes\boldsymbol{m}_h\}, \tag{5.12}$$

where α^F is evaluated point-wise at face $\mathscr{F}$ through

$$\alpha^F(\boldsymbol{u}_h) = \Lambda\max\left(\left|\boldsymbol{n}^F\cdot\boldsymbol{u}_h^+\right|,\left|\boldsymbol{n}^F\cdot\boldsymbol{u}_h^-\right|\right) \tag{5.13}$$

with $\Lambda = 2$ for the momentum equation and $\Lambda = 1$ for the energy equation.

5.3.3. Diffusive term

Following *Hennink et al.* and *Tiberga et al.* [174], [181], the diffusive term is discretized using the Symmetric Interior Penalty (SIP) method. We limit ourselves to laminar incompressible flow and consider a Newtonian fluid with constant viscosity. For this reason, the standard SIP bilinear form is used instead of the generalization outlined in [181]:

$$a^{diff}(\boldsymbol{m}_h,\mathbf{v}_h) = \sum_{\mathscr{T}\in\mathscr{T}_h}\int_{\mathscr{T}}\frac{\mu}{\rho}\nabla\boldsymbol{m}_h\cdot\nabla\boldsymbol{v}_h + \sum_{\mathscr{F}\in\mathscr{F}^i\cup\mathscr{F}^D}\int_{\mathscr{F}}\eta^F\,[[\boldsymbol{m}_h]]\,[[\boldsymbol{v}_h]] - \sum_{\mathscr{F}\in\mathscr{F}^i\cup\mathscr{F}^D}\int_{\mathscr{F}}\boldsymbol{n}^F\cdot\left([[\boldsymbol{v}_h]]\left\{\frac{\mu}{\rho}\nabla\boldsymbol{m}_h\right\} + [[\boldsymbol{m}_h]]\left\{\frac{\mu}{\rho}\nabla\boldsymbol{v}_h\right\}\right) \tag{5.14}$$

$$l^{diff}(\boldsymbol{v}_h) = \sum_{\mathscr{F}\in\mathscr{F}^D}\int_F\left(\eta^F\boldsymbol{m}^D\cdot\boldsymbol{v}_h - \boldsymbol{m}_h^D\cdot\frac{\mu}{\rho}\nabla\boldsymbol{v}_h\cdot\boldsymbol{n}^F\right). \tag{5.15}$$

An optimum value of the penalty parameter is calculated through [187]

$$\eta^F = \max\left(\frac{\mu^+}{\rho},\frac{\mu^-}{\rho}\right)\max\left(card\left(\mathscr{F}^T\right)\frac{\mathfrak{E}_{\mathscr{P},\mathscr{T}}}{\mathfrak{L}_{\mathscr{T}}}\right), \tag{5.16}$$

where $card\left(\mathscr{F}^T\right)$ represents the number of faces of element $\mathscr{T}$ and $\mathfrak{E}_{\mathscr{P},\mathscr{T}}$ is a factor which takes into account the polynomial order of the finite element basis and test functions and the type of elements used:

$$\mathfrak{E}_{\mathscr{P},\mathscr{T}} = \begin{cases} (P+1)^2, & \text{for quadrilaterals and hexahedra} \\ \frac{(P+1)(P+d)}{d}, & \text{for simplices.} \end{cases} \tag{5.17}$$

Here, d denotes the dimensionality of the element (1 for a line element, 2 for a triangle and 3 for a tetrahedron).

$\mathfrak{L}_{\mathscr{T}}$ is a length scale defined as

$$\mathfrak{L}_{\mathscr{T}} = f \frac{||T||_{leb}}{||F||_{leb}} \tag{5.18}$$

where $||T||_{leb}$ indicates the Lebesgue measure of the element, and $||F||_{leb}$ indicates the Lebesgue measure of the face respectively. Finally, $f = 2$ for boundary faces, and $f = 1$ for internal faces. For the SIP discretization of the diffusive term in the energy equation, we substitute k for $\frac{\mu}{\rho}$ and substitute T_h for $\boldsymbol{m}_h$.

5.3.4. Continuity terms

The discretized continuity equation consists of the following discrete divergence operator and right-hand side term [188], [189]:

$$a^{div}(\boldsymbol{u}_h, q_h) = -\sum_{\mathscr{T}\in\mathscr{T}_h} \int_{\mathscr{T}} q \nabla\cdot \boldsymbol{u}_h + \sum_{\mathscr{F}\in\mathscr{F}^i\cup F^D} \int_{\mathscr{F}} \{q\} [[\boldsymbol{u}_h]]\cdot \boldsymbol{n}^F \tag{5.19}$$

$$l^{div}(q) = \sum_{\mathscr{F}\in\mathscr{F}^D} \int_{\mathscr{F}} q\left(\boldsymbol{u}^D\cdot\boldsymbol{n}^F\right). \tag{5.20}$$

5.3.5. Source terms

The momentum equation contains two source terms, i.e. the Darcy source term responsible for the attenuation of the velocity at the solid-liquid interface and the Boussinesq approximation responsible for modelling natural convection. The Darcy source term is imposed implicitly through the bilinear operator $a^{source}(\boldsymbol{m}_h, \boldsymbol{v_h})$:

$$a^{source}(\boldsymbol{m}_h, \boldsymbol{v_h}) = \sum_{\mathscr{T}\in\mathscr{T}_h} \int_{\mathscr{T}} C \frac{(1-\phi_l)}{\phi_l^3 + b} \frac{\boldsymbol{m}_h\cdot\boldsymbol{v_h}}{\rho_l}. \tag{5.21}$$

For the liquid fraction, a finite element approximation of the same order as the mass flux is used. To obtain the finite element approximation of the liquid fraction, the liquid fraction is calculated from the temperature at each quadrature point (see equation 5.3), and the values at the quadrature points are subsequently projected onto the finite element basis.

The Boussinesq approximated is imposed explicitly through the linear right hand side term $l^{source}(\boldsymbol{v_h}, T_h)$:

$$l^{source}(\boldsymbol{v_h}, T_h) = \sum_{\mathscr{T}\in\mathscr{T}_h} \int_{\mathscr{T}} \rho_l \beta (T_h - T_m)\, \boldsymbol{v_h}\cdot\boldsymbol{g}. \tag{5.22}$$

5.4. Temporal discretization and numerical solution procedure

In this work, implicit time-stepping is performed using the backward differentiation formulae (BDF) [178], [180], [189]. The time derivatives for a generic unknown quantity ϕ and for a constant time-step Δt is therefore written as

$$\frac{\partial \phi}{\partial t} \approx \frac{\gamma_0}{\Delta t}\phi^{n+1} + \sum_{j=1}^{\mathscr{M}} \frac{\gamma_j}{\Delta t}\phi^{n+1-j}, \tag{5.23}$$

where $\mathscr{M}$ is the order of the BDF scheme. In the present work, the second-order BDF scheme is used, with $\gamma_0 = {}^3/_2$, $\gamma_1 = -2$ and $\gamma_2 = {}^1/_2$. Special treatment is used for the temporal discretization and time-integration of the enthalpy transport equation, as is explained in section 5.4.1. The coupled momentum and continuity equations are solved in a segregated way using a pressure correction method (see section 5.4.2). The full solution algorithm, including the coupling between the energy, momentum and continuity equations, is described in section 5.4.3.

5

5.4.1. Iterative solution of the energy equation

Applying BDF2 time-integration (and assuming a constant time-step), the discretized energy accumulation term is written as

$$\sum_{\mathscr{T}\in\mathscr{T}_h}\int_{\mathscr{T}} w_h \frac{\partial H_h}{\partial t} = \sum_{\mathscr{T}\in\mathscr{T}_h}\int_{\mathscr{T}} w_h \frac{3H_h^{n+1} - 4H_h^n + H_h^{n-1}}{2\Delta t}. \tag{5.24}$$

Inserting the discretized energy accumulation term into the variational formulation of the energy equation results in the following form:

$$\sum_{\mathscr{T}\in\mathscr{T}_h}\int_{\mathscr{T}} w_h \frac{3H_h^{n+1} - 4H_h^n + H_h^{n-1}}{2\Delta t} + a^{conv}(\boldsymbol{m}_h, T_h^{n+1}, w_h) + a^{diff}(T_h^{n+1}, w_h) = l^{conv}(\boldsymbol{u}_h, w_h) + l^{diff}(w_h). \tag{5.25}$$

This equation is highly non-linear in the unknown H_h^{n+1}, due to the discontinuous nature of the enthalpy-temperature relationship (see equation 5.2) and therefore cannot be solved in a straightforward manner. Building on the work of *Swaminathan et al.* [115], *Nedjar et al.* [116] and *Faden et al.*[118], we expand the unknown H_h^{n+1} around the temperature:

$$H_h^{n+1,i+1} = H_h^{n+1,i} + \left.\frac{dH}{dT}\right|_{n+1,i}\left(T^{n+1,i+{}^1/_2} - T^{n+1,i}\right), \tag{5.26}$$

where the superscript $i+1$ refers to the new iteration, and $i+{}^1/_2$ refers to an intermediate value between two iterations. Inserting the expansion into the discretized energy equation yields the 'linearized' discretized energy equation:

$$\sum_{\mathcal{T}\in\mathcal{T}_h}\int_{\mathcal{T}} w_h \frac{3H_h^{n+1,i}-4H_h^{n}+H_h^{n-1}}{2\Delta t} + \sum_{\mathcal{T}\in\mathcal{T}_h}\int_{\mathcal{T}} \frac{dH}{dT}\Big|_{n+1,i} w_h \frac{3T_h^{n+1,i+1/2}-3T_h^{n+1,i}}{2\Delta t}$$
$$+ a^{conv}(\boldsymbol{m}_h, T_h^{n+1,i+1/2}, w_h) + a^{diff}(T_h^{n+1,i+1/2}, w_h) = l^{conv}(\boldsymbol{u}_h, w_h) + l^{diff}(w_h). \quad (5.27)$$

The linearized discretized energy equation contains only the intermediate temperature $T_h^{n+1,i+1/2}$ as the unknown variable. Solving the linearized energy equation for the intermediate temperature is equivalent to a single step in a Newton iteration. The remaining challenge is now to define a suitable approximation of the enthalpy-temperature derivative, which is undefined at the melting point.

In this work, the following formulation is used:

$$\frac{dH}{dT} \approx \begin{cases} \omega\rho_s c_{p,s}, & T \le T_m \\ \omega\rho_l c_{p,l}, & T > T_m, \end{cases} \quad (5.28)$$

where $\omega > 1$ is a parameter to speed up the convergence (1.5 was used in the present work). Upon convergence, the linearization term $\left(\frac{dH}{dT}\Big|_{n+1,i}\left(T^{n+1,i+1/2}-T^{n+1,i}\right)\right)$ approaches zero. Therefore, for a strict enough convergence criterion, the exact form of the enthalpy-temperature derivative has a negligible effect on the result of the numerical solution, and the use of the current approximation is justified [116]. Finally, we would like to mention that instead of updating the thermal conductivity at each iteration according to the latest position of the solid-liquid interface, the thermal conductivity at the newest time-step is estimated using extrapolation from the previous two time-steps (see section 5.4.3) and is therefore kept constant during the non-linear enthalpy-temperature iterations.

The iterative solution procedure is described by the following steps:

1. Initialize the enthalpy at the new time-step $H^{n+1,i}$ using the extrapolation from the previous time-steps (see equation 5.38).

2. Solve the discretized linearized energy transport equation (equation 5.27) to obtain the solution for the intermediate temperature $T_h^{n+1,i+1/2}$.

3. Update the volumetric enthalpy at the quadrature points applying the Taylor linearization:

$$H_h^{n+1,i+1}\Big|_{qp} = H_h^{n+1,i}\Big|_{qp} + \frac{dH}{dT}^{n+1,i}\left(T_h^{n+1,i+1/2}-T_h^{n+1,i}\right)\Big|_{qp}. \quad (5.29)$$

4. At the quadrature points, calculate the temperature from the updated enthalpy values through the enthalpy-temperature relationship (see equation 5.2):

$$T_h^{n+1,i+1} = T\left(H_h^{n+1,i+1}\right). \quad (5.30)$$

5. Calculate the solution coefficients of the enthalpy and temperature at the latest iteration, by projecting the values at the quadrature points onto the finite element basis for each element:

$$\mathbb{M}H_h^{n+1,i+1} = \sum_{qp=1}^{n} \left(w|_{qp} H^{n+1,i+1}|_{qp} v_h \right), \quad \mathbb{M}T_h^{n+1,i+1} \left(T_h^{n+1,i+1} v_h \right) = \sum_{qp=1}^{n} \left(w|_{qp} T|_{qp} v_h \right), \tag{5.31}$$

where $w|_{qp}$ are the quadrature weights and $\mathbb{M}$ is the mass matrix.

6. Check whether the convergence criterion (see equation 5.32) is satisfied. If not, return to step 2. If yes, move to the solution of the momentum equation (see figure 5.2).

Through our approach, the energy equation is solved in conservative form through a series of non-linear enthalpy-temperature iterations, within a prescribed tolerance. The advantages of our approach for solving melting and/or solidification problems as opposed to the apparent heat capacity method or the source-based enthalpy approach are an inherent conservation of thermal energy, no dependency on use of a so-called mushy zone for smearing the latent heat peak, and a comparatively fast convergence of the energy equation per time-step.

Convergence criterion

To ensure the final solution of the linearized energy transport equation corresponds to the solution of the original energy transport equation (see equation 5.4), a suitable convergence criterion is defined:

$$\max \left(\frac{res}{\int_\Omega H_h^{n+1,i+1} dV}, \left(\frac{\int_\Omega \left(\left[T_h^{n+1,i+1} - T_h^{n+1,i} \right]^2 \right)}{\int_\Omega \left(\left[T_h^{n+1,i+1} \right]^2 \right)} \right)^{1/2} \right) < tol. \tag{5.32}$$

This convergence criterion depends on two parts. The second part is the L^2 norm of the temperature difference between the current and the previous iteration. The justification for this part of the convergence criterion is that upon convergence, the linearization term should be equal to zero (see equation 5.26). In other words, the L^2 norm of the temperature difference between the current and the previous iteration should be minimized. The first part of the convergence criterion consists of an energy conservation check. This is done by inserting the solution vectors into the original discretized energy equation (i.e. prior to linearization, see equation 5.9) and selecting the zeroth order polynomial $v_h = 1$ as test function. Therefore, all terms containing the gradients and/or jumps of the test-function are equal to zero (except for the jumps at the boundaries) and the residual is defined as:

$$res = \sum_{\mathscr{T}\in\mathscr{T}_h}\int_{\mathscr{T}} v_h \cdot \frac{3H_h^{n+1,i+1} - 4H_h^n + H_h^{n-1}}{2\Delta t} +$$
$$\sum_{\mathscr{F}\in\mathscr{F}^N}\int_{\mathscr{F}} \left(\boldsymbol{n}^F \cdot \boldsymbol{u}_h\right)\rho_l c_{p,l} T_h^{n+1,i+1} \cdot v_h + \sum_{\mathscr{F}\in\mathscr{F}^D}\int_{\mathscr{F}} \max\left(0, \boldsymbol{n}^F \cdot \boldsymbol{u}_h^D\right)\rho_l c_{p,l} T_h^{n+1,i+1} \cdot v_h$$
$$+ \sum_{\mathscr{F}\in\mathscr{F}^D}\int_{\mathscr{F}} \eta^F [[T_h^{n+1,i+1}]][[\mathbf{v}_h]] - \sum_{\mathscr{F}\in\mathscr{F}^D}\int_{\mathscr{F}} \left(\{\{k\nabla T_h^{n+1,i+1}\}\} \cdot \boldsymbol{n}^F [[v_h]]\right)$$
$$+ \sum_{\mathscr{F}\in\mathscr{F}^D}\int_{\mathscr{F}} \min\left(0, \mathbf{n}^F \cdot \boldsymbol{u}_h^D\right)\rho_l c_{p,l} T_h^D \cdot v_h - \sum_{\mathscr{F}\in\mathscr{F}^D}\int_{\mathscr{F}} \left(\eta^F T_h^D \cdot v_h\right). \quad (5.33)$$

The residual is thus a measure of the energy loss or gain after each iteration, which is a measure of how far the solution to the linearized equation is from satisfying thermal energy conservation. The residual is scaled with the total thermal energy in the system in order to represent a relative error.

5

5.4.2. Pressure correction method

The coupled continuity and momentum equations are solved in a segregated way, applying the following pressure correction scheme [174], [181], [189]:

1. Obtain a predictor for the mass flux $\boldsymbol{m}$ by solving the linear system which corresponds to the semi-discrete form (see equation 5.9)

$$\left(\frac{\gamma_0}{\Delta t}\mathbb{M} + \mathbb{N}\right)\hat{\boldsymbol{m}}^{n+1} = -\mathbb{D}^T p^n + \boldsymbol{f}. \quad (5.34)$$

   Here, $\mathbb{M}$ is the mass matrix, $\mathbb{N}$ contains the implicit parts of the discrete convection and diffusion terms, $\mathbb{D}$ is the discrete divergence operator and $\boldsymbol{f}$ collects all the explicit terms (i.e. explicit terms from the discretization of the time derivative, boundary conditions and source terms). The convective term is linearized by replacing the convective field $\boldsymbol{u}^{n+1}$ with the predictor $\frac{\boldsymbol{m}^{n+1,*}}{\rho_l}$.

2. Solve a Poisson equation to obtain the pressure-difference at the new time-step

$$\left(\frac{\Delta t}{\gamma_0}\mathbb{D}\mathbb{M}^{-1}\mathbb{D}^T\right)\delta p^{n+1} = \mathbb{D}\hat{\boldsymbol{m}}^{n+1} - b_p, \quad (5.35)$$

   where b_p represents the fully-discrete right hand side of the continuity equation (see equation 5.20). Subsequently, the pressure may be updated,

$$p^{n+1} = p^n + \delta p^{n+1}. \quad (5.36)$$

3. Correct the mass flux, such that it satisfies the discrete continuity equation

$$\boldsymbol{m}^{n+1} = \hat{\boldsymbol{m}}^{n+1} - \frac{\Delta t}{\gamma_0}\mathbb{M}^{-1}\mathbb{D}^T\delta p^{n+1}. \quad (5.37)$$

5.4.3. Full solution algorithm

The full set of discretized transport equations is solved using a one-way coupling method between the energy and the momentum equation. The algorithm to find the solution vectors $\boldsymbol{m}^{n+1}$, $\boldsymbol{p}^{n+1}$, $\boldsymbol{H}^{n+1}$ and $\boldsymbol{T}^{n+1}$ at a new time-step $n+1$ consists of the following steps, as shown in figure 5.2.

1. Obtain predictors for the temperature T, enthalpy H, mass flux $\boldsymbol{m}$, pressure $\boldsymbol{p}$, liquid fraction α and thermal conductivity k, using a second-order extrapolation from previous time-steps:
$$\phi^{n+1,*} = 2\phi^{n} - \phi^{n-1}. \tag{5.38}$$
2. Solve the discretized energy equation through a series of Newton iterations until convergence is achieved, as described in section 5.4.1.
3. Solve the coupled momentum and continuity equations using the pressure correction method described in section 5.4.2.
4. Repeat steps 3 and 4 for a number of n outer iterations. In this work, 2 outer iterations were deemed sufficient based on a sensitivity analysis.

5.4.4. Implementation and numerical solution

The DG-FEM formulation of the linearized enthalpy approach for simulating melting and solidification heat transfer problems was validated with three different test cases: the 1D Stefan problem, octadecane melting in a square enclosure [71] and gallium melting in a rectangular enclosure [67]. The linearized enthalpy approach was implemented in the in-house DG-FEM based computational fluid dynamics solver *DGFlows*. A hierarchical set of orthogonal modal basis functions (normalized Legendre polynomials to be specific) was used and all integrals were evaluated with a Gaussian quadrature set with polynomial accuracy of $3P_m - 1$ [190], [191]. The meshes were generated with the open-source software tool Gmsh [192]. METIS [193] is used to partition the mesh, and the MPI-based software library PETSc [194] is used to assemble and solve all linear systems with iterative Krylov methods. The pressure-Poisson system is solved with the conjugate gradient method and a block jacobi preconditioner, where the submatrix within each MPI process is preconditioned with an incomplete Cholesky decomposition. The linear systems for the linearized enthalpy and momentum equations are solved with GMRES, with a block Jacobi preconditioner and successive over-relaxation for the submatrix within each MPI process. In order to reduce the required computational time, the pressure matrix and its preconditioner are only assembled and computed once (since the pressure matrix is the same at each time step [174]), and the Krylov solvers are initialized with the solution predictors (see section 5.4) in order to speed up the convergence.

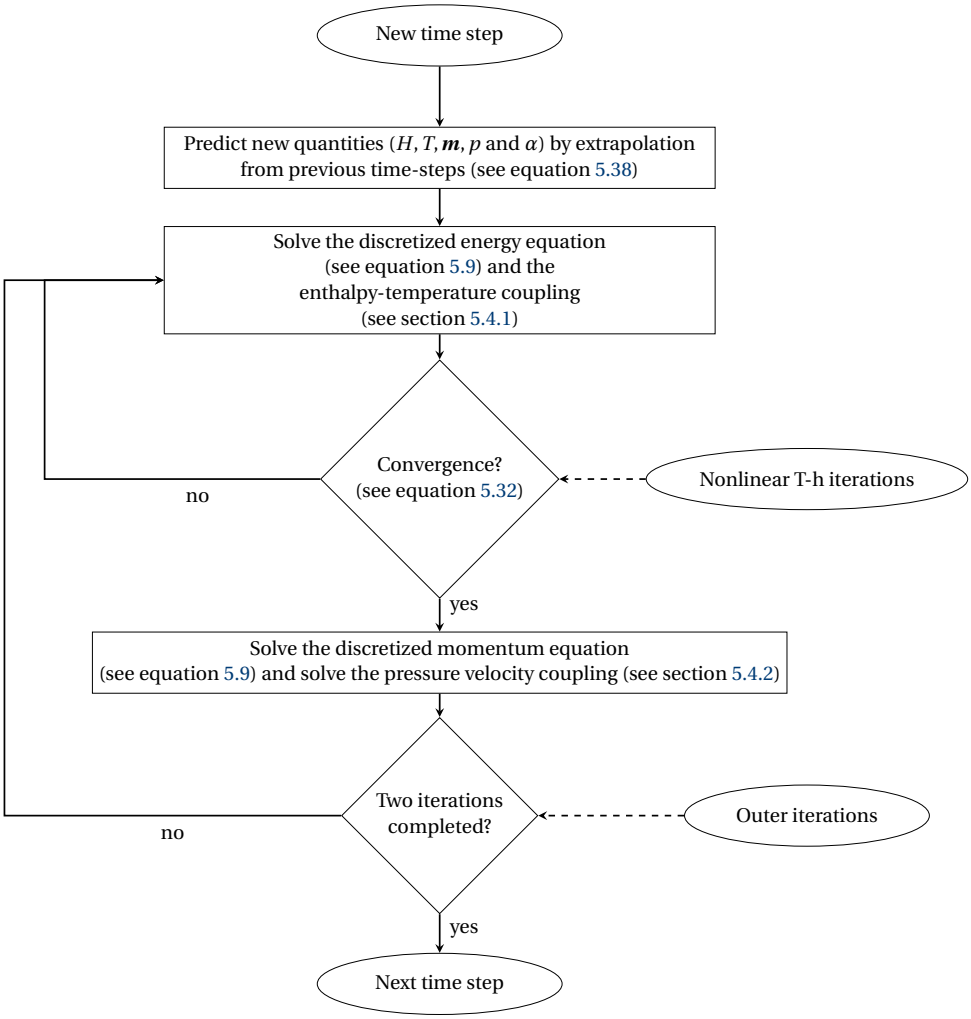

Figure 5.2: Flowchart of the solution algorithm, including the non-linear temperature-enthalpy iterations and the coupling of the energy and the momentum equations.

5.5. Results and discussion

5.5.1. Case 1: 1D Stefan problem

The one-dimensional Stefan problem was chosen for the first test case because the absence of convection and the presence of an analytical solution enabled a step-wise validation of the proposed numerical method, as well as a quantitative evaluation of the error in the numerical solution. The problem consists of a one-dimensional rod of length $l = 0.05\,\text{m}$, with a temperature of $T(x, t = 0) = 278\,\text{K}$. At $t > 0$, the temperature at the left side is suddenly lowered below the melting temperature: $T(0, t) = 268\,\text{K} < T_m$ and the right side is described by a homogeneous Neumann boundary condition, $\frac{\partial T}{\partial x}\Big|_{t,L} = 0$. The phase change material matches the thermophysical properties of water (see table 5.1). The same density is used for the solid and the liquid phases, to avoid any issues regarding volume expansion and mass conservation.

Table 5.1: Thermophysical properties used in the one-dimensional Stefan problem (corresponding to the thermophysical properties of water).

Property	Solid	Liquid
Density [kg m^{-3}]	1000	1000
Specific heat capacity [J kg^{-1}]	4200	2100
Thermal conductivity [W m^{-1} K^{-1}]	2.16	0.575
Latent heat [J kg^{-1}]	333000	
Melting Temperature [K]	273	

The entire problem is described by one pair of heat conduction equations, i.e. one heat conduction equation for the solid phase and one for the liquid phase [111]:

$$\begin{cases} \frac{\partial T_l}{\partial t} = \alpha_l \frac{\partial^2 T_l}{\partial x^2}, & 0 \le x < s(t) \\ \frac{\partial T_s}{\partial t} = \alpha_s \frac{\partial^2 T_s}{\partial x^2}, & x \ge s(t). \end{cases} \tag{5.39}$$

The displacement of the solid-liquid interface in time is described by the following two conditions, where 's' represents the solid-liquid interface:

$$\begin{cases} T_l = T_s = T_m \\ \rho_s L \frac{ds(t)}{dt} = k_s \frac{\partial T_s}{\partial x}\Big|_{x=s(t)} - k_l \frac{\partial T_l}{\partial x}\Big|_{x=s(t)}. \end{cases} \tag{5.40}$$

The analytical solution to the 1D Stefan problem is well known and given by *Voller et al.* [111]

$$s(t) = 2\lambda \left(\alpha_s t\right)^{1/2}, \tag{5.41}$$

where λ is the solution to the following transcendental equation:

$$\frac{\lambda L \pi^{1/2}}{c_s \left[T_m - T(0,t)\right]} = \frac{\exp\left(-\lambda^2\right)}{\text{erf}(\lambda)} - \frac{k_l}{k_s} \frac{\alpha_s^{1/2} \left[T(x,0) - T_m\right] \exp\left(-\alpha_s \lambda^2 / \alpha_l\right)}{\alpha_l^{1/2} \left[T_m - T_l(0,t\right] \text{erfc}\left(\lambda \left(k_s / k_l\right)^{1/2}\right)}. \tag{5.42}$$

The analytical solution for the temperature is given by

$$T = \begin{cases} \frac{T_m - T(0,t)}{\text{erf}(\lambda)} \text{erf}\left(\frac{x}{2(\alpha_s t)^{1/2}}\right) + T(0,t), & x < s(t) \\ T_m, \quad x = s(t) \\ T(x,0) - \frac{T(x,0) - T_m}{\text{erfc}\left(\lambda\left(\alpha_s/\alpha_l\right)^{1/2}\right)} \text{erfc}\left(\frac{x}{2(\alpha_l t)^{1/2}}\right), & x > s(t). \end{cases} \tag{5.43}$$

Figure 5.3 shows the numerical versus the analytical solution, for both the temperature field and the solid-liquid interface position. 128 equally sized linear elements and BDF2 time-integration with a time-step of $\Delta t = 0.1s$ were used. The tolerance was set to $tol = 10^{-6}$. The numerical solid-liquid interface position was found based on $H_{num} = \rho_s c_{p,s} T_m + 0.5\rho_l L$. For the temperature field, excellent agreement with the analytical results was observed and it is nearly impossible to distinguish the numerical and analytical solutions by eye. On the other hand, although the overall agreement with the analytical solution is good, the numerical solution for the solid-liquid interface position 'jumps' in time. This is due to the numerical solid-liquid interface being localized at one of the element edges, until the enthalpy has jumped past the latent heat peak. The 'time-jumping' of the numerical solid-liquid interface position is therefore inherent to the discontinuous Galerkin finite element discretization.

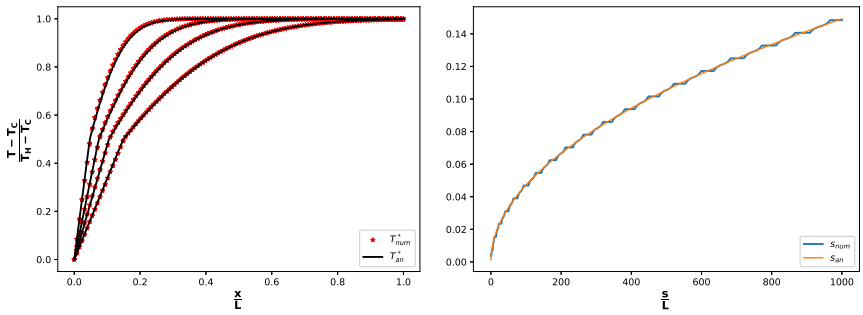

(a) Temperature field at 100, 250, 500 and 1000 s.

(b) Solid-liquid interface position.

Figure 5.3: Numerical versus analytical solution for a 1D Stefan problem, with 128 linear elements, and a time-step of $\Delta t = 0.1$ s with BDF2 time-integration. $tol = 10^{-6}$.

In figure 5.4, the L^2 norm of the error

$$\left(\frac{\int_\Omega \left(\left[T^*_{num} - T^*_{an} \right]^2 \right)}{\int_\Omega \left(\left[T^*_{an} \right]^2 \right)} \right)^{1/2} \tag{5.44}$$

versus the number of elements is depicted. Here, the normalized temperatures are used, i.e. $T^* = \frac{T - T_C}{T_H - T_c}$ with $T_C = 268\,\text{K}$ and $T_H = 278\,\text{K}$. The errors continue to decrease with an increasing amount of elements and approach very small values, indicating that the numerical solution converges to the analytical solution. For both the linear and the quadratic elements, approximately linear ($O(h)$) convergence rates were achieved. Note that the elements are only discontinuous at the element edges: within each element, a

continuous finite element approximation is used. Since the solid-liquid interface is most of the time located somewhere within an element, we believe the sub-optimal linear convergence rate is a consequence of the use of continuous polynomials for approximating the discontinuities in the enthalpy and temperature fields at the interface. Also recall the 'trapping' of the solid-liquid interface position at the element edges, until both nodal enthalpy values have moved past the latent heat peak. The current results are in line with theoretical predictions that the optimal convergence rate for a Stefan problem with a finite element method and implicit tracking of the solid-liquid interface is $O(h)$ [121]. Possibly, a faster mesh convergence could be obtained using adaptive mesh refinement in the vicinity of the solid-liquid interface [126] or an extended finite element method [101].

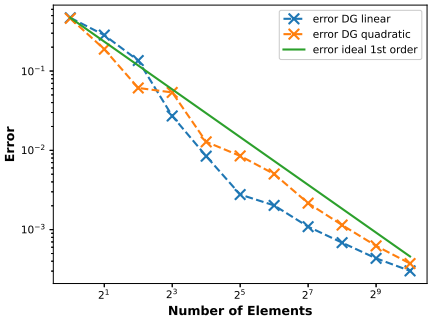

Figure 5.4: Mesh convergence rate based on the L^2 norm of the error in the temperature field. The total time was 250 s and the timestep was $\Delta t = 0.1$ s.

5.5.2. Case 2: melting of octadecane in a square cavity

The second benchmark case featured a square cavity of dimensions $L \times H = 40\,\text{mm} \times 40\,\text{mm}$, filled with n-octadecane as the phase-change material (PCM). At the initial temperature of $T_0 = 298.15\,\text{K}$, the entire PCM is solid. At $t = 0$, the left wall is suddenly heated to $T_H = 308.15\,\text{K}$. The right wall is kept constant at $T_C = 298.15\,\text{K}$ and the rest of the walls are adiabatic. The thermophysical properties of n-octadecane are given in table 5.2. This particular benchmark case was chosen for the following 2 reasons:

1. The availability of recent experimental measurements, with relatively well described boundary conditions, including PIV measurements of the flow field [71].

2. The availability of a recent numerical investigation with a linearized enthalpy approach and the finite volume method (FVM) [118], to compare the performance of the present method against.

Table 5.2: Thermophysical properties of n-octadecane [71].

Property	Solid	Liquid
Density [kg m^{-3}]	867	775.6
Specific heat capacity [J kg^{-1}]	1900	2240
Thermal conductivity [W m^{-1} K^{-1}]	0.32	0.15
Latent heat [J kg^{-1}]	243680	
Melting Temperature [K]	301.15	
Thermal expansion coefficient [1/K]	$8.36 \cdot 10^{-4}$	
Dynamic viscosity [Pas]	$3.75 \cdot 10^{-3}$	

Figure 5.5 depicts the absolute velocity contours at respectively one and two hours after the onset of melting as measured experimentally using PIV (top two images) and numerically (bottom two images). Qualitatively, a good agreement was observed between the experimental data and the simulation results. The onset of the natural circulation loop, as seen in the PIV results, is well captured by the numerical method. As a consequence of the natural convection flow, the heat transfer to the solid-liquid interface is enhanced and the rate of melting is accelerated.

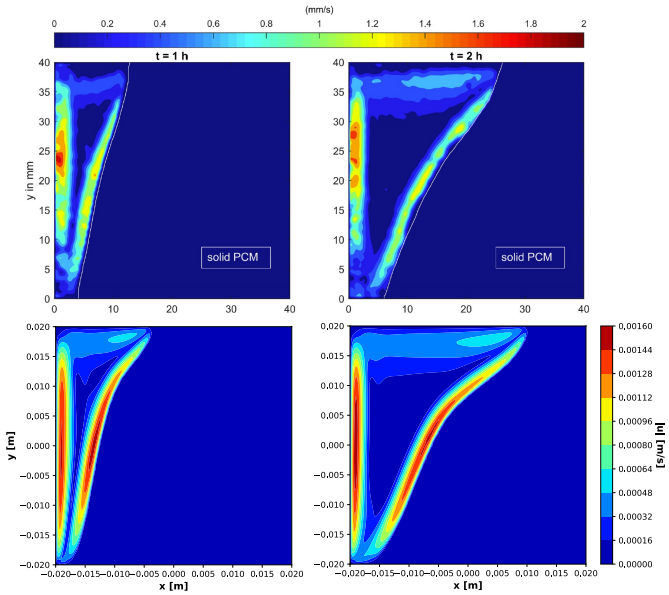

Figure 5.5: Absolute velocity contours for melting of n-octadecane in a square enclosure, at respectively 3600 s and 7200 s. Qualitative comparison between experimental campaign (top) and numerical campaign (bottom). Numerical campaign performed with 'linearized enthalpy approach' coupled to a SIP-DG numerical method. 200×200 $P = \{2,1,1,1\}$ elements were used. Time-integration was performed with the BDF2 finite difference scheme and $\Delta t = 0.25$ s.

Figure 5.6 shows the results from a mesh convergence analysis, for both the solid-liquid interface position and the temperature plotted on the line $y = 0$ mm through the centre of the domain. All meshes consist of equally sized quadrilateral elements. Two different hierarchical sets of orthogonal basis functions were used, respectively $P = \{2,1,1,1\}$ and $P = \{3,2,2,2\}$ for the mass flux, pressure, enthalpy and temperature. Both sets of polynomial orders displayed visually similar results for $P = \{2,1,1,1\}$ and $P = \{3,2,2,2\}$ with the finer meshes of 200×200 and 400×400 elements.

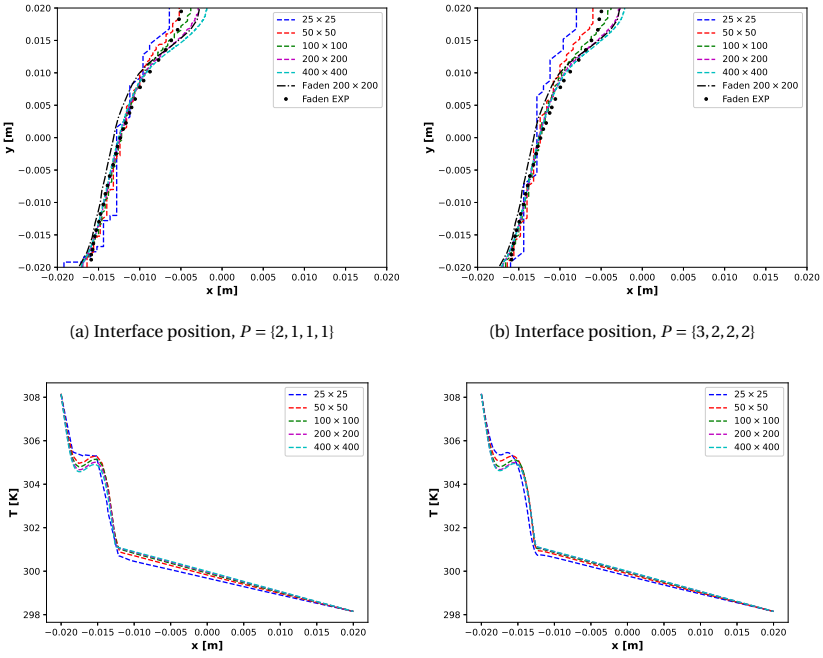

(a) Interface position, $P = \{2,1,1,1\}$

(b) Interface position, $P = \{3,2,2,2\}$

(c) Temperature, $P = \{2,1,1,1\}$

(d) Temperature,$P = \{3,2,2,2\}$

Figure 5.6: Mesh convergence study based on interface position and temperature at the line $y = 0$ mm. Two sets of finite element polynomial orders are selected, these are $P = \{2,1,1,1\}$ and $P = \{3,2,2,2\}$. BDF2 time-stepping with $\Delta t = 0.5$ s was used for a total simulation time of 3600 s.

To provide insight on the mesh convergence rates, table 5.3 depicts the average number of inner iterations, the total liquid fraction, and the L^2-norms of errors in the temperature, enthalpy and the absolute velocity (see equation 5.44). Quantitative mesh convergence studies for solid-liquid phase change problems are rare and this is the first time such a study has been performed for the solution of solid-liquid phase change problems with a discontinuous Galerkin method.

The number of inner iterations do not grow excessively with an increasing mesh-size, although for the finest meshes of 400×400 elements a relatively large number of iterations was needed to obtain convergence. This was probably a consequence of keeping the time-step constant at $\Delta t = 0.5$, for the higher mesh resolutions a smaller time-step could be more suitable. The differences in the total liquid fraction are small, even be-

tween the finest and the coarsest mesh, possibly due to the good energy conservation properties of the current numerical method. For the L^2 norms, the normalized quantities were used, i.e. $T^* = \frac{T - T_C}{T_H - T_c}$ with $T_c = 298.15\,\text{K}$ and $T_H = 308.15\,\text{K}$ and $|u|^* = \frac{|u|}{max(|u|)}$. Since no analytical solution is available for this problem, the numerical solution for the finest mesh (i.e. 400×400 and $P = \{3,2,2,2\}$) was used as the reference solution. For both the $P = \{2,1,1,1\}$ and the $P = \{3,2,2,2\}$ meshes, the L^2 error norms for the first 3 meshes (less than 100×100 elements) appeared to decrease slowly (less than O(h)), whilst the error decreased with a rate close to O(h) from the 100×100 elements mesh onwards.

Overall, these numerical results indicate that also for a two-dimensional melting problem with fluid flow, the present DG-FEM linearized enthalpy approach suffers from sub-optimal mesh convergence. This conclusion is in line with theoretical predictions [121] and our observations from the 1D Stefan problem. However, since the mesh of 400×400 with $P = \{3,2,2,2\}$ was used as the reference solution, the calculated errors might not correspond to the 'true' errors of the numerical solution.

Table 5.3: Relevant quantities from the mesh convergence analysis for the octadecane melting in a square cavity case. BDF2 time-integration with a time-step of $\Delta t = 0.5\,\text{s}$ was used for a total simulation time of 3600 s.

Polynomial order	Mesh size	Average number of inner iterations	Total liquid fraction	L^2_T	L^2_H	L^2_U
$P = \{2,1,1,1\}$	25×25	4.95, 2.29	0.212	2.24(-1)	3.89(-1)	4.99(-1)
	50×50	6.64, 1.89	0.210	1.62(-1)	2.58(-1)	3.25(-1)
	100×100	9.27, 1.93	0.213	1.04(-1)	1.95(-1)	2.09(-1)
	200×200	13.03, 1.85	0.212	4.39(-2)	1.12(-1)	9.97(-2)
	400×400	24.95, 2.27	0.218	2.50(-2)	8.35(-2)	6.86(-2)
$P = \{3,2,2,2\}$	25×25	5.67, 1.83	0.190	2.74(-1)	3.89(-1)	6.10(-1)
	50×50	7.00, 1.86	0.202	1.84(-1)	2.92(-1)	4.12(-1)
	100×100	9.51, 1.78	0.210	1.01(-1)	1.93(-1)	2.40(-1)
	200×200	13.59, 1.89	0.213	3.87(-2)	1.04(-1)	9.66(-2)
	400×400	33.92, 4.03	0.216	N/A	N/A	N/A

Figure 5.7 depicts the interface position after respectively 1h, 2h, 3h and 4h of simulation time. Based on the results from the mesh convergence, the 200×200 $P = \{2,1,1,1\}$ mesh was selected for the final simulations. This mesh was considered a good compromise between accuracy and computational affordability. The time step was set to $\Delta t = 0.25s$ based on a time-step sensitivity analysis[1]. A good agreement with both the previous numerical campaign [118] and the experimental results [71] was observed. Compared to the experimental campaign, the numerical results predict a faster melting rate (although the shape of the melting fronts are very similar and a better agreement with the experimental results was obtained as compared to the reference simulations of *Faden et al.* [118]). Possible reasons for the over-prediction of the melting rate are:

[1]The time-sensitivity analysis is included in the numerical data repository at https://doi.org/10.5281/zenodo.6802375.

1. The simulations were performed in two dimensions, whereas the experimental domain is a cubical cavity. Ignoring the effect of the walls in the third dimension leads to an over-estimation of the melting rate, of which the severity depends on the dimensions of the problem and the *Prandtl* number of the phase change material [195]. For high *Prandtl* materials such as octadecane, the over-estimation of the melting rate in a 2D simulation is less serious then for low *Prandtl* materials.

2. Even though the experimental setup was thermally insulated , some heat losses to the environment were still present during the experimental campaign [71]. However, fully adiabatic walls were assumed in the numerical simulations.

3. The present numerical campaign uses the Boussinesq approximation and does not consider the expansion of the octadecane during melting. It has been shown that the use of a constant density model will lead to an over-prediction of the melting rate, as opposed to the use of a variable density model [196].

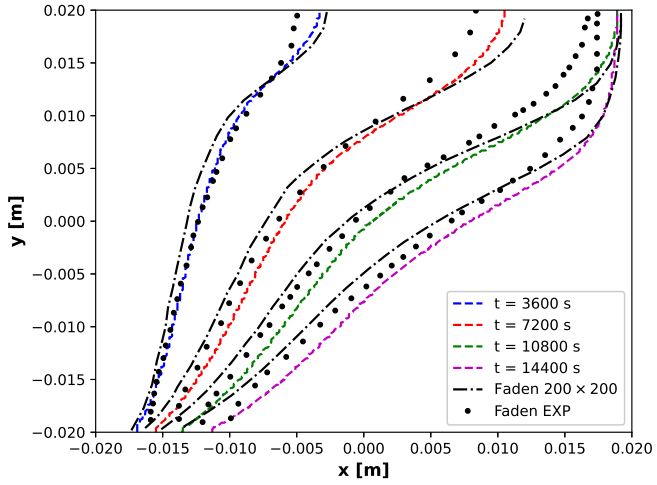

Figure 5.7: Octadecane melting in a square enclosure. Interface position at respectively 3600 s, 7200 s, 10800 s, 14400 s. The mesh consisted of 200×200 $P = \{2,1,1,1\}$ elements. BDF2 time-stepping with a time step of $\Delta t = 0.25$ s was used. Previous numerical campaign of *Faden et al.* [71] and experimental campaign are plotted for comparison.

5.5.3. Case 3: melting of gallium in a rectangular cavity

The third benchmark case featured gallium melting in a rectangular cavity of dimensions $L \times H = 88.9\,\text{mm} \times 63.5\,\text{mm}$. At the initial temperature of $T_0 = 301.3\,\text{K}$, the entire PCM is solid. At $t = 0$, the left wall is suddenly heated to $T_H = 311\,\text{K}$. The right wall is kept constant at $T_C = 301.3\,\text{K}$ and the rest of the walls are adiabatic. The thermophysical properties of gallium are given in table 5.4. Similar to the melting of n-octadecane in a square enclosure, this benchmark features the melting of a PCM in a natural convection flowfield. However, there were several reasons to include this additional benchmark case:

1. The different thermophysical properties of Gallium and the different aspect ratio of this enclosure lead to a significantly different behavior of the flowfield and the evolution of the melting front. Therefore, the gallium melting in a rectangular enclosure case contributes to further validation of the 'linearized enthalpy approach' with SIP-DG method.

2. For the 2D numerical case, multicellular flow is observed, possibly due to the onset of the Rayleigh-Benard instability (this was not the case in 3D simulations of the gallium melting problem, leading to an overall different outcome [197]). The number of vortices present in the multicellular flow depends on the resolution of the mesh and the accuracy of the numerical schemes [124].

3. The Gallium melting in a rectangular enclosure by *Gau et al.* [67], later repeated by *CampBell and Coster* and *Ben David et al.* using non-intrusive experimental methods in the form of x-ray radioscopy and ultrasound doppler velocimetry respectively [68], [69], is one of the classic melting and solidification experiments and is often used for numerical validation purposes. Examples are the validation of the source-based enthalpy approach [113], the grid refinement study performed by *Hannoun et al.* to find the correct 2D numerical solution [124] and the validation of the FEM and DG-FEM source-based enthalpy methods developed by *Belhamadia et al.* [198] and *Schroeder et al.* [130].

Table 5.4: Thermophysical properties of gallium [124].

Property	Solid	Liquid
Density [kg m^{-3}]	6093	6093
Specific heat capacity [J kg^{-1}]	381.5	381.5
Thermal conductivity [W m^{-1} K^{-1}]	32	32
Latent heat [J kg^{-1}]	80160	
Melting Temperature [K]	302.78	
Thermal expansion coefficient [1/K]	$1.2 \cdot 10^{-4}$	
Dynamic viscosity [Pas]	$1.81 \cdot 10^{-3}$	

Figure 5.8 shows the results from a mesh convergence analysis for the absolute velocity plotted on the line $y = 31.75$mm through the centre of the domain. All meshes consist of equally sized quadrilateral elements. Compared to the octadecane melting case, the difference in results between the $P = \{3,2,2,2\}$ and the $P = \{2,1,1,1\}$ polynomial sets is more significant. Possibly, the multicellular flow patterns, which are a particular feature of the 2D Gallium melting case, are better captured with a higher order finite element basis function for the mass flux and the pressure. Indeed, also *Hannoun et al.* observed differences in results when using a second order as opposed to a first order finite volume upwind scheme for the convection term [124]. One can see that for both the $P = \{3,2,2,2\}$ and the $P = \{2,1,1,1\}$ basis function sets, the results for the 280×200 and the 560×400 meshes appear qualitatively similar, although no full mesh convergence was achieved.

Relevant quantities from the mesh convergence analysis are given in table 5.3 (i.e. the average number of inner iterations, the total liquid fraction, and the L^2-norms of errors in the temperature, enthalpy and the absolute velocity). Similar to the octadecane melting case, the differences in total liquid fraction between the different meshes are small. Up to a mesh size of 280×200 elements, the number of inner iterations do not grow excessively with an increasing mesh size. However, for the mesh size of 560×400 elements, a large number of inner iterations was needed in order to converge the energy equation, especially for the $P = \{3,2,2,2\}$ basis function set. It is expected that the use of a smaller time-step will speed up the convergence of the non-linear enthalpy-temperature iterations for the finer meshes. Regarding the L^2 error norms, similar errors are observed for the first three mesh sizes with respect to the finest mesh of 560×400 elements with both the $P = \{2,1,1,1\}$ and the $P = \{3,2,2,2\}$ basis function sets. We believe this is due to the inability of the coarse meshes to properly resolve the multicellular flow, leading to an incorrect prediction of the number of vortices. With respect to the 140×100 mesh, the 280×200 mesh presents a significant decrease in error. From the current numerical results, it is difficult to deduct the mesh convergence rate. However, based on the observations from the 1D Stefan problem and the octadecane melting in a rectangular enclosure case, we expect the mesh convergence to be around O(h).

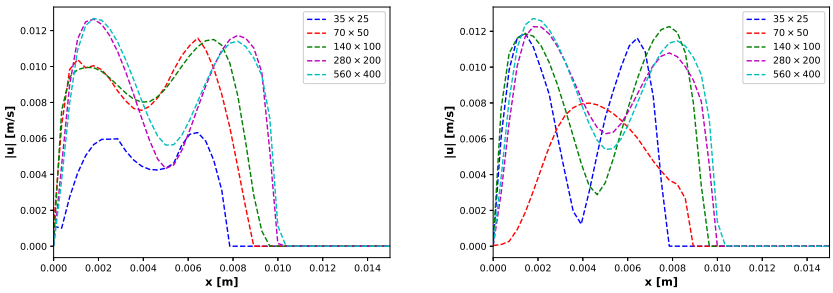

(a) Absolute velocity, $P = \{2,1,1,1\}$

(b) Absolute velocity, $P = \{3,2,2,2\}$

Figure 5.8: Mesh convergence study based on the absolute velocity at the line $y = 31.75$ mm. Two sets of finite element polynomial orders are selected, these are $P = \{2,1,1,1\}$ and $P = \{3,2,2,2\}$ for mass flux, pressure and enthalpy, temperature respectively. BDF2 time-stepping with $\Delta t = 0.025$ s was used for a total simulation time of 85 s.

Table 5.5: Relevant quantities from mesh convergence analysis for the gallium melting in a rectangular container case. BDF2 time-integration with a time-step of $\Delta t = 0.025$ was used and the total simulation time was 85s.

Polynomial order	Mesh size	Average number of inner iterations	Total liquid fraction	L^2_T	L^2_H	L^2_U
$P = \{2,1,1,1\}$	35×25	5.86, 1.00	0.108	1.62(-1)	1.86(-1)	6.24(-1)
	70×50	7.90, 1.00	0.110	1.50(-1)	1.41(-1)	7.49(-1)
	140×100	10.86, 1.00	0.110	1.42(-1)	1.47(-1)	7.38(-1)
	280×200	23.34, 1.21	0.108	1.59(-2)	4.84(-2)	1.00(-1)
	560×400	70.91, 15.78	0.110	2.93(-3)	1.63(-2)	1.56(-2)
$P = \{3,2,2,2\}$	35×25	6.86, 1.01	0.108	1.37(-1)	1.65(-1)	6.89(-1)
	70×50	8.80, 1.00	0.109	1.15(-1)	1.31(-1)	6.29(-1)
	140×100	13.82, 1.11	0.109	1.20(-1)	1.22(-1)	6.47(-1)
	280×200	18.53, 1.12	0.109	1.55(-2)	5.34(-2)	1.01(-1)
	560×400	231.32, 152.01	0.109	N/A	N/A	N/A

Figure 5.9 depicts the contour plots of the absolute velocity at various time-steps. The right image shows the results obtained with the present numerical campaign, the left image depicts the reference solution of *Hannoun et al.* [124]. Amongst the different meshes, we selected the 280×200 mesh for our final simulations with a time-step of $\Delta t = 0.025s$. Contrary to the octadecane melting case, the $P = \{3,2,2,2\}$ basis function set was used because the results with the 280×200 mesh (in particular the number of vortices) remained stable for different time step sizes as opposed to the $P = \{2,1,1,1\}$ basis function set[2]. As mentioned earlier, we belief the resolution of the multicellular flow patterns benefits from the use of a higher order finite element basis function set. The results obtained with the current numerical campaign and the results from the reference solution appear to be almost identical, despite differences in the modelling approach ('linearized enthalpy approach' versus 'source-based enthalpy approach') and the numerical method (DG versus FVM). The mesh resolution is equal to 0.3175 mm, similar to the mesh resolution of 0.4 mm used for the grid-converged simulations of *Schroeder et al.*, who also used a DG-FEM method for modelling solid-liquid phase change with quadratic elements for the velocity and the temperature [130]. Like-wise, qualitatively similar results were obtained with a significantly coarser grid as compared to the reference simulations of *Hannoun et al.* [124], where a 840×600 uniform grid was used. Overall, the results from the Gallium melting case indicate the potential benefit of using discontinuous Galerkin methods for modelling melting/solidification problems, especially those where large gradients in the flowfield are present, as an alternative to the conventionally used finite volume method.

[2]This was observed from the time step refinement, which is included in the numerical data repository at https://doi.org/10.5281/zenodo.6802375

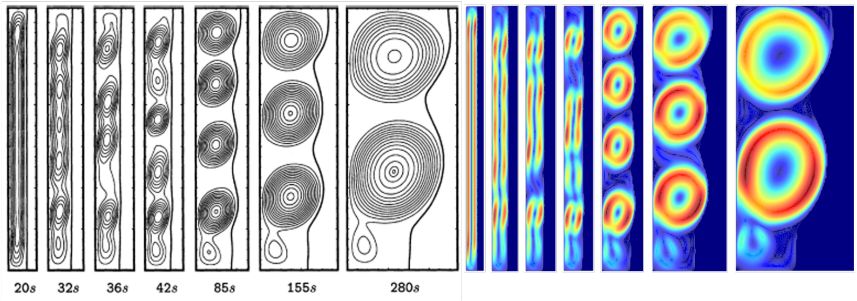

Figure 5.9: Absolute velocity contours for melting of gallium in a square enclosure, at respectively 20 s, 32 s, 36 s, 42 s, 85 s, 155 s and 280 s. Left image shows the results as obtained by the numerical benchmark of *Hannoun et al.* [124], the right image shows the results from the current numerical campaign. 280×200 $P = \{3,2,2,2\}$ elements were used. Time-integration was performed using the BDF2 finite difference scheme and $\Delta t = 0.025$ s..

The results from the mesh refinement studies performed for the 1D Stefan, octadecane melting and gallium melting cases indicate that the proposed DG-FEM method is able to solve solid-liquid phase change problems with an accuracy of around O(h). Therefore, in the vicinity of the solid-liquid interface, a lower order method with refined mesh might be preferable. As the results from the gallium case show, regions with strong gradients in the velocity field could still benefit from a higher order discontinuous Galerkin method. Most likely, the same would apply to areas of interest far away from the solid-liquid interface (for instance in problems where the phase change is highly localized), although this was not investigated in the present paper. Combining the current DG-FEM 'linearized enthalpy approach' method with adaptive grid refinement (see for instance *Belhamadia et al.* [126]) could be the next step towards the development of more accurate and computationally efficient numerical methods for solving solid-liquid phase change problems. Another interesting approach could be the use of an extended finite element basis (such as proposed by *Chessa et al.* [101]) which provides a better treatment of discontinuous solutions within the element as opposed to the classical polynomial finite element basis functions.

5.5.4. Case 4: transient freezing in a square channel

The fourth and final benchmark case features transient freezing in a square duct, using the experimental results from chapter 3 for additional validation of the proposed DG-FEM solid-liquid phase change model. So far, solid-liquid phase change models have been predominantly validated using experimental data for melting or freezing in an enclosure, characterized by a natural convection flow regime. This is mainly because of the lack of suitable experimental data for transient freezing in internal flow, where forced convection plays a role. This final benchmark case therefore serves to illustrate the validity of the proposed DG-FEM method for a wide variety of melting and solidification problems, as well as to demonstrate the suitability of the experimental campaign from chapter 3 for numerical validation purposes.

Figure 5.10 shows a sketch of the two-dimensional computational domain, including the dimensions and the prescribed boundary condition. The transient temperature response measured by the thermocouples located in the centre of the cold plate, $T = T_c(t)$ (see section 3.3.3) was imposed as boundary condition at the bottom and the rest of the cold plate was simulated through a conjugate heat transfer simulation with the water flowing through the test section above. To model the conjugate heat transfer, the energy equations for the solid metal domain and the 'liquid' PCM domain are solved simultaneously with no explicit interface condition being imposed. The momentum equation is solved only within the 'liquid' PCM domain. Unlike the previous two cases, here a total of three outer iterations was used, to take into account the additional coupling between the energies of the metal cold plate and the fluid of the water flowing above.

To avoid a conflict between the imposed uniform inflow condition and zero gradient outflow conditions and the presence of an ice layer, the test section was extended by 10cm in both directions. Apart from the bottom of the cold plate and the inflow boundary, the other boundaries were assumed to be adiabatic and the front and back were modelled with a symmetry boundary condition, due to the 2D nature of the simulation. We simulated the case corresponding to $Re = 474$, $T_{in} \approx 4.7\,^{\circ}\mathrm{C}$ and $T_{c,set} = -10\,^{\circ}\mathrm{C}$. An inflow velocity of $\vec{u}_{in,x} = 1.44\,\mathrm{cm\,s^{-1}}$, $\vec{u}_{in,y} = 0\,\mathrm{cm\,s^{-1}}$ was set and the following fits were used for the transient behaviour of the cold plate and the inlet temperature (see section 3.3.3 for more detail regarding the choice of the boundary conditions):

$$T_c = 273 - 8.202 + 6.826\exp\left(-6.404\frac{t}{3600}\right) - 0.775\tanh\left(0.431\frac{t}{3600}\right) \tag{5.45}$$

$$T_{in} = 273 + 4.671 - 0.046\exp\left(-1.346\frac{t}{3600}\right), \tag{5.46}$$

where $t = 0$ is the onset of ice formation in the experiment.

The base mesh consists of 84,500 elements with a resolution of $\Delta x \cdot \Delta y = 0.25\,\mathrm{cm} \cdot 0.05\,\mathrm{cm}$ in the test section and a resolution of $\Delta x \cdot \Delta y = 0.25\,\mathrm{cm} \cdot 0.035\,\mathrm{cm}$ in the cold plate. In addition, two areas of interest were selected for performing local mesh refinement. Near the inlet the mesh was refined three times (so the resolution became 8 times finer), and in the center of the channel the mesh was refined two times. The refined mesh consists of approximately 380,000 elements. Finally, a grading was applied in the streamwise direction: towards the inlet, the length of each element decreased according to $\Delta x_{elem} = \frac{1}{1.033}\Delta x_{elem-1}$ and away from the inlet the length of each element increased according to $\Delta x_{elem} = \frac{1}{1.002}\Delta x_{elem-1}$. A time-step of $\Delta t = 0.1\,\mathrm{s}$ was used throughout the simulation.

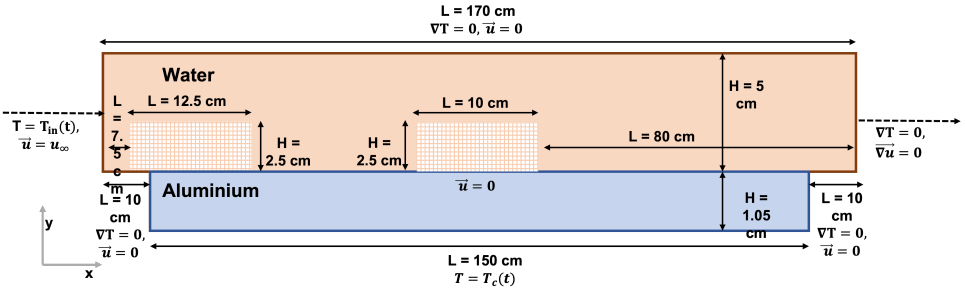

Figure 5.10: Sketch of computational domain for simulating ice growth in a forced convection channel flow. The red and blue colors are used to distinguish the two different materials (i.e. water and aluminium). The square rosters in the water domain represent the two areas where mesh refinement was applied, i.e. at the inlet (8 times refined) and the center of the test section (4 times refined).

In order to reduce the complexity of the numerical model and to keep the simulations computationally affordable, the following simplifications were made:

1. Approximation of the experimental domain by a two-dimensional numerical domain, hereby neglecting the wall effect in the third dimension. This was done to keep the simulations computationally affordable.

2. The use of constant and isotropic thermophysical properties in each phase (see table 3.1), except for a temperature dependent thermal expansion coefficient (see equation 3.8) which was used together with the *Boussinesq* approximation to model mixed convection effects within the channel. A similar approach was used by *Belhamadia et al.* [198] to simulate the freezing of water in a cubic cavity, who obtained a very good agreement with the experimental reference data [76].

3. The use of an equal density for the solid and liquid phases. This is done to avoid the numerically complexity regarding the expansion of the water upon freezing [196].

4. Assumption of incompressible flow.

5. Use of the 'sensible enthalpy' only formulation for the convection of heat [184].

Figure 5.11 shows the results for the ice layer at the inlet and the absolute velocity profile at $x = 5$ cm obtained after the first 5 min, for three different mesh sizes. With respect to the reference mesh of approximately 380,000 elements, the other two meshes were coarsened 2 and 4 times in both the x and y directions, resulting in a mesh size of respectively 4 and 16 times smaller. The results for all three meshes for the velocity profile overlap and cannot be distinguished by eye. For the ice layer, the three meshes produce similar results although the finer meshes result in a smoother solution of the solid-liquid phase boundary. Therefore, the 380,000 mesh size was considered fully mesh convergent and was used throughout the rest of the transient simulations.

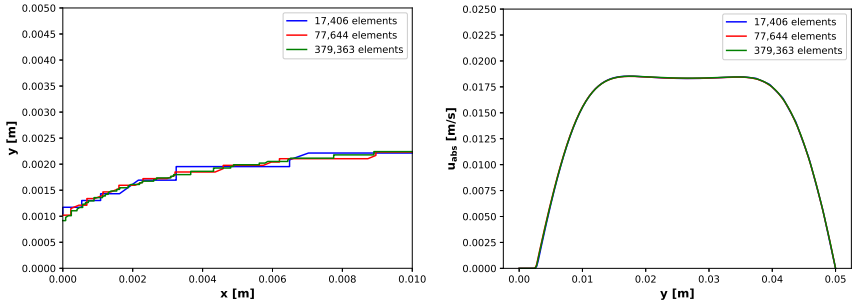

(a) Ice profile at inlet of test section.

(b) Velocity profile at $x = 5$ cm at inlet of test section.

Figure 5.11: Mesh refinement study for both the ice layer and the absolute velocity profile at the inlet. 3 meshes were considered, consisting of approximately 380000, 77644 and 17406 elements respectively.

Figure 5.12 shows the transient development of the ice layer obtained experimentally and numerically, for both the inlet and the center of the channel. Near the inlet the thickness of the ice layer increases with the downstream distance. The spatial gradient in the ice layer becoming smaller as the distance to the inlet ($x = 0$) increases and near the center of the channel the ice-profile appears to be (almost) flat, indicating the heat transfer is (close to) one-dimensional. A very good agreement with the experimental results was obtained, with the difference between the numerical results and experimental measurements on the sub-milli metre scale.

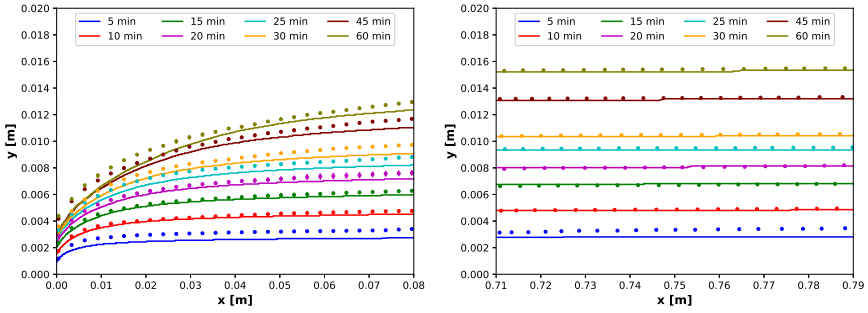

(a) At inlet of test section.

(b) In the centre of the test section.

Figure 5.12: Comparison between experimental (see chapter 3) and numerical ice profiles for different times after the onset of ice-formation. Two locations are shown, i.e. at the inlet of the test-section and at the centre. The experimental conditions were: $Re = 474$, $T_{in} \approx 4.7\,^{\circ}$C, $T_{c,set} = -10\,^{\circ}$C. The error bars for the experimental ice layer measurements at the inlet are given based on the statistical analysis of the five independent measurements performed for this case (see figure 3.3), the error bars for the experimental ice layer measurements at the center of the channel are given based on the conservative error estimate of $\sigma = 0.2$ mm.

Figure 5.13 shows the comparison between the experimental and numerical absolute velocity profiles, evaluated at $x = 5$ cm and $x = 75$ cm. A reasonable agreement between the experimental and numerical velocity profiles was obtained, however some discrepancies were observed. At $x = 5$cm, the numerical velocity profiles have two local maxima, both left and right of the center, whereas the experimentally measured velocity profiles only have one local maximum located around the center of the domain. At $x = 75$ cm, the experimental and numerical velocity profiles display similar behaviour and a better agreement was observed between the experimental and numerical results as opposed to the results for $x = 5$ cm. Both follow a (near) parabolic velocity profile, with the velocity profile becoming more narrow as the ice layer thickens. However, the velocity values measured in the experiment were slightly higher then those obtained in the simulation. In addition, whereas the numerically calculated velocity profiles appear to be fully symmetric, the experimental velocity profiles appear to be slightly skewed towards the bottom wall of the test section, especially for the smaller ice thicknesses. Please note that the numerical simulations showed no evidence of (significant) buoyancy during the transient development of the ice-layer in the laminar channel flow, similar to the PIV measurements.

Possible explanations for the observed discrepancies are:

1. The numerical simulations were performed using a two-dimensional computational domain. The absence of the wall effect in the third dimension could lead to a different result for the numerical flow field than for the experimental flow-field. Indeed, it has been shown that the shape of the velocity profiles in rectangular channel deviates from classical Poiseuille flow. The stream-wise velocity profiles tend to be steeper near the walls and flatter near the center of the channel [199]. The transversal velocity components are largest near the entrance of the channel; for fully developed flow, the flow is approximately two-dimensional [200], explaining why a better agreement was obtained between the measured velocity profiles and our 2D simulations at the center of the channel as compared to close to the inlet.

2. The assumptions used for the numerical simulation, including the use of the *Boussinesq* approximation for modelling buoyancy effects, the use of constant and isotropic thermophysical properties for the solid and liquid phases and the approximations of the inlet and boundary conditions. For the inlet conditions a uniform velocity profile was assumed, based on the predicted outlet condition of the contracting nozzle. However, the exact inlet conditions were not measured experimentally, since it was not possible to measure the velocity profile within the development length of $L = 13.5$cm prior to the start of the test section.

3. Possible systematic errors when performing the experiments.

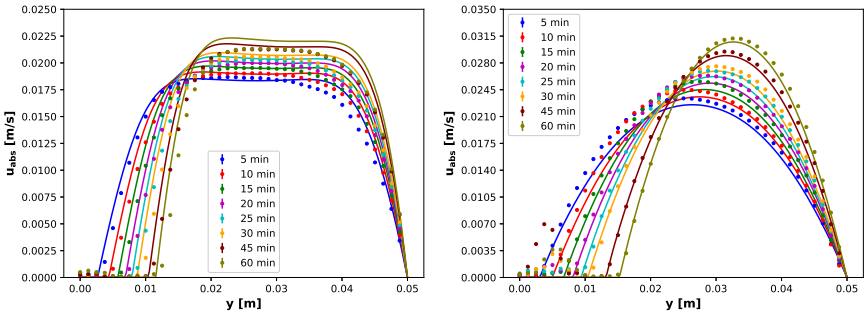

(a) $x = 5\,\text{cm}$ (b) $x = 75\,\text{cm}$

Figure 5.13: Comparison between experimental (see chapter 3) and numerical velocity profiles evaluated at a distance of $x = 5\,\text{cm}$ and $x = 75\,\text{cm}$ from the inlet of the channel for different times after the onset of ice-formation. The experimental conditions were: $Re = 474$, $T_{in} \approx 4.7\,^{\circ}\text{C}$, $T_{c,set} = -10\,^{\circ}\text{C}$. Due to the small uncertainty on the experimental profiles, the error bars are not visible.

5.6. Conclusion & recommendations

This chapter presents a novel method for the numerical solution of solid-liquid phase change problems, where the 'linearized enthalpy approach' was coupled to a discontinuous Galerkin framework. Compared to the apparent heat capacity method and the source-based approach, the 'linearized enthalpy approach' has the advantage of being inherently thermal energy conservative, having a comparatively fast convergence of the energy equation for each time-step, and not depending on the use of a so-called mushy zone. DG-FEM was selected for its attractive features, i.e. local conservation, the possibility for upwinding, an arbitrarily high order of accuracy, high parallelization efficiency and high geometric flexibility. In particular, DG-FEM has the potential of offering a higher spatial resolution as compared to the finite-volume method, resulting in a more accurate and computationally efficient numerical method. The present numerical method was validated with the one-dimensional Stefan problem and the two-dimensional melting of octadecane in a square cavity and melting of gallium in a rectangular cavity cases. For the one-dimensional Stefan problem, the numerical method converged to the analytical solution and for both the octadecane, gallium and transient freezing in a channel cases, a good agreement between the current numerical campaign and the experimental and numerical reference solutions was observed. The results for the transient freezing in a channel case demonstrated both the suitability of the experimental campaign from chapter 3 for numerical validation purposes, and the applicability of the proposed DG-FEM melting and solidification method to a wide variety of cases.

Comparatively few iterations were needed to solve the energy equation at each time-step and the number of iterations appeared to scale well with an increasing time-step. For both the one-dimensional Stefan problem and the 2D octadecane melting in a square cavity cases, approximately linear ($O(h)$) convergence rates were observed regardless of the element order. This sub-optimal mesh convergence rate was a consequence of the deteriorated solution quality in the vicinity of the solid-liquid interface, due to the discontinuous enthalpy and temperature solutions when undergoing phase change. For the gallium melting in a rectangular cavity case an increase in performance from increasing the polynomial order of the finite element basis could be observed. As the results from the Gallium case show, mainly solid-liquid phase change problems with strong gradients in the flowfield can benefit from the present higher order DG-FEM method. Possibly, the same applies to problems with regions of interest far away from the solid-liquid interface. In order to take full advantage of the arbitrarily high order of accuracy of the DG-FEM numerical method, we recommend combining the current approach with adaptive grid refinement or an extended finite element basis as a next step towards the development of more accurate and computationally efficient numerical methods for modelling melting and solidification.

Data Availability

The numerical data for cases 1-3 can be found at https://doi.org/10.5281/zenodo.6802375. The numerical data for case 4 can be found at https://doi.org/10.5281/zenodo.7602394. The 1D DG-FEM code used for simulating the 1D Stefan problem is made publicly available at https://doi.org/10.5281/zenodo.6801339.

6

A Finite Volume Parallel Adaptive Mesh Refinement Method for Solid-Liquid Phase Change

We present a finite volume adaptive mesh refinement method for solid-liquid phase change problems with convection. Three different refinement criteria were constructed for the solid-liquid interface , the flow-field and the temperature field respectively. For the solid-liquid interface, the cells undergoing phase change were refined based on the maximum difference in the liquid fraction over the cell faces. For the flow field and the temperature field, an error indicator was used based on the cell residual method. To maintain a high parallelization efficiency, a dynamic load balancing procedure was used. The adaptive mesh refinement strategy was verified through three different test cases, these are the gallium melting in both 2D and 3D cavities, and the molten salt reactor freeze-valve. Very good agreement was obtained between the adaptive mesh results and the reference solutions on a uniformly refined grid with significantly less degrees of freedom, showing the potential of the current approach for developing computationally efficient numerical methods for solid-liquid phase change problems.

This chapter is based on B.J. Kaaks, M. Rohde, J.L. Kloosterman, D. Lathouwers. A Finite Volume Parallel Adaptive Mesh Refinement Method for Solid-Liquid Phase Change. Submitted for publication.

6.1. Introduction

Adaptive meshing strategies have successfully been developed for a variety of applications, such as large eddy simulations of turbulent flow [201], [202], vortex dominated flows [203], [204], multiphase flow [205], [206] and ship hydrodynamics [207]. However, for solid-liquid phase change problems with convection, few contributions are reported in literature. *Palle et al.* [208] presented a finite element method with adaptive mesh refinement for melting and solidification problems using the Zienkiewicz and Zhu error estimator [209]. *Lan et al.* [210] developed an adaptive mesh refinement algorithm for solidification problems using the finite volume method, employing the normalized gradient or an estimate for the normalized truncation error as the refinement criterion. However, it was difficult to establish a universal rule for a cost-effective refinement procedure using the aforementioned approach. Using a similar gradient based error estimation approach, *Mencinger et al.* [211] presented an r-adaptive finite volume method for the numerical simulation of melting in a 2D cavity. A simple moving finite element mesh technique was presented in *Tenchev et al.* [212], which concentrates nodes in the vicinity of the phase change front. In addition, several finite element remeshing methods have been developed based on an equidistribution of the edge interpolation error, using an estimation of the Hessian [125], [213], [214] or a gradient recovery approach [126] as the basis for the error estimate and the construction of the metric tensor used to modify the mesh. Compared to adaptive mesh refinement, adaptive remeshing can lead to a more optimal distribution of the error (and therefore requiring less elements). However, the grid generation and the projection of variables unto the new mesh also presents a more significant computational overhead compared to the adaptive mesh refinement (and coarsening) procedure.

In the present work, we present an adaptive finite volume mesh refinement algorithm for melting and solidification problems using OpenFOAM. The cell residual error estimate of *Jasak et al.* [134], [135] is used for estimating the error in the solution for the flow-field and the temperature field, which has proven to be a more accurate error estimate compared to the traditional truncation based error estimates for the finite volume method. In addition, the elements in the vicinity of the solid-liquid interface are refined based on the maximum difference in the liquid fraction over the cell faces. With these refinement criteria, we expect to obtain a locally high resolution in both the solid-liquid interface and the critical flow and heat transfer regions, hereby achieving a high numerical accuracy at affordable computational cost. To ensure a high parallelization efficiency of our code, changes to the mesh are followed by a dynamic load balancing step, using the dynamic mesh library of *Rettenmeier et al.* [215]. The performance of the proposed adaptive mesh refinement algorithm was demonstrated for three test cases: Gallium melting in a 2D cavity, Gallium melting in a 3D cavity and a MSFR freezeplug design. This is the first time that the cell residual error estimate of *Jasak et al.* has been used as a refinement criterion for solid-liquid phase change simulations, and that an adaptive mesh refinement strategy for solid-liquid phase change problems has been applied to a more complex problem involving both solid-liquid phase change and conjugate heat transfer.

The remainder of this chapter is organized as follows. In section 6.2 we describe our numerical discretization and matrix solution procedure, the adaptive mesh refinement implementation in OpenFOAM and our refinement criterion. In section 6.3 we demonstrate the performance of our adaptive mesh refinement against 3 cases: gallium melting in a 2D cavity, gallium melting in a 3D cavity and the MSFR freezeplug. Finally, in section 6.4 we present our conclusions.

6.2. Numerical Methodology

6.2.1. Adaptive Mesh Refinement

An h-adaptive refinement approach was used to dynamically obtain high mesh resolution only in the regions where the estimated numerical error exceeds a certain threshold. To this end, a custom-built OpenFOAM solver for solid-liquid phase change simulations was coupled to the adaptive mesh refinement library developed by *Rettenmeier et al.* [215], of which an OpenFOAM v9 port is available in the blastFOAM project [216]. This library presents a major enhancement of the standard AMR functionality present in OpenFOAM, introducing AMR for arbitrary polyhedral cell shapes and 2D and 2.5D (i.e. axisymmetric) cases, whereas the standard version of OpenFOAM only supports AMR for hexahedral cells in 3D. In addition, the AMR library of *Rettenmeier et al.* features dynamic load balancing, maintaining a high parallelization efficiency during adaptive mesh refinement and therefore greatly enhancing the computational efficiency.

When solving a transient problem using parallel computing, AMR will change the load on the processors. The processor with the largest load becomes a bottleneck, which may significantly reduce the parallelization efficiency [215]. Using the dynamic load balancing (DLB) implementation of *Rettenmeier et al.* [215], the cells were redistributed among the processors following a refinement step, based on a user-prescribed maximum imbalance. To ensure that refined sibling cells remain on the same sub-domain, the refinement history was imposed as constraint during both the initial decomposition and during the redistribution.

The AMR library in OpenFOAM consists of three classes, these are the refinement engine (which contains the permanent mesh data, the functions to create the connectivity structures of the mesh and the functions to select the candidates for refinement or coarsening), the mesh cutter (which splits the parent cells into 8 or 4 child cells for 3D or 2D cases respectively), and the refinement tree containing the history of refinement (following an octree and quadtree approach for the 3D and 2D cases respectively) [202]. Here, cell level = 0 corresponds to the original cells, cell level = 1 corresponds to the first level of refinement etcetera. See figure 6.1 for a schematic of the adaptive mesh refinement. After each refinement step, the solution needs to be mapped between the parent and the child cells. OpenFOAM adopts a pseudo-staggered approach where variables (e.g. velocity and pressure) are stored as volume fields and defined at the cell-centers, whereas the convective flux is defined as a surface field and stored at the face centers [215]. The mapping of the cell-centered volume fields is straightforward: for each refinement step, the child-cells receive the cell-centered value of the parent cell whereas for a coarsening step, the volume average of the child cells' cell-centered values is set on the parent cell centers [215]. The mapping of the convective flux is more compli-

cated however, since new faces internal to the parent cell are not related to any master face. A good approximation of the convective flux on those fields is obtained from an arithmetical averaging of the face-centred velocity field $\mathbf{u_f}$ of the four adjacent neighbouring faces (which receive their values from the master face) [205], [215]. Due to the non-conservative mapping of the surface fields, a pressure correction step is introduced after each AMR step to ensure a divergence free mass flux field.

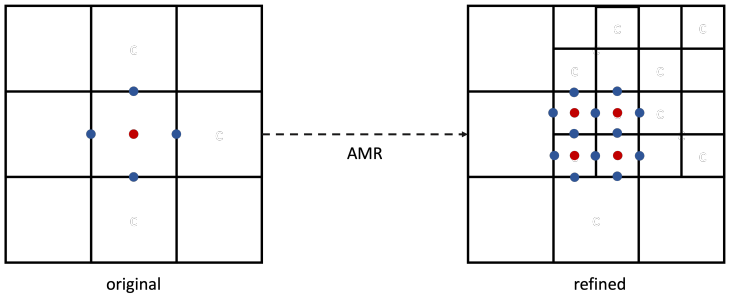

Figure 6.1: Schematic of adapive mesh refinement (in 2D, following the quadtree approach). The variables are stored as volume fields at the cell-centers (red dots) and the fluxes are stored as surface fields at the face centers (blue dots).

6.2.2. Refinement Criterion

In this work, three different refinement criteria are proposed. To obtain a sharp solid-liquid interface, the cells undergoing a rapid variation of the liquid fraction are flagged for refinement. This is done based on the maximum difference of the liquid fraction over the cell faces. Subsequently, the cells are refined up to the maximum refinement level. The refinement criterion for the solid-liquid interface is thus expressed as:

$$\begin{cases} \text{if } \left(max([[\phi_l]]_f) > 0.01 \wedge \text{ cell level} < \text{maximum cell level}\right) \text{ refine} \\ \text{if } \left(max([[\phi_l]]_f) < 0.001 \wedge \text{ cell level} >= 1\right) \text{ coarsen} \end{cases} \tag{6.1}$$

Here, $[[\cdot]]_f$ is the jump operator, defined as the face value of the cell minus the face value of the adjacent neighbouring cell.

To accurately resolve the flow field and the temperature field, the numerical discretization errors are estimated based on the cell residual error estimate developed by *Jasak et al.* [134], [135], [217]. The cell residual, similar to the residual error estimate for the finite element method, uses the inconsistency between the face interpolated values and the cell volume integration of the finite volume method as a measure of the numerical discretization error (see figure 6.2 for a graphical representation of this inconsistency).

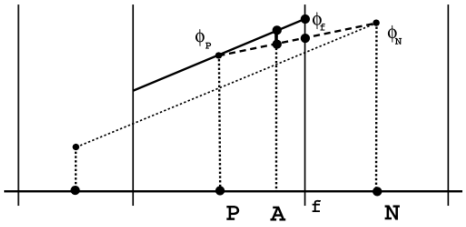

Figure 6.2: Inconsistency between the face interpolation and the cell volume integration, taken from [135]. Here, P is the centre of the control volume, N is the center of the neighbouring cell and f is the face between cell P and neighbour N. The face interpolation (the dashed line, assuming a linear variation between P and N) and the cell volume integration (solid line, assuming a linear variation over the control volume) predict a different value of the generic variable ϕ at an arbitrary point A inside the cell.

For the steady state transport equation of a generic conserved quantity ϕ (scalar or vector) the cell residual is calculated as [134]:

$$r_{P,steady}(\phi) = \int_{V_P} \left[\nabla\cdot(\mathbf{u}\phi) - \nabla(\gamma\nabla\phi) - S - \mathscr{L}\phi_P\right] dV$$
$$= \sum_f \left(\mathbf{s}\left[\mathbf{u}_f\phi_f - \gamma_f\left(\nabla\phi\right)_f\right] - SV_P - \mathscr{L}\phi_P V_P\right) \quad (6.2)$$

Here, γ is the diffusion coefficient and $S(\phi) = \mathscr{S} + \mathscr{L}\phi$ represents the linear decomposition of the source term. The subscript 'P' denotes the center of the control volume. To obtain the cell residual, the face values are calculated assuming a linear variation of ϕ over the control volume (instead of through a linear interpolation between the cell centre values ϕ_P and ϕ_N as is the case in standard finite volume discretization, see figure 6.2):

$$\phi_f = \phi_P + (\mathbf{x_f} - \mathbf{x_P})\cdot\nabla\phi_P, \quad \left(\nabla\phi\right)_f = \nabla\phi_P. \quad (6.3)$$

Here, $\mathbf{x}$ is the position vector.

In transient calculations, the numerical discretization accuracy is determined through both the temporal and spatial discretization. Decisions on the mesh refinement will be based on the estimate of the spatial error only, whilst the temporal error estimate can be used for the purpose of automatic time step control [217]. In this work, automatic time step control is based on the maximum value of the Courant number, to ensure stability of the simulation. Taking the transient term into account, the cell residual for the transient transport equation is calculated as [217]:

$$r_{P,transient}(\phi) = \int_{V_P} \frac{\partial\phi}{\partial t} dV + r_{P,s}(\phi). \quad (6.4)$$

Since $r_{P,t}$ has the dimensions of $\frac{[\phi][\mathbb{L}]^3}{[\mathbb{T}]}$, with $\mathbb{L}$ the characteristic length scale and $\mathbb{T}$ the characteristic time scale, an appropriate normalization is needed to obtain the magnitude of the error [134]. The normalization is based on the characteristic convection and diffusion transport for the control volume. The normalization factor is calculated as $F_{norm} = F_{conv} + F_{diff} + \mathscr{L}$, where $F_{diff} = \frac{1}{V_P}\sum_f \left[|\mathbf{s}|\frac{\gamma f}{|\mathbf{d}|}\right]$ (i.e. approximation of the total diffusion transport matrix coefficient) and $F_{conv} = \frac{1}{V_P}\sum_f max(\mathbf{u}_f \cdot \mathbf{s}, 0)$ (i.e. estimation of the convective transport matrix coefficient). Here, $\mathbf{s}$ is the outward-pointing face area vector and $\mathbf{d}$ is the vector pointing from the cell center to the neighbouring cell center. Since the error contribution from the linear part of the source term ($\mathscr{L}\phi_P$) scales with the error in ϕ_P, the matrix coefficient corresponding to the linear part of the source ($\mathscr{L}$) should be included into the normalization. The residual error estimate (REE) now becomes:

$$e_r(\phi) = \frac{r_{P,t}(\phi)}{V_P F_{norm}}. \tag{6.5}$$

The above form of the residual error estimate gives the absolute error estimate. However, for transient solid-liquid phase change simulations, the natural convection loop can strengthen (or weaken) over time and therefore it is difficult to specify an appropriate absolute error as a refinement criterion for the flow field. Instead, the absolute error in the flow field is normalized using the maximum absolute velocity value in the domain (max(|$\mathbf{u}$|)). To avoid attributing too much importance to very low velocity values in the early stages of the simulation, the normalization factor's lower bound is set at the absolute velocity value for which $Pe = 1$, i.e. $\frac{\alpha}{\mathbb{L}}$ with α the thermal diffusivity and $\mathbb{L}$ the characteristic length scale. Please note that the cell residual for the velocity is a vector, whereas OpenFOAM only supports scalar refinement criteria. As such, the Euclidean norm of the cell residual is used. The final form of the relative residual error estimate for the flow field is:

$$e_{r,rel}(|\mathbf{u}|) = \frac{|r_{P,t}(\mathbf{u})|}{V_P \times F_{norm} \times \max\left(\max(|\mathbf{u}|), {}^{\alpha}/_{\mathbb{L}}\right)}. \tag{6.6}$$

The estimated absolute numerical discretization error in the temperature field is normalized using the temperature difference over the domain:

$$e_{r,rel}(T) = \frac{|r_{P,t}(T)|}{V_P \times F_{norm} \times (\max(T) - \min(T))}. \tag{6.7}$$

If the estimated error exceeds the tolerance level, the cells are refined until the maximum refinement level is reached. Vice versa, the cell is coarsened once the estimated error is smaller than one fifth of the error tolerance:

$$\begin{cases} \text{if } \left(e_{r,rel}(|\mathbf{u}|, T) > tol \wedge \text{cell level} < \text{maximum cell level}\right) \text{ refine} \\ \text{if } \left(e_{r,rel}(|\mathbf{u}|, T) < {}^{1}/_{5}\, tol \wedge \text{cell level} >= 1\right) \text{ coarsen} \end{cases} \tag{6.8}$$

The three adaptive mesh refinement criteria for the solid-liquid interface (see equation 6.1), the velocity field and the temperature field (see equation 6.8) are evaluated simultaneously. For a cell to be refined, either one of the refinement criteria needs to be true. For a cell to be coarsened, both the coarsening criteria need to be true. In general, since the velocity in the solid-liquid interface is equal to zero, the refinement criteria take effect in different parts of the domain.

6.2.3. Numerical Solution Procedure

The coupled energy and momentum equations (see chapter 5) were implemented in OpenFOAM v9 and solved using the finite volume method. Compared to the SIP-DG implementation, there were the following differences in the model equations:

- The use of a different approximation for the enthalpy-temperature derivative:

$$\frac{dH}{dT} \approx \begin{cases} (1-\phi_l)\rho_s c_{p,s} + \phi_l \rho_l c_{p,l}, & T \neq T_m \\ \frac{\rho_l L}{2\epsilon}, T = T_m. \end{cases} \tag{6.9}$$

  Here, ϵ is a small parameter.

- The use of the following formulation for the enthalpy-temperature update:

$$H^{n+1,i+1} = H^{n+1,i} + \omega \frac{dH}{dT}\left(T^{n+1,i+1/2} - T^{n+1,i}\right) \tag{6.10a}$$

$$T^{n+1,i+1} = T(H^{n+1,i+1}), \tag{6.10b}$$

  where $\omega \leq 1$ is a damping parameter to ensure stability.

- The use of the following convergence criterion:

$$\max\left[res, \max\left(T^{n+1,i+1} - T^{n+1,i}\right)\right] < tol. \tag{6.11}$$

  Here, tol = 10^{-6}. *res* is the scaled residual of the original formulation of the transport equation (see equation 5.1) which is calculated using the known solution values after each iteration:

$$res = \frac{\int_\Omega (\left(\frac{\partial H}{\partial t} + \nabla \cdot (\boldsymbol{u}H) - \nabla \cdot (k \nabla T)\right) dV}{\int_\Omega \frac{H}{\Delta t} dV}. \tag{6.12}$$

- Following the approach of *Galione et al.* [218], the latent heat release is scaled with the solid or liquid density depending on whether the material is melting or freezing.

The diffusive term was discretized using the second order linear differencing scheme, and the convective terms were discretized using OpenFOAM's second order *linearUpwind* scheme (which obtains second order accuracy by applying an explicit gradient based correction to the standard upwind scheme). The time derivatives were discretized

using the second order BDF2 formulation. To reduce the computational overhead from the adaptive mesh refinement, the mesh update was performed once per every five time steps. To ensure a smooth transition between the different refinement levels and reduce the numerical discretization error due to mesh skewness, four buffer layers were used between each refinement level.

The resulting matrix equations are solved using GAMG (with Gauss-Seidel smoother) for the pressure equation and the stabilized bi-conjugate gradient matrix solver (PBiCGStab) (with DILU preconditioner) for the momentum and energy equations. The matrix tolerances are set to 10^{-8} for the pressure and pressure correction equations, (with an additional relative tolerance of 0.05 for solving the initial pressure correction steps), 10^{-12} for the momentum equation and 10^{-10} for the energy equation. To solve the velocity-pressure coupling, 5 PISO steps are used. Finally, three outer corrector steps are used to solve the coupling between the energy and the momentum equations.

The full solution algorithm can be summarized by the following steps:

1. Evaluate the refinement criterion, update the mesh and perform the pressure correction to compensate for the non-conservative mapping of the surface fields, ensuring a divergence free mass flux field (once per every five time steps).
2. Solve the momentum equation to obtain the velocity predictor.
3. Solve the energy equation through a series of non-linear enthalpy-temperature iterations until convergence is reached.
4. Solve the pressure equation and perform the velocity correction steps (in this work, 5 velocity corrector steps are used).
5. Repeat steps 2-4 until the total number of outer iterations has been reached (in this work, 3 outer correctors are used).

6.3. Results and Discussion

6.3.1. Melting of gallium in a 2D cavity

The first test case is the melting of gallium in a 2D rectangular enclosure of $L \times H = 88.9\,\text{mm} \times 63.5\,\text{mm}$. The initial temperature is $T_0 = 301.3\,\text{K}$ and at $t = 0\,\text{s}$, the left wall is suddenly heated to $T_H = 311.0\,\text{K}$ with the right wall being kept at $T_C = 301.3\text{K}$. The bottom and top walls are considered to be adiabatic. Due to the multi-cellular flow pattern, this problem is known to be sensitive to the mesh size, requiring a high spatial resolution to correctly predict the number of flow cells at each given time step [124]. For this reason, the melting of gallium in a 2D rectangular cavity is a challenging first test case for the adaptive mesh refinement technique presented in this paper.

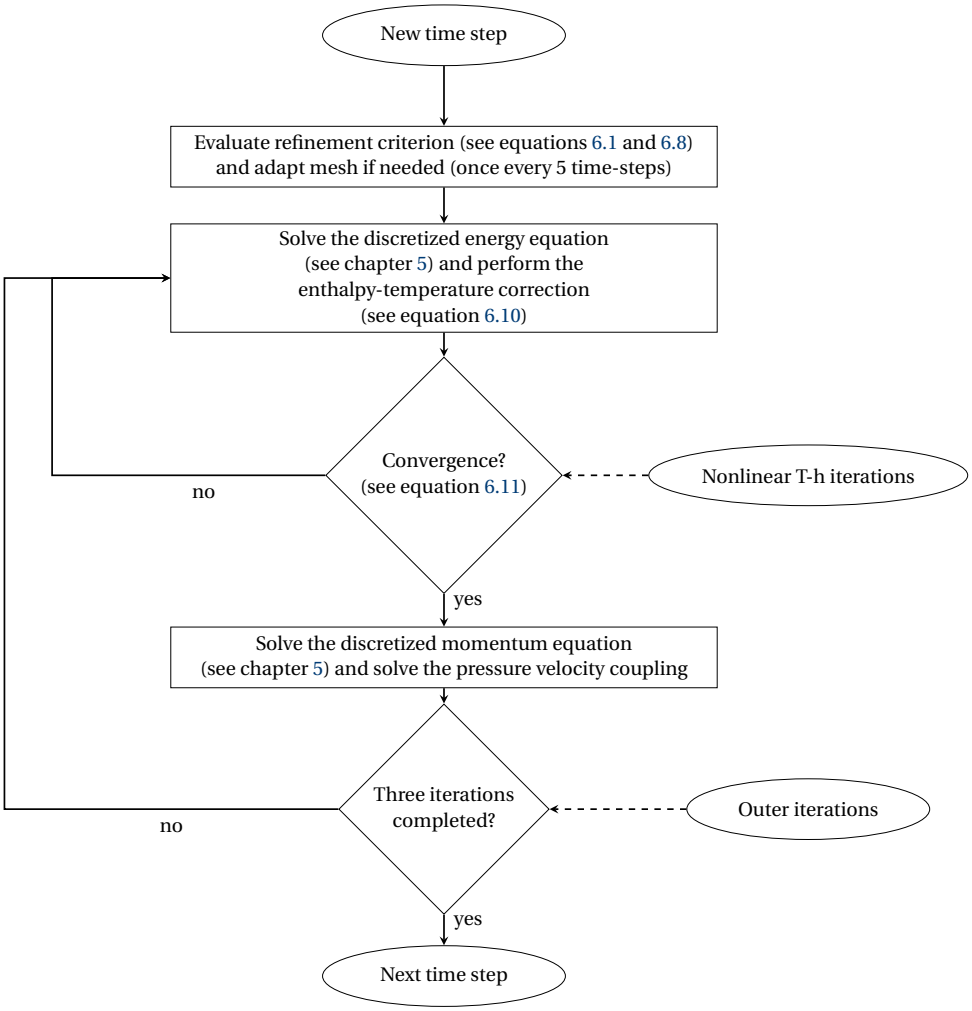

Figure 6.3: Flowchart of the solution algorithm, including the adaptive mesh refinement step, non-linear temperature-enthalpy iterations and the coupling of the energy and the momentum equations.

Results are presented at five different times (i.e. 20 s, 32 s, 42 s, 85 s, 120 s), using both a uniform mesh of 1120 × 800 quadrilateral cells (i.e. the reference mesh) and an adaptive mesh. The adaptive mesh consists of a 70 × 50 coarse mesh at cell level 0 with a maximum local refinement level of 4. At the highest cell level, the resolution therefore corresponds to that of the uniform reference mesh. The tolerance level for the estimated numerical discretization error in the flow field was set to $e_{r,rel}(|u|) < 0.0025$. No refinement criterion was imposed for the numerical discretization error in the temperature field. Simulations were performed for four progressively coarser uniform meshes (with 560 × 400, 280 × 200, 140 × 100 and 70 × 50 elements respectively), in order to better quantify the performance of the adaptive mesh. For all cases, adaptive time stepping was used based on a maximum Courant number of $Co = 3$, with the maximum time-step size set to $\Delta t = 0.025$ s. The thermophysical properties of gallium are given in table 5.4.

Figure 6.4 shows the solution for the normalized absolute velocity $|u|^* = \frac{|u|}{\max(|u|)}$, obtained with the uniform mesh of 1120 × 800 hexahedral elements. Here, $\max(|u|)$ corresponds to the maximum absolute velocity. At all times, the reference solution is in good agreement with the benchmark results of *Hannoun et al.* [124]. Figure 6.5 shows the estimated relative numerical discretization error in the flow field, obtained using the element residual error estimate of *Jasak et al.* [134]. Consistent with expectations, the largest errors were observed near the left boundary, the solid-liquid interface and around the boundaries of the flow cells (where the highest vorticity is to be expected). Please note that these errors correspond to the estimated discretization error at each given time step, and not to the total accumulated numerical discretization error throughout the numerical simulation (to obtain the latter, one would have to solve the error transport equation).

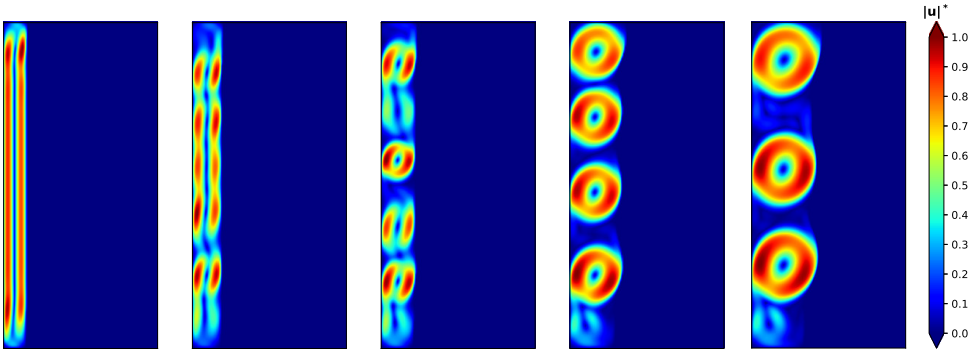

(a) 20 s (b) 32 s (c) 42 s (d) 85 s (e) 120 s

Figure 6.4: Normalized absolute velocity contour plots of gallium melting in a 2D cavity. Results were obtained using the uniform reference grid of 1120 x 800 elements.

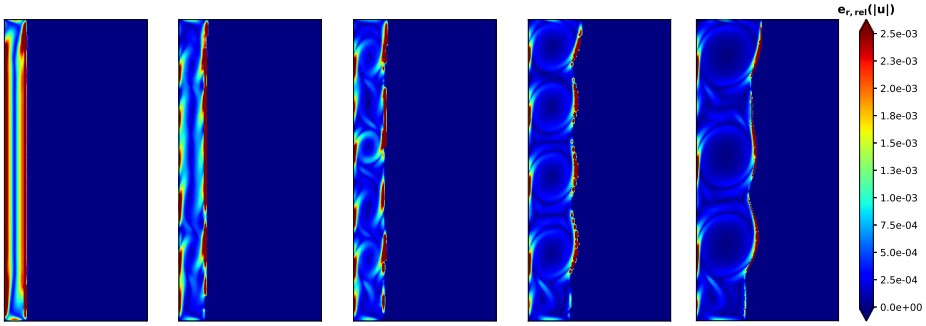

(a) 20 s (b) 32 s (c) 42 s (d) 85 s (e) 120 s

Figure 6.5: Estimated relative error in the absolute velocity for gallium melting in a 2D cavity. Results were obtained using the uniform reference grid of 1120 x 800 elements.

Figure 6.6 shows the solution for the normalized absolute velocity $|u|^*$, obtained with the adaptive mesh. A very good agreement was observed between the results with the (significantly smaller) adaptive mesh and the results on the uniform mesh of 1120×800 elements, demonstrating the potential of the proposed adaptive mesh refinement approach. Figure 6.7 shows the cell level for the adaptive mesh. The highest degree of refinement was found near the left boundary, the solid-liquid interface and around the boundaries of the vortices. The pattern of refinement qualitatively matches the adapted meshes obtained by *Belhamadia et al.* [126] who used a finite element higher order reconstruction approach for a posteriori error estimation, indicating the element residual error estimate for the finite volume method predicts a similar distribution of the numerical error.

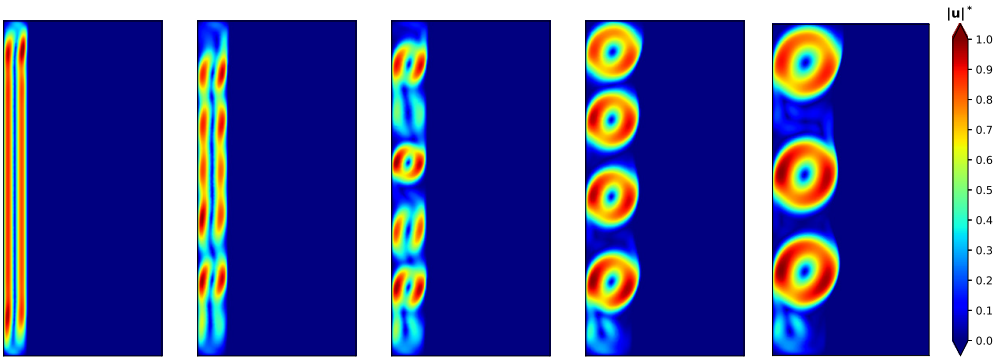

(a) 20 s (b) 32 s (c) 42 s (d) 85s (e) 120 s

Figure 6.6: Normalized absolute velocity contour plots of gallium melting in a 2D cavity. Results were obtained using the adaptive mesh grid.

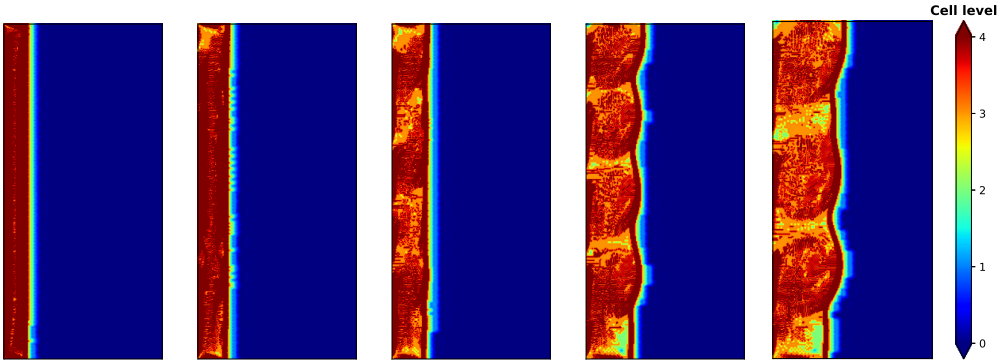

(a) 20 s (b) 32 s (c) 42 s (d) 85 s (e) 120 s

Figure 6.7: Cell levels of adaptive mesh grid for gallium melting in a 2D cavity.

Table 6.1 shows the L^2 relative difference (against the reference solution) for the 5 different times, evaluated for the absolute velocity field and calculated for five different meshes, i.e. the adaptive mesh and four different uniform meshes of progressively decreasing resolution. In addition, the number of cells for the adaptive mesh at each evaluated time step is given. The finest uniform mesh of size 1120×800 elements is used as the reference solution. The L^2 relative difference is given by:

$$\left(\frac{\int_V \left[|u|^* - |u|^*_{ref} \right]^2 dV}{\int_V \left[|u|^*_{ref} \right]^2 dV} \right)^{1/2} \tag{6.13}$$

To calculate the L^2 relative difference, the solution data from the adaptive mesh or one of the uniform coarser meshes was interpolated onto the reference mesh using a cubic 2D interpolant, such that the locations of the data points matched. Subsequently, the integrals were numerically approximated using the trapezium method. The L^2 relative differences between the adaptive solution and the uniform reference solution are below 5 % for all times. The number of cells for the adaptive mesh are between 50000 and 70000, which is a similar mesh size as the uniform 280×200 mesh. Compared to the 280×200 uniform mesh, the relative difference between the adaptive mesh and the reference solution is much smaller for all times. For the coarsest uniform meshes of 140×100 and 70×50 elements, very large differences were obtained, due to the inability of the coarsest meshes to properly resolve the multicellular flow patterns, leading to an incorrect prediction of the number of convective cells. As such, the analysis of the L^2 relative differences demonstrates that our adaptive mesh refinement approach can lead to similar numerical accuracy (as the uniform 1120×800 mesh) at significantly lower computational cost.

Table 6.1: L^2 relative difference of the adaptive mesh and four progressively coarser uniform grids (with 560 × 280, 280 × 200, 140 × 100 and 70 × 50 elements respectively) against the reference solution (with a uniform grid of 1120 × 560).

Time	Number of Cells (AMR)	$L^2_{\|u\|}$ (AMR)	$L^2_{\|u\|}$ (560 × 400)	$L^2_{\|u\|}$ (280 × 200)	$L^2_{\|u\|}$ (140 × 100)	$L^2_{\|u\|}$ (70 × 50)
20 s	50,681	0.0100	0.0254	0.0827	0.2367	0.4529
32 s	55,901	0.0398	0.0343	0.1401	0.3631	0.4757
42 s	50,498	0.0357	0.0596	0.5769	0.6502	0.6976
85 s	65,141	0.0500	0.0743	0.2040	0.7140	0.7074
120 s	69,254	0.0469	0.1030	0.1101	0.3330	0.7777

6.3.2. Melting of gallium in a 3D cavity

The melting of gallium in a 3D cuboid enclosure of $L \times H \times W = 88.9\,\text{mm} \times 63.5\,\text{mm} \times 38.1\,\text{mm}$ was selected for the second benchmark case. To reduce the computational cost, a half-sized computational domain of $L \times H \times W = 88.9\,\text{mm} \times 63.5\,\text{mm} \times 19.05\,\text{mm}$ was used, where a symmetry condition was applied at the center plane, at z=0. The initial temperature is $T_0 = 301.3\,\text{K}$ and at $t = 0\,\text{s}$, the left wall is suddenly heated to $T_H = 311.0\,\text{K}$ with the right wall being kept at $T_C = 301.3\,\text{K}$. All other walls are considered to be adiabatic. The flow structure of the gallium melting in a 3D cavity case is known to differ significantly from that of the 2D case, due to the wall effect in the third dimension [219]. For this reason, the gallium melting in a 3D case is a suitable benchmark case for demonstrating the performance of our adaptive mesh method in three dimensions. The adaptive mesh consisted of a uniform background mesh of $70 \times 50 \times 10$ elements, with a maximum cell refinement level of 3 and an error threshold of $e_{r,rel}(|U|) < 0.01$[1]. Compared to the 2D case, less strict refinement criteria were imposed due to the high computational cost associated with performing a solid-liquid phase change simulation in three dimensions. Again, adaptive time stepping was used based on a maximum Courant number of $Co = 3$, with the maximum time-step size set to $\Delta t = 0.025\text{s}$.

Figures 6.8 and 6.9 show the normalized absolute velocity and the corresponding cell levels after 120s, 360s and 600s. The flow features differed significantly between the 3D and the 2D case. Due to the suppression of the flow by the wall in the third dimension, the vortical structure in the melt is not as strong as in the 2D case. In addition, the multicellular flow patterns observed in the 2D simulations were absent in the 3D simulations, possibly due to the onset of a 3D instability destroying the formation of any 'long-lived' multi-vortex structures [197]. The flow in the melt is refined quite uniformly, with the strongest refinement found near the solid-liquid interface and the left and top walls.

[1] Again, no refinement criterion was imposed for the numerical discretization error in the temperature field.

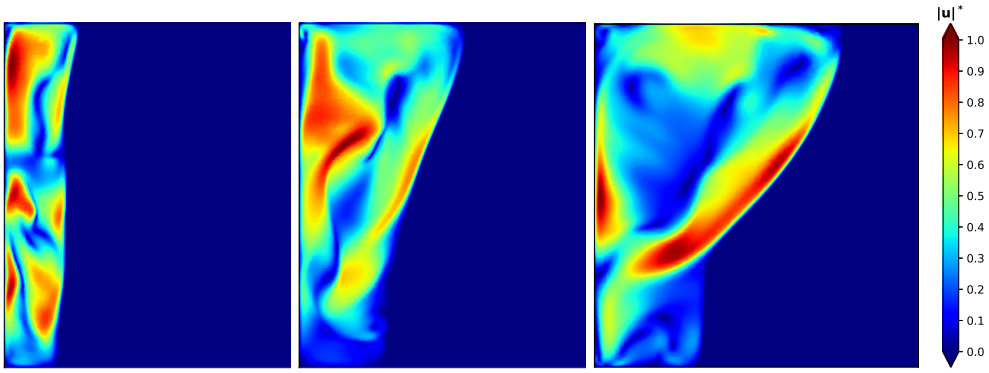

(a) 120 s (b) 360 s (c) 600 s

Figure 6.8: Normalized absolute velocity contour plots of gallium melting in a 3D cavity, at z=0 (central plane). Results were obtained using the adaptive mesh grid.

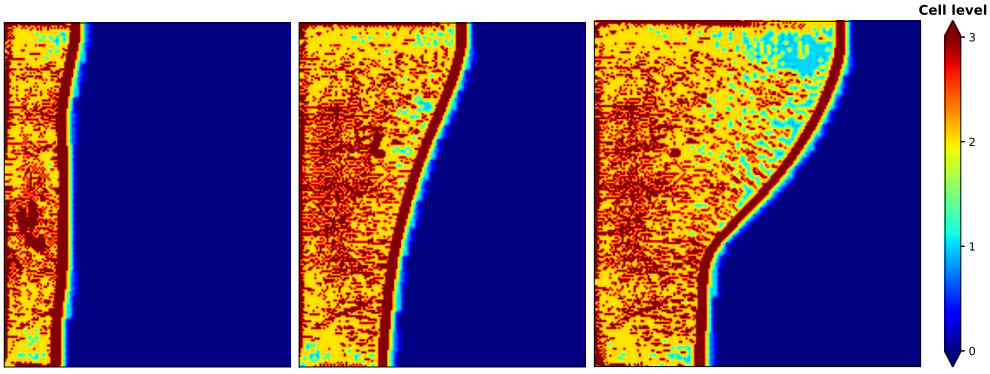

(a) 120 s (b) 360 s (c) 600 s

Figure 6.9: Cell level of the adaptive mesh for gallium melting in a 3D cavity, at z=0 (central plane).

Table 6.2 shows the total number of cells at the different times. Please note that for the gallium melting in a 3D cavity case, no uniform reference solution was generated due to the very high computational costs involved. Even with adaptive mesh refinement, the total number of elements used is still very high (though significantly less than when uniformly applying the maximum refinement level, which would result in a mesh size of $560 \times 400 \times 80 = 17,920,000$ elements). As mentioned before, isotropic mesh refinement was used in this work. Possibly, an anisotropic refinement strategy could yield similarly accurate results with even smaller mesh sizes, in particular for the 3D case. However, as of yet anisotropic mesh refinement has not been implemented in OpenFOAM.

Table 6.2: Total number of cells of the adaptive mesh at different simulation times for the gallium melting in a 3D cuboid cavity case.

Time	Number of Cells (AMR)
120 s	1,574,517
180 s	1,904,714
360 s	2,586,220
480 s	2,989,777
600 s	3,225,292
750 s	3,554,208
900 s	3,831,464
1020 s	4,086,880
1140 s	4,187,673

Figure 6.10 shows the solid-liquid interface position at different times. The results from the present numerical campaign were compared with those of *Kumar et al.* [219], and the experimental results of *Gau et al.* [67]. Overall, a good agreement was observed between the results from the current numerical campaign and those of *Kumar et al.*. Compared to the experimental measurements, both the current numerical campaign and the one of *Kumar et al.* slightly over-predict the melting rate at the earlier times (until approximately $t = 600\,\text{s}$). On the other hand, at later times the results from the present numerical campaign under-predict the melting rate. A possible cause for the discrepancies between the numerical results and the experimental measurements is the thermal inertia of the experiment during the start-up phase, the use of the intrusive measurement techniques and the overall lack of thermal insulation during the experiment [67]. However, the discrepancy could also be a consequence of modelling assumptions such as the use of the *Boussinesq* approximation or imposing adiabatic boundary conditions on the bottom, top, front and back walls. Compared to the arbitrary Lagrangian-Eulerian formulation of *Kumar et al.* [219], the results from the present numerical campaign predict an overall lower melting rate. This discrepancy may be caused by factors such as the mesh resolution, the time resolution and a difference in solid-liquid phase change modelling approach. Please note that the present formulation guarantees the conservation of the thermal energy through the convergence criterium (see equation 6.11).

6.3.3. The MSFR freeze plug

For the third and final test case, the Molten Salt Fast Reactor (MSFR) freeze valve was considered. The MSR freeze-valve was chosen as the final test case in order to demonstrate the applicability of our adaptive mesh refinement method to problems of industrial significance. Figure 6.11 shows the geometry of the freeze-plug and its boundary conditions. For this test case, the single plug design was selected, with a recess depth of 0.1 m. This design was chosen due to its relative simplicity compared to other freeze-plug designs, making it a suitable demonstration case for the proposed adaptive mesh refinement strategy. The freeze valve consists of a cylinder of salt with a radius of $R = 0.1\,\text{m}$ and a height of $H = 0.3\,\text{m}$, surrounded by a metal wall with a thickness of $\delta = 1\,\text{cm}$, of which the bottom 0.2 m consists of copper and the top 0.1 m consists of hastelloy. The thermophysical properties of the salt, the copper and the hastelloy are

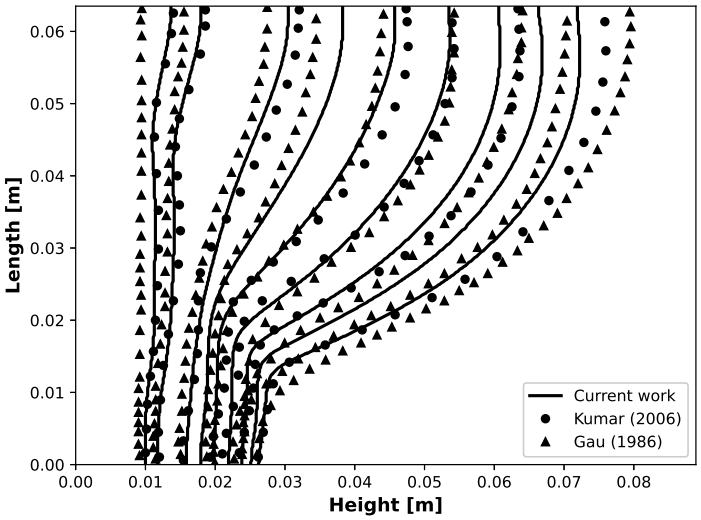

Figure 6.10: Solid liquid interface position for the gallium melting in a 3D cavity, at z = 0 (central plane). The results from the current numerical campaign are compared with the experimental results of *Gau et al.* [67], and the results from the numerical campaign of *Kumar et al.* [219].Results are shown for 120 s, 180 s, 360 s, 480 s, 600 s, 750 s, 900 s, 1020 s and 1140 s.

given in table 6.3. Due to the axisymmetrical nature of the problem, the 3D geometry is approximated by a 5° wedge with a thickness of one cell, and OpenFOAM's wedge boundary condition[2] is applied to the front and back face of the wedge. A segregated approach was adopted for the conjugate heat transfer modelling. Thus, separate matrix equations were solved for each region, and the temperature at the region interfaces was calculated through harmonic averaging:

$$T_{IF} = \frac{T_\alpha \times (k_\alpha/\delta_\alpha) + T_\beta \times \left(k_\beta/\delta_\beta\right)}{k_\alpha/\delta_\alpha + k_\beta/\delta_\beta}. \tag{6.14}$$

Here, α and β refer to the neighbouring cells at each side of the interface, and δ refers to the distance from the cell-centroid to the interface.

The initial mesh consists of a uniform 110×300 quadrilateral mesh, and a maximum time-step size of 0.25 s was used throughout the simulations, with a maximum Co number of $Co = 3$. For this case, conductive heat transfer through the metal walls played a significant role in determining the heat transfer rate. As such, a refinement criterion based on the solid-liquid interface and the numerical discretization error in the flow field alone was not deemed sufficient, as opposed to the previous two cases. Therefore, the estimated relative numerical discretization error in the temperature field was included in the refinement criterion. The numerical solution was found to be more sensitive to small errors in the numerical discretization of the temperature field than of the flow field. A

[2]The wedge boundary condition features an axisymmetrical boundary condition using a rotational transformation to map between a cartesian and cylindrical/spherical coordinate system.

maximum refinement level was set of 2, an error threshold of $e_{r,rel}(|U|) < 0.01$ was set for the flow field and an error threshold of $e_{r,rel}(T) < 0.0001$ was set for the temperature field.

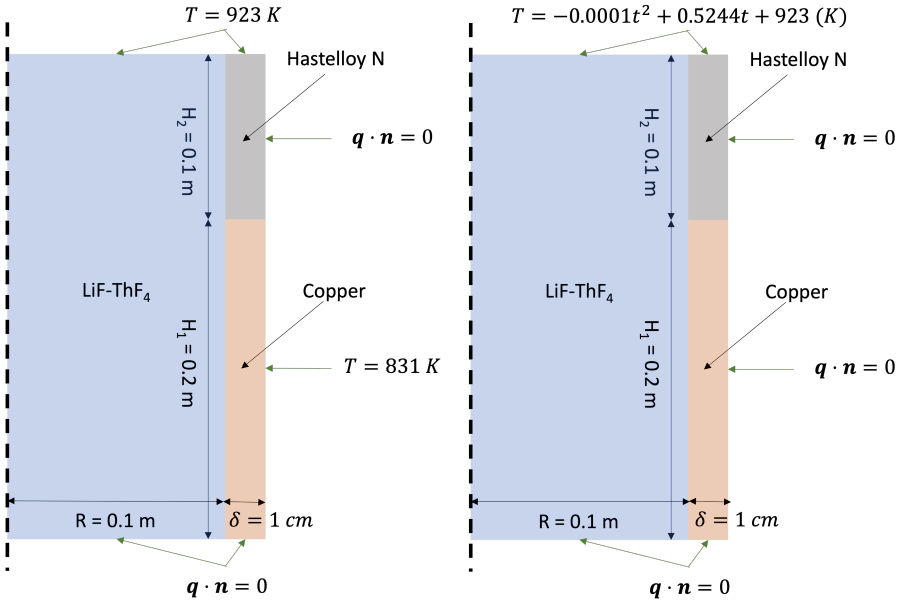

(a) steady state (b) transient

Figure 6.11: Geometry and boundary conditions of the MSFR freeze-plug (single plug, decay heat design), for both the steady and the transient case.

Table 6.3: Thermophysical properties of the salt, copper and hastelloy [29], [33], [35].

Property	$LiF\text{-}ThF_4$		Hastelloy-N	Copper
	Solid	Liquid		
Thermal conductivity [$W\,m^{-1}\,K^{-1}$]	1.5	1.5	23.6	401
Density [$kg\,m^{-3}$]	4502	4390	8860	8960
Specific heat capacity [$J\,kg^{-1}\,K^{-1}$]	815	1000	578	377
Latent heat [$J\,kg^{-1}$]	$1.59 \cdot 10^5$		-	-
Melting temperature [K]	841		-	-
Thermal expansion coefficient [K^{-1}]	$2.5 \cdot 10^{-4}$		-	-
Dynamic viscosity [Pa s]	$7.5 \cdot 10^{-3}$		-	-

In order to simulate the melting of the freeze-plug, first a steady-state solution of the freeze-plug needs to be obtained. For the steady-state simulation, the top temperature was set to 923 K and the temperature of the right copper boundary was set to 831 K. Adiabatic boundary conditions were imposed at the bottom boundaries and at the right hastelloy wall. The simulation was run for 25000 s in order to reach the steady-state solution. Subsequently, the steady-state freeze-plug solution is used as the initial condition

for the transient melting of the freeze-plug case.

Figure 6.12 shows the results for the steady state freeze-plug, the absolute velocity, the liquid fraction and the cell level. Compared to the freeze-plug shape obtained by *Tiberga et al.* [29], the present simulations predict a smaller curvature of the solid-liquid interface. This is believed to be due to the effect of natural convection (which was not considered by *Tiberga et al.*). Indeed, a recirculation zones was present near the solid-liquid interface. Near the cold copper wall, the salt flows down along the freeze front towards the center of the domain (bottom leg of the recirculation zone). Subsequently, the salt is recirculated back towards the hastelloy wall (top leg of the recirculation zone). Hereby, the mixing within the salt is enhanced, resulting in an overall flatter steady-state freeze-plug shape compared to a conduction-only simulation. The cells are most significantly refined close to the hastelloy wall and the solid-liquid interface, where the largests velocities are reached. The predicted numerical discretization error in the temperature field for the copper and hastelloy regions was very small, resulting in no refinement within these regions.

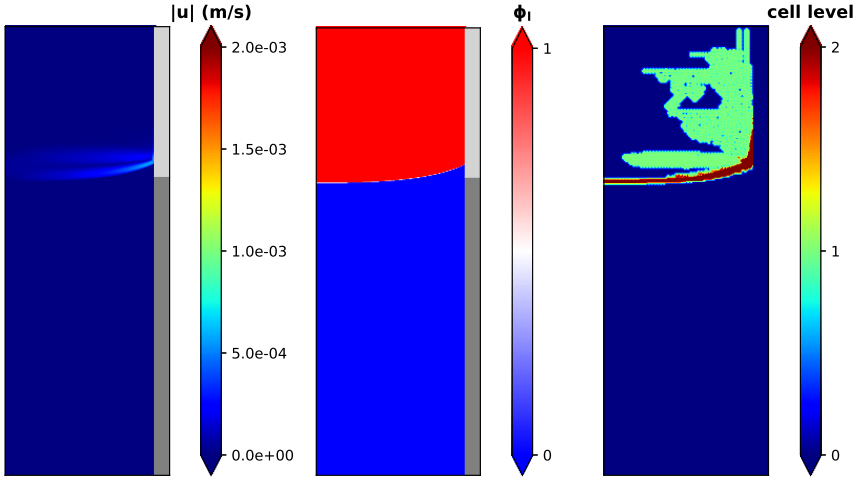

(a) $|u|$ (m/s) (b) ϕ_l (c) cell level

Figure 6.12: Numerical solution for the steady state freeze-plug case (which is the initial condition for the transient solution) for the absolute velocity (a), the liquid fraction (b) and the cell level (c), obtained with the adoptive mesh. The light and dark grey regions in the velocity and liquid fraction solutions refer to the hastelloy and the copper regions respectively, where these fields are not being calculated.

To start the transient simulation, the top boundary condition was changed from $T = 923\,\mathrm{K}$ to $T(t) = -0.0001t^2 + 0.5244t + 923\,\mathrm{K}$, representing the average temperature increase as a result of the decay heat following a reactor shutdown [29]. In addition, a zero-gradient condition was imposed at the right copper boundary, since the cooling system has now been switched off. Figures 6.13, 6.14 and 6.15 show the results for the transient case for the absolute velocity, the liquid fraction and the cell level, evaluated after 500 s, 1000 s, 1500 s and 2000 s. Since the hastelloy has a higher thermal conductivity than the salt, the heat from the top penetrates further into the hastelloy wall compared to the salt, resulting in higher temperatures in the vicinity of the hastelloy wall compared to the center of the domain. As a result, the salt starts to flow up along the hastelloy wall, enhancing the mixing in the liquid salt layer above the freeze-plug. When the freeze-plug starts to melt, an additional recirculation zone appears between the solid-liquid interface and the copper wall, increasing the melting rate at the top of the freeze-plug (but decreasing the melting rate at the sides, thus prolonging the opening time as shown by *Kaaks, Pater et al.* [220] and *Aji* [63]). The cells are most significantly refined close to the hastelloy wall, the solid-liquid interface and at the top of the domain, where most of the recirculation takes place. Few cells are refined in the copper and the hastelloy walls, indicating that the largest numerical discretization errors are present in the salt. As the salt melts, a gap starts to appear between the freeze-plug and the copper wall in which recirculation of the salt takes place, effectively shifting the heat transfer from the copper wall to the top of the freeze plug. Close to the copper wall, a thin layer of cells in the frozen layer of salt (located below the solid-liquid interface position) was also refined, attributed to the importance of the heat transfer through the copper wall during the melting of the freeze valve.

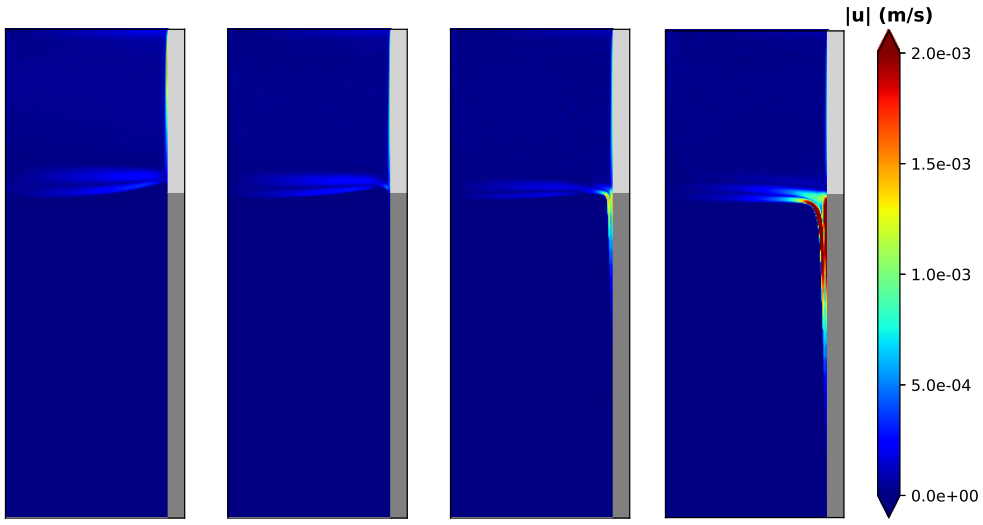

(a) 500 s (b) 1000 s (c) 1500 s (d) 2000 s

Figure 6.13: Numerical solution for the transient freeze-plug case for the absolute velocity, obtained with an adaptive mesh. The light and dark grey regions refer to the hastelloy and the copper respectively.

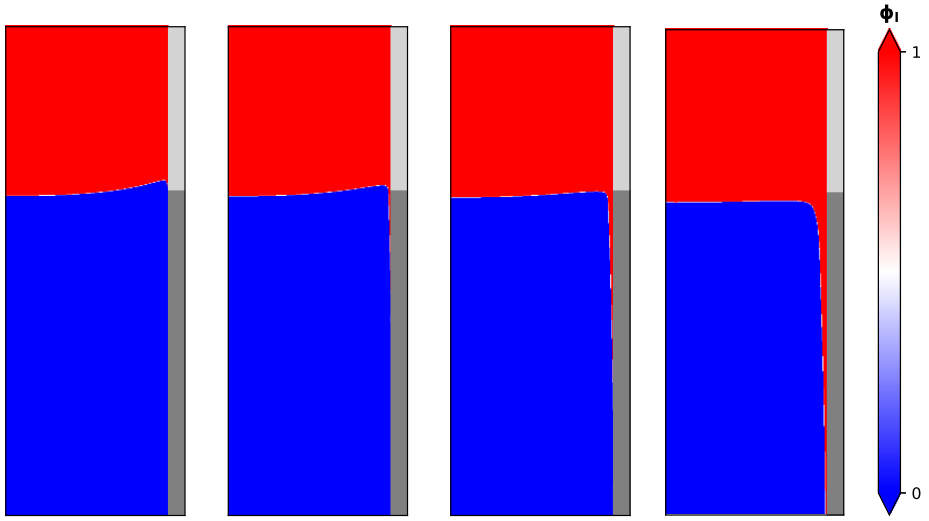

(a) 500 s (b) 1000 s (c) 1500 s (d) 2000 s

Figure 6.14: Numerical solution for the transient freeze-plug case for the liquid fraction, obtained with an adaptive mesh. The light and dark grey regions refer to the hastelloy and the copper respectively.

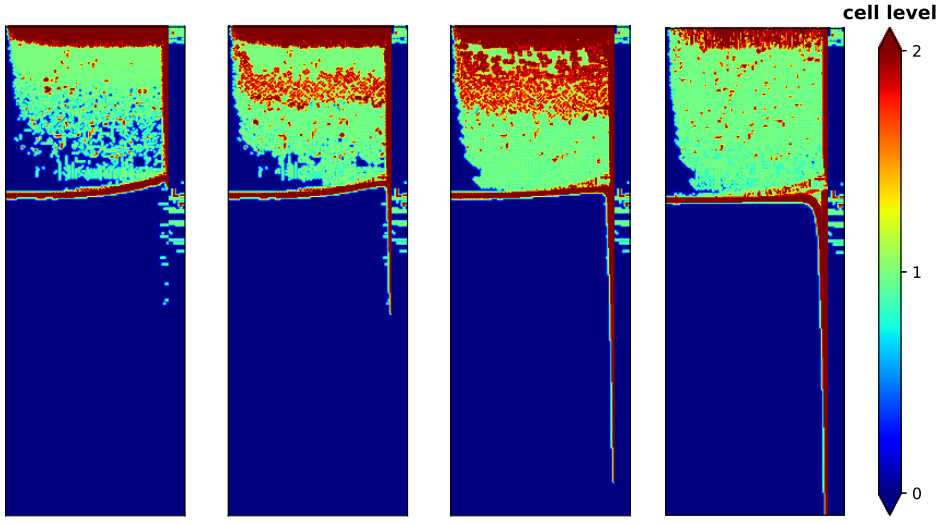

(a) 500 s (b) 1000 s (c) 1500 s (d) 2000 s

Figure 6.15: Cell level of the adaptive mesh for the MSFR freeze-valve.

Figure 6.16 shows the relative total solid fraction of the freeze-plug at the metal wall for the adaptive mesh and three uniform meshes consisting of 440 × 1200, 220 × 600 and 110 × 300 elements. The total solid fraction of the freeze-plug at the metal wall (at $x = 0.1$ m) was calculated for each mesh at a time interval of 25 s by approximating the integral of $\phi_s|_{x=0.1\,\mathrm{m}} = 1 - \phi_l|_{x=0.1\,\mathrm{m}}$ over the height (y) using the trapezium rule. The relative total solid fraction was obtained by normalizing the total solid fractions with the reference solid fraction, evaluated for the 440 × 1200 mesh at $t = 0$:

$$X_s^* = \frac{\int_0^{y=0.3\,\mathrm{m}} \left(1 - \phi_l(t)|_{x=0.1m}\right) dy}{\int_0^{y=0.3\,\mathrm{m}} \left(1 - \phi_l^{ref}(t = 0\,\mathrm{s})|_{x=0.1\mathrm{m}}\right) dy} \tag{6.15}$$

The relative solid fraction at the copper wall is the quantity of interest for the melting of the MSFR freeze valve, since the freeze valve is expected to fall into the drainage tank below once it has become detached from the solid wall. As such, $X_s^* = 0$ corresponds to the opening time of the freeze-valve. The opening time is much longer than the 715 s predicted by *Tiberga et al.* [29]. Therefore, including the role of natural convection appears to result in a prolonged opening time of the freeze plug.

A very good agreement was obtained between the adaptive mesh and the reference mesh with 440 × 1200 elements. On the other hand, the coarser meshes over-predicted the opening time, with a difference of more than 200 s in the predicted opening time between the coarsest mesh of 110 × 300 elements and the finest mesh of 440 × 1200 elements. At all times, the number of elements of the adaptive mesh was smaller than the 220×600 uniform mesh (see table 6.4). As such, it is evident that the adaptive mesh yields similarly accurate results compared to the uniform mesh with 440 × 1200 elements, at a much lower computational cost.

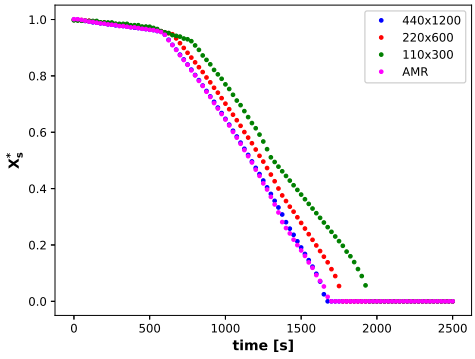

Figure 6.16: Relative solid fraction of the freeze-plug at the metal wall (R = 0.1 m), showing the melt trajectory of the plug. Results from the adaptive mesh were compared to the solutions of three progressively coarser uniform meshes.

Table 6.4: Total number of cells of the adaptive mesh at different simulation times for the MSFR freeze valve melting case.

Time	Number of Cells (AMR)
0 s	47,583
500 s	73,260
1000 s	83,427
1500 s	98,280
2000 s	84,030

6.4. Conclusions

This work present a finite volume adaptive mesh refinement method for solid-liquid phase change problems. Separate refinement criteria were used for the solid-liquid interface and the flow-field. For the solid-liquid interface, the cells undergoing the phase transition were flagged based on the maximum face jump in the liquid fraction and refined up to a user-specified refinement level. For the flow field and the temperature field, the cell-residual method of *Jasak et al.* [134] was used to estimate the numerical discretization error, and the cells which exceeded the user-specified error tolerance were refined until the maximum refinement level was reached. To maintain a high parallelization efficiency during the adaptive mesh refinement, a dynamic load balancing procedure was used. The adaptive mesh refinement strategy was verified for three different test cases, these are the gallium melting in a 2D rectangular cavity case, the gallium melting in a 3D cuboid cavity case and the MSFR freeze-plug. For the gallium melting in a 2D cavity case, a very good agreement was obtained between the adaptive mesh and the uniform reference mesh. The uniform reference mesh was more than 10 times larger than the adaptive mesh, demonstrating the potential of the proposed adaptive mesh refinement approach to locally achieve a high resolution with limited computational cost. For the gallium melting in a 3D case, we demonstrated very good agreement between the solution with the adaptive mesh and the numerical and experimental reference solutions. The results for the MSFR freeze-valve demonstrated the applicability of our adaptive mesh refinement strategy to more complex solid-liquid phase change problems which also involved conjugate heat transfer, with a very good agreement obtained between the predicted opening time with the uniform reference mesh and the more than five times smaller adaptive mesh. Although the current results appear to be very promising, possibly the use of an anisotropic adaptive mesh refinement strategy (contrary to the current isotropic mesh refinement approach) could lead to an even more computationally efficient numerical framework for solving solid-liquid phase change problems.

Data Availability

The numerical data generated for the melting of gallium in the 2D and the 3D cavities and the melting of the freeze valve can be found under the associated link: `https://doi.org/10.5281/zenodo.10058162`. In addition, the developed OpenFOAM solvers for solid-liquid phase change with adaptive mesh refinement have been made publicly available: see : `https://doi.org/10.5281/zenodo.10074609`.

7

A NUMERICAL BENCHMARK FOR MODELLING PHASE CHANGE IN MOLTEN SALT REACTORS

Mateusz Pater and Bouke Kaaks

The design of a molten salt reactor is largely based on CFD simulations. Phase change plays an important role in the safety of the reactor, but numerical modelling of phase change is particularly challenging. Therefore, the knowledge of the margin of error of CFD simulations involving phase change is very important. Relevant experimental validation data is lacking. For this reason, a numerical benchmark designed after the freeze valve is proposed. The benchmark consists of five stages, where with each step more complexity is added. The step-wise addition of complexity allows for pinpointing potential sources of discrepancy. Results were obtained with three different codes: STAR-CCM+, OpenFOAM, and DGFlows. The results were found to be largely consistent between the codes, however the addition of conjugate heat transfer introduced some discrepancies. These results indicate that careful consideration is needed when coupling conjugate heat transfer solvers with solid-liquid phase change models.

This chapter is based on M.Pater, B.J. Kaaks, B. Lauritzen, D.Lathouwers. A numerical benchmark for modelling phase change in molten salt reactors. Published in *Annals of Nuclear Energy 194* (2023), (Pater, Kaaks et al., 2023).

7.1. Introduction

The design of the freeze valve relies heavily on numerical simulations to obtain predictions of its melting time. Experimental studies suitable for numerical validation have mainly focused on the melting of pure metals or paraffin wax in rectangular or cylindrical enclosures, such as those performed by *Gau et al.* [67], *Jones et al.* [78], and *Faden et al.* [118] and do not include the full complexity of the MSFR freeze valve design. For this reason, it is of paramount importance that sufficient knowledge is obtained regarding the accuracy of currently used numerical modelling approaches and their possible limitations in predicting the melting behaviour of the MSFR and any other similar freeze valve design.

Recently, a multiphysics numerical benchmark for codes dedicated to the MSFR was proposed [47], and results were compared for six different codes [174], [221]–[224]. The simplicity of the benchmark and its step-by-step approach made it a suitable tool for testing the performance of various codes and detecting possible discrepancies. In a similar fashion, we propose a two-dimensional numerical benchmark based on one of the MSFR freeze valve designs [61], to compare the solid-liquid phase change modelling capabilities and their coupling with fluid flow and conjugate heat transfer models of different numerical codes.

The benchmark consists of five different stages and with each stage, complexity is added as the model evolves towards a more realistic representation of the MSFR freeze valve. The first stage consists of a variation on the classical Stefan problem, however featuring a time-dependent temperature boundary condition that is representative of shut-down conditions in the MSFR. In the second stage, volumetric heating is added to model the influence of radiation and heat deposition from the fuel salt on the melting of the freeze plug. In the third stage, solid walls are added to the freeze valve geometry and conjugate heat transfer modelling is required in addition to solving the melting problem. In the fourth stage, the role of natural convection on the melting behaviour is investigated, and in the fifth and final stage, forced convection is added, mimicking the recirculation of the fuel salt above the freeze valve. In this work, three different numerical codes are used to compare the results for the five benchmark stages: an in-house code DGFlows developed at Delft University of Technology [179], [181], [225], the commercial code STAR-CCM+ [226], and the open-source code OpenFOAM [227]. The step-wise addition of complexity allowed for identifying at which steps discrepancies between the results provided by the codes would arise.

The remainder of this chapter is organized as follows. In section 7.2, the various modelling approaches of the three codes are presented. In section 7.3, the five benchmark stages are introduced, and the results of the codes are discussed and compared. Finally, section 7.4 summarizes the most important results of this MSFR freeze valve numerical benchmark study and presents the conclusions.

7.2. Characteristics of the codes used

A short description of each code used in this benchmark is presented below.

7.2.1. STAR-CCM+

The following description of STAR-CCM+ version 2020.2 used in this benchmark is based on the User Guide (). CFD modules of STAR-CCM+ utilize the finite volume method and solve the Navier-Stokes equations in each computational cell. The software is able to model multiphase flow using Eulerian and Lagrangian approaches.

Volume of fluid

A phase change problem is a multiphase problem, as more than one thermodynamic state of the matter – in our case, solid and liquid – are present and interact with each other within the same system. In order to model phase change in STAR-CCM+, the Volume of Fluid approach, traditionally used for tracking interfaces between gases and liquids [228], is used by the software. Volume of Fluid is a simple model based on the Eulerian formulation of a multiphase fluid, where two or more immiscible phases share an interface. Mass, momentum, and energy are treated as mixture quantities rather than phase quantities. The dynamic viscosity and thermal conductivity are volume-weighted, and the specific heat is mass-weighted. Conservation equations are solved for the mixture in a computational cell. The mesh must be fine enough to resolve the interface between the phases.

Phases are described by the phase volume fraction ϕ_i:

$$\phi_i = \frac{V_i}{V}, \tag{7.1}$$

where V_i is the volume of phase i in the cell of volume V. The phase mass conservation equation is:

$$\frac{\partial}{\partial t}\int_V \phi_i \, dV + \oint_s \phi_i \boldsymbol{v} \cdot d\boldsymbol{s} = \int_V \left(S_{\phi_i} - \frac{\phi_i}{\rho_i}\frac{D\rho_i}{Dt} \right) dV - \int_V \frac{1}{\rho_i} \nabla \cdot (\phi_i \rho_i \boldsymbol{v}_{d,i}) \, dV, \tag{7.2}$$

where $\boldsymbol{s}$ is the surface area vector, $\boldsymbol{v}$ is the mixture velocity, $\boldsymbol{v}_{d,i}$ is the diffusion velocity, S_{ϕ_i} is a source term of phase i, and $D\rho_i/Dt$ is the Lagrangian derivative of the phase densities ρ_i.

A Segregated Multiphase Temperature model is activated in STAR-CCM+ in order to solve the total energy equation. The temperature is the solved variable and the enthalpy is computed from the temperature according to the multiphase equation of state. In our STAR-CCM+ model, the convective flux in the Volume of Fluid transport equation is discretized using a second-order scheme. The second-order convection scheme is used to solve the energy equation as well.

Melting-solidification

The solid-liquid interface is not tracked directly by the software; instead, an enthalpy formulation is used to determine the relative fraction of the solid and liquid phases:

$$H_{tot} = H_{sens} + (1 - \phi_s)L, \tag{7.3}$$

where H_{tot} is the total enthalpy, H_{sens} is the sensible enthalpy, L is the latent heat and ϕ_s is the relative solid volume fraction. For linearized melting, the liquid fraction corresponds to the fraction of the latent heat of fusion that has been absorbed by the system. In STAR-CCM+, each mesh cell is characterized by an individual value of the relative solid volume fraction. If the material's solidus and liquidus points are the same, a difference of 0.002 K is introduced automatically between them so that it is possible for the software to take the latent heat into account in a phase change problem. This way, the relative solid volume fraction between fully solid and fully liquid states is calculated as:

$$\phi_s = \frac{T_{liquidus} - T}{T_{liquidus} - T_{solidus}}. \tag{7.4}$$

One of the optional models for phase change in STAR-CCM+ is a Melting-Solidification Flow Stop model. With the help of this functionality, the flow is stopped in a cell when a specified solid fraction is exceeded. To avoid assigning velocities to the cells undergoing melting and to resemble the way in which DGFlows and OpenFOAM treat phase change, the default solid fraction value of 1 has been changed to 0.01. This way, the momentum equations are solved only in the cells that have (almost) fully undergone phase change to the liquid state.

Conjugate heat transfer

Coupled heat transfer between a liquid and an adjoining solid, i.e. conjugate heat transfer, is modelled with the use of an interface between the two materials. Each material has its own thermal boundary conditions, and the interface can have an additional heat source S. The energy conservation equation at the interface is:

$$q_{fluid} + q_{solid} = -S, \tag{7.5}$$

where q_{fluid} is the normal heat flux value from the fluid through the boundary and q_{solid} is the normal heat flux value leaving through the boundary into the solid. The equation is solved for each side of the interface with the use of a linearized heat flux taking into account secondary gradients:

$$\boldsymbol{q} = k\left[(T_w - T_c)\boldsymbol{B} + \nabla T_c - (\nabla T_c \cdot \boldsymbol{\Delta x})\boldsymbol{B}\right] \tag{7.6a}$$

$$\boldsymbol{B} = \frac{\hat{\boldsymbol{n}}}{\hat{\boldsymbol{n}} \cdot \boldsymbol{\Delta x}} \tag{7.6b}$$

$$\boldsymbol{\Delta x} = \boldsymbol{x_1} - \boldsymbol{x_0}, \tag{7.6c}$$

where T_w and T_c are the wall and cell temperatures, respectively, $\hat{\boldsymbol{n}}$ is the normal vector, and $\boldsymbol{\Delta x}$ is a vector pointing from the centroid of cell 0 to the centroid of cell 1, lying on opposing sides of the interface.

7.2.2. OpenFOAM

OpenFOAM [227] is the leading open-source CFD software. In this work, a phase-change model based on the 'linearized enthalpy approach' [119], [225] has been implemented in OpenFOAM v8, distributed by the OpenFOAM foundation. The OpenFOAM solver used was a predecessor to the parallel adaptive mesh refinement solver for solid-liquid phase change presented in chapter 6. In this solver, slightly different formulations for the enthalpy-temperature derivative and the convergence criterion were used. Here,

$$\frac{dH}{dT} \approx \frac{1}{2}\left(\rho_s c_{p,s} + \rho_l c_{p,l}\right) \tag{7.7}$$

$$H^{n+1,i+1} = H^{n+1,i} + \frac{dH}{dT}\left(T^{n+1,i+1/2} - T^{n+1,i}\right) \tag{7.8}$$

The convergence criterion is defined as:

$$max\left[res, \sum_{n_{elem}=0}^{n_{elem}=N_{elem}} \left(T^{n+1,i+1} - T^{n+1,i}\right)\right] < tol. \tag{7.9}$$

In this work, $tol = 10^{-6}$. Here, res is the initial residual of the iterative matrix solver and N is the total number of cells. Upon convergence, the difference between the old and the new temperature values approaches zero and the solution to the 'linearized enthalpy equation' approaches the solution to the original enthalpy transport equation in conservative form.

7.2.3. DGFlows

DGFlows is an in-house CFD code based on the discontinuous Galerkin Finite Element Method (DG-FEM), developed at the Radiation Science and Technology Department of Delft University of Technology [179], [181]. DG-FEM combines attractive features of the finite element and finite volume methods, such as an arbitrarily high order of accuracy, high geometric flexibility, local conservation of vector and scalar fields, possibility for upwinding and a compact numerical stencil facilitating efficient parallelization of the solution procedure [179], [181]. To model phase change, the 'linearized enthalpy approach' has been implemented in DGFlows (see chapter 5).

7.2.4. Current limitations of the solid-liquid phase change solvers

Numerical methods for solving solid-liquid phase change problems are characterized by certain limitations. First of all, the discontinuous enthalpy and material properties at the solid-liquid interface can produce strong gradients which are difficult to capture numerically. Therefore, many phase change models assume that properties such as density or thermal conductivity remain temperature-independent and utilize an approximation function such that the enthalpy change is modelled smoothly over a predefined temperature range (the so-called mushy zone). In addition, a very fine mesh is often needed in the vicinity of the solid-liquid interface to accurately resolve the gradients. In particular the density change, and accompanying volume changes and secondary flow effects, can

be challenging from a numerical modelling perspective. Accurate modelling of the density change during solid-liquid phase change would require the use of a fully compressible fluid approach and special treatment of the volume expansion effects, as shown by *Faden et al.* [196]. To reduce complexity of the numerical approach and not distract from the focus of the benchmark, we assumed a constant density in our simulations.

Furthermore, modelling the flow within the (porous) solid-liquid interface zone may be a considerable challenge. In our case, we considered isothermal phase change and we did not consider microscale phase change phenomena (such as phase segregation, dendrite formation etc. analyzed by *Tano et al.* [48]). Therefore, we have a sharp interface between the solid and the liquid salt, and the Navier-Stokes equations may be solved by simply damping the velocities in the solid phase. Lastly, strong temperature gradients at the interface and accompanying thermal stresses may produce cracking phenomena in the solid. Modelling these phenomena requires the coupling of the phase change model to an additional solid mechanics model and was not considered in the present work.

7.3. Results and discussion

A numerical benchmark is proposed based on the MSFR freeze valve design described by *Giraud et al.* [61]. The freeze valve is a key passive safety feature unique to the MSFR, and is designed to melt in case of a reactor anomaly, draining the fuel salt into an emergency drainage system. The benchmark consists of five stages. With each new stage an additional level of complexity is introduced, as the model converges towards a more realistic design of the MSFR freeze valve. The calculated temperatures, position of the melting front, and velocities are compared amongst the three different codes, to provide a first indication of the consistency between different solid-liquid phase-change modelling approaches and to identify possible sources of discrepancies between the codes.

In the first stage of the benchmark, the fuel salt undergoes melting inside a two-dimensional cavity encompassing the salt domain. The heat source, modelled after the decay heat of the MSFR, is located at the top boundary of the model. The heat is conducted towards the bottom part of the domain, where phase change takes place. In the second stage, a volumetric heat source is added to the entire salt volume to mimic the heat deposition due to neutrons and photons arriving at the freeze valve's location, originating from the reactor core above. This heat source follows asimilar time-dependent function as the decay heat. In the third stage, a solid wall is added to the side of the freeze valve geometry. Conjugate heat transfer is modelled to investigate the effect of heat conduction in the metal and subsequent heat exchange between the salt domain and the metal wall resulting in the melting of salt next to the wall. In the fourth stage, momentum equations are implemented with the use of a Boussinesq approximation, and the natural circulation takes place in the salt volume, making the melting process more realistic. In the last, fifth stage of the benchmark, movement of the top boundary is added to impose forced convection that is present in the reactor, where the molten fuel salt above the freeze valve is recirculated.

7.3.1. Stage 1

Description

To accommodate as many different software suites as possible and to keep the computational cost affordable, a two-dimensional Cartesian geometry was chosen for the benchmark. Due to the symmetric nature of the modelled freeze valve, the geometry is cut in half at the symmetry axis to save computational resources.

The model geometry is a 200mm high and 100mm wide rectangle (see figure 7.1). The bottom and right boundaries are adiabatic, no-slip walls. The left boundary is the symmetry axis. The symmetry axis is characterized by the normal components and gradients of all variables being set to zero, and zero fluxes across the axis. The top boundary is a no-slip wall with a variable-temperature boundary condition.

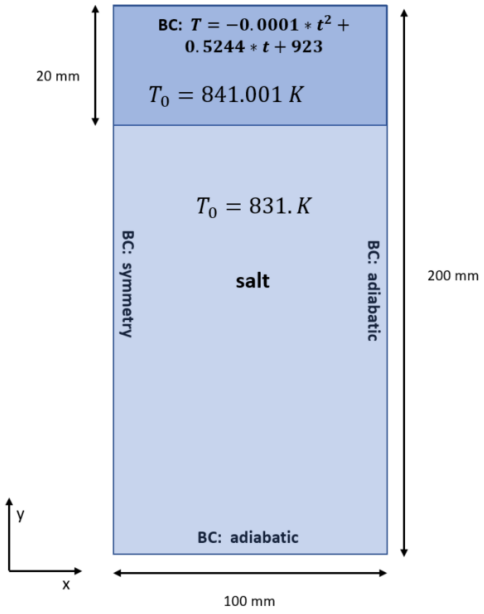

Figure 7.1: Geometry with boundary (marked as "BC") and initial conditions (marked as T_0) of stage 1. The dark blue color indicates the molten salt, and the light blue color indicates the solid salt.

The decay heat of the MSFR expressed as power P is characterized by the following formula derived by *Tano Retamales et al.* [229]:

$$P(t) = 6.45908 \cdot 10^6 - 6.92 \cdot 10^5 \cdot \ln(t) \qquad (\mathrm{W m^{-3}}), \tag{7.10}$$

with t measured in seconds. From the decay heat, *Tiberga et al.* [29] derived an equation for the average temperature of the shut-down reactor:

$$T(t) = -0.0001\,t^2 + 0.5244\,t + 923 \qquad (\mathrm{K}), \tag{7.11}$$

which is used as the time-dependent boundary condition at the upper wall that controls the melting process. The bottom 90% of the freeze valve geometry is initially at 831 K

(frozen salt), i.e. there is 10 K of subcooling, and the top 10% is just above the melting point, at 841.001 K.

Since the essence of the benchmark is the phase change modelling and associated fluid flow and conjugate heat transfer, we use the same constant density for the solid and for the liquid phase. The thermophysical properties of the salt, taken from *Tiberga et al.* [29], are listed in table 6.3.

The computational grid is uniform and made up from 200 × 100 squares. The time step is 0.5s. Aset of different time steps and mesh refinements were investigated in a sensitivity analysis. The time steps analyzed on the 200 × 100 mesh were the following: 2.0, 1.0, 0.5, and 0.1s. The mesh refinements with the 0.5s time step were: 50 × 25, 100 × 50, 200 × 100, and 400 × 200. Stage 1 is in principle a one-dimensional heat conduction problem. Temperatures and the melting front at the centerline after 2500s obtained by the three codes are directly compared.

Implementation

In both OpenFOAM and STAR-CCM+, the diffusion terms were discretized using a central differencing scheme and a second order upwind scheme was used for the convection terms. Therefore, both the velocity and the temperature are second order accurate in space. In DGFlows, linear elements were used for the temperature, enthalpy, and pressure, and quadratic elements were used for the velocity (recall the use of a mixed order formulation), leading to a second order accurate discretization of the temperature, enthalpy, and pressure, and a third order accurate discretization of the velocity. In all three codes, a second order implicit time-stepping scheme was used (i.e. BDF2).

In STAR-CCM+, in stages 1–3, a maximum number of 30 inner iterations were used as a stopping criterion for the implicit unsteady solver. The segregated flow solver was frozen at the beginning of the simulation, which in STAR-CCM+ jargon means that no momentum equations were solved and the velocities were zero for stages 1–3. For both OpenFOAM and DGFlows, non-linear enthalpy-temperature coupling iterations were performed until the desired error tolerance of $tol < 10^{-6}$ was reached. No option was available to avoid solving the momentum equation, however the specified boundary and initial conditions and omission of the Boussinesq source term correctly led to zero velocities throughout the domain.

Results

After the simulated time reached 2500 s, the temperature distribution (figure 7.2) and melting front position (table 7.1) were derived. The three codes yielded very similar results. The melting front positions differed by less than 1 mm, which implies that the methods used for calculating one-dimensional heat conduction and resulting phase change are equivalent.

Table 7.1: Final melting front position in stages 1 and 2 of the benchmark (in mm) obtained by the three codes.

Code	DGFlows	STAR-CCM+	OpenFOAM
Stage 1	147.312	147.426	147.048
Stage 2	146.393	146.180	146.000

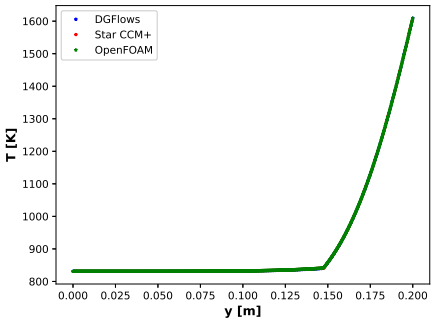

Figure 7.2: Temperature vs. y-coordinates for the three codes obtained in stage 1 of the benchmark.

Results of the sensitivity analysis

Figure 7.3 shows the temperature and table 7.2 compares the position of the melting front at the symmetry axis at the end of the simulation for all time step sensitivity analysis cases. In the same fashion, results of the mesh sensitivity analysis are shown in figure 7.4 (temperature) and table 7.3 (melting front).

Table 7.2: Time sensitivity analysis on the solid-liquid interface position for the three codes obtained in stage 1, with the position given in mm.

Δt (s)	STAR-CCM+	OpenFOAM	DGFlows
2.0	147.415	147.048	147.312
1.0	147.423	147.048	147.312
0.5	147.426	147.048	147.312
0.1	147.428	147.048	147.312

Table 7.3: Mesh sensitivity analysis on the solid-liquid interface position for the three codes obtained in stage 1, with the position given in mm.

mesh size	STAR-CCM+	OpenFOAM	DGFlows
50×25	147.536	144.271	146.771
100×50	147.484	146.109	147.370
200×100	147.426	147.048	147.312
400×200	147.425	147.031	147.335

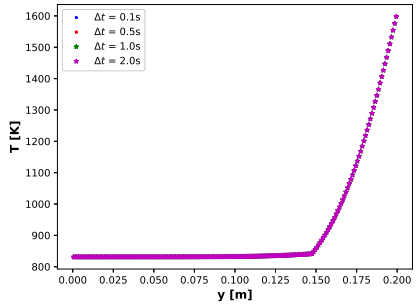

(a) STAR-CCM+

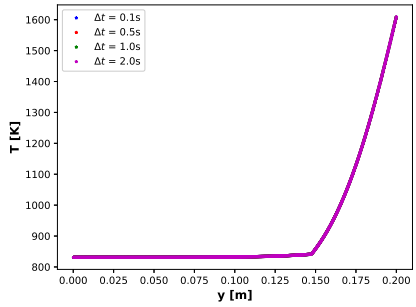

(b) OpenFOAM

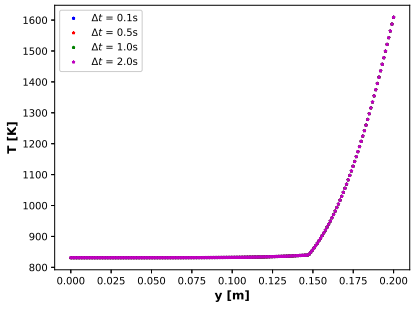

(c) DGFlows

Figure 7.3: Temperature vs. y-coordinates for the three codes obtained in the time step sensitivity analysis of stage 1.

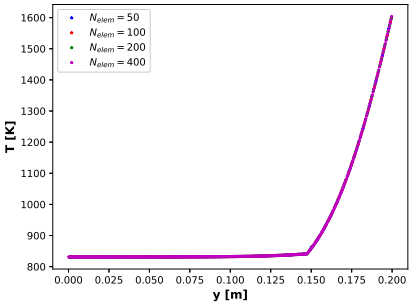

(a) STAR-CCM+

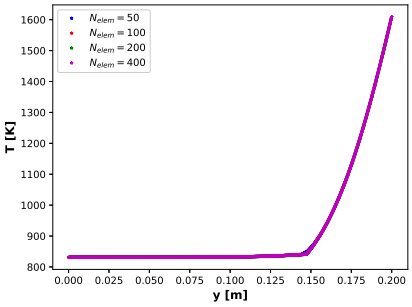

(b) OpenFOAM

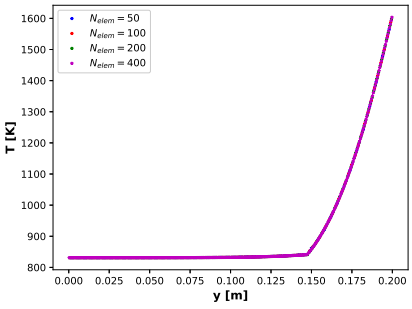

(c) DGFlows

Figure 7.4: Temperature vs. y-coordinates for the three codes obtained in the mesh refinement sensitivity analysis of stage 1.

The time step sensitivity analysis suggests that for stage 1, i.e. with no natural circulation, the model is time-step independent for the 200 × 100 mesh. STAR-CCM+ is the only code with very small changes to the melting front position with an increasing time step, whereas the results obtained by OpenFOAM and DGFlows are exactly the same for each time step studied. The mesh refinement sensitivity analysis suggests that the 200 × 100 mesh yields an accurate result while taking a lower amount of computing time than the more refined case. Surprisingly, even the coarsest mesh of 50 × 25 elements produced good results, whereas Stefan problems are known to be sensitive to the resolution of the mesh [97], [124]. Possibly, this is because the large temperature differences over the entire domain lead to a relatively small contribution of the latent heat peak to the total energy balance.

7.3.2. Stage 2

Description

In a nuclear reactor, radiation is emitted from within the fuel. Energetic neutrons and photons travel within the reactor vessel and heat up the reactor structures. In a molten salt reactor, this heat can also be transferred to the salt that has not undergone fission, such as the solid plug located in the freeze valve. By approximating this heat source to 1% of the decay heat of the reactor, a time-dependent volumetric heat source H_S is added to the energy equation in the entire salt region of our model [229]:

$$H_S(t) = 6.45908 \cdot 10^4 - 6.92 \cdot 10^3 \cdot \ln(t) \qquad (\mathrm{W\,m^{-3}}). \tag{7.12}$$

Results

After the simulated time of 2500 s, the temperature distribution (figure 7.5) and melting front position (table 7.1) were derived. As in stage 1, the three codes yielded similar results. The temperatures are slightly higher than in stage 1 due to the additional heat source, and the melting front shifted by approximately 1 mm towards the bottom.

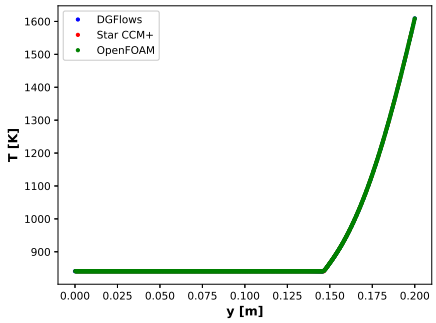

Figure 7.5: Temperature vs. y-coordinates for the three codes obtained in stage 2 of the benchmark.

7.3.3. Stage 3

Description

As the next step approaching the design of the MSFR freeze valve, a 10 mm thick pipe wall, meshed in the same way as the salt volume, is added to the right side of the model (see figure 7.6). The pipe is made of Hastelloy N with properties taken from *Tiberga et al.* [29] and listed in table 6.3.

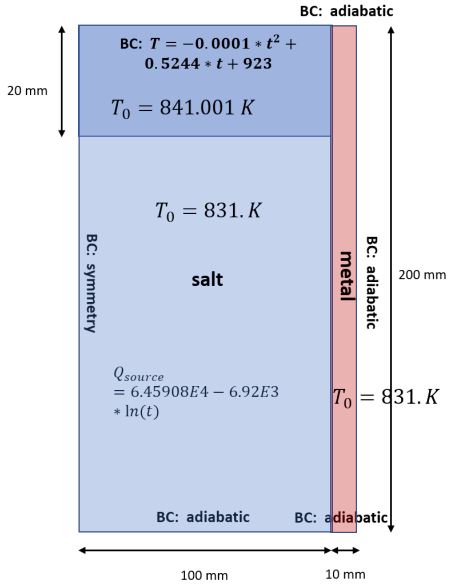

Figure 7.6: Geometry with boundary (marked as "BC") and initial conditions (marked as T_0) of stage 3. The dark blue color indicates the molten salt, the light blue color indicates the solid salt, and the pink color represents the metal wall.

Conjugate heat transfer relations are applied on the interface between the salt and the metallic wall. All other boundaries of the pipe wall are adiabatic, including the top boundary. The initial wall temperature is 831 K. In stage 3, gravity is discarded to analyze how heat conduction from the wall in itself affects the melting process.

Since significant complexity is added to the third benchmark stage, an additional mesh and time step convergence study was performed. The mesh refinements with the 0.5s time step were: 100 × 55, 200 × 110, 400 × 220, and 800 × 440. Based on the results of the mesh refinement, the 800 × 440 mesh was selected for the final result. Therefore, compared to the mesh-converged solution of stages 1 and 2, the meshing in the third stage is refined by a factor of four. The time steps analyzed for the 800 × 440 mesh were 0.5s and 0.1s. Very little change was observed, suggesting that at these conditions our models are fully converged with respect to the time step.

Implementation

In STAR-CCM+, the wall is a separate solid region with its own properties. A contact interface was created between the wall and the salt and a conjugate heat transfer relation was added (see chapter 6).

In OpenFOAM, the mesh was decomposed into a solid part (for the Hastelloy) and a liquid part (for both the molten and the frozen salt), each with their own set of thermophysical properties and their own set of initial and boundary conditions. The temperature at the metal-salt interface was calculated based on a harmonic averaging of the heat fluxes (see section 7.2.2).

In DGFlows, a material tag was added to the solid and the liquid region, where for each tag a set of thermophysical properties wasassigned. At the metal-salt interface, the no-slip condition was imposed, however no explicit treatment was needed for the energy equation as the temperature continuity condition at the interface follows naturally from the penalty terms included in the SIP-DG formulation (see chapter 5).

Results

Figure 7.7 shows the temperature obtained in the third stage with the OpenFOAM model. Whereas the models for stages 1 and 2 yielded quasi one-dimensional results, this was no longer the case for stage 3, since the addition of the metal wall produced a variation of the temperature in the x-direction. Because all boundaries of the metal wall were adiabatic (see figure 7.6), no heat was conducted into the metal wall from the top and therefore the highest temperature values were found within the salt. Due to the better thermal conductive properties of Hastelloy N compared to the salt, below a height of approximately $y = 0.17$ m, higher temperatures and an enhanced melting rate were observed in the vicinity of the wall. The melting fronts for the mesh-converged solution of 800×440 cells obtained by the three codes are plotted in figure 7.8. Whereas a near-perfect agreement between the three codes was observed for the previous two stages, a discrepancy could now be seen between the melt front positions of DGFlows on the one hand, and OpenFOAM and STAR-CCM+ on the other. The discrepancy was largest in the region close to the Hastelloy wall.

To further shed light on this matter, three locations of interest were chosen, for which results were probed along a vertical line, at: $x = 0$mm, $x = 75$mm, and $x = 95$mm. Temperature profiles for all three probes at $t = 2500$s are plotted in figure 7.9. From the temperature probes, one can observe that far away from the Hastelloy wall, at $x = 0$, the agreement between the three codes is excellent, however as one moves closer to the wall, DGFlows produces different results from the other codes.

The results for benchmark stage 3 show that the conjugate heat transfer between the solid wall and the melting salt appears to introduce a discrepancy in the modelling behaviour of the three codes. A separate validation was performed for the conjugate heat transfer without phase change with the use of a different model, where virtually identical results were observed between DGFlows and STAR-CCM+. Based on these observations, we believe the coupling between the conjugate heat transfer and the non-linear phase change phenomena are the source of disagreement between DGFlows on the one hand, and STAR-CCM+ and OpenFOAM on the other.

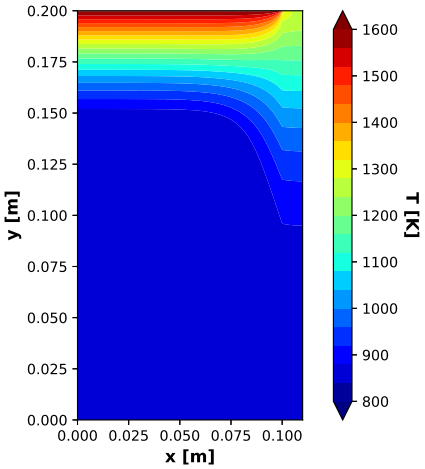

Figure 7.7: Temperature contour plot for the entire geometry of stage 3; results taken from OpenFOAM. The 800 × 440 mesh was used with a time step of $\Delta t = 0.5$ s.

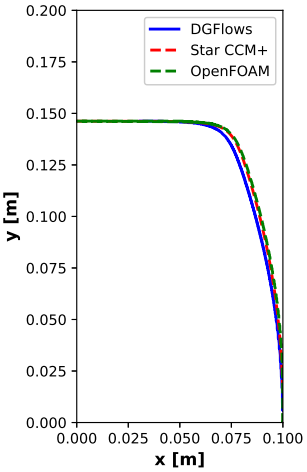

Figure 7.8: Melting front positions obtained by the three codes in stage 3. The 800 × 440 mesh was used with a time step of $\Delta t = 0.5$ s.

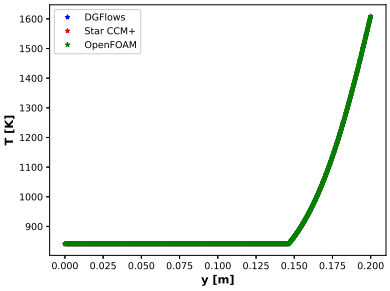

(a) $x = 0$ mm

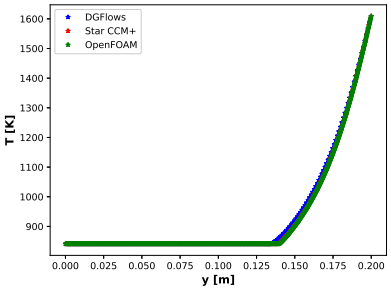

(b) $x = 75$ mm

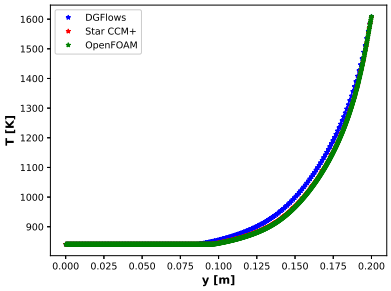

(c) $x = 90$ mm

Figure 7.9: Temperature vs. y-coordinates for the three codes obtained in stage 3 of the benchmark. Results taken at three different x locations.

Note that the three codes adopt different modelling strategies for the conjugate heat transfer. OpenFOAM solves the heat equation in the salt and metal domains sequentially (i.e. first the heat equation in the salt is solved, then the heat equation in the metal), whereas in DGFlows the heat equation is solved for the full domain and no distinction is made between the solid and the liquid regions. In STAR-CCM+, a segregated solver was used, which is a method similar to the one used by OpenFOAM.

It is possible that the simultaneous solution of the heat transport equation leads to a faster melting in the vicinity of the Hastelloy wall with respect to a sequential solution of the heat transport equations, since the salt immediately experiences the presence of the enhanced heat transfer through the metal wall, instead of the solution of the heat transfer through the metal wall lagging behind that of the salt. However, the discrepancy between the codes was expected to decrease for smaller time steps, which was not the case, see section 7.3.3. Due to a lack of a suitable analytical or experimental reference solution, it is uncertain which of the three codes produces the most correct results. For now, the coupling of the conjugate heat transfer and solid-liquid phase change modelling is identified as a potential source of discrepancy between numerical software and we recommend to take this matter into consideration when modelling the MSFR freeze valve.

Results of the Sensitivity Analysis

Figure 7.10 shows the results of the mesh refinement sensitivity study. With every refinement step, the difference between the results from the previous coarser mesh and the new finer mesh becomes smaller. STAR-CCM+ showed the largest sensitivity to the mesh size, whereas DGFlows' results did not vary significantly between the different mesh refinement cases. Possibly, this is due to the high accuracy of the discontinuous Galerkin method in calculating the discontinuity in the temperature gradient at the interface between the solid and the liquid salt, thus preserving the overall accuracy of the numerical scheme at the metal wall. It was decided that the 800×440 mesh should be used for this and next benchmark stages. Figure 7.11 shows the sensitivity of the temperature results to the time step. For all three codes, very little difference could be observed between a time step of $\Delta t = 0.5$s and $\Delta t = 0.1$s, and therefore $\Delta t = 0.5$s was used for the rest of the analysis of stage 3.

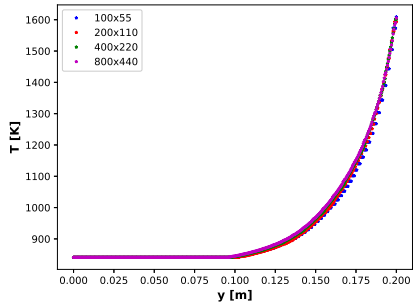

(a) STAR-CCM+

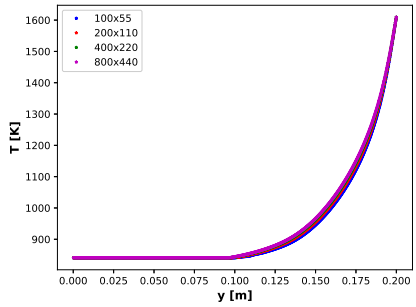

(b) OpenFOAM

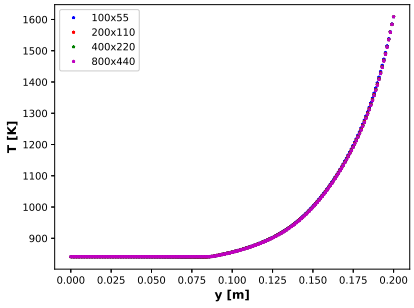

(c) DGFlows

Figure 7.10: Temperature vs. y-coordinates for the three codes obtained in the mesh refinement sensitivity analysis of stage 3. Results shown for $x = 90$ mm. Here, a time step of $\Delta t = 0.5$ s was used.

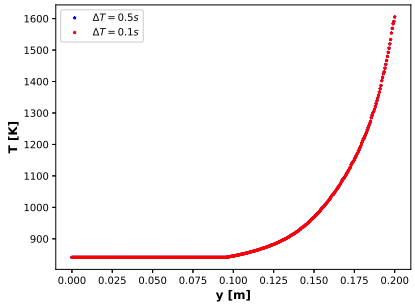

(a) STAR-CCM+

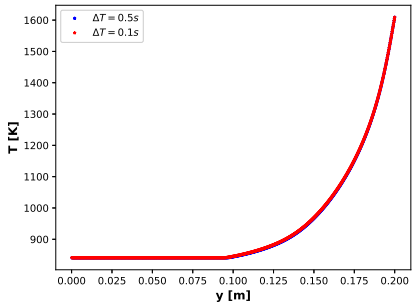

(b) OpenFOAM

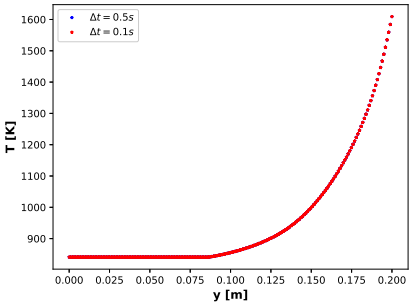

(c) DGFlows

Figure 7.11: Temperature vs. y-coordinates for the three codes obtained in the time step sensitivity analysis of stage 3. Results shown for $x = 90$ mm. Here, a mesh of 800×440 elements was used.

7.3.4. Stage 4

Description

In stage 4, the effects of natural circulation are included. Salt closest to the heated wall will have a lower density and will start flowing upwards. To model the free convection of the salt, the *Boussinesq* approximation is used and a fully laminar and incompressible flow is assumed.

Implementation

The time step was lowered to 0.1 s for stages 4 and 5 to account for the increased convergence requirements (i.e. Courant number below 1) when changing the model from conduction only to convective phase change. In STAR-CCM+, in stages 4 and 5, the maximum number of inner iterations was changed from 30 to 90 to achieve better convergence. In both OpenFOAM and DGFlows, three outer iterations were added to better resolve the velocity-temperature coupling. Computational requirements increased significantly from stage 3 to stage 4, as a set of new equations is added to the model in addition to reducing the time step and increasing the number of iterations.

Results

Figure 7.12 shows the absolute flow velocity for the fourth benchmark stage, also showing the streamlines. A maximum velocity of around $u = 4\,\mathrm{mm\,s^{-1}}$ is reached, corresponding to a Reynolds number of $Re \approx 468$. Therefore, the assumption of laminar flow was justified. Two recirculation zones were observed, one near the top of the domain where the salt is being heated and one near the melting front, with the salt flowing up along the warmer Hastelloy wall and down along the melting front.

Figure 7.13 shows a comparison of the melting front positions for all three codes. The addition of natural convection, as opposed to heat conduction dominated phase change, results in an increase of the melting rate and compared to stage 3, more of the salt has melted. However, similarly to what has been observed by *Aji et al.* [63], the presence of natural convection slows down the melting of the freeze plug at the sides, thus prolonging its opening time. Instead, the heat transfer is shifted towards the top side of the plug.

In addition, a significantly better agreement was observed between the three codes, possibly because the higher heat transfer within the bulk of the salt, induced by the natural convection, reduces the local effect the solid wall has on the overall melting rate. The better agreement in stage 4, as opposed to stage 3, further supports the hypothesis that the coupling of the heat transfer within the salt and the metal domains was the source of discrepancy between STAR-CCM+, OpenFOAM, and DGFlows.

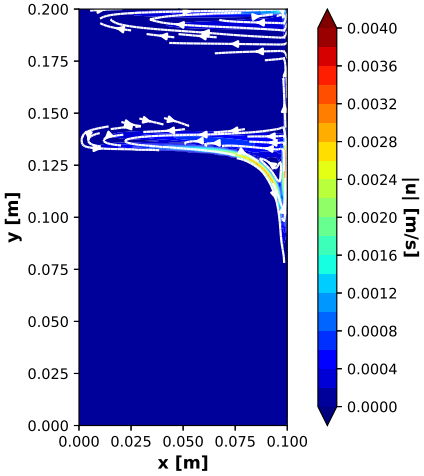

Figure 7.12: Contour plot of the flow field with streamlines for stage 4. Results obtained with OpenFOAM, with a 800 × 440 mesh and a time step of $\Delta t = 0.1$ s. A cut-off velocity of $4 \cdot 10^{-5}\,\mathrm{m\,s^{-1}}$ (i.e. approximately 1% of the maximum velocity) was used for the streamlines.

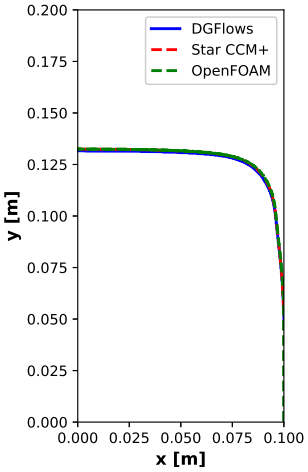

Figure 7.13: Melting front positions obtained by the three codes in stage 4. The 800 × 440 mesh was used with a time step of $\Delta t = 0.1$ s.

Figure 7.14 depicts the absolute velocity profiles for all three codes, evaluated at the same x-locations selected for stage 3 (i.e. $x = 0$ mm, $x = 75$ mm, and $x = 90$ mm). Figure 7.15 shows the temperature profiles at these locations. Similar results were obtained for the absolute velocity profiles for all three codes, although small differences are still visible. Interestingly, for $y = 90$ mm, the velocity results for OpenFOAM appear to deviate from those obtained by STAR-CCM+ and DGFlows; the code predicts a lower peak value of the velocity around $y = 0.12$m. Regarding the temperature profiles, an excellent agreement between the three codes was obtained, with the results hardly distinguishable from each other.

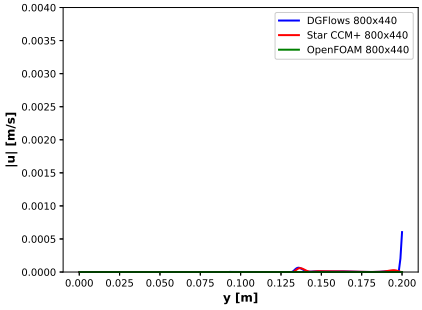

(a) $x = 0$ mm

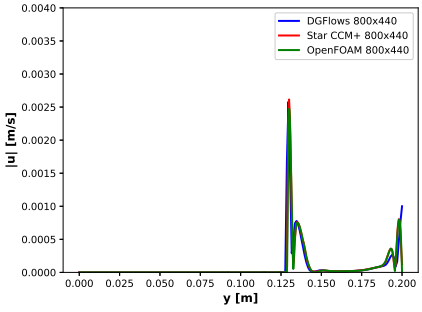

(b) $x = 75$ mm

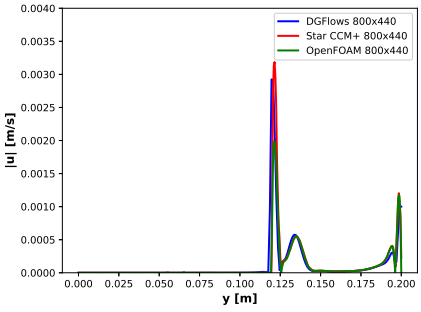

(c) $x = 90$ mm

Figure 7.14: Absolute velocity profiles obtained by the three codes in stage 4. Results taken at three different x locations.

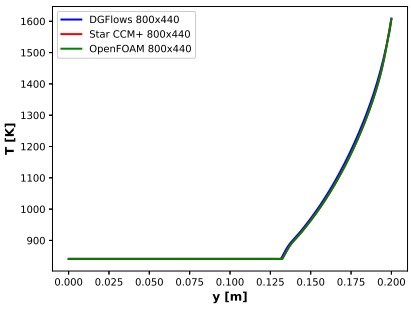

(a) $x = 0$ mm

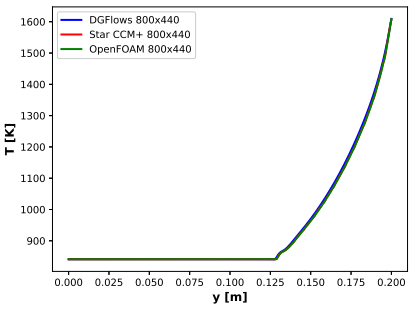

(b) $x = 75$ mm

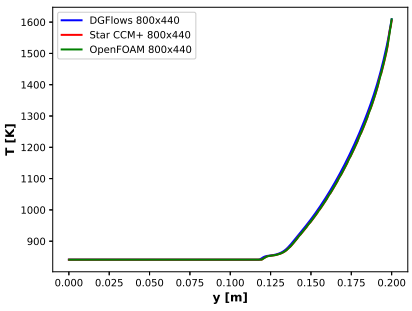

(c) $x = 90$ mm

Figure 7.15: Temperature vs. y-coordinates for the three codes obtained in stage 4. Results taken at three different x locations.

7.3.5. Stage 5

Description

In a molten salt reactor, the fuel salt above the top of the freeze valve is not stagnant but in motion, both during normal operation and emergency drainage of the fuel salt into the dump tanks. The movement of the salt at the freeze valve's top boundary could influence the dynamics of the phase change. In our model, circulation is enforced by moving the top lid in the positive x direction with a tangential velocity of 0.01 $\mathrm{m\,s^{-1}}$. This value was sufficiently high to influence the melting behaviour of the freeze valve, but sufficiently low such that our assumption of laminar flow is still valid.

Results

Figure 7.16 shows the absolute velocity and figure 7.17 shows the melting front positions for stage 5. Compared to stage 4, higher velocities were observed in the recirculation zone near the top of the domain, as a consequence of the velocity boundary condition now imposed at the top wall. However, this boundary condition does not seem to significantly impact the flow in the rest of the domain. Whilst the differences between the fourth and the fifth benchmark stage are small, the higher degree of mixing at the top leads to a small increase of the melting rate, as was seen from the overall position of the melting front. Similarly to stage 4, a very good agreement was observed between the three codes.

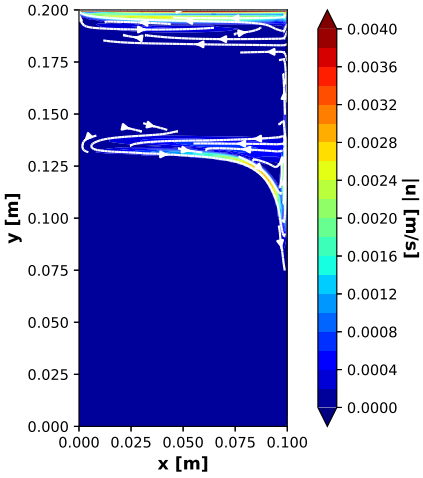

Figure 7.16: Contour plot of the flow field with streamlines for stage 5. Results obtained with OpenFOAM, with a 800 × 400 mesh and a time step of $\Delta t = 0.01$s. A cut-off velocity of $4 \cdot 10^{-5}\,\mathrm{m\,s^{-1}}$ was used for the streamlines.

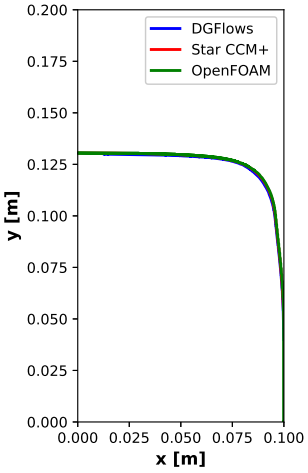

Figure 7.17: Melting front positions obtained by the three codes in stage 5. The 800 × 440 mesh was used with a time step of $\Delta t = 0.01$ s.

Finally, one can now have a look at the development of the melting front from the simpler to the more detailed model, depicted in figure 7.18. The changes in the shape of the melting front between stages 2 and 3, and 3 and 4 are substantial and show the importance of conjugate heat transfer and natural convection. An important figure of merit in the MSFR freeze valve design is the opening time, which is one of the factors that determine whether the proposed design meets the safety requirements. Omitting the Hastelloy wall from the simulations would result in a considerable over-prediction of the freeze valve opening time. On the other hand, neglecting the role of natural convection would lead to an under-prediction of the valve opening time.

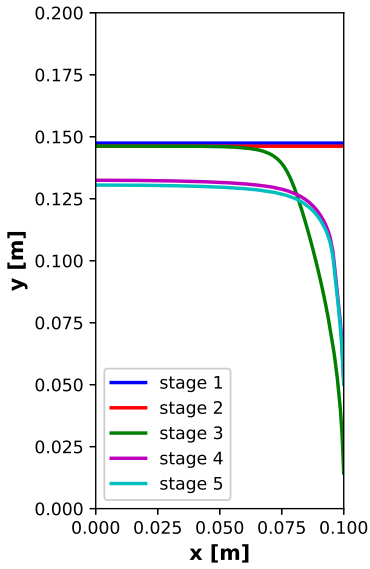

Figure 7.18: Melting front positions obtained in all stages of the benchmark by STAR-CCM+.

7.4. Conclusions

Due to the lack of suitable experimental benchmark data, experimental validation of MSFR freeze valve models is very difficult. In order to help overcome this challenge, this work proposes a numerical benchmark for the MSFR freeze valve consisting of five different stages. A principal feature of this benchmark is a step-wise addition of complexity with every stage of the benchmark. This allows for pinpointing which parts of the model introduce discrepancies between different software suites. Additionally, this benchmark can easily be replicated in other CFD codes. In the present work, results of the benchmark were obtained using solid-liquid phase change models and flow and conjugate heat transfer solvers implemented in STAR-CCM+, OpenFOAM and DGFlows. For all three codes, the melting front position, temperature profiles, and absolute velocity profiles were compared. The results from the benchmark demonstrate a consistent performance of the three codes' phase change models and flow solvers. However, a discrepancy between the results of DGFlows on the one hand, and STAR-CCM+ and OpenFOAM on the other, was observed when adding conjugate heat transfer to the benchmark. This may indicate a different performance of segregated conjugate heat transfer approaches as opposed to fully coupled ones for modelling solid-liquid phase change. For this reason, we recommend carefully considering the conjugate heat transfer modelling approach when simulating the MSFR freeze valve or any other problem where a coupling between conjugate heat transfer and solid-liquid phase change phenomena plays a role. The results from all three codes have been placed in an online repository, and interested users of CFD codes are invited to carry out the benchmark exercise and compare their results and findings with ours, which can help further develop numerical tools dedicated to phase change and molten salt reactors.

Data Availability

Data presented in the figures, to be used for comparison with more codes, can be found under the associated link: https://doi.org/10.5281/zenodo.7821693.

8

CONCLUSIONS AND RECOMMENDATIONS

This thesis presents a combined experimental and numerical investigation of melting and solidification phenomena in a Molten Salt Fast Reactor (MSFR), one of the most promising generation IV nuclear reactor concepts. Melting and solidification plays a role during both the normal and transient operation of the reactor. In line with the goals of the SAMOSAFER project (i.e. developing and demonstrating the safety barriers of the MSFR), we mainly focus on the latter. Two accident scenarios where melting and freezing play a role are the possible freezing inside the heat exchanger and the melting of the freeze plug during an emergency draining of the reactor core. To prevent the salt from heating up to a degree at which structural damage may occur, the freeze plug needs to melt within approximately 480 s [56]. Therefore, an accurate numerical modelling of melting and solidification is important for the design and safety of the MSFR. However, despite decades of research, melting and solidification problems are still challenging to solve numerically due to the underlying mathematical complexity of tracking the evolving solid-liquid interface and resolving the sharp gradients in the enthalpy and the thermophysical properties within the phase change region. Therefore, numerical solvers need to be validated with high quality experimental data. This chapter highlights the most important outcomes of this dissertation, in addition to providing some recommendations for future research.

8.1. Outcomes of this dissertation

This thesis consists of both an experimental and a numerical part. The experimental investigations were primarily motivated by the lack of experimental data for the transient development of an ice layer in forced internal flow. Before starting this thesis, only one experimental study had been published concerning the transient solidification of water flowing over a chilled flat plate [94]. A second experimental study was published whilst in the process of constructing the ESPRESSO experimental facility [52]. In addition, the majority of the numerical articles still compare their results to the classic melting experiment performed by *Gau et al.* [67] in 1986, in which the results may have been affected by the use of intrusive measurement techniques and the use of insufficient thermal insulation. The numerical work performed aims to address the need for more efficient melting and solidification models, which can capture the solid-liquid interface and resolve the recirculation zones in the fluid region with the desired accuracy at a more affordable computational cost. The most important outcomes of this thesis can be summarized as follows:

- A new experimental facility (ESPRESSO) was designed and built for conducting solid-liquid phase change experiments in forced internal flow (chapter 2). The study of the transient development of an ice-layer in forced internal flow is of particular interest for the safety analysis of the MSFR, since it relates to the possible freezing inside the heat exchanger following a ULOF or fuel salt overcooling accident. The ESPRESSO facility consists of a water tunnel capable of reaching both laminar and turbulent flow rates. Ice is grown from a cold plate at the bottom of the square channel test section. Water was selected as the phase change material, because it is liquid at room temperature (meaning no additional heating of the setup is required to prevent the phase change material from solidifying), it has well known thermophysical properties, its melting point of 0 °C is sufficiently close to room temperature and it has a similar Pr as the fuel salt at lower temperatures. The ESPRESSO facility is distinguished from other solid-liquid phase change experimental setups by its well-described experimental boundary conditions, obtained through a careful design of the flow inlet (settling chamber and converging nozzle) and the cold plate. Full optical access from the top and the side enables non-intrusive optical measurements of the development of the ice-layer, the velocity fields and the temperature fields at each downstream location in the channel.

- PIV measurements were performed for the transient development of an ice layer in laminar channel flow (chapter 3), for both the inlet and the center of the channel. The measurements at the inlet are an important novelty of the present experimental campaign, since so far ice measurements at the inlet were only performed under steady state conditions [82], [83], with transient measurements only being performed at the center of the channel where the heat transfer is (close to) one-dimensional [52], [94]. In addition, an approximation to the experimental cold plate boundary condition was obtained from the recordings of 8 equally spaced thermocouples, which can be used as input for numerical models. As such, a comprehensive and well-described experimental data set was generated for transient freezing in laminar internal flow to be used for numerical validation purposes.

- Non-intrusive temperature measurements were performed for the transient development of an ice layer in laminar channel flow using LIF (chapter 4). Few non-intrusive temperature measurements have been performed for solid-liquid phase change experiments, and LIF has only been used once before in a solid-liquid phase change experiment to measure the temperature evolution during the melting of n-octadecane in a cuboid cavity by *Gong et al.* [133]. Compared to the work performed by *Gong et al.*, the present work featured several improvements to the experimental method. These were the use of a two color (instead of a one color) LIF technique to compensate for a possible change in dye concentration and optics during ice growth, the use of a post-processing algorithm to remove striations and other artefacts, and a detailed analysis of the uncertainty in the measured temperature fields. With this approach an absolute temperature uncertainty of between $\sigma = 0.3\,^{\circ}\mathrm{C}$ and $\sigma = 0.5\,^{\circ}\mathrm{C}$ was obtained, which is comparable to related LIF temperature measurement campaigns. Good results could be obtained for a sufficiently large temperature range of approximately 15 °C, however the scattering of the laser light from the ice layer introduced some artefacts, especially near the inlet of the channel where the ice-water interface is curved instead of flat.

- The onset of ice formation was found to coincide with a sudden increase of the cold plate temperature, which was therefore used to identify the zero time instant in our experiments (chapters 3 and 4). This was attributed to subcooling occurring in the thermal boundary layer prior to nucleation. Approximately 2 °C of subcooling was measured experimentally a short time before ice formation occurred by *Savino et al.* [94] using a thermocouple probe, as well as in the non-intrusive LIF temperature measurements performed in chapter 4. The sequence of the thermocouple recordings (with T0 at the inlet being the first to note a sudden temperature increase and T7 at the exit the last) showed that ice nucleation started at the inlet of the channel, with the ice crystals rapidly spreading over the cold plate surface towards the exit of the channel.

- An energy-conservative DG-FEM approach for solid-liquid phase change was developed and validated, based on the 'linearized enthalpy approach' (chapter 5). The discontinuous Galerkin method was selected for its combination of attractive features from both the finite volume and the finite element methods, these are local conservation, the possibility for upwinding, an arbitrarily high order of accuracy, high parallelization efficiency, and high geometric effiency. A good agreement was obtained for all four reference cases, these were the 1D Stefan problem, the melting of octadecane in a square cavity, the melting of gallium in a rectangular cavity and the freezing of water in a laminar 2D channel flow (using the experimental data from chapter 3 for validation). Apart from providing additional validation of the developed DG-FEM solver, the good agreement obtained between the numerical simulation and the experimental results from chapter 3 also illustrated the suitability of the generated experimental data for the transient development of an ice-layer in a laminar square channel flow for numerical validation purposes.

- An overall O(h) convergence rate was obtained using the energy-conservative DG-FEM approach for solid-liquid phase change (chapter 5). The sub-optimal mesh convergence rate was a consequence of the poor resolution of the discontinuous enthalpy and non-smooth temperature solutions at the solid-liquid interface when using a continuous polynomial solution space within the elements. However, as the results from the melting of gallium in a rectangular case (characterized by the presence of multicellular flow patterns) show, solid-liquid phase change problems with strong gradients in the flowfield can benefit from the use of a higher order DG-FEM method.

- A parallel finite volume adaptive mesh refinement method for solid-liquid phase change was developed in OpenFOAM (chapter 6). To maintain a high parallelization efficiency, changes to the mesh were followed by a dynamic load balancing step. Three different refinement criteria were constructed for the solid-liquid interface, the flow-field and the temperature field respectively. For the solid-liquid interface, the cells undergoing phase change were flagged based on the maximum jump in the liquid fraction over the cell faces, and refined up to the maximum refinement level. For the flow-field and the temperature field, an error indicator was used based on the cell residual method from *Jasak et al.* [134]. The adaptive mesh refinement strategy was tested for three reference cases, these were the 2D melting of gallium in a rectangular cavity, the 3D melting of gallium in a cuboid cavity, and the melting of the MSFR freeze-plug. A very good agreement was obtained between the adaptive mesh results and the reference solutions on a uniformly fine grid with significantly less degrees of freedom. In addition, an overall higher accuracy was obtained when using the adaptive mesh compared to uniform meshes with a similar number of mesh elements. This demonstrates the potential of the proposed finite volume adaptive mesh refinement approach as a more computationally efficient numerical method for solid-liquid phase change problems.

- A numerical benchmark was proposed for modelling phase change in molten salt reactors (chapter 7), designed after the MS(F)R freeze valve. The benchmark consists of five stages, with a step wise addition of complexity to allow for identifying potential sources of discrepancy between different numerical codes. Results were obtained using three different approaches for modelling solid-liquid phase change: the volume of fluid method implemented in the commercial finite volume multiphysics modelling software STAR-CCM+, the linearized enthalpy approach implemented in the open-source finite volume computational fluid dynamics software OpenFOAM and the linearized enthalpy approach implemented in the TU-Delft in-house discontinuous Galerkin computational fluid dynamics code DGFlows. Overall, a good agreement was obtained between the three codes for all five stages. However, a discrepancy was observed between the results of DGFlows on the one hand and STAR-CCM+ and OpenFOAM on the other hand when adding conjugate heat transfer to the benchmark. The discrepancy mainly manifested itself in the vicinity of the metal wall, and was possibly due to a different performance of the segregated conjugate heat transfer modelling approach adopted by STAR-CCM+ and OpenFOAM as opposed to the fully coupled approach adopted by DGFlows. For this reason, we recommend some caution when simulating a problem involving both conjugate heat transfer and solid-liquid phase change modelling, such as the MS(F)R freeze valve.

8.2. Recommendations for future research

The work described in this thesis addresses the need for high quality experimental data for the transient development of an ice-layer in laminar internal flow, as well as the need for more computationally efficient numerical models for solid-liquid phase change. However, solid-liquid phase change is a vast area of research, and a lot of work still remains to be done. In the remainder of this chapter, we provide some starting points for follow-up investigations.

8.2.1. Continued experimental investigations

In this work, experimental data was generated for the transient development of an ice-layer in a laminar square channel flow cooled from below, using planar particle image velocimetry and laser induced fluorescence for measuring the flow field and the temperature field respectively. Whilst this work demonstrates the potential of LIF as a non-intrusive temperature measurement technique, further improvements are needed in order to use LIF for generating high fidelity experimental data for numerical validation purposes especially for small temperature ranges of less than 15 °C. These improvements could consist of ensuring a very clean entry surface for the laser sheet (with less air bubbles, dirt particles or surface roughness), using a camera with a larger dynamic range and removing the artefacts in the vicinity of the solid-liquid interface through additional post-processing routines. In addition, upgrading the current PIV setup from a planar to a stereoscopic configuration would allow us to measure the velocities in the spanwise (z) direction, hereby gaining insight into the possible generation of secondary flow during the transient development of the ice-layer. By simultaneously measuring the velocity

and the temperature fields, the heat fluxes can be determined. This could be of particular interest during the subcooling phase prior to the onset of ice-formation, where the subcooling possibly leads to enhanced natural convection. We therefore believe simultaneous (stereoscopic) PIV and LIF measurements could become the new standard in solid-liquid phase change experiments.

Moreover, we recommend extending the present experimental campaign to studying the transient development of an ice-layer in a square channel under a turbulent or transitional flow regime. Previous investigations showed that the solid-liquid interface can become unstable in a turbulent flow regime [85], [86], with different forms of ice formation (such as a smooth transient ice-layer, a step-transition ice-layer, and a wavy ice-layer) for certain combinations of the cooling parameter and the Reynolds number [88], [89]. The dominant factor controlling the stability of the ice-water interface is believed to be the heat flux from the flow above the interface into the ice [86], with the turbulent intensity abruptly increasing at the locations where the ice-transition (smooth or step) was observed [90]. Recently, the wavelength of the ice-layer instability was hypthesized to correlate with the length of the shear production zone of turbulent kinetic energy within the trough behind a wave in the ice-layer, based on planar PIV measurements [96]. The exact interplay between the production of turbulent kinetic energy, the turbulent heat fluxes, and the development of ice layer instabilities is thus still an active topic of investigation and future experimental investigations using PIV (possibly combined with LIF to measure the turbulent heat fluxes) could contribute to a better physical understanding hereof. In addition, few numerical methods have been developed so far which couple solid-liquid phase change and turbulence modelling and experimental validation of these methods is lacking. The proposed follow-up investigation for ice growth in turbulent internal flow can therefore serve as a basis for numerical validation of models involving both solid-liquid phase change and turbulence.

8.2.2. Improving and extending the proposed numerical methods

As part of this thesis, two new numerical solvers were developed for solid-liquid phase change problems. These were an energy-conservative DG-FEM approach and a finite volume parallel adaptive meshing method, both based on the 'linearized enthalpy approach'. Very similar results were obtained with the finite volume parallel adaptive meshing method as the reference solution on a uniform grid with significantly less degrees of freedom. However, even further reduction in computational cost could be achieved when using an anisotropic adaptive mesh refinement strategy (as opposed to the current isotropic refinement approach). This would require the implementation of a new binary refinement tree and a mesh cutter that splits the cells in one-direction only, as well as the development of directional refinement criteria (for instance using the Hessian matrices for metric-based refinement) [207], [230].

Although some solid-liquid phase change problems can benefit from the use of a higher order DG-FEM method due to a more accurate solution of the recirculation zones in the fluid region and other parts of the domain with strong gradients in the velocity or temperature fields, overall a sub-optimal mesh convergence rate of O(h) was obtained, which is comparable to low order numerical schemes such as those used in the finite volume method. Therefore, further extensions to the proposed DG-FEM solid-liquid phase change solver are needed in order to take full advantage of its arbitrarily high order of accuracy. An obvious improvement would be the coupling of the current DG-FEM approach to an adaptive meshing method. With the discontinuous Galerkin method, hp-refinement can be performed, where the mesh is adaptively refined close to areas of interest such as the solid-liquid interface (h-refinement) and the expansion order is increased in fluid regions with high strain rates or vorticity (p-refinement) [231].

In addition, the current DG-FEM method can benefit from the use of shock-capturing techniques. For instance, it has been shown that the accuracy in smooth parts of the solution domain can be preserved using a hierarchical reconstruction approach to recompute the coefficients of the polynomials inside the troubled cells (for instance those containing a discontinuity) with a MUSCL or WENO limiting procedure [232], [233]. Alternatively, sub-cell resolution of the discontinuity can be obtained by a-posteriori recalculating the solution in the troubled cells using a finite volume scheme on the subgrid level [234], [235] or by an adaptive addition of numerical dissipation to the solution within the troubled cell through a non-linear filter [236]. Another approach is the augmentation of the standard finite element basis function set by a set of enrichment functions that can capture the jump in the gradient (weak discontinuity) and the primal fields (strong discontinuity) [101], [127], [128]. Extended finite element or discontinuity enriched finite element methods have already been applied successfully to phase change problems [101] as well as to problems in solid mechanics featuring strong discontinuities such as bone fracture [128]. However, using an extended or discontinuity enriched finite element basis would constitute a substantial change to the numerical method, as opposed to being a simple extension hereof. On the other hand, a very interesting approach was presented recently where the computational mesh was deformed to align inter-element boundaries with discontinuities in the solution, using an optimization formulation which simultaneously penalized Gibb's phenomena and distorted meshes [237]. Such an approach would be highly applicable to the discontinuous Galerkin method, where inter-element solution discontinuities are naturally supported and the arbitrarily high order of accuracy allows the piecewise smooth solution to be accurately represented by very coarse high-order discretizations.

Finally, apart from the need for developing numerically more accurate solid-liquid phase change models, several other challenges with respect to solid-liquid phase change modelling are currently still being investigated. Some of the most important remaining challenges are briefly introduced below:

- The coupling of solid-liquid phase change and turbulence modelling. The main difficulty here is the correct modelling of the turbulence near the solid-liquid interface. A variety of approaches have been adopted in literature, including the use of modified low-Reynolds RANS turbulence models (for instance by including Darcy source terms in the $k-\epsilon$ equations [238]–[240], the use of a high Reynolds

RANS turbulence model with modified wall functions [241], the use of an LES model [242] or through direct numerical simulation [243], [244]. In particular for low-Reynolds RANS, LES or DNS, maintaining a sufficiently high grid solution near the moving solid-liquid interface is challenging. Possibly, adaptive mesh refinement could be beneficial here. In addition, the modifications made to the low-Reynolds RANS equations or to the high-Reynolds wall-functions are ad-hoc (though to some extent justifiable) and have not been validated experimentally or through a high fidelity DNS simulation. Suitable experimental data for the validation of turbulence closure near an evolving solid-liquid interface is lacking (although a very interesting experimental study was recently performed by *Bushuk et al.* [96]).

- Accounting for the density change during solid-liquid phase change. In most numerical studies, the *Boussinesq* approximation is used to model the natural convection within the liquid phase and the density change accompanying the phase change is neglected. The easiest approach is to neglect the secondary flow induced by the volume expansion and simply scale the latent heat with the solid/liquid density ratio, hereby compensating for the error made in the energy balance when assuming equal solid and liquid densities [218]. However, this approach may not be applicable to all situations, such as close contact melting where a volume expansion upon melting results in a thicker melt gap. For this reason, recently a variable density model was proposed by *Faden et al.* [196].

- Often, solid-liquid phase change is coupled to other physics phenomena, such as neutronics [49] or solid-settling [245]–[247]. In the case of the MSFR freeze-valve, it could be very interesting to couple solid-liquid phase and solid mechanic models in order to predict the possibility of the plug fracturing after partial melting.

- The coupling of microscale and macroscale phase change phenomena. The microstructure of the solid can affect macroscopic properties such as the thermal-conductivity. For instance, *Tano et al.* [48] calculated a highly anisotropic thermal conductivity tensor from the microstructure of solidified FLiNaK predicted with a phase field model. At the moment, most (if not all) studies using a macroscopic phase change model assume a constant, isotropic thermal conductivity within the solid phase.

BIBLIOGRAPHY

[1] "Paris agreement", United Nations, Tech. Rep., 2015.

[2] "Global warming of 1.5 °C", International Panel on Climate Change, Tech. Rep., 2018.

[3] "The European Green Deal", European Commission, Tech. Rep., 2020.

[4] P. M. Forster, C. J. Smith, T. Walsh, *et al.*, "Indicators of global climate change 2022: Annual update of large-scale indicators of the state of the climate system and human influence", *Earth System Science Data*, vol. 15, no. 6, pp. 2295–2327, 2023.

[5] P. Friedlingstein, M. O'sullivan, M. W. Jones, *et al.*, "Global carbon budget 2022", *Earth System Science Data Discussions*, vol. 2022, pp. 1–159, 2022.

[6] "World energy outlook 2022", International Energy Agency, Tech. Rep., 2022.

[7] "Repowereu: Affordable, secure and sustainable energy for europe", European Commission, Tech. Rep., 2022.

[8] "Nuclear power in a clean energy system", International Energy Agency, Tech. Rep., 2019.

[9] B. W. Brook, A. Alonso, D. A. Meneley, J. Misak, T. Blees, and J. B. van Erp, "Why nuclear energy is sustainable and has to be part of the energy mix", *Sustainable Materials and Technologies*, vol. 1, pp. 8–16, 2014.

[10] Generation IV International Forum, "A Technology Roadmap for Generation IV Nuclear Energy Systems", Tech. Rep., 2002, GIF–002–00.

[11] E. Bettis, R. Schroeder, G. Cristy, H. Savage, R. Affel, and L. Hemphill, "The aircraft reactor experiment—design and construction", *Nucl. Sci. Eng*, vol. 2, no. 6, pp. 804–825, 1957.

[12] E. Bettis, W. Cottrell, E. Mann, J. Meem, and G. Whitman, "The aircraft reactor experiment—operation", *Nuclear Science and Engineering*, vol. 2, no. 6, pp. 841–853, 1957.

[13] R. C. Robertson, "Msre design & operations report part 1 description of reactor design", Oak Ridge National Lab.(ORNL), Oak Ridge, TN (United States), Tech. Rep., 1965.

[14] P. N. Haubenreich and J. Engel, "Experience with the molten-salt reactor experiment", *Nuclear Applications and technology*, vol. 8, no. 2, pp. 118–136, 1970.

[15] R. C. Robertson, "Conceptual design study of a single-fluid molten-salt breeder reactor.", comp.; Oak Ridge National Lab.(ORNL), Oak Ridge, TN (United States), Tech. Rep., 1971.

[16] J. Serp, M. Allibert, O. Beneš, *et al.*, "The molten salt reactor (MSR) in generation IV: Overview and perspectives", *Progress in Nuclear Energy*, vol. 77, pp. 308–319, 2014, ISSN: 01491970. DOI: 10.1016/j.pnucene.2014.02.014.

[17] D. Zhang, L. Liu, M. Liu, *et al.*, "Review of conceptual design and fundamental research of molten salt reactors in china", *International Journal of Energy Research*, vol. 42, no. 5, pp. 1834–1848, 2018.

[18] R. Yoshioka, "Nuclear energy based on thorium molten salt", in *Molten Salts Chemistry*, Elsevier, 2013, pp. 471–496.

[19] V. Ignatiev, O. Feynberg, I. Gnidoi, *et al.*, "Molten salt actinide recycler and transforming system without and with th–u support: Fuel cycle flexibility and key material properties", *Annals of Nuclear Energy*, vol. 64, pp. 408–420, 2014.

[20] A. Nuttin, D. Heuer, A. Billebaud, *et al.*, "Potential of thorium molten salt reactorsdetailed calculations and concept evolution with a view to large scale energy production", *Progress in Nuclear Energy*, vol. 46, no. 1, pp. 77–99, 2005, ISSN: 01491970. DOI: 10.1016/j.pnucene.2004.11.001.

[21] L. Mathieu, D. Heuer, R. Brissot, *et al.*, "The thorium molten salt reactor: Moving on from the MSBR", *Progress in Nuclear Energy*, vol. 48, no. 7, pp. 664–679, 2006, ISSN: 01491970. DOI: 10.1016/j.pnucene.2006.07.005.

[22] L. Mathieu, D. Heuer, E. Merle-Lucotte, *et al.*, "Possible configurations for the thorium molten salt reactor and advantages of the fast non moderated version", *Nuclear Science and Engineering*, vol. 161, no. 1, pp. 78–89, 2009, ISSN: 00295639. DOI: 10.13182/NSE07-49.

[23] "Gif r&d outlook for generation iv nuclear energy systems: 2018 update", Generation IV International Forum, Tech. Rep., 2018.

[24] D. Gerardin, M. Allibert, D. Heuer, A. Laureau, E. Merle-Lucotte, and C. Seuvre, "Design evolutions of Molten Salt Fast Reactor", *International conference on Fast Reactors and Related Fuel Cycles*, pp. 1–10, 2017.

[25] D. Heuer, E. Merle-Lucotte, M. Allibert, M. Brovchenko, V. Ghetta, and P. Rubiolo, "Towards the thorium fuel cycle with molten salt fast reactors", *Annals of Nuclear Energy*, vol. 64, pp. 421–429, 2014, ISSN: 03064549. DOI: 10.1016/j.anucene.2013.08.002.

[26] H. Rouch, O. Geoffroy, P. Rubiolo, *et al.*, "Preliminary thermal-hydraulic core design of the Molten Salt Fast Reactor (MSFR)", *Annals of Nuclear Energy*, vol. 64, pp. 449–456, 2014, ISSN: 03064549. DOI: 10.1016/j.anucene.2013.09.012. [Online]. Available: http://dx.doi.org/10.1016/j.anucene.2013.09.012.

[27] R. Hargraves and R. Moir, "Liquid fluoride thorium reactors: An old idea in nuclear power gets reexamined", *American Scientist*, vol. 98, no. 4, pp. 304–313, 2010.

[28] T. J. Dolan, *Molten salt reactors and thorium energy*. Woodhead Publishing, 2017.

[29] M. Tiberga, D. Shafer, D. Lathouwers, M. Rohde, and J. L. Kloosterman, "Preliminary investigation on the melting behavior of a freeze-valve for the Molten Salt Fast Reactor", *Annals of Nuclear Energy*, vol. 132, pp. 544–554, 2019, ISSN: 18732100. DOI: 10.1016/j.anucene.2019.06.039. [Online]. Available: https://doi.org/10.1016/j.anucene.2019.06.039.

[30] R. Roper, M. Harkema, P. Sabharwall, *et al.*, "Molten salt for advanced energy applications: A review", *Annals of Nuclear Energy*, vol. 169, p. 108 924, 2022, ISSN: 18732100. DOI: 10.1016/j.anucene.2021.108924. [Online]. Available: https://doi.org/10.1016/j.anucene.2021.108924.

[31] N. S. Patel, V. Pavlík, and M. Boča, "High-Temperature Corrosion Behavior of Superalloys in Molten Salts–A Review", *Critical Reviews in Solid State and Materials Sciences*, vol. 42, no. 1, pp. 83–97, 2017, ISSN: 15476561. DOI: 10.1080/10408436.2016.1243090. [Online]. Available: http://dx.doi.org/10.1080/10408436.2016.1243090.

[32] G. Zheng and K. Sridharan, "Corrosion of Structural Alloys in High-Temperature Molten Fluoride Salts for Applications in Molten Salt Reactors", *Jom*, vol. 70, no. 8, pp. 1535–1541, 2018, ISSN: 15431851. DOI: 10.1007/s11837-018-2981-2. [Online]. Available: https://doi.org/10.1007/s11837-018-2981-2.

[33] O. Beneš and R. J. Konings, "Thermodynamic properties and phase diagrams of fluoride salts for nuclear applications", *Journal of Fluorine Chemistry*, vol. 130, no. 1, pp. 22–29, 2009, ISSN: 00221139. DOI: 10.1016/j.jfluchem.2008.07.014.

[34] O. Benes, M. Salanne, M. Levesque, and R. Konings, "Physico-Chemical properties of the MSFR fuel salt Evaluation and Viability of Liquid Fuel Fast Reactor System", Tech. Rep., 2013.

[35] E. Capelli, O. Beneš, M. Beilmann, and R. J. Konings, "Thermodynamic investigation of the LiF-ThF4 system", *Journal of Chemical Thermodynamics*, vol. 58, pp. 110–116, 2013, ISSN: 00219614. DOI: 10.1016/j.jct.2012.10.013.

[36] E. Capelli, "Thermodynamic characterization of salt components for molten salt reactor fuel", Ph.D. dissertation, Delft University of Technology Delft, The Netherlands, 2016.

[37] J. Ocádiz Flores, "Molten salt reactor chemistry: Structure and equilibria", Ph.D. dissertation, Delft University of Technology Delft, The Netherlands, 2021.

[38] J. C. Ard, J. A. Yingling, K. E. Johnson, *et al.*, "Development of the Molten Salt Thermal Properties Database - Thermochemical (MSTDB-TC), example applications, and LiCl\RbCl and UF3-UF4 system assessments", *Journal of Nuclear Materials*, vol. 563, p. 153 631, 2022, ISSN: 00223115. DOI: 10.1016/j.jnucmat.2022.153631. [Online]. Available: https://doi.org/10.1016/j.jnucmat.2022.153631.

[39] M. Poschmann, P. Bajpai, B. W. Fitzpatrick, and M. H. Piro, "Recent developments for molten salt systems in Thermochimica", *Calphad: Computer Coupling of Phase Diagrams and Thermochemistry*, vol. 75, no. August, p. 102 341, 2021, ISSN: 03645916. DOI: 10.1016/j.calphad.2021.102341. [Online]. Available: https://doi.org/10.1016/j.calphad.2021.102341.

[40] R. O. Scarlat, M. R. Laufer, E. D. Blandford, *et al.*, "Design and licensing strategies for the fluoride-salt-cooled, high-temperature reactor (fhr) technology", *Progress in Nuclear Energy*, vol. 77, pp. 406–420, 2014.

[41] B. R. Betzler, F. Heidet, B. Feng, C. Rabiti, T. Sofu, and N. R. Brown, "Modeling and simulation functional needs for molten salt reactor licensing", *Nuclear Engineering and Design*, vol. 355, p. 110 308, 2019.

[42] S. Beils, D. Gérardin, A. C. Uggenti, *et al.*, "Application of the lines of defence method to the molten salt fast reactor in the framework of the samofar project", *EPJ Nuclear Sciences & Technologies*, vol. 5, p. 18, 2019.

[43] D. Rodrigues, G. Durán-Klie, and S. Delpech, "Pyrochemical reprocessing of molten salt fast reactor fuel: Focus on the reductive extraction step", *Nukleonika*, vol. 60, no. 4, pp. 907–914, 2015.

[44] D. E. Chavez, S. R. Yang, R. Vaghetto, and Y. A. Hassan, "Experimental investigation of single helium bubbles rising in flinak molten salt", *International Journal of Heat and Fluid Flow*, vol. 92, p. 108 875, 2021.

[45] S. F. Ashley, G. T. Parks, W. J. Nuttall, C. Boxall, and R. W. Grimes, "Thorium fuel has risks", *Nature*, vol. 492, no. 7427, pp. 31–33, 2012.

[46] M. Allibert, E. Merle, S. Delpech, *et al.*, "Preliminary proliferation study of the molten salt fast reactor", *EPJ Nuclear Sciences & Technologies*, vol. 6, p. 5, 2020.

[47] M. Tiberga, R. G. G. de Oliveira, E. Cervi, *et al.*, "Results from a multi-physics numerical benchmark for codes dedicated to molten salt fast reactors", *Annals of Nuclear Energy*, vol. 142, p. 107 428, 2020, ISSN: 18732100. DOI: 10.1016/j.anucene.2020.107428. [Online]. Available: https://doi.org/10.1016/j.anucene.2020.107428.

[48] M. Tano, P. Rubiolo, and O. Doche, "Progress in modeling solidification in molten salt coolants", *Modelling and Simulation in Materials Science and Engineering*, vol. 25, no. 7, 2017, ISSN: 1361651X. DOI: 10.1088/1361-651X/aa8345.

[49] G. Cartland Glover, A. Skillen, D. Litskevich, *et al.*, "On the numerical modelling of frozen walls in a molten salt fast reactor", *Nuclear Engineering and Design*, vol. 355, no. March, p. 110 290, 2019, ISSN: 00295493. DOI: 10.1016/j.nucengdes.2019.110290. [Online]. Available: https://doi.org/10.1016/j.nucengdes.2019.110290.

[50] N. Le Brun, G. F. Hewitt, and C. N. Markides, "Transient freezing of molten salts in pipe-flow systems: Application to the direct reactor auxiliary cooling system (DRACS)", *Applied Energy*, vol. 186, pp. 56–67, 2017, ISSN: 03062619. DOI: 10.1016/j.apenergy.2016.09.099. [Online]. Available: http://dx.doi.org/10.1016/j.apenergy.2016.09.099.

[51] M. Liu, J. Hughes, A. Ali, and E. Blandford, "Conceptual design of a freeze-tolerant Direct Reactor Auxiliary Cooling System for Fluoride-salt-cooled High-temperature Reactors", *Nuclear Engineering and Design*, vol. 335, no. April, pp. 54–70, 2018, ISSN: 00295493. DOI: 10.1016/j.nucengdes.2018.04.019. [Online]. Available: https://doi.org/10.1016/j.nucengdes.2018.04.019.

[52] V. Voulgaropoulos, N. L. Brun, A. Charogiannis, and C. N. Markides, "Transient freezing of water between two parallel plates: A combined experimental and modelling study", *International Journal of Heat and Mass Transfer*, vol. 153, p. 119 596, 2020, ISSN: 00179310. DOI: 10.1016/j.ijheatmasstransfer.2020.119596. [Online]. Available: https://doi.org/10.1016/j.ijheatmasstransfer.2020.119596.

[53] C. Zeng, X. Chu, L. Liu, M. Liu, and H. Gu, "Performance evaluation of DRACS system of molten salt reactors using a transient solidification model", *Nuclear Engineering and Design*, vol. 386, no. August 2021, p. 111 565, 2022, ISSN: 00295493. DOI: 10.1016/j.nucengdes.2021.111565. [Online]. Available: https://doi.org/10.1016/j.nucengdes.2021.111565.

[54] C. Fiorina, D. Lathouwers, M. Aufiero, *et al.*, "Modelling and analysis of the MSFR transient behaviour", *Annals of Nuclear Energy*, vol. 64, pp. 485–498, 2014, ISSN: 03064549. DOI: 10.1016/j.anucene.2013.08.003. [Online]. Available: http://dx.doi.org/10.1016/j.anucene.2013.08.003.

[55] R. Li, S. Wang, A. Rineiski, D. Zhang, and E. Merle-Lucotte, "Transient analyses for a molten salt fast reactor with optimized core geometry", *Nuclear Engineering and Design*, vol. 292, pp. 164–176, 2015, ISSN: 00295493. DOI: 10.1016/j.nucengdes.2015.06.011.

[56] M. Brovchenko, D. Heuer, E. Merle-Lucotte, *et al.*, "Design-related studies for the preliminary safety assessment of the molten salt fast reactor", *Nuclear Science and Engineering*, vol. 175, no. 3, pp. 329–339, 2013, ISSN: 00295639. DOI: 10.13182/NSE12-70.

[57] M. Richardson, "Development of freeze valve for use in the msre", Oak Ridge National Lab.(ORNL), Oak Ridge, TN (United States), Tech. Rep., 1962.

[58] Z. Qinhua, "Mechanism study of freeze-valve for molten salt reactor (msr)", 2014.

[59] Q. Li, Z. Tang, Y. Fu, Z. Li, and N. Wang, "Preliminary study of the use of freeze-valves for a passive shutdown system in molten salt reactors", in *ASME/NRC Pump and Valve Symposium*, American Society of Mechanical Engineers, vol. 99328, 2014, pp. 325–341.

[60] X. Y. Jiang, H. J. Lu, Y. S. Chen, Y. Fu, and N. X. Wang, "Numerical and experimental investigation of a new conceptual fluoride salt freeze valve for thorium-based molten salt reactor", *Nuclear Science and Techniques*, vol. 31, no. 2, Feb. 2020, ISSN: 22103147. DOI: 10.1007/s41365-020-0729-5.

[61] J. Giraud, V. Ghetta, P. Rubiolo, and M. Tano Retamales, "Development of a cold plug valve with fluoride salt", *Progress in the Science and Technology of Nuclear Reactors using Molten Salts*, vol. 5, no. 9, 2019. [Online]. Available: https://doi.org/10.1051/epjn/2019005.

[62] M. Ilham, I. Kuncoro Aji, and T. Okawa, "Numerical investigation on the effects of fundamental design parameters on freeze plug performance in molten salt reactors", *Nuclear Engineering and Design*, vol. 403, no. December 2022, p. 112 144, 2023, ISSN: 00295493. DOI: 10.1016/j.nucengdes.2022.112144. [Online]. Available: https://doi.org/10.1016/j.nucengdes.2022.112144.

[63] I. Kuncoro Aji, "Investigation of basic parameters in developing high-performance freeze valvefor molten salt reactor", Ph.D. dissertation, University of Electro-Communications, 2020.

[64] C. van Dijk, "Investigating the effect of freeze plug inclination angle on melting behaviour with the linearised enthalpy method", M.S. thesis, Delft University of Technology Delft, The Netherlands, 2023.

[65] M. Pater, C. R. Bahl, E. Bryndt Klinkby, A. Vigand Schofield, and B. Lauritzen, "Computational fluid dynamics model for a C-shaped sodium hydroxide freeze valve", *International Journal of Heat and Fluid Flow*, vol. 103, no. August, p. 109 202, 2023, ISSN: 0142727X. DOI: 10.1016/j.ijheatfluidflow.2023.109202. [Online]. Available: https://doi.org/10.1016/j.ijheatfluidflow.2023.109202.

[66] B. M. Chisholm, S. L. Krahn, and A. G. Sowder, "A unique molten salt reactor feature – The freeze valve system: Design, operating experience, and reliability", *Nuclear Engineering and Design*, vol. 368, no. August, p. 110 803, 2020, ISSN: 00295493. DOI: 10.1016/j.nucengdes.2020.110803. [Online]. Available: https://doi.org/10.1016/j.nucengdes.2020.110803.

[67] C. Gau and R. Viskanta, "Melting and solidification of a Pure Metal on a Vertical Wall", *Journal of Heat Transfer*, vol. 108, pp. 174–181, 1986.

[68] T. A. Campbell and J. N. Koster, "Visualization of liquid-solid interface morphologies in gallium subject to natural convection", *Journal of Crystal Growth*, vol. 140, no. 3-4, pp. 414–425, 1994, ISSN: 00220248. DOI: 10.1016/0022-0248(94)90318-2.

[69] O. Ben-David, A. Levy, B. Mikhailovich, and A. Azulay, "3D numerical and experimental study of gallium melting in a rectangular container", *International Journal of Heat and Mass Transfer*, vol. 67, pp. 260–271, 2013, ISSN: 0017-9310. DOI: 10.1016/j.ijheatmasstransfer.2013.07.058. [Online]. Available: http://dx.doi.org/10.1016/j.ijheatmasstransfer.2013.07.058.

[70] J. Vogel and D. Bauer, "Phase state and velocity measurements with high temporal and spatial resolution during melting of n -octadecane in a rectangular enclosure with two heated vertical sides", *International Journal of Heat and Mass Transfer*, vol. 127, pp. 1264–1276, 2018, ISSN: 0017-9310. DOI: 10.1016/j.ijheatmasstransfer.2018.06.084. [Online]. Available: https://doi.org/10.1016/j.ijheatmasstransfer.2018.06.084.

[71] M. Faden, C. Linhardt, S. Höhlein, A. König-Haagen, and D. Brüggemann, "Velocity field and phase boundary measurements during melting of n-octadecane in a cubical test cell", *International Journal of Heat and Mass Transfer*, vol. 135, pp. 104–114, 2019, ISSN: 00179310. DOI: 10.1016/j.ijheatmasstransfer.2019.01.056. [Online]. Available: https://doi.org/10.1016/j.ijheatmasstransfer.2019.01.056.

[72] M. Tiberga, "Development of a high-fidelity multi-physics simulation tool for liquid-fuel fast nuclear reactors", Ph.D. dissertation, Delft University of Technology Delft, The Netherlands, 2020.

[73] D. V. Boger and J. W. Westwater, "Effect of buoyancy on the melting and freezing process", *Journal of Heat Transfer*, vol. 89, no. 1, pp. 81–89, 1967, ISSN: 15288943. DOI: 10.1115/1.3614327.

[74] E. M. Sparrow, S. Ramadhyani, and S. V. Patankar, "Effect of subcooling on cylindrical melting", *Journal of Heat Transfer*, vol. 100, no. 3, pp. 395–402, 1978, ISSN: 15288943. DOI: 10.1115/1.3450821.

[75] N. W. Hale, R. Viskanta, and W. Lafayette, "Photographic observation of the solid-liquid interface motion during melting of a solid heated from an isothermal vertical wall", *Mechanical Engineering*, vol. 5, pp. 329–337, 1978.

[76] T. A. Kowalewski and M. Rebow, "Freezing of Water in a Differentially Heated Cubic Cavity", *International Journal of Computational Fluid Dynamics*, vol. 11, no. 3-4, pp. 193–210, 1999, ISSN: 10618562. DOI: 10.1080/10618569908940874.

[77] F. L. Tan, "Constrained and unconstrained melting inside a sphere", *International Communications in Heat and Mass Transfer*, vol. 35, no. 4, pp. 466–475, 2008.

[78] B. J. Jones, D. Sun, S. Krishnan, and S. V. Garimella, "Experimental and numerical study of melting in a cylinder", *International Journal of Heat and Mass Transfer*, vol. 49, no. 15-16, pp. 2724–2738, 2006, ISSN: 00179310. DOI: 10.1016/j.ijheatmasstransfer.2006.01.006.

[79] R. D. Zerkle and J. E. Sunderland, "The effect of liquid solidification in a tube upon laminar-flow heat transfer and pressure drop", *Journal of Heat Transfer*, vol. 90, no. 2, pp. 183–189, 1968, ISSN: 15288943. DOI: 10.1115/1.3597471.

[80] A. P. Arora and J. R. Howell, "An investigation of the freezing of supercooled liquid in forced turbulent flow inside circular tubes", *International Journal of Heat and Mass Transfer*, vol. 16, no. 11, pp. 2077–2085, 1973, ISSN: 00179310. DOI: 10.1016/0017-9310(73)90110-5.

[81] J. C. Mulligan and D. D. Jones, "Experiments on heat transfer and pressure drop in a horizontal tube with internal solidification", *International Journal of Heat and Mass Transfer*, vol. 19, no. 2, pp. 213–219, 1976, ISSN: 00179310. DOI: 10.1016/0017-9310(76)90115-0.

[82] T. Hirata, R. R. Gilpin, K. C. Cheng, and E. M. Gates, "The steady state ice layer profile on a constant temperature plate in a forced convection flow- I. Laminar regime", *International Communications in Heat and Mass Transfer*, vol. 22, pp. 1425–1433, 1979.

[83] Y. Kikuchi, Y. Shigemasa, and T. Ogata, "Steady-State Freezing of Liquids in Laminar Flow Between Two Parallel Plates.", *Journal of Nuclear Science and Technology*, vol. 23, no. 11, pp. 979–991, 1986, ISSN: 00223131. DOI: 10.3327/jnst.23.979.

[84] M. C. Holmes-Cerfon and J. A. Whitehead, "Instability and freezing in a solidifying melt conduit", *Physica D: Nonlinear Phenomena*, vol. 240, no. 2, pp. 131–139, 2011, ISSN: 01672789. DOI: 10.1016/j.physd.2010.10.009. [Online]. Available: http://dx.doi.org/10.1016/j.physd.2010.10.009.

[85] T. Hirata, R. R. Gilpin, and K. C. Cheng, "The steady state ice layer profile on a constant temperature plate in a forced convection flow-II. The transition and turbulent regimes", *International Journal of Heat and Mass Transfer*, vol. 22, no. 10, pp. 1435–1443, 1979, ISSN: 00179310. DOI: 10.1016/0017-9310(79)90206-0.

[86] R. R. Gilpin, T. Hirata, and K. C. Cheng, "Wave formation and heat transfer at an ice-water interface in the presence of a turbulent flow", *Journal of Fluid Mechanics*, vol. 99, no. 3, pp. 619–640, 1980, ISSN: 14697645. DOI: 10.1017/S0022112080000791.

[87] N. Seki, S. Fukusako, and G. W. Younan, "Ice-formation phenomena for water flow between two cooled parallel plates", *Journal of Heat Transfer*, vol. 106, no. 3, pp. 498–505, 1984, ISSN: 15288943. DOI: 10.1115/1.3246706.

[88] T. Hirata and H. Matsuzawa, "Study of ice shape on freezing of flowing water in a pipe", *Transactions of the Japan Society of Mechanical Engineers Series B*, vol. 53, no. 486, pp. 553–559, 1987, ISSN: 03875016. DOI: 10.1299/kikaib.53.553.

[89] B. Weigand and H. Beer, "Solidification of flowing liquid in an asymmetric cooled parallel-plate channel", *International Communications in Heat and Mass Transfer*, vol. 19, no. 1, pp. 17–27, 1992, ISSN: 07351933. DOI: 10.1016/0735-1933(92)90060-U.

[90] M. Tago, S. Fukusako, M. Yamada, and A. Horibe, "An experimental study of ice-layer transition phenomena in a rectangular duct containing water flow", *Wärme- und Stoffübertragung*, vol. 28, no. 1-2, pp. 37–47, 1993, ISSN: 00429929. DOI: 10.1007/BF01579620.

[91] T. Hirata and M. Ishihara, "Freeze-off conditions of a pipe containing a flow of water", *International Journal of Heat and Mass Transfer*, vol. 28, no. 2, pp. 331–337, 1985, ISSN: 00179310. DOI: 10.1016/0017-9310(85)90066-3.

[92] M. N. Özişik and J. C. Mulligan, "Transient freezing of liquids in forced flow inside circular tubes", *Journal of Heat Transfer*, vol. 91, no. 3, pp. 385–389, 1969, ISSN: 15288943. DOI: 10.1115/1.3580190.

[93] B. Weigand and H. Beer, "Transient freezing of liquids in forced laminar flow inside a parallel plate channel", *Wärme- und Stoffübertragung*, vol. 27, no. 2, pp. 77–84, 1992, ISSN: 00429929. DOI: 10.1007/BF01590122.

[94] J. M. Savino, "Experimental and analytical study of the transient solidification of a warm liquid flowing over a chilled flat plate", National Aeronautics and Space Administration, Tech. Rep., 1967.

[95] E. Ramudu, B. H. Hirsh, P. Olson, and A. Gnanadesikan, "Turbulent heat exchange between water and ice at an evolving ice-water interface", *Journal of Fluid Mechanics*, vol. 798, pp. 572–597, 2016, ISSN: 14697645. DOI: 10.1017/jfm.2016.321.

[96] M. Bushuk, M. Bushuk, D. M. Holland, T. P. Stanton, A. Stern, and C. Gray, "Ice scallops: a laboratory investigation of the ice-water interface", *Journal of Fluid Mechanics*, vol. 873, pp. 942–976, 2019, ISSN: 14697645. DOI: 10.1017/jfm.2019.398.

[97] M. Lacroix and V. R. Voller, "Finite difference solutions of solidification phase change problems: Transformed versus fixed grids", *Numerical Heat Transfer, Part B: Fundamentals*, vol. 17, no. 1, pp. 25–41, 1990, ISSN: 15210626. DOI: 10.1080/10407799008961731.

[98] R. Viswanath and Y. Jaluria, "A comparison of different solution methodologies for melting and solidification problems in enclosures", *Numerical Heat Transfer, Part B: Fundamentals*, vol. 24, no. 1, pp. 77–105, 1993, ISSN: 15210626. DOI: 10.1080/10407799308955883.

[99] S. Chen, B. Merriman, S. Osher, and P. Smereka, "A Simple Level Set Method for Solving Stefan Problems", *Journal of Computational Physics*, vol. 135, no. 1, pp. 8–29, 1997, ISSN: 00219991. DOI: 10.1006/jcph.1997.5721.

[100] H. Zhang, L. L. Zheng, and T. Y. Hou, "A curvilinear level set formulation for highly deformable free surface problems with application to solidification", *Numerical Heat Transfer, Part B: Fundamentals*, vol. 34, no. 1, pp. 1–30, 1998, ISSN: 15210626. DOI: 10.1080/10407799808915045.

[101] J. Chessa, P. Smolinski, and T. Belytschko, "The extended finite element method (XFEM) for solidification problems", *International Journal for Numerical Methods in Engineering*, vol. 53, no. 8, pp. 1959–1977, 2002, ISSN: 00295981. DOI: 10.1002/nme.386.

[102] L. Tan and N. Zabaras, "A level set simulation of dendritic solidification with combined features of front-tracking and fixed-domain methods", *Journal of Computational Physics*, vol. 211, no. 1, pp. 36–63, 2006, ISSN: 10902716. DOI: 10.1016/j.jcp.2005.05.013.

[103] A. A. Wheeler, W. J. Boettinger, and G. B. McFadden, "Phase-field model for isothermal phase transitions in binary alloys", *Physical Review A*, vol. 45, no. 10, pp. 7424–7439, 1992, ISSN: 10502947. DOI: 10.1103/PhysRevA.45.7424.

[104] R. Kobayashi, "Modeling and numerical simulations of dendritic crystal growth", *Physica D: Nonlinear Phenomena*, vol. 63, no. 3-4, pp. 410–423, 1993, ISSN: 01672789. DOI: 10.1016/0167-2789(93)90120-P.

[105] S. G. Kim, W. T. Kim, and T. Suzuki, "Phase-field model for binary alloys", *Physical Review E - Statistical Physics, Plasmas, Fluids, and Related Interdisciplinary Topics*, vol. 60, no. 6, pp. 7186–7197, 1999, ISSN: 1063651X. DOI: 10.1103/PhysRevE.60.7186.

[106] W. J. Boettinger, J. A. Warren, C. Beckermann, and A. Karma, "Phase-field simulation of solidification", *Annual Review of Materials Science*, vol. 32, pp. 163–194, 2002, ISSN: 00846600. DOI: 10.1146/annurev.matsci.32.101901.155803.

[107] Y. Sun and C. Beckermann, "Sharp interface tracking using the phase-field equation", *Journal of Computational Physics*, vol. 220, no. 2, pp. 626–653, 2007, ISSN: 10902716. DOI: 10.1016/j.jcp.2006.05.025.

[108] C. Bonacina, G. Comini, A. Fasano, and M. Primicerio, "Numerical solution of phase-change problems", *International Journal of Heat and Mass Transfer*, vol. 16, no. 10, pp. 1825–1832, 1973, ISSN: 00179310. DOI: 10.1016/0017-9310(73)90202-0.

[109] K. Morgan, "A numerical analysis of freezing and melting with convection", *Computer Methods in Applied Mechanics and Engineering*, vol. 28, no. 3, pp. 275–284, 1981, ISSN: 00457825. DOI: 10.1016/0045-7825(81)90002-5.

[110] Q. T. Pham, "A fast, unconditionally stable finite-difference scheme for heat conduction with phase change", *International Journal of Heat and Mass Transfer*, vol. 28, no. 11, pp. 2079–2084, 1985, ISSN: 00179310. DOI: 10.1016/0017-9310(85)90101-2.

[111] V. Voller and M. Cross, "Accurate solutions of moving boundary problems using the enthalpy method", *International Journal of Heat and Mass Transfer*, vol. 24, no. 3, pp. 545–556, 1981, ISSN: 00179310. DOI: 10.1016/0017-9310(81)90062-4.

[112] V. R. Voller, M. Cross, and N. C. Markatos, "An enthalpy method for convection/diffusion phase change", *International Journal for Numerical Methods in Engineering*, vol. 24, no. 1, pp. 271–284, 1987, ISSN: 10970207. DOI: 10.1002/nme.1620240119.

[113] A. D. Brent, V. R. Voller, and K. J. Reid, "Enthalpy-porosity technique for modeling convection-diffusion phase change: Application to the melting of a pure metal", *Numerical Heat Transfer*, vol. 13, no. 3, pp. 297–318, 1988, ISSN: 01495720. DOI: 10.1080/10407788808913615.

[114] M. Yao and A. Chait, "An alternative formulation of the apparent heat capacity method for phase–change problems", *Numerical Heat Transfer, Part B: Fundamentals*, vol. 24, no. 3, pp. 279–300, 1993, ISSN: 15210626. DOI: 10.1080/10407799308955894.

[115] C. R. Swaminathan and V. R. Voller, "On the enthalpy method", *International Journal of Numerical Methods for Heat & Fluid Flow*, vol. 3, no. 3, pp. 233–244, 1993, ISSN: 09615539. DOI: 10.1108/eb017528.

[116] B. Nedjar, "An enthalpy-based finite element method for nonlinear heat problems involving phase change", *Computers and Structures*, vol. 80, no. 1, pp. 9–21, 2002, ISSN: 00457949. DOI: 10.1016/S0045-7949(01)00165-1.

[117] K. Krabbenhoft, L. Damkilde, and M. Nazem, "An implicit mixed enthalpy-temperature method for phase-change problems", *Heat and Mass Transfer/Waerme- und Stoffuebertragung*, vol. 43, no. 3, pp. 233–241, 2007, ISSN: 09477411. DOI: 10.1007/s00231-006-0090-1.

[118] M. Faden, A. König-Haagen, and D. Brüggemann, "An optimum enthalpy approach for melting and solidification with volume change", *Energies*, vol. 12, no. 5, 2019, ISSN: 19961073. DOI: 10.3390/en12050868.

[119] B. J. Kaaks, J. W. A. Reus, M. Rohde, J. L. Kloosterman, and D. Lathouwers, "NUMERICAL STUDY OF PHASE-CHANGE PHENOMENA : A CONSERVATIVE LINEARIZED ENTHALPY APPROACH", in *Nureth (2019)*, 2022, pp. 1–13. DOI: 10.5281/ZENODO.5704671.

[120] A. König-Haagen, E. Franquet, E. Pernot, and D. Brüggemann, "A comprehensive benchmark of fixed-grid methods for the modeling of melting", *International Journal of Thermal Sciences*, vol. 118, pp. 69–103, 2017, ISSN: 12900729. DOI: 10.1016/j.ijthermalsci.2017.04.008.

[121] J. W. Jerome and M. E. Rose, "Error Estimates for the Multidimensional Two-Phase Stefan Problem", *Mathematics of Computation*, vol. 39, no. 160, p. 377, 1982, ISSN: 00255718. DOI: 10.2307/2007320.

[122] R. H. Nochetto, "Error Estimates for Two-Phase Stefan Problems in Several Space Variables, I: Linear Boundary Conditions", *Calcolo*, vol. 22, no. 4, pp. 457–499, 1985.

[123] M. Azaïez, F. Jelassi, M. M. Brahim, and J. Shen, "Two Phases Stefan Problem with Smoothed Enthalpy", *Communications in Mathematical Sciences*, vol. 14, no. 6, pp. 1625–1641, 2016.

[124] N. Hannoun, V. Alexiades, and T. Z. Mai, "Resolving The Controversy Over Tin And Gallium Melting In A Rectangular Cavity Heated From The Side", *Numerical Heat Transfer, Part B: Fundamentals*, vol. 44, no. 3, pp. 253–276, 2003, ISSN: 15210626. DOI: 10.1080/713836378.

[125] I. Danaila, R. Moglan, F. Hecht, and S. Le Masson, "A Newton method with adaptive finite elements for solving phase-change problems with natural convection", *Journal of Computational Physics*, vol. 274, pp. 826–840, 2014, ISSN: 10902716. DOI: 10.1016/j.jcp.2014.06.036. [Online]. Available: http://dx.doi.org/10.1016/j.jcp.2014.06.036.

[126] Y. Belhamadia, A. Fortin, and T. Briffard, "A two-dimensional adaptive remeshing method for solving melting and solidification problems with convection", *Numerical Heat Transfer; Part A: Applications*, vol. 76, no. 4, pp. 179–197, 2019, ISSN: 15210634. DOI: 10.1080/10407782.2019.1627837. [Online]. Available: https://doi.org/10.1080/10407782.2019.1627837.

[127] S. Soghrati, A. M. Aragon, C. A. Duarte, and P. H. Geubelle, "An interface-enriched generalized FEM for problems with discontinuous gradient fields", *International Journal for Numerical Methods in Engineering*, vol. 89, pp. 991–1008, 2012.

[128] J. Zhang, S. J. van den Boom, F. van Keulen, and A. M. Aragón, "A stable discontinuity-enriched finite element method for 3-D problems containing weak and strong discontinuities", *Computer Methods in Applied Mechanics and Engineering*, vol. 355, pp. 1097–1123, 2019, ISSN: 00457825. DOI: 10.1016/j.cma.2019.05.018. [Online]. Available: https://doi.org/10.1016/j.cma.2019.05.018.

[129] J. S. Cagnone, K. Hillewaert, and N. Poletz, "A discontinuous Galerkin method for multiphysics welding simulations", *Key Engineering Materials*, vol. 611-612, pp. 1319–1326, 2014, ISSN: 16629795. DOI: 10.4028/www.scientific.net/KEM.611-612.1319.

[130] P. W. Schroeder and G. Lube, "Stabilised dG-FEM for incompressible natural convection flows with boundary and moving interior layers on non-adapted meshes", *Journal of Computational Physics*, vol. 335, pp. 760–779, 2017, ISSN: 10902716. DOI: 10.1016/j.jcp.2017.01.055. [Online]. Available: http://dx.doi.org/10.1016/j.jcp.2017.01.055.

[131] R. Nourgaliev, H. Luo, B. Weston, *et al.*, "Fully-implicit orthogonal reconstructed Discontinuous Galerkin method for fluid dynamics with phase change", *Journal of Computational Physics*, vol. 305, pp. 964–996, 2016, ISSN: 10902716. DOI: 10.1016/j.jcp.2015.11.004. [Online]. Available: http://dx.doi.org/10.1016/j.jcp.2015.11.004.

[132] S. Stepanov, M. Vasilyeva, and V. I. Vasil'ev, "Generalized multiscale discontinuous Galerkin method for solving the heat problem with phase change", *Journal of Computational and Applied Mathematics*, vol. 340, pp. 645–652, 2018, ISSN: 03770427. DOI: 10.1016/j.cam.2017.12.004. [Online]. Available: https://doi.org/10.1016/j.cam.2017.12.004.

[133] W. Gong, "Heat storage of PCM inside a transparent building brick : Experimental study and LBM simulation on GPU Heat storage of PCM inside a transparent building brick : experimental study and LBM simulation on GPU", Ph.D. dissertation, INSA de Lyon, 2015.

[134] H. Jasak and A. D. Gosman, "Residual Error Estimate for the Finite Volume Method", *Numerical Heat Transfer Part B: Fundamentals*, vol. 39, no. 0, pp. 1–19, 2001.

[135] H. Jasak and A. D. Gosman, "Element residual error estimate for the finite volume method", *Computers and Fluids*, vol. 32, no. 2, pp. 223–248, 2003, ISSN: 00457930. DOI: 10.1016/S0045-7930(02)00004-X.

[136] E. Large and C. D. Andereck, "Penetrative Rayleigh-Be´nard convection in water near its maximum density point", *Physics of Fluids*, vol. 26, no. 9, 2014, ISSN: 10897666. DOI: 10.1063/1.4895063. [Online]. Available: http://dx.doi.org/10.1063/1.4895063.

[137] V. Kumar, M. Kumawat, A. Srivastava, and S. Karagadde, "Mechanism of flow reversal during solidification of an anomalous liquid", *Physics of Fluids*, vol. 29, no. 12, 2017, ISSN: 10897666. DOI: 10.1063/1.5005139. [Online]. Available: http://dx.doi.org/10.1063/1.5005139.

[138] J. W. C.O. Popiel, "Thermophysical properties", *Heat transfer engineering*, vol. 19, no. 3, pp. 87–101, 1998. DOI: 10.1016/b978-075065082-3/50010-3.

[139] M. T. Retamales, "Developement of multi-physical multiscale models for molten salts at high temperature and their experimental validation", Ph.D. dissertation, Université Grenoble Alpes, 2018.

[140] D. Coles, "Transition in circular Couette flow", *Journal of Fluid Mechanics*, vol. 21, pp. 385–425, 1965.

[141] R. M. Manglik and A. E. Bergles, "Heat transfer and pressure drop correlations for the rectangular offset strip fin compact heat exchanger", *Experimental Thermal and Fluid Science*, vol. 10, no. 2, pp. 171–180, 1995, ISSN: 08941777. DOI: 10.1016/0894-1777(94)00096-Q.

[142] P. Teertstra, M. Yovanovich, and J. Culham, "Analytical Forced Convection Modeling of Plate Fin Heat Sinks", *Journal of Electronics Manifacturing*, vol. 10, pp. 253–261, 2001. DOI: 10.1109/STHERM.1999.762426.

[143] W. P. Jones and B. E. Launder, "The calculation of low-Reynolds-number phenomena with a two-equation model of turbulence", *International Journal of Heat and Mass Transfer*, vol. 16, no. 6, pp. 1119–1130, 1973, ISSN: 00179310. DOI: 10.1016/0017-9310(73)90125-7.

[144] R. D. Mehta and P. Bradshaw, "Technical notes of design for small low speed wind tunnels", *the Aeronautical Journal of the Royal Aeronautical Society*, no. 7, 1, 445, 446 & 448, 1979, ISSN: 0001-9240.

[145] J. Scheiman, "Comparison of Experimental and Theoretical Turbulence Reduction Characteristics for Screens, Honeycomb, and Honeycomb-Screen Combinations.", *NASA Technical Paper*, no. December 1981, 1981, ISSN: 01488341.

[146] J. H. Bell and R. D. Mehta, "for Small Low-Speed Wind Tunnels", Tech. Rep. August, 1988, pp. 1–39.

[147] T. Morel, "Design of 2D Wind Tunnel Contractions", *Journal of Fluid Engineering*, no. June 1977, pp. 371–377, 1977.

[148] L. Kumar, B. S. Manjunath, R. J. Patel, *et al.*, "Experimental investigations on melting of lead in a cuboid with constant heat flux boundary condition using thermal neutron radiography", *International Journal of Thermal Sciences*, vol. 61, pp. 15–27, 2012, ISSN: 12900729. DOI: 10.1016/j.ijthermalsci.2012.06.014. [Online]. Available: http://dx.doi.org/10.1016/j.ijthermalsci.2012.06.014.

[149] R. J. Adrian and J. Westerweel, *Particle Image Velocimetry*, 1st ed. Cambridge University Press, 2011, ISBN: 978-0-521-44008-0.

[150] C. Kuan-Cheng, J. Ouazzani, and F. Rosenberger, "Mixed convection between horizontal plates-II. Fully developed flow", *International Journal of Heat and Mass Transfer*, vol. 30, no. 8, pp. 1655–1662, 1987, ISSN: 00179310. DOI: 10.1016/0017-9310(87)90311-5.

[151] Z. Lipnicki and B. Weigand, "An experimental and theoretical study of solidification in a free-convection flow inside a vertical annular enclosure", *International Journal of Heat and Mass Transfer*, vol. 55, no. 4, pp. 655–664, 2012, ISSN: 00179310. DOI: 10.1016/j.ijheatmasstransfer.2011.10.044. [Online]. Available: http://dx.doi.org/10.1016/j.ijheatmasstransfer.2011.10.044.

[152] M. Z. M. Rizan, F. L. Tan, and C. P. Tso, "An experimental study of n-octadecane melting inside a sphere subjected to constant heat rate at surface", *International Communications in Heat and Mass Transfer*, vol. 39, no. 10, pp. 1624–1630, 2012, ISSN: 07351933. DOI: 10.1016/j.icheatmasstransfer.2012.08.003. [Online]. Available: http://dx.doi.org/10.1016/j.icheatmasstransfer.2012.08.003.

[153] B. J. Kaaks, D. Lathouwers, J.-L. Kloosterman, and M. Rohde, "Transient Freezing of Water in a Square Duct: Anexperimental Benchmark", *SSRN Electronic Journal*, 2023. DOI: 10.2139/ssrn.4360285.

[154] Z. Chen, D. Gao, and J. Shi, "Experimental and numerical study on melting of phase change materials in metal foams at pore scale", *International Journal of Heat and Mass Transfer*, vol. 72, pp. 646–655, 2014, ISSN: 00179310. DOI: 10.1016/j.ijheatmasstransfer.2014.01.003. [Online]. Available: http://dx.doi.org/10.1016/j.ijheatmasstransfer.2014.01.003.

[155] J. Sakakibara and R. J. Adrian, "Whole field measurement of temperature in water using two-color laser induced fluorescence", *Experiments in Fluids*, vol. 26, no. 1-2, pp. 7–15, 1999, ISSN: 07234864. DOI: 10.1007/s003480050260.

[156] F. Lemoine, Y. Antoine, M. Wolff, and M. Lebouche, "Simultaneous temperature and 2D velocity measurements in a turbulent heated jet using combined laser-induced fluorescence and LDA", *Experiments in Fluids*, vol. 26, no. 4, pp. 315–323, 1999, ISSN: 07234864. DOI: 10.1007/s003480050294.

[157] M. Bruchhausen, F. Guillard, and F. Lemoine, "Instantaneous measurement of two-dimensional temperature distributions by means of two-color planar laser induced fluorescence (PLIF)", *Experiments in Fluids*, vol. 38, no. 1, pp. 123–131, 2005, ISSN: 07234864. DOI: 10.1007/s00348-004-0911-2.

[158] S. Funatani, N. Fujisawa, and H. Ikeda, "Simultaneous measurement of temperature and velocity using two-colour LIF combined with PIV with a colour CCD camera and its application to the turbulent buoyant plume", *Measurement Science and Technology*, vol. 15, no. 5, pp. 983–990, 2004, ISSN: 09570233. DOI: 10.1088/0957-0233/15/5/030.

[159] S. Grafsronningen and A. Jensen, "Simultaneous PIV/LIF measurements of a transitional buoyant plume above a horizontal cylinder", *International Journal of Heat and Mass Transfer*, vol. 55, no. 15-16, pp. 4195–4206, 2012, ISSN: 00179310. DOI: 10.1016/j.ijheatmasstransfer.2012.03.060.

[160] M. C. Coolen, R. N. Kieft, C. C. Rindt, and A. A. Van Steenhoven, "Application of 2-D LIF temperature measurements in water using a Nd:YAG laser", *Experiments in Fluids*, vol. 27, no. 5, pp. 420–426, 1999, ISSN: 07234864. DOI: 10.1007/s003480050367.

[161] P. Lavieille, F. Lemoine, G. Lavergne, and M. Lebouché, "Evaporating and combusting droplet temperature measurements using two-color laser-induced fluorescence", *Experiments in Fluids*, vol. 31, no. 1, pp. 45–55, 2001, ISSN: 07234864. DOI: 10.1007/s003480000257.

[162] J. Sakakibara, K. Hishida, and M. Maeda, "Vortex structure and heat transfer in the stagnation region of an impinging plane jet (simultaneous measurements of velocity and temperature fields by digital particle image velocimetry and laser-induced fluorescence)", *International Journal of Heat and Mass Transfer*, vol. 40, no. 13, pp. 3163–3176, 1997, ISSN: 00179310. DOI: 10.1016/S0017-9310(96)00367-5.

[163] K. Hishida and J. Sakakibara, "Combined planar laser-induced fluorescence-particle image velocimetry technique for velocity and temperature fields", *Experiments in Fluids*, vol. 29, no. SUPPL. 1, 2000, ISSN: 07234864. DOI: 10.1007/s003480070015.

[164] A. S. Nebuchinov, Y. A. Lozhkin, A. V. Bilsky, and D. M. Markovich, "Combination of PIV and PLIF methods to study convective heat transfer in an impinging jet", *Experimental Thermal and Fluid Science*, vol. 80, pp. 139–146, 2017, ISSN: 08941777. DOI: 10.1016/j.expthermflusci.2016.08.009. [Online]. Available: http://dx.doi.org/10.1016/j.expthermflusci.2016.08.009.

[165] J. Sakakibara and R. J. Adrian, "Measurement of temperature field of a Rayleigh-Bénard convection using two-color laser-induced fluorescence", *Experiments in Fluids*, vol. 37, no. 3, pp. 331–340, 2004, ISSN: 07234864. DOI: 10.1007/s00348-004-0821-3.

[166] H. J. Seuntiëns, R. N. Kieft, C. C. M. Rindt, and A. A. Van Steenhoven, "2D temperature measurements in the wake of a heated cylinder using LIF", *Experiments in Fluids*, vol. 31, no. 5, pp. 588–595, 2001, ISSN: 07234864. DOI: 10.1007/s003480100338.

[167] A. Charogiannis, J. Sik An, V. Voulgaropoulos, and C. N. Markides, "Structured planar laser-induced fluorescence (S-PLIF) for the accurate identification of interfaces in multiphase flows", *International Journal of Multiphase Flow*, vol. 118, pp. 193–204, 2019, ISSN: 03019322. DOI: 10.1016/j.ijmultiphaseflow.2019.06.002. [Online]. Available: https://doi.org/10.1016/j.ijmultiphaseflow.2019.06.002.

[168] M. Stiti, A. Labergue, F. Lemoine, S. Leclerc, and D. Stemmelen, "Temperature measurement and state determination of supercooled droplets using laser-induced fluorescence", *Experiments in Fluids*, vol. 60, no. 4, pp. 1–13, 2019, ISSN: 07234864. DOI: 10.1007/s00348-018-2672-3. [Online]. Available: http://dx.doi.org/10.1007/s00348-018-2672-3.

[169] L. K. Hjertager, B. H. Hjertager, N. G. Deen, and T. Solberg, "Measurement of turbulent mixing in a confined wake flow using combined PIV and PLIF", *Canadian Journal of Chemical Engineering*, vol. 81, no. 6, pp. 1149–1158, 2003, ISSN: 00084034. DOI: 10.1002/cjce.5450810604.

[170] M. M. Breunig, H. P. Kriegel, R. T. Ng, and J. Sander, "LOF: Identifying Density-Based Local Outliers", *SIGMOD 2000 - Proceedings of the 2000 ACM SIGMOD International Conference on Management of Data*, pp. 93–104, 2000. DOI: 10.1145/342009.335388.

[171] P. T. Boggs and J. E. Rogers, "Orthogonal distance regression", *Contemporary mathematics*, vol. 112, pp. 183–194, 1990. DOI: 10.1090/conm/112/1087109.

[172] B. Cockburn and C. W. Shu, "Runge-Kutta Discontinuous Galerkin methods for convection-dominated problems", *Journal of Scientific Computing*, vol. 16, no. 3, pp. 173–261, 2001, ISSN: 08857474.

[173] D. N. Arnold, F. Brezzi, B. Cockburn, and L. Donatella Marini, "Unified analysis of discontinuous Galerkin methods for elliptic problems", *SIAM Journal on Numerical Analysis*, vol. 39, no. 5, pp. 1749–1779, 2001, ISSN: 00361429. DOI: 10.1137/S0036142901384162.

[174] M. Tiberga, D. Lathouwers, and J. L. Kloosterman, "A multi-physics solver for liquid-fueled fast systems based on the discontinuous Galerkin FEM discretization", *Progress in Nuclear Energy*, vol. 127, no. May, p. 103 427, 2020, ISSN: 01491970. DOI: 10.1016/j.pnucene.2020.103427. [Online]. Available: https://doi.org/10.1016/j.pnucene.2020.103427.

[175] A. Crivellini, V. D'Alessandro, and F. Bassi, "A Spalart–Allmaras turbulence model implementation in a discontinuous Galerkin solver for incompressible flows", *Journal of Computational Physics*, vol. 241, pp. 388–415, May 2013, ISSN: 00219991. DOI: 10.1016/j.jcp.2012.12.038. [Online]. Available: https://linkinghub.elsevier.com/retrieve/pii/S002199911300034X.

[176] F. Bassi, A. Ghidoni, A. Perbellini, *et al.*, "A high-order Discontinuous Galerkin solver for the incompressible RANS and k–ω turbulence model equations", *Computers & Fluids*, vol. 98, pp. 54–68, Jul. 2014, ISSN: 00457930. DOI: 10.1016/j.compfluid.2014.02.028. [Online]. Available: https://linkinghub.elsevier.com/retrieve/pii/S0045793014000917.

[177] G. Noventa, F. Massa, F. Bassi, A. Colombo, N. Franchina, and A. Ghidoni, "A high-order Discontinuous Galerkin solver for unsteady incompressible turbulent flows", *Computers & Fluids*, vol. 139, pp. 248–260, Nov. 2016, ISSN: 00457930. DOI: 10.1016/j.compfluid.2016.03.007. [Online]. Available: https://linkinghub.elsevier.com/retrieve/pii/S0045793016300524.

[178] B. Krank, N. Fehn, W. A. Wall, and M. Kronbichler, "A high-order semi-explicit discontinuous Galerkin solver for 3D incompressible flow with application to DNS and LES of turbulent channel flow", *Journal of Computational Physics*, vol. 348, pp. 634–659, 2017, ISSN: 10902716. DOI: 10.1016/j.jcp.2017.07.039. [Online]. Available: http://dx.doi.org/10.1016/j.jcp.2017.07.039.

[179] M. Tiberga, A. Hennink, J. L. Kloosterman, and D. Lathouwers, "A high-order Discontinuous Galerkin solver for the incompressible RANS equations coupled to the k-e turbulence model", *Computers and Fluids*, 2020.

[180] B. Klein, F. Kummer, M. Keil, and M. Oberlack, "An extension of the SIMPLE based discontinuous Galerkin solver to unsteady incompressible flows", *International Journal for Numerical Methods in Fluids*, vol. 77, no. 10, pp. 571–589, Apr. 2015, ISSN: 02712091. DOI: 10.1002/fld.3994. [Online]. Available: https://onlinelibrary.wiley.com/doi/10.1002/fld.3994.

[181] A. Hennink, M. Tiberga, and D. Lathouwers, "A pressure-based solver for low-Mach number flow using a discontinuous Galerkin method", *Journal of Computational Physics*, vol. 425, p. 109 877, 2021, ISSN: 10902716. DOI: 10.1016/j.jcp.2020.109877. [Online]. Available: https://doi.org/10.1016/j.jcp.2020.109877.

[182] M. Sabat, A. Larat, A. Vié, and M. Massot, *On the development of high order realizable schemes for the Eulerian simulation of disperse phase flows: A convex-state preserving discontinuous galerkin method*, 2014. DOI: 10.1260/1757-482X.6.3.247.

[183] E. J. Ching, S. R. Brill, M. Barnhardt, and M. Ihme, "A two-way coupled Euler-Lagrange method for simulating multiphase flows with discontinuous Galerkin schemes on arbitrary curved elements", *Journal of Computational Physics*, vol. 405, p. 109 096, 2020, ISSN: 10902716. DOI: 10.1016/j.jcp.2019.109096. [Online]. Available: https://doi.org/10.1016/j.jcp.2019.109096.

[184] A. König-Haagen, E. Franquet, M. Faden, and D. Brüggemann, "Influence of the convective energy formulation for melting problems with enthalpy methods", *International Journal of Thermal Sciences*, vol. 158, no. July, 2020, ISSN: 12900729. DOI: 10.1016/j.ijthermalsci.2020.106477.

[185] N. Fehn, W. A. Wall, and M. Kronbichler, "On the stability of projection methods for the incompressible Navier–Stokes equations based on high-order discontinuous Galerkin discretizations", *Journal of Computational Physics*, vol. 351, pp. 392–421, 2017, ISSN: 10902716. DOI: 10.1016/j.jcp.2017.09.031. [Online]. Available: https://doi.org/10.1016/j.jcp.2017.09.031.

[186] K. A. Cliffe, E. J. C. Hall, and P. Houston, "ADAPTIVE DISCONTINUOUS GALERKIN METHODS FOR EIGENVALUE PROBLEMS ARISING IN INCOMPRESSIBLE FLUID Copyright © by SIAM . Unauthorized reproduction of this article is prohibited . Copyright © by SIAM . Unauthorized reproduction of this article is prohibited .", *Siam Journal on Scientific Computing*, vol. 31, no. 6, pp. 4607–4632, 2010.

[187] M. Drosson and K. Hillewaert, "On the stability of the symmetric interior penalty method for the Spalart-Allmaras turbulence model", *Journal of Computational and Applied Mathematics*, vol. 246, pp. 122–135, 2013, ISSN: 03770427. DOI: 10.1016/j.cam.2012.09.019. [Online]. Available: http://dx.doi.org/10.1016/j.cam.2012.09.019.

[188] B. Cockburn, G. Kanschat, and D. Schötzau, "A locally conservative Ldg method for the incompressible Navier-Stokes equations", *Mathematics of Computation*, vol. 74, no. 251, pp. 1067–1095, 2004.

[189] K. Shahbazi, P. F. Fischer, and C. R. Ethier, "A high-order discontinuous Galerkin method for the unsteady incompressible Navier-Stokes equations", *Journal of Computational Physics*, vol. 222, no. 1, pp. 391–407, 2007, ISSN: 10902716. DOI: 10.1016/j.jcp.2006.07.029.

[190] G. Mengaldo, D. De Grazia, D. Moxey, P. E. Vincent, and S. J. Sherwin, "Dealiasing techniques for high-order spectral element methods on regular and irregular grids", *Journal of Computational Physics*, vol. 299, pp. 56–81, 2015, ISSN: 10902716. DOI: 10.1016/j.jcp.2015.06.032. [Online]. Available: http://dx.doi.org/10.1016/j.jcp.2015.06.032.

[191] P. Solin, K. Segeth, and I. Dolezel, *Higher-Order Finite Element Methods*, 1st ed., Chapman and Hall, Ed. New York: CRC Press, 2003, ISBN: 9781584884385.

[192] C. Geuzaine and J.-F. Remacle, "Gmsh: A 3-D finite element mesh generator with built-in pre- and post-processing facilities", *International Journal for Numerical Methods in Engineering*, vol. 79, no. 11, pp. 1309–1331, Sep. 2009, ISSN: 00295981. DOI: 10.1002/nme.2579. [Online]. Available: https://onlinelibrary.wiley.com/doi/10.1002/nme.2579.

[193] G. Karypis and V. Kumar, "A Fast and High Quality Multilevel Scheme for Partitioning Irregular Graphs", *SIAM Journal on Scientific Computing*, vol. 20, no. 1, pp. 359–392, Jan. 1998, ISSN: 1064-8275. DOI: 10.1137/S1064827595287997. [Online]. Available: http://epubs.siam.org/doi/10.1137/S1064827595287997.

[194] S. Balay, W. D. Gropp, L. C. McInnes, and B. F. Smith, "Efficient Management of Parallelism in Object-Oriented Numerical Software Libraries", in *Modern Software Tools for Scientific Computing*, Boston, MA: Birkhäuser Boston, 1997, pp. 163–202. DOI: 10.1007/978-1-4612-1986-6{_}8.

[195] N. Hu, L. W. Fan, and Z. Q. Zhu, "Can the numerical simulations of melting in a differentially-heated rectangular cavity be rationally reduced to 2D? A comparative study between 2D and 3D simulation results", *International Journal of Heat and Mass Transfer*, vol. 166, p. 120 751, 2021, ISSN: 00179310. DOI: 10.1016/j.ijheatmasstransfer.2020.120751. [Online]. Available: https://doi.org/10.1016/j.ijheatmasstransfer.2020.120751.

[196] M. Faden, A. König-Haagen, E. Franquet, and D. Brüggemann, "Influence of density change during melting inside a cavity: Theoretical scaling laws and numerical analysis", *International Journal of Heat and Mass Transfer*, vol. 173, 2021, ISSN: 00179310. DOI: 10.1016/j.ijheatmasstransfer.2021.121260.

[197] K. Wittig and P. A. Nikrityuk, "Three-dimensionality of fluid flow in the benchmark experiment for a pure metal melting on a vertical wall", *IOP Conference Series: Materials Science and Engineering*, vol. 27, no. 1, 2011, ISSN: 17578981. DOI: 10.1088/1757-899X/27/1/012054.

[198] Y. Belhamadia, A. S. Kane, and A. Fortin, "An enhanced mathematical model for phase change problems with natural convection", *International Journal of numerical analysis and modeling, Series B*, vol. 3, no. 2, pp. 192–206, 2012.

[199] A. S. Berman, "Laminar flow in channels with porous walls", *Journal of Applied Physics*, vol. 24, no. 9, pp. 1232–1235, 1953, ISSN: 00218979. DOI: 10.1063/1.1721476.

[200] G. Hwang and Y. Cheng, "Developing laminar flow and heat transfer in a square duct with one-walled injection and suction", *International Journal of Heat and Mass Transfer*, vol. 36, no. 9, pp. 2429–2440, 1993.

[201] O. Antepara, O. Lehmkuhl, R. Borrell, J. Chiva, and A. Oliva, "Parallel adaptive mesh refinement for large-eddy simulations of turbulent flows", *Computers and Fluids*, vol. 110, pp. 48–61, 2015, ISSN: 00457930. DOI: 10.1016/j.compfluid.2014.09.050. [Online]. Available: http://dx.doi.org/10.1016/j.compfluid.2014.09.050.

[202] L. m. Li, D. q. Hu, Y. c. Liu, *et al.*, "Large eddy simulation of cavitating flows with dynamic adaptive mesh refinement using OpenFOAM", *Journal of Hydrodynamics*, vol. 32, no. 2, pp. 398–409, 2020, ISSN: 18780342. DOI: 10.1007/s42241-019-0041-1.

[203] S. J. Kamkar, A. M. Wissink, V. Sankaran, and A. Jameson, "Feature-driven Cartesian adaptive mesh refinement for vortex-dominated flows", *Journal of Computational Physics*, vol. 230, no. 16, pp. 6271–6298, 2011, ISSN: 10902716. DOI: 10.1016/j.jcp.2011.04.024. [Online]. Available: http://dx.doi.org/10.1016/j.jcp.2011.04.024.

[204] J. P. Magalhães, D. M. Albuquerque, J. M. Pereira, and J. C. Pereira, "Adaptive mesh finite-volume calculation of 2D lid-cavity corner vortices", *Journal of Computational Physics*, vol. 243, pp. 365–381, 2013, ISSN: 10902716. DOI: 10.1016/j.jcp.2013.02.042.

[205] D. Deising, D. Bothe, and H. Marschall, "Direct numerical simulation of mass transfer in bubbly flows", *Computers and Fluids*, vol. 172, pp. 524–537, 2018, ISSN: 00457930. DOI: 10.1016/j.compfluid.2018.03.041.

[206] O. Antepara, N. Balcázar, J. Rigola, and A. Oliva, "Numerical study of rising bubbles with path instability using conservative level-set and adaptive mesh refinement", *Computers and Fluids*, vol. 187, pp. 83–97, 2019, ISSN: 00457930. DOI: 10.1016/j.compfluid.2019.04.013.

[207] J. Wackers, G. Deng, A. Leroyer, P. Queutey, and M. Visonneau, "Adaptive grid refinement for hydrodynamic flows", *Computers and Fluids*, vol. 55, pp. 85–100, 2012, ISSN: 00457930. DOI: 10.1016/j.compfluid.2011.11.004. [Online]. Available: http://dx.doi.org/10.1016/j.compfluid.2011.11.004.

[208] N. Palle and J. A. Dantzig, "An adaptive mesh refinement scheme for solidification problems", *Metallurgical and Materials Transactions A: Physical Metallurgy and Materials Science*, vol. 27, no. 3, pp. 707–717, 1996, ISSN: 10735623. DOI: 10.1007/bf02648957.

[209] C. Zienkiewicz and J. Z. Zhu, "A simple error estimator and adaptive procedure for practical engineering analysis", *International Journal for Numerical Methods in Engineering*, vol. 24, no. January 1986, pp. 337–357, 1987.

[210] C. W. Lan, C. C. Liu, and C. M. Hsu, "An adaptive finite volume method for incompressible heat flow problems in solidification", *Journal of Computational Physics*, vol. 178, no. 2, pp. 464–497, 2002, ISSN: 00219991. DOI: 10.1006/jcph.2002.7037.

[211] J. Mencinger, "Numerical simulation of melting in two-dimensional cavity using adaptive grid", *Journal of Computational Physics*, vol. 198, no. 1, pp. 243–264, Jul. 2004, ISSN: 00219991. DOI: 10.1016/j.jcp.2004.01.006.

[212] R. T. Tenchev, J. A. Mackenzie, T. J. Scanlon, and M. T. Stickland, "Finite element moving mesh analysis of phase change problems with natural convection", *International Journal of Heat and Fluid Flow*, vol. 26, no. 4 SPEC. ISS. Pp. 597–612, 2005, ISSN: 0142727X. DOI: 10.1016/j.ijheatfluidflow.2005.03.003.

[213] P. Nithiarasu, "Adaptive finite element procedure for solidification problems", *Warme- und Stoffubertragung Zeitschrift*, vol. 36, no. 3, pp. 223–229, 2000, ISSN: 00429929. DOI: 10.1007/s002310050389.

[214] Y. Belhamadia, A. Fortin, and É. Chamberland, "Three-dimensional anisotropic mesh adaptation for phase change problems", *Journal of Computational Physics*, vol. 201, no. 2, pp. 753–770, 2004, ISSN: 00219991. DOI: 10.1016/j.jcp.2004.06.022.

[215] D. Rettenmaier, D. Deising, Y. Ouedraogo, *et al.*, "Load balanced 2D and 3D adaptive mesh refinement in OpenFOAM", *SoftwareX*, vol. 10, p. 100 317, 2019, ISSN: 23527110. DOI: 10.1016/j.softx.2019.100317. [Online]. Available: https://doi.org/10.1016/j.softx.2019.100317.

[216] *blastFoam: A solver for compressible multi-fluid flow with application to high-explosive detonation*, Apr. 13, 2020. [Online]. Available: https://github.com/synthetik-technologies/blastfoam.

[217] H. Jasak, "Error analysis and estimation for the finite volume method with applications to fluid flows.", 1996.

[218] P. A. Galione, O. Lehmkuhl, J. Rigola, and A. Oliva, "Fixed-grid numerical modeling of melting and solidification using variable thermo-physical properties - Application to the melting of n-Octadecane inside a spherical capsule", *International Journal of Heat and Mass Transfer*, vol. 86, pp. 721–743, 2015, ISSN: 00179310. DOI: 10.1016/j.ijheatmasstransfer.2015.03.033. [Online]. Available: http://dx.doi.org/10.1016/j.ijheatmasstransfer.2015.03.033.

[219] V. Kumar, F. Durst, and S. Ray, *Modeling moving-boundary problems of solidification and melting adopting an arbitrary lagrangian-eulerian approach*. 2006, vol. 49, pp. 299–331, ISBN: 1040779050. DOI: 10.1080/10407790500379981.

[220] M. Pater, B. Kaaks, B. Lauritzen, and D. Lathouwers, "A numerical benchmark for modelling phase change in molten salt reactors", *Annals of Nuclear Energy*, vol. 194, no. August, p. 110 093, 2023, ISSN: 0306-4549. DOI: 10.1016/j.anucene.2023.110093.

[221] J. A. Blanco, P. Rubiolo, and E. Dumonteil, "Neutronic modeling strategies for a liquid fuel transient calculation", *International Conference on Physics of Reactors: Transition to a Scalable Nuclear Future, PHYSOR 2020*, vol. 2020-March, p. 1016, 2020. DOI: 10.1051/epjconf/202124706013.

[222] E. Cervi, S. Lorenzi, L. Luzzi, and A. Cammi, "Multiphysics analysis of the MSFR helium bubbling system: A comparison between neutron diffusion, SP3 neutron transport and Monte Carlo approaches", *Annals of Nuclear Energy*, vol. 132, pp. 227–235, 2019, ISSN: 18732100. DOI: 10.1016/j.anucene.2019.04.029. [Online]. Available: https://doi.org/10.1016/j.anucene.2019.04.029.

[223] C. Fiorina, I. Clifford, M. Aufiero, and K. Mikityuk, "GeN-Foam: A novel OpenFOAM® based multi-physics solver for 2D/3D transient analysis of nuclear reactors", *Nuclear Engineering and Design*, vol. 294, pp. 24–37, 2015, ISSN: 00295493. DOI: 10.1016/j.nucengdes.2015.05.035. [Online]. Available: http://dx.doi.org/10.1016/j.nucengdes.2015.05.035.

[224] J. Groth-Jensen, A. Nalbandyan, E. B. Klinkby, B. Lauritzen, P. Sabbagh, and A. V. Pedersen, "Verification of multiphysics coupling techniques for modeling of molten salt reactors", *Annals of Nuclear Energy*, vol. 164, p. 108 578, 2021, ISSN: 18732100. DOI: 10.1016/j.anucene.2021.108578. [Online]. Available: https://doi.org/10.1016/j.anucene.2021.108578.

[225] B. J. Kaaks, M. Rohde, J. L. Kloosterman, and D. Lathouwers, "An energy-conservative DG-FEM approach for solid–liquid phase change", *Numerical Heat Transfer, Part B: Fundamentals*, vol. 0, no. 0, pp. 1–27, 2023, ISSN: 15210626. DOI: 10.1080/10407790.2023.2211231. [Online]. Available: https://doi.org/10.1080/10407790.2023.2211231.

[226] *Simcenter star-ccm+ documentation. version 2020.2*, 2020.

[227] H. Weller, G. Tabor, H. Jasak, and C. Fureby, "A tensorial approach to computational continuum mechanics using object orientated techniques", *Computers in Physics*, vol. 12, pp. 620–631, Nov. 1998. DOI: 10.1063/1.168744.

[228] C. W. Hirt and B. Nichols, "Volume of fluid (vof) method for the dynamics of free boundaries", *Journal of Computational Physics*, vol. 39, pp. 201–225, 1981.

[229] M. Tano Retamales, P. Rubiolo, J. Giraud, and V. Ghetta, "Multiphysics study of the draining transients in the Molten Salt Fast Reactor", in *International Congress on Advances in Nuclear Power Plants (ICAPP 2018)*, 2018.

[230] J. Wackers, G. Deng, E. Guilmineau, *et al.*, "Can adaptive grid refinement produce grid-independent solutions for incompressible flows?", *Journal of Computational Physics*, vol. 344, pp. 364–380, 2017, ISSN: 10902716. DOI: 10.1016/j.jcp.2017.04.077. [Online]. Available: http://dx.doi.org/10.1016/j.jcp.2017.04.077.

[231] A. Papoutsakis, S. S. Sazhin, S. Begg, I. Danaila, and F. Luddens, "An efficient Adaptive Mesh Refinement (AMR) algorithm for the Discontinuous Galerkin method: Applications for the computation of compressible two-phase flows", *Journal of Computational Physics*, vol. 363, pp. 399–427, 2018, ISSN: 10902716. DOI: 10.1016/j.jcp.2018.02.048. [Online]. Available: https://doi.org/10.1016/j.jcp.2018.02.048.

[232] M. T. Henry de Frahan, S. Varadan, and E. Johnsen, "A new limiting procedure for discontinuous Galerkin methods applied to compressible multiphase flows with shocks and interfaces", *Journal of Computational Physics*, vol. 280, pp. 489–509, 2015, ISSN: 10902716. DOI: 10.1016/j.jcp.2014.09.030. [Online]. Available: http://dx.doi.org/10.1016/j.jcp.2014.09.030.

[233] J. Zhu, J. Qiu, and C. W. Shu, "High-order Runge-Kutta discontinuous Galerkin methods with a new type of multi-resolution WENO limiters", *Journal of Computational Physics*, vol. 404, p. 109 105, 2020, ISSN: 10902716. DOI: 10.1016/j.jcp.2019.109105. [Online]. Available: https://doi.org/10.1016/j.jcp.2019.109105.

[234] M. Dumbser and R. Loubère, "A simple robust and accurate a posteriori sub-cell finite volume limiter for the discontinuous Galerkin method on unstructured meshes", *Journal of Computational Physics*, vol. 319, pp. 163–199, 2016, ISSN: 10902716. DOI: 10.1016/j.jcp.2016.05.002. [Online]. Available: http://dx.doi.org/10.1016/j.jcp.2016.05.002.

[235] F. Vilar, "A posteriori correction of high-order discontinuous Galerkin scheme through subcell finite volume formulation and flux reconstruction", *Journal of Computational Physics*, vol. 387, pp. 245–279, 2019, ISSN: 10902716. DOI: 10.1016/j.jcp.2018.10.050. [Online]. Available: https://doi.org/10.1016/j.jcp.2018.10.050.

[236] K. T. Panourgias and J. A. Ekaterinaris, "A nonlinear filter for high order discontinuous Galerkin discretizations with discontinuity resolution within the cell", *Journal of Computational Physics*, vol. 326, pp. 234–257, 2016, ISSN: 10902716. DOI: 10.1016/j.jcp.2016.08.049. [Online]. Available: http://dx.doi.org/10.1016/j.jcp.2016.08.049.

[237] M. J. Zahr and P. O. Persson, "An optimization-based approach for high-order accurate discretization of conservation laws with discontinuous solutions", *Journal of Computational Physics*, vol. 365, pp. 105–134, 2018, ISSN: 10902716. DOI: 10.1016/j.jcp.2018.03.029. [Online]. Available: https://doi.org/10.1016/j.jcp.2018.03.029.

[238] W. Shyy, Y. Pang, G. B. Hunter, D. Y. Wei, and M. H. Chen, "Modeling of turbulent transport and solidification during continuous ingot casting", *International Journal of Heat and Mass Transfer*, vol. 35, no. 5, pp. 1229–1245, 1992, ISSN: 00179310. DOI: 10.1016/0017-9310(92)90181-Q.

[239] P. J. Prescott and F. P. Incropera, "The effect of turbulence on solidification of a binary metal alloy with electromagnetic stirring", *Journal of Heat Transfer*, vol. 117, pp. 716–724, 1995, ISSN: 15288943. DOI: 10.1115/1.2822604.

[240] M. R. Aboutalebi, M. Hasan, and R. Guthrie, "Coupled turbulent flow, heat, and solute transport in continuous casting processes", *Metallurgical and Materials Transactions B*, vol. 26B, 1995, ISSN: 10407782. DOI: 10.1080/10407780590911639.

[241] N. Chakraborty, "The effects of turbulence on molten pool transport during melting and solidification processes in continuous conduction mode laser welding of copper-nickel dissimilar couple", *Applied Thermal Engineering*, vol. 29, no. 17-18, pp. 3618–3631, 2009, ISSN: 13594311. DOI: 10.1016/j.applthermaleng.2009.06.018. [Online]. Available: http://dx.doi.org/10.1016/j.applthermaleng.2009.06.018.

[242] L. Zhang, J. Deng, W. Sun, Z. Ma, G. H. Su, and L. Pan, "Performance analysis of natural convection in presence of internal heating, strong turbulence and phase change", *Applied Thermal Engineering*, vol. 178, no. June, 2020, ISSN: 13594311. DOI: 10.1016/j.applthermaleng.2020.115602.

[243] A. Kidess, S. Kenjereš, B. W. Righolt, and C. R. Kleijn, "Marangoni driven turbulence in high energy surface melting processes", *International Journal of Thermal Sciences*, vol. 104, pp. 412–422, 2016, ISSN: 12900729. DOI: 10.1016/j.ijthermalsci.2016.01.015.

[244] L. A. Couston, E. Hester, B. Favier, J. R. Taylor, P. R. Holland, and A. Jenkins, "Topography generation by melting and freezing in a turbulent shear flow", *Journal of Fluid Mechanics*, vol. 911, pp. 1–37, 2021, ISSN: 14697645. DOI: 10.1017/jfm.2020.1064.

[245] Y. Kozak and G. Ziskind, "Novel enthalpy method for modeling of PCM melting accompanied by sinking of the solid phase", *International Journal of Heat and Mass Transfer*, vol. 112, pp. 568–586, 2017, ISSN: 00179310. DOI: 10.1016/j.ijheatmasstransfer.2017.04.088. [Online]. Available: http://dx.doi.org/10.1016/j.ijheatmasstransfer.2017.04.088.

[246] M. Faden, A. König-Haagen, S. Höhlein, and D. Brüggemann, "An implicit algorithm for melting and settling of phase change material inside macrocapsules", *International Journal of Heat and Mass Transfer*, vol. 117, pp. 757–767, 2018, ISSN: 00179310. DOI: 10.1016/j.ijheatmasstransfer.2017.10.033. [Online]. Available: https://doi.org/10.1016/j.ijheatmasstransfer.2017.10.033.

[247] D. Hummel, S. Beer, and A. Hornung, "A conjugate heat transfer model for unconstrained melting of macroencapsulated phase change materials subjected to external convection", *International Journal of Heat and Mass Transfer*, vol. 149, p. 119 205, 2020, ISSN: 00179310. DOI: 10.1016/j.ijheatmasstransfer.2019.119205. [Online]. Available: https://doi.org/10.1016/j.ijheatmasstransfer.2019.119205.

A

ESPRESSO DESIGN DRAWINGS AND FINALIZED SETUP

This appendix features additional illustrations of the ESPRESSO facility. Figure A.2 shows the design drawings used as a basis for the construction and figure A.1 shows a photograph of the completed setup.

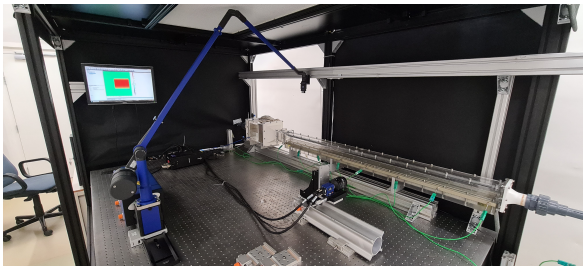

(a)

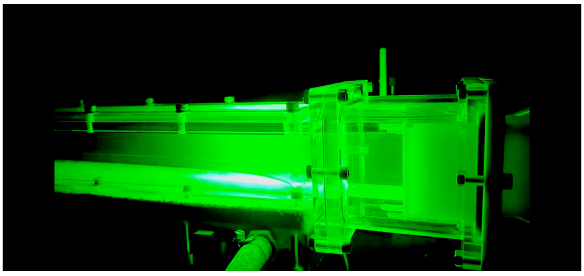

(b)

Figure A.1: Fotograph of the constructed ESPRESSO facility (a) and the ESPRESSO facility during a PIV measurement of the transient ice growth (b).

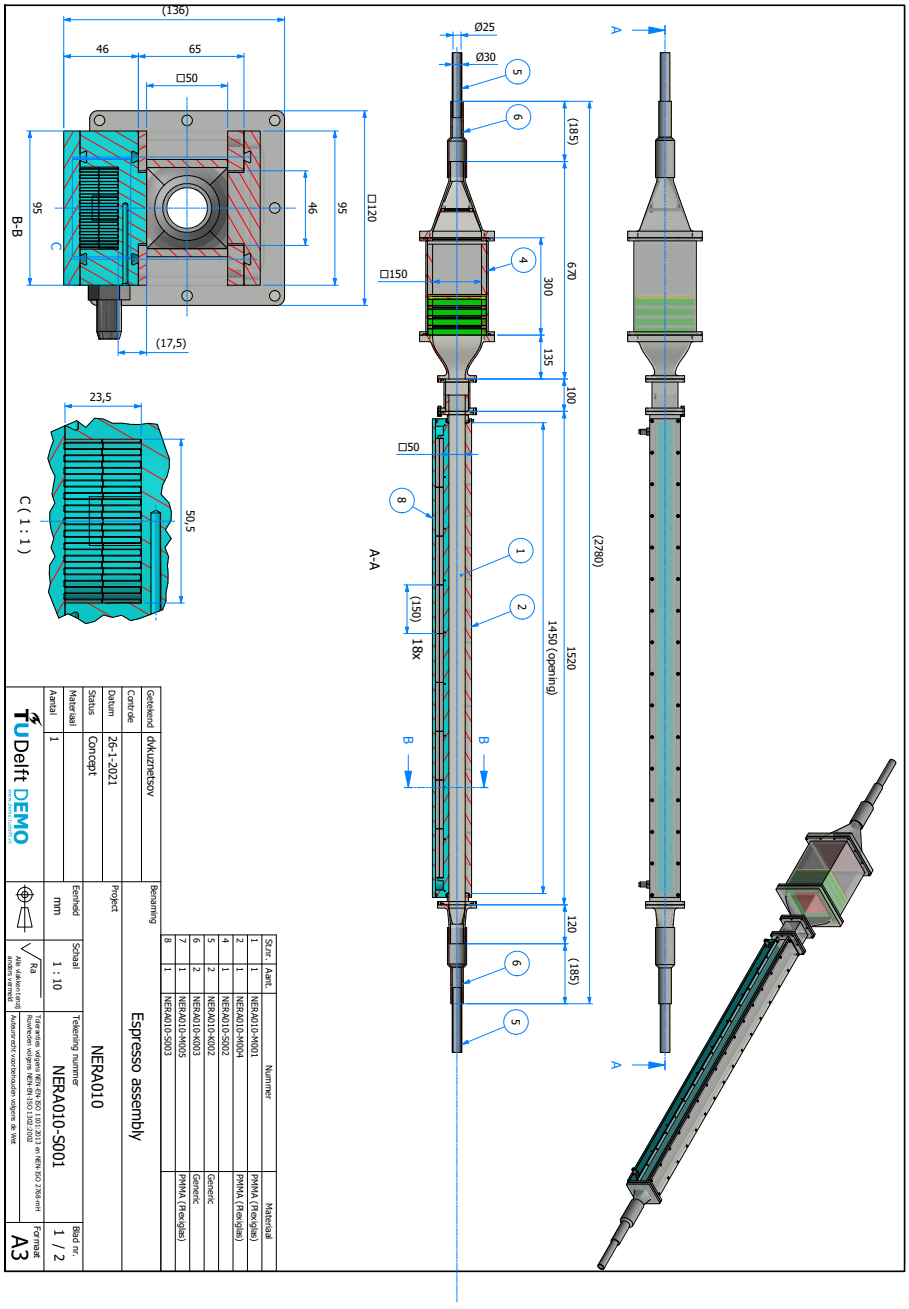

Figure A.2: Construction drawings of the ESPRESSO facility.

NOMENCLATURE

Abbreviations

AMR	Adaptive Mesh Refinement
AOI	Area Of Interest
CMOS	Complementary Metal Oxide Semiconductor
DG-FEM	Discontinuous-Galerkin Finite Element Method
DRACS	Direct Auxiliary Cooling System
EAN	Ethyl-ammonium nitrate
EDS	Emergency Drainage System
ESPRESSO	ExPeriment for REmelting and Salt SOlidification
FHR	Fluoride-salt-cooled High-temperature Reactor
FOV	Field Of View
FVM	Finite Volume Method
HTF	Heat Transfer Fluid
LIF	Laser Induced Fluorescence
MSFR	Molten Salt Fast Reactor
MSR	Molten Salt Reactor
MSRB	Molten Salt Breeder Reactor
MSRE	Molten Salt Reactor Experiment
PCM	Phase Change Material
PIV	Particle Image Velocimetry
PMMA	Poly(Methyl MethAcrylate)
PTU	Programmable Timing Unit
ROR	Region Of Reference
SAMOSAFER	Severe Accident Modelling and Safety Assessment for Fluid-fuel Energy Reactors
SWATH	Salt at Wall: Thermal ExcHanges
ULOF	Unprotected Loss of Flow

Dimensions

d	diameter (m)
D_h	hydraulic diameter (m)
H, W, L	height, width, length (m)
x, y, z	cartesian coordinate system (m)

Physical quantity

λ	wave length (nm)
ϕ	flow rate ($\mathrm{L\,s^{-1}}$) or ($\mathrm{L\,min^{-1}}$)
C	concentration $\mathrm{kg\,m^{-3}}$
g	gravitational acceleration ($\mathrm{m\,s^{-2}}$)
H	volumetric enthalpy ($\mathrm{J\,m^{-3}}$)
I	fluorescent energy per unit volume ($\mathrm{W\,m^{-3}}$)
m	mass flux ($\mathrm{kg\,m^{-2}\,s^{-1}}$)
P	power (W
p	pressure (Pa)
q	heat flux ($\mathrm{W\,m^{-2}}$
t	time (s, min or h)
T	temperature (°C or K)
u	velocity ($\mathrm{m\,s^{-1}}$)
X_s^*	relative total solid fraction

Thermophysical property

α	thermal diffusivity ($\mathrm{m^2\,s^{-1}}$)
β	thermal expansion coefficient ($\mathrm{K^{-1}}$)
μ	dynamic viscosity (Pa s)
ρ	density ($\mathrm{kg\,m^{-3}}$)
c_p	specific heat ($\mathrm{J\,kg^{-1}\,K^{-1}}$)
k	thermal conductivity ($\mathrm{W\,m^{-1}\,K}$)
L	latent heat of fusion ($\mathrm{kJ\,kg^{-1}}$)

Optics

δ_z	depth of view
f	focal length of the camera
$f^\#$	aperture of the camera
G	image intensity
M_0	magnification factor
Z_0	image distance from the center of the lens to the image plane
z_0	object distance to the effective center of the lens

Fluorescence

ϵ	fluorescence re-adsorption correction coefficient
ϕ	quantum efficiency of the dye
I_0	incident light flux ($\mathrm{W\,m^{-2}}$)

Numerical discretization (general)

Γ	boundary
γ	generalized diffusion coefficient
$\gamma_{0,1,2,\ldots}$	coefficients of the backward differentiation formulae
δ	distance from the cell center to the

	neighbouring cell center
d	vector pointing from the cell center to the neighbouring cell center
n	normal vector
s	outward-pointing face area vector
x	position vector
Ω	computational domain
ϕ	generic variable

Discontinuous Galerkin method

$[[\cdot]]$	jump operator
η	penalty parameter
$\mathbb{D}$	discrete divergence operator
$\mathbb{M}$	mass matrix
$\mathbb{N}$	operator containing implicit parts of the discrete convection and diffusion terms
f	lumped explicit terms
r	point on an element face
$\mathscr{F}$	face
$\mathscr{H}$	numerical flux function
$\mathscr{P}$	order of element
$\mathscr{T}$	element
$\mathscr{V}$	solution space
$\{\cdot\}$	average operator
d	dimension of element
v_h, w_h, q_h	test functions
w	(quadrature) weights

Adaptive finite volume method

$\mathbb{L}$	characteristic length scale
$\mathbb{T}$	characteristic time scale
$\mathscr{L}$	matrix coefficient corresponding to the linear component of the source term
A	Area (m^2
e_r	estimated numerical discretization error
F_{norm}	normalization factor
r_P	cell residual
V	Volume (m^3

Linearized enthalpy model parameters

ω	parameter to either speed up the convergence or stabilize the iteration of the enthalpy-temperature coupling scheme
$\phi_{l/s}$	liquid / solid fraction
b	small parameter to prevent division by zero
C	Darcy constant
res	residual
tol	tolerance

Dimensionless numbers

$\theta_c = \frac{T_m - T_C}{T_H - T_m}$	cooling parameter
$Pe = RePr$	Péclet number
$Pr = \frac{\mu c_p}{k}$	Prandtl number
$Ra = \frac{g\beta\Delta T H^3}{\nu\alpha}$	Rayleigh number
$Re = \frac{\rho u D_h}{\mu}$	Reynolds number
$Ri = \frac{Ra}{PrRe^2}$	Richardson number
$Stk = \frac{\rho_p d_p^2}{18\mu} \frac{u_\infty}{H}$	particle Stokes number

Other symbols

Δ	incremental difference
σ	uncertainty
C_F	correction factor
N	Number of samples
s	solid-liquid interface position

Subscripts

α	corresponding to the temperature sensitive dye
β	corresponding to the reference dye
∞	bulk
Ω	over the computational domain
c	of the cold plate
f	at the cell face
h	finite element approximation
l	liquid
m	at the melting point
P	at the cell center
p	of the particle
R	corresponding to the ratio between the two dyes
s	solid
0	initial
an	analytical
c,set	of the cold plate setpoint
c,set	of the inlet setpoint
C	cold
ex	of the exit
H	hot
in	of the inlet
num	numerical
qp	at a quadrature point
rel	relative
$sens$	sensible
$stat$	statistical
sys	systematic
tot	total

Superscripts

$*$	normalized
D	Dirichlet
i	internal / at iteration 'i'
N	Neumann
n	at time step 'n'

ACKNOWLEDGEMENTS

First and foremost, I would like to thank my promotors Dr. Martin Rohde, Dr. Danny Lathouwers and Prof. Jan-Leen Kloosterman for giving me the opportunity to pursue and complete a PhD at the Reactor Physics and Nuclear Materials group. During these four years, Martin and Danny were my daily supervisors for respectively the experimental and the numerical parts of my thesis, and they helped me to become the independent researcher I am today. In particular, Danny told me to be precise and not to be too easily satisfied with seemingly good results, which is a common trap during numerical model development and implementation. During the initial stage of my PhD were I was struggling with the complex mathematics behind the discontinuous Galerkin approach, Danny remained patient and guided me through the fundamentals during several fruitful discussions. During my meetings with Martin, his enthusiasm and curiosity often sparked new questions, potentially opening up new research directions. Martin's optimism and can-do mentality helped me to remain calm during more troublesome times, for instance when the construction of my experimental setup was facing delays or my experimental setup had broken down.

A particular shout-out goes to our lab technicians Dick de Haas and John Vlieland, as well as Dimitri Kuznetsov from DEMO, for their help in designing and building the ESPRESSO experimental facility. ESPRESSO was Dick's final large project as a lab technician at the RPNM group, since he retired in 2022. With the four of us, we had regular meetings to discuss the design, and make sure the parts remained within budget (which sometimes required creative solutions). An additional thanks goes to Pieter van den Oever and Reinier den Oudsten from DEMO, who were involved during the final construction phase.

The work in this thesis was performed in the framework of the Euratom Horizon 2020 SAMOSAFER project. I am grateful for being part of this project and by having the opportunity to meet many wonderful colleagues from the European MSFR community. In particular, I would like to thank Mateusz Pater, whom was a visiting student from DTU, Denmark (one of the SAMOSAFER observers). We worked together with me on developing a numerical benchmark for modelling phase change in molten salt reactors, which resulted in a joint paper publication. Mateusz, it was a pleasure working with you!

I was very happy to be part of the RPNM group, with it's fun and relaxed atmosphere and wonderful group of colleagues. In particular, I would like to thank Marco and Aldo who helped me get started with DGFlows and advised me on my implementation of the solid-liquid phase change model, and Sebastian, who joined as a lab technician in late 2022 and who helped me setup the LIF experimental campaign. I would like to thank my fellow PhD / postdoc colleagues Jaen, Oscar, Thomas, Daniel, Marc, Tibi, Celebrity, Andries, Denis, Nick, Ana, Jelte, Ruben, Mikolaj, Aron, Lukasz and Anand for the fun times both inside and outside the office. Especial shout-out to Nick and Ana, with whom I travelled to Berkeley, California to attend the Molten Salt Reactor boot-camp. The hike

in Yosemite national park (and the four hour drive back-and-forth) together with Nick proved to be one of the most memorable experiences during my PhD travels. I would also like to thank Jeroen, Chris, Julian and Floor, who I had the pleasure to supervise for their master's thesis or internship.

I would like to conclude by thanking my close friends and paranymphs Vincent and Justus. Their friendship is one of the most valuable things to me and I am grateful to share the defense stand with them. I would also like to thank my good friend Wouter, whom has always been there for me whenever I needed him, whether it was to take care of my cats or during times of emotional need. Another thanks to my parents Arjan and Ligia and my brothers Ysbrandt, Mante and Ruben for their support and unfavering faith in me during these four years. Finally, I would like to thank my girlfriend Xiaolin for all the support she gave me throughout my PhD. We fell in love during the first year of my (and her own) PhD and we shared our PhD journey together. Her love and companionship during this time enriched my life in ways I hadn't foreseen.

List of Publications

Journal papers

5. **B.J.Kaaks**, S. Couweleers, D. Lathouwers, J.L. Kloosterman, M. Rohde. Non-intrusive temperature measurements for transient freezing in laminar internal flow using laser induced fluorescence, *Experimental Thermal and Fluid Science* **155**, 111184 (2024). doi:10.1016/j.expthermflusci.2024.111184

4. **B.J.Kaaks**, J.L. Kloosterman, M. Rohde, D. Lathouwers. A finite volume parallel adaptive mesh refinement method for solid-liquid phase change, *Numerical Heat Transfer, Part B: Fundamentals* (2023). *Under review.*

3. **B.J.Kaaks**, D.Lathouwers, M.Rohde, J.L. Kloosterman. Transient freezing of water in a square channel: an experimental investigation, *Experimental Heat Transfer* (2023). *Under review.*

2. M. Pater, **B.J. Kaaks**, B. Lauritzen and D. Lathouwers. A numerical benchmark for modelling phase change in molten salt reactors, *Annals of Nuclear Energy* **194**, 110093 (2023). doi:10.1016/j.anucene.2023.110093.

1. **B.J. Kaaks**, M. Rohde, J.L. Kloosterman and D. Lathouwers. An energy-conservative DG-FEM approach for solid–liquid phase change, *Numerical Heat Transfer, Part B: Fundamentals* **84** (2023). doi:10.1080/10407790.2023.2211231.

Conference papers

1. **B.J. Kaaks**, J.W.A. Reus, M. Rohde, J.L. Kloosterman and D. Lathouwers. Numerical study of phase change phenomena: a conservative linearized enthalpy approach. In: *Proc. 19th International Topical Meeting on Nuclear Reactor Thermal Hydraulics (NURETH 19)*. Brussels, Belgium (2022).

ABOUT THE AUTHOR

Bouke Johannes Kaaks was born in 1996 in Rotterdam, Netherlands. During the first 9 years of his life, he moved around a lot, living in Belgium, France, England and Sweden. In 2005, he moved to Enschede in the Netherlands and moved again to Wassenaar in 2008, were he lived until graduating high school (Dutch VWO, bilingual gymnasium). In 2014, he started the bachelor's degree of Molecular Science and Technology at Delft University of Technology and Leiden University, which he graduated cum laude. This included a 6 months exchange at Ecole Polytechnique Fédérale de Lausanne, where he followed master's courses in nuclear engineering. After graduating in 2017, he enrolled in the master's program in Chemical Engineering at Delft University of Technology, where he specialized in process engineering. During his master's thesis at SCK-CEN in Belgium, he developed a special interest in (computational) fluid dynamics. His master's thesis paved the way for his PhD studies at the Reactor Physics and Nuclear Materials group, which resulted in the present dissertation. After completing the PhD degree, he will start a new position as thermal hydraulic engineer at Thorizon.